Engineering Shelf-Stable Affibody-Functionalized Hydrogels for Controlled Dual Release of Bone Morphogenetic Protein-2 and Interleukin-4

by

Jonathan Dorogin

A dissertation accepted and approved in partial fulfillment of the

requirements for the degree of

Doctor of Philosophy

In Bioengineering

Dissertation Committee:

Robert E. Guldberg, Chair

Marian H. Hettiaratchi, Advisor

Parisa Hosseinzadeh, Core Member

Kaitlin C. Fogg, Core Member

Victoria J. DeRose, Institutional Representative

University of Oregon
&
Oregon State University

Winter 2025

© 2025 Jonathan Dorogin
This work is openly licensed via CC BY-ND 4.0

DISSERTATION ABSTRACT

Jonathan Dorogin

Doctor of Philosophy in Bioengineering

Title: Engineering Shelf-Stable Affibody-Functionalized Hydrogels for Controlled Dual Release of Bone Morphogenetic Protein-2 and Interleukin-4

Wound healing is a complex and dynamic process involving the coordinated activity of multiple proteins across three stages: inflammation, proliferation, and remodeling. In the event of traumatic bone fractures, aspects of the healing cascade may be disrupted, leading to non-unions and permanent disability. Current clinical strategies for bone fracture repair deliver the osteogenic growth factor bone morphogenetic protein-2 (BMP-2) in supraphysiological doses. However, large doses lead to non-localized release and ectopic bone growth, and a single exogenous protein fails to mimic the multifaceted nature of wound healing. This work addresses these limitations by developing affinity-based protein delivery platforms using affibodies—small protein binders—to independently control the release of the anti-inflammatory cytokine interleukin-4 (IL-4) alongside BMP-2 to modulate inflammation and bone regeneration.

High- and low-affinity affibodies specific to BMP-2 or IL-4 were identified from a yeast surface display library via magnetic- and fluorescent-activated cell sorting. When conjugated into polyethylene glycol-maleimide (PEG-Mal) hydrogels, formulations with high-affinity protein-specific affibodies reduced the release of BMP-2 and IL-4. In vitro studies demonstrated that BMP-2-specific affibodies inhibited the osteogenic differentiation of C2C12 myoblasts, while IL-4-specific affibodies modulated macrophage polarization in THP-1 cells. Computational modeling predicted that BMP-2-specific affibodies interfere with BMP-2 cell receptor binding domains. A mathematical model was developed to determine factors impacting protein release from multi-component affibody-conjugated hydrogels. The model predicted that protein-specific affibody affinity and concentration tune protein release.

The affibody-conjugated hydrogels were reinforced within polycaprolactone (PCL) tubular scaffolds, enhancing the hydrogels' mechanical properties and enabling surgical implantation. Scaffold-reinforced affibody-conjugated hydrogels were lyophilized for extended shelf storage. Lyophilized hydrogels retained there mechanical and controlled release properties upon

rehydration. In vivo studies in rats demonstrated that subcutaneously implanted affibody-conjugated hydrogels locally retained more BMP-2 over 21 days compared to affibody-free hydrogels. In a 6-mm femoral defect pilot study, bone bridging occurred in 3 out of 4 rats treated with affibody-conjugated hydrogels, compared to 1 out of 3 rats treated without affibodies.

These findings underscore the potential of affibody-conjugated hydrogels as versatile platforms for independently controlled protein delivery, offering a promising strategy to emulate natural wound healing cascade and improving bone fracture repair outcomes.

This dissertation includes previously published and unpublished coauthored material.

CURRICULUM VITAE

NAME OF AUTHOR: Jonathan Dorogin

GRADUATE AND UNDERGRADUATE SCHOOLS ATTENDED:

University of Oregon, Eugene
McMaster University, Hamilton, Canada
University of Waterloo, Waterloo, Canada

DEGREES AWARDED:

Doctor of Philosophy, Bioengineering, 2025, University of Oregon
Master of Applied Science, Biomedical Engineering, 2018, McMaster University
Bachelor of Applied Science, Honours Nanotechnology Engineering, 2016, University of Waterloo

PROFESSIONAL EXPERIENCE:

Research and Development Consultant, Trillium Meditec, Jan. 2019 – Sept.2020
Special Projects Engineer, The Stronach Group, Jan 2014 – Sept 2015
Research Assistant, The Institute for Quantum Computing, Sept 2013 – Dec 2013
Manufacturing Engineering Intern, General Electric, Jan 2013 – May 2013
Technician/Analyst, Teledyne Optech, May 2012 – Sept 2012

GRANTS, AWARDS, AND HONORS:

BMES Medtronic Student Design Competition – 2nd Place, Biomedical Engineering Society, 2024
CAS Future Leaders Top 100, American Chemical Society, 2024
Cameron Innovation Fellowship, University of Oregon, 2024

Post Graduate Scholarship – Doctoral, Natural Sciences and Engineering Research Council, 2022
Travel Awards, Tissue Engineering and Regenerative Medicine International Society, 2022
Mitacs Innovation Award, Mitacs, Dec. 2020
Engineering Summertech Fellowship, The Forge at McMaster University, 2020
Trainee Travel Award, Canadian Chapter – Controlled Release Society, 2020
Norman Esch Entrepreneurial Award, University of Waterloo, 2016
Merit Entrance Scholarship, University of Waterloo, 2011

PUBLICATIONS:

Singh, A.; **Dorogin, J**.; Baker, K.; Que, J.; Schimmer, P.; Dowdall, N.; Delfino, A.; Hoare, T. Corked Microcapsules Enabling Controlled Ultrasound-Mediated Protein Delivery. ACS Appl. Mater. Interfaces 2024, 16 (41), 56199–56210. https://doi.org/10.1021/acsami.4c14615.

Dorogin, J.; Benz, M. A.; Moore, C. J.; Benoit, D. S. W.; Hettiaratchi, M. H. Recombinant and Synthetic Affibodies Function Comparably for Modulating Protein Release. Cel. Mol. Bioeng. 2024. https://doi.org/10.1007/s12195-024-00815-0.

Pan, Z.; **Dorogin, J**.; Lofts, A.; Randhawa, G.; Xu, F.; Slick, R.; Abraha, M.; Tran, C.; Lawlor, M.; Hoare, T. Injectable and Dynamically Crosslinked Zwitterionic Hydrogels for Anti-Fouling and Tissue Regeneration Applications. Advanced Healthcare Materials 2024, 13 (19), 2304397. https://doi.org/10.1002/adhm.202304397.

Fosnacht, K. G.; **Dorogin, J**.; Jefferis, P. M.; Hettiaratchi, M. H.; Pluth, M. D. An Expanded Palette of Fluorescent COS/H2S-Releasing Donors for H2S Delivery, Detection, and In Vivo Application. Angewandte Chemie International Edition 2024, 63 (24), e202402353. https://doi.org/10.1002/anie.202402353.

Svendsen, J. E.; Ford, M. R.; Asnes, C. L.; Oh, S. C.; **Dorogin, J**.; Fear, K. M.; O'Hara-Smith, J. R.; Harms, M. J.; Hosseinzadeh, P.; Hettiaratchi, M. H. Applying Computational Protein Design to Engineer Affibodies for Affinity-Controlled Delivery of Vascular Endothelial Growth Factor and Platelet-Derived Growth Factor. bioRxiv December 21, 2024, p 2024.12.18.629300. https://doi.org/10.1101/2024.12.18.629300.

Mozipo, E. A.; Galindo, A. N.; Khachatourian, J. D.; Harris, C. G.; **Dorogin, J**.; Spaulding, V. R.; Ford, M. R.; Singhal, M.; Fogg, K. C.; Hettiaratchi, M. H. Statistical Optimization of Hydrazone-Crosslinked Hyaluronic Acid Hydrogels for Protein Delivery. J. Mater. Chem. B 2024, 12 (10), 2523–2536. https://doi.org/10.1039/D3TB01588B.

Dorogin, J.; Hochstatter, H. B.; Shepherd, S. O.; Svendsen, J. E.; Benz, M. A.; Powers, A. C.; Fear, K. M.; Townsend, J. M.; Prell, J. S.; Hosseinzadeh, P.; Hettiaratchi, M. H. Moderate-Affinity Affibodies Modulate the Delivery and Bioactivity of Bone Morphogenetic Protein-2 (Adv. Healthcare Mater. 26/2023). Advanced Healthcare Materials 2023, 12 (26), 2370164. https://doi.org/10.1002/adhm.202370164.

Dorogin, J.; Townsend, J. M.; Hettiaratchi, M. H. Biomaterials for Protein Delivery for Complex Tissue Healing Responses. Biomater. Sci. 2021, 9 (7), 2339–2361. https://doi.org/10.1039/D0BM01804J.

Xu, F.; Gough, I.; **Dorogin, J**.; Sheardown, H.; Hoare, T. Nanostructured Degradable Macroporous Hydrogel Scaffolds with Controllable Internal Morphologies via Reactive Electrospinning. Acta Biomaterialia 2020, 104, 135–146. https://doi.org/10.1016/j.actbio.2019.12.038.

De France, K. J.; Badv, M.; **Dorogin, J**.; Siebers, E.; Panchal, V.; Babi, M.; Moran-Mirabal, J.; Lawlor, M.; Cranston, E. D.; Hoare, T. Tissue Response and Biodistribution of Injectable Cellulose Nanocrystal Composite Hydrogels. ACS Biomater. Sci. Eng. 2019, 5 (5), 2235–2246. https://doi.org/10.1021/acsbiomaterials.9b00522.

ACKNOWLEDGMENTS

It felt strange to write an acknowledgement for my capstone project during my Bachelor's degree. It felt more strange to write the acknowledgements for my Master's degree. Now, here we are, feeling awkward once more. At least this time, it's a terminal degree… We've made it. And by "we", it most definitely is a *WE*. This thesis and this project could not have been done without the support of so many people. I hope I don't miss any names.

To Marian, thank you for taking a chance on me. Thank you for help and invaluable guidance, and introducing me to the world of affibodies (and affinity, in general). (I think) I've grown and learned a lot over these last 4.5 years. Your expertise has allowed me to flourish as a scientist, and your writing chops have forced me to become a better writer. I was able to explore so many fun and interesting topics in our lab, and I got to take part in so many fantastic interdisciplinary studies and collaborations. Okay, I have to thank others now.

To my fantastic undergrads, Henry, Morrhyssey, and Payton – THANK YOU! I really couldn't have asked for a better group of kiddos to work with. I could write entire chapters about each of you, but that'd be too much. Thank you for making me think hard about the science, and for making me smile about non-science things. This feels impersonal. You'll each get a card.

To my lab mates, past and present – know that you'll always a soft spot in my heart. To those of you who adopted some of my ridiculous vocabulary, thank you for making the poopoo-garbage days not so poopoo-garbage, and preventing me from going cuckoo-bananas. Thank you for accepting me as I am.

To my coworkers outside the lab – keep in touch, okay? If we were collaborators on a project, thank you for your dedication and help. This PhD would not have been completed

without you. This PhD would not have been possible even with the non-collaborator bunch of you. You're all valuable in your own special ways!

To my committee members, Bob, Parisa, Vicki, and Kaitlin – Thank you for your thoughtful questions and guidance throughout my degree. Without your all-round expertise, I would not have explored the many avenues of science that I had. Also, thanks for listening to me ramble super quickly once to twice per year during our meetings.

Thank you to the Knight Campus community for letting me be highly energetic, and flourish here. I appreciate your patience for every time I didn't sign up for a course, or that I needed to order something for the GSA or the BMES. Without naming names, thank you for dealing with my international student problems (of which there were many).

Thank you to my friends, both near and far, who have been there for me during this PhD. Moving to a new country during the Covid-19 pandemic to join a new program and a new lab definitely posed its challenges, and I'm so grateful to have had each and every one of you there for me. I appreciate my Eugene/Portland folks entertaining my urge to go to concerts, go hiking, playing sports, and going to art classes. To my Toronto peeps, I'm super appreciative of you always being ready to hang out for the 3 days I would be home on my way to Europe.

To my family – thank you for your encouragement and support. This has been the longest period of time that I have been this far away. Mom, dad, Netta, Babushka, Thank you for constantly being my cheerleaders and making me feel proud even of all the miniscule achievements. Even if I don't vocalize it well, I value every moment we got to share during this PhD. I also could not have done this without my extended family, which conveniently only lived 2 hours away, instead of 8 hours of air travel. Sandra, J1, Zeli – having you here in the early goings made the transition so much easier. You opened your house to me and made us feel so

welcome. It's also been a pleasure watching Zeli grow during this PhD. To Helena and Jiři, thank you for the laughs, the visits, and the cappuccinos.

To my wonderful wife, (Dr.) Cathy – I would be remiss to not acknowledge your never-ending support. I could write an entire thesis of acknowledgements for you. From encouraging me to keep going even during my struggles, and from celebrating all of my achievements, you have been there with me every step of the way. I am so lucky to have someone like you, who is headstrong, adventurous, and ambitious. I can't wait to see what life has in store for us in the next chapter!

The investigations herein were supported in part by the National Institutes of Health, the Natural Sciences and Engineering Research Council, the Department of Defense, Collins Medical Trust, and the Wu Tsai Human Performance Alliance.

DEDICATION

To whomever is reading this, for whatever reason you're reading this. I hope you're having a good day and that get the information you're looking for.

To my uncle, Viktor, who just barely missed the completion of this degree. Rest in peace.

TABLE OF CONTENTS

Chapter Page

CURRICULUM VITAE 5
ACKNOWLEDGMENTS 8
DEDICATION 11
TABLE OF CONTENTS 12
LIST OF FIGURES 18
LIST OF EQUATIONS 19
LIST OF TABLES 19
Chapter 1 - Biomaterials for Protein Delivery for Complex Tissue Healing Responses 20
Introduction 20
The Role of Proteins in the Healing Cascade 20
Tunable Biomaterial Properties to Enhance Tissue Healing 24
Biomaterial Strategies for Protein Delivery and Presentation 26
Physical Encapsulation 27
Covalent Conjugation 29
Extracellular Matrix-based Materials 30
Engineered Protein-Material Affinities 33
Multiple Protein Delivery 35
Strategies to Improve Tissue Integration 36
Tissue Targeting Materials 37
Tissue Mimicking Materials 38
Environmentally-Responsive Materials 39
Multi-Component Strategies 41
Current Market-Available Options 44
Future Outlooks 45
Conclusions 46
Objective 47
Chapter 2 - Moderate-Affinity Affibodies Modulate the Delivery and Bioactivity of Bone Morphogenetic Protein-2 49
Abstract 49
Introduction 49
Results and Discussion 53

Magnetic-Activated Cell Sorting Depleted Over 99% of the Yeast Display Library Diversity 53
Fluorescence-Activated Cell Sorting Identified BMP-2-Specific Affibodies 53
Characterization of BMP-2 Binding to Monoclonal Yeast Affibodies 55
Collection and Characterization BMP-2-Specific Affibodies 57
Characterization of Soluble Affibody-BMP-2 Binding Interactions 58
Computational Predictions of Affibody Binding to BMP-2 60
Affibodies Do Not Impact C2C12 Cell Viability or Proliferation 61
Affibody-BMP-2 Binding Reduces Alkaline Phosphatase Activity of C2C12 Cells 62
Synthesis of Affibody-Conjugated Poly(Ethylene Glycol)-Maleimide Hydrogels 64
Encapsulation and Controlled Release of BMP-2 from Affibody-Conjugated PEG-Mal Hydrogels 65
BMP-2 Bioactivity upon Release from Affibody-Conjugated PEG-Mal Hydrogels 67
Conclusion 70
Acknowledgements 72
Materials and Methods 72
Protein Modifications 72
Yeast growth and induction 72
Magnetic Activated Cell Sorting 73
Fluorescence-Activated Cell Sorting 74
Gene Sequencing of Monoclonal Affibody Yeast 75
Monoclonal Affibody Yeast Characterization 75
Transformation of BMP-2-Specific Affibodies into *E. coli* 76
Collection and Purification of Soluble BMP-2-Specific Affibodies 77
Circular Dichroism of Pure and Soluble Affibodies 77
Native Ion Mass Spectrometry of Pure and Soluble Affibodies 78
Characterizing Binding Interactions of Pure and Soluble Affibodies via BioLayer Interferometry 78
Computational Prediction of Binding Interaction Between BMP-2 and Pure Affibodies 79
Cell Culture 79
C2C12 Cytocompatibility Assay for Affibodies 80
C2C12 Alkaline Phosphatase Activity Assay 80
Synthesis of Affibody-Conjugated Poly(Ethylene Glycol)-Maleimide Hydrogels 81
Encapsulation and Controlled Release of BMP-2 from Affibody-Conjugated PEG-Mal Hydrogels 81

Statistical Analysis 82
Chapter 3 - Recombinant and Synthetic Affibodies Function Comparably for Modulating Protein Release 84
Abstract 84
Purpose 84
Methods 84
Results 84
Conclusions 85
Introduction 85
Methods and Results 86
Bacterial expression and purification of recombinant affibodies 86
Synthesis and purification of synthetic affibodies 87
Characterization of synthetic and recombinant affibodies 87
Endotoxin removal and quantification of synthetic and recombinant affibodies 88
BMP-2 release from hydrogels conjugated with synthetic and recombinant affibodies 88
Results 89
Recombinant and synthetic affibodies display similar characteristics 89
Synthetic affibodies contain fewer endotoxins than recombinant affibodies 91
Recombinant and synthetic affibodies similarly control BMP-2 encapsulation and release 92
Discussion 93
Acknowledgements: 94
Statement of Declaration 94
Chapter 4 - Identification and Characterization of Interleukin-4-Specific Affibodies for Modulating Macrophage Polarization 95
Introduction 95
Materials and Methods 98
Yeast growth and induction 98
Affibody Identification from yeast surface display (MACS) 98
Binding Checks and Fluorescence Activated Cell Sorting 99
Gene Sequencing 100
Monoclonal Yeast Characterization 101
Transformation of IL-4-Specific Affibodies into E. coli 101
Collection and Purification of Soluble affibodies 102
Synthetic affibody synthesis 103
Characterization of affibodies 103

Computational Predictions of binding 104
Monocyte Cell culture 105
Polarization assays 105
Synthesis of hydrogels and controlled release 107
Results 108
Identification of IL-4-specific affibodies using magnetic and fluorescence activated cell sorting 108
Transformation, expansion, collection and purification of recombinant IL-4-specific affibodies 111
Synthesis, collection and purification of synthetic affibodies 112
Characterization of affibodies 112
Computational prediction of affibody docking 115
Impacts of affibodies on THP-1 polarization 116
Controlled Release from affibody-conjugated PEG-Mal hydrogels 120
Discussion 121
Conclusions 124
Chapter 5 - Factors Affecting Protein Release from Multipeptide and Multiaffibody-Conjugated Hydrogels 126
Introduction 126
Materials and Methods 130
Preparation of affibodies and peptides. 130
Preparation of hydrogels 131
Controlled Release from Hydrogels 131
JMP software inputs 132
Results 134
Affibody characteristics 134
Effects of RGD Concentration on BMP-2 Release 135
Effects of RGD and Affibody Affinity on BMP-2 Release 135
Effects of Affibody concentration on BMP-2 Release 136
Effects of Multiple Affibodies and Multiple Payloads on Protein Release 137
Normalization of data 139
Statistical analysis of combined datasets 139
Least Squares Fit Models for BMP-2 Dataset 140
Least Squares Fit Models for IL-4 Dataset 141
Random Forest Predictive Models for BMP-2 Dataset 142

Random Forest Predictive Models for IL-4 Dataset 143
Discussion 145
Conclusion 148
Chapter 6 - Shelf-Stable Melt Electrowritten Scaffold-Reinforced Affibody-Conjugated Hydrogels for Controlled Protein Delivery 150
Introduction 150
Materials and Methods 153
Affibody synthesis 153
Poly ε-caprolactone scaffold fabrication 155
Physical Characterization of Tubular MEW Scaffolds 155
Synthesis of affibody-conjugated PEG hydrogels 155
Effects of affibody and RGD peptide conjugation on hydrogel mesh size 156
Fabrication of scaffold-reinforced hydrogels 157
Lyophilization of affibody-conjugated hydrogels 157
Mechanical and rheological characterization of reinforced hydrogels 157
Controlled protein release from MEW scaffold-reinforced hydrogels 158
Mechanical and rheological characterization of lyophilized hydrogels 159
Controlled protein release from lyophilized hydrogels 159
In vivo implantation of scaffold-reinforced hydrogels 159
In vivo mineralization of scaffold-reinforced hydrogels 160
Statistical Analysis 161
Results 161
MEW scaffolds improve hydrogel integrity without affecting stiffness 162
Effect of affibodies and RGD peptides on hydrogel mesh size 164
Scaffold-reinforcement reduce cumulative protein release, but affibodies mitigate these effects 165
Lyophilized hydrogels can be rehydrated while maintaining bulk mechanical properties 166
Lyophilized hydrogels release more BMP-2 than fresh hydrogels, but at similar rates of release 168
Affibody-conjugation leads to prolonged localized protein retention in vivo 169
Affibody-conjugated hydrogels do not inhibit BMP-2 activity in the regeneration of bone 170
Discussion 171
Conclusions 173
Chapter 7 - Conclusions 175

BIBLIOGRAPHY 181

LIST OF FIGURES

Figure Page
Figure 1.1 Distinction between wound healing, tissue healing, and tissue regeneration..... 22
Figure 1.2: Proteins involved in the normal healing cascade specific to bone tissue repair..... 22
Figure 1.3: Disruption of proteins involved in the bone healing cascade impairs tissue regeneration..... 24
Figure 1.4: Overview of biomaterial strategies for protein presentation. 27
Figure 1.5: Modulation of heparin sulphation degree differentially affects diffusion of proteins from heparin-based hydrogels..... 32
Figure 1.6: Delivery of saporin into MCF-7 breast cancer cells using pH-sensitive hyaluronic acid nanogels..... 38
Figure 1.7: Use of 3D-printed, microgel-loaded microcages for protein delivery 43
Figure 2.1: Identification of BMP-2-specific affibodies using cell sorting of a yeast surface display library 54
Figure 2.2: Identification and characterization of yeast-displayed BMP-2-specific affibodies ... 56
Figure 2.3: Soluble affibody characterization..... 58
Figure 2.4: Binding interactions of soluble affibodies with BMP-2 measured by biolayer interferometry 59
Figure 2.5: Computational predictions of BMP-2 binding with affibodies or BMP receptors..... 61
Figure 2.6: Effects of BMP-2 affibodies on viability, growth, and alkaline phosphate activity of C2C12 skeletal myoblasts..... 63
Figure 2.7: Release of BMP-2 from affibody-conjugated PEG-Mal hydrogels 67
Figure 2.8: ALP activity of C2C12 cells as a function of BMP-2 release from affibody-conjugated PEG-Mal hydrogels..... 70
Figure 3.1: Properties of recombinant and synthetic affibodies 90
Figure 3.2: Endotoxin levels of recombinant and synthetic affibodies before and after endotoxin removal using spin columns..... 91
Figure 3.3: Encapsulation and cumulative release of BMP-2 from affibody-conjugated hydrogels 93
Figure 4.1: Identification of IL-4-specific affibodies 110
Figure 4.2: SDS-PAGE from Affibody_1 (A) and Affibody_2 (B) expression, collection, and purification..... 111
Figure 4.3: Characterization of IL-4-specific affibodies using MALDI, CD, and BLI..... 114
Figure 4.4: Computational docking predictions for IL4-Rα (cyan) and the Affibody_1 (magenta) and Affibody_2 (green) affibodies to IL-4 (white)..... 115
Figure 4.5: Optimization of THP-1 differentiation protocol from monocytes to macrophages . 116
Figure 4.6: TNF-α secretion from THP-1 cells after incubation with 2-200 nM recombinant affibodies for 72 hours..... 117
Figure 4.7: Gene expression of macrophages with various stimuli, quantified by RT-qPCR.... 118
Figure 4.8: Troubleshooting of THP-1s upon differentiation with PMA and incubation with various stimuli..... 120
Figure 4.9: Encapsulation efficiency and protein release experiments from affibody-conjugated hydrogels..... 121
Figure 5.1: Simple tree-based predictive models..... 129
Figure 5.2: Effects of RGD concentrations in affibody-conjugated hydrogels on BMP-2 protein release 135

Figure 5.3: Effects of 1 mM RGD in high- and low-affinity affibody-conjugated hydrogels on BMP-2 protein release 136
Figure 5.4: Effects of affibody concentration on BMP-2 protein release 137
Figure 5.5: Cumulative BMP-2 and IL-4 release from dual-affibody-conjugated PEG-mal hydrogels 138
Figure 5.6: Least squares fit models for BMP-2 dataset 141
Figure 5.7: Least squares fit models for IL-4 dataset 142
Figure 5.8: Random Forest Predictive Model for BMP-2 dataset 143
Figure 5.9: Random Forest Predictive Model for IL-4 dataset 144
Figure 6.1: Fabrication of MEW scaffolds and scaffold-reinforced hydrogels 163
Figure 6.2: Rheological properties of hydrogels with and without MEW scaffold reinforcement and conjugated affibodies 164
Figure 6.3: Effects of affibody and RGD conjugation on hydrogel mesh size. 165
Figure 6.4: Effects of scaffold reinforcement on protein encapsulation and release 166
Figure 6.5: Effects of lyophilization and rehydration on mechanical properties of affibody-conjugated hydrogels 167
Figure 6.6: BMP-2 release from fresh and lyophilized hydrogel 169
Figure 6.7: Retention of fluorescently labeled BMP-2 in scaffold-reinforced affibody-conjugated hydrogels 3 weeks after in vivo implantation in subcutaneous pockets on the backs of rats 170
Figure 6.8: Treatment of a 6-mm femoral defect with scaffold-reinforced affibody-conjugated hydrogels loaded with 5 μg of BMP-2 171

LIST OF EQUATIONS

Equation Page
Equation 2.1: Library diversity estimation as a function of CFUs, dilution, and culture volume 74
Equation 2.2: Unit conversion from mdegrees to molar ellipticity 78
Equation 4.1: Gene expression as a function of change in threshold cycles 107
Equation 5.1: Linear regression formula 128
Equation 5.2: Least Squares Fit model for linear regressions 128
Equation 6.1: Quantification of average molecular weight between crosslinks 157
Equation 6.2: Mesh size quantified by Equilibrium Swelling Theory 157
Equation 6.3: Korsmeyer-Peppas diffusion model 159

LIST OF TABLES

Table Page
Table 5.1: Independent variables for JMP model 133
Table 5.2: Dependent variables for JMP model 133
Table 5.3: Affibody dissociation constants obtained by BLI 134
Table 5.4: Independent variable values as a function of release media at different pHs 139

Chapter 1 - Biomaterials for Protein Delivery for Complex Tissue Healing Responses

From Dorogin, J., Townsend, J.M., and Hettiaratchi, M.H. 2021. Biomaterials for protein delivery for complex tissue healing responses. *Biomaterials Science*. 9(7):2339-2361.

Introduction

Tissue injuries such as critically-sized bone defects, cartilage injuries, spinal cord injuries, and chronic skin ulcers pose major clinical challenges because they do not readily heal without intervention. Functional tissue regeneration, the process of cell proliferation and tissue repair, is governed by complex mechanisms that involve a carefully coordinated cascade of cytokines, growth factors, metabolites, and multiple cell types that is difficult to effectively mimic with clinical therapies.[1] In the case of non-healing tissue defects, the normal healing paradigm (inflammation, proliferation, and remodeling) is impaired or ceases to progress due to ineffective protein signaling caused by poor tissue revascularization, injury severity, and systemic factors such as age and chronic disease.[2] The use of implantable biomaterials to provide the missing building blocks and bridge the gap in the tissue repair process has been a major focus in the field of tissue engineering. Identification of biomaterials that can effectively mimic the healing process and restore missing protein signaling observed in disrupted tissue repair may overcome limitations of current clinically-approved treatment strategies and permit robust tissue regeneration.[3]

The Role of Proteins in the Healing Cascade

A major driving factor of successful healing is the appropriately timed presentation of proteins involved in the healing cascade.[4] Although not fully understood for all tissue types, numerous proteins guide the phases of wound healing (e.g., inflammation, proliferation, and remodeling), including cytokines involved in cell recruitment and growth factors to promote cell differentiation and extracellular matrix (ECM) deposition.[5] Altogether, the wound healing paradigm involves both the breakdown of cells and tissues due to damage as well as cell proliferation leading to regeneration and remodeling. Tissue healing, like wound healing,

consists of both cellular breakdown and repair, but more broadly encompasses both wounds that occur due to distinct injury or trauma and events involved in maintaining tissue homeostasis. For instance, bone fractures and skin injuries are classified as wounds, but the gradual erosion of cartilage or demyelination of an axon are not necessarily caused by specific traumatic events. As such, bone fractures and other types of traumatic injuries may be classified as both wound and tissue healing, but gradual tissue degeneration such as axon demyelination and cartilage breakdown would only be considered tissue healing processes. Figure 1.1 depicts the distinctions between tissue regeneration, wound healing, and tissue healing, as we have described them in this review.

The healing response is initiated by damage to the tissue, which causes ruptured blood vessels to fill the injury site with blood and clotting factors that create an ECM-rich hematoma.[6] The hypoxic environment of the hematoma promotes the secretion of hypoxia inducible factor-1α (HIF-1α), which plays an important role in vascularization and angiogenesis. Platelet activation and degranulation within the newly formed ECM promotes the release of inflammatory mediators such as platelet-derived growth factor (PDGF), interleukin 1 (IL-1), IL-6, IL-8, tumor necrosis factor-α (TNFα), and transforming growth factor β1 (TGF-β1).[7] The released cytokines act to recruit additional neutrophils, which amplify the signal, and eventually promote the release of monocyte chemoattractant protein-1 (MCP-1) to attract monocytes and T-lymphocytes.[8] During the proliferative phase, progenitor cells, epithelial cells, and mesenchymal stem cells are recruited by the release of a multitude of morphogenic factors, such as fibroblast growth factors (FGFs), insulin-like growth factors (IGFs), bone morphogenetic proteins (BMPs), vascular endothelial growth factor (VEGF), and transforming growth factors (TGF-βs).[9] These cells deposit ECM molecules, such as collagen, which are ultimately replaced and remodeled to resemble the ECM composition of healthy tissue. The numerous cell types and array of protein signals that participate in the healing process highlight its complex nature and the need for precisely timed events to achieve successful tissue regeneration.

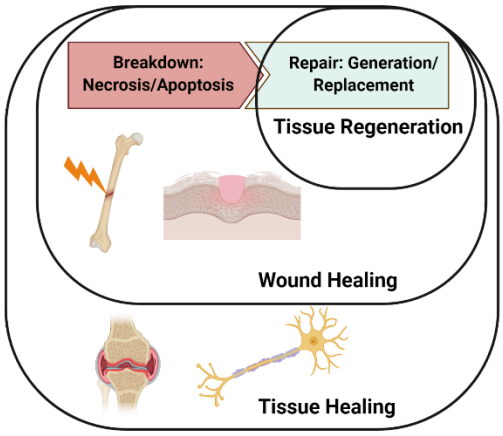


Figure 1.1 Distinction between wound healing, tissue healing, and tissue regeneration. The wound healing paradigm involves both the breakdown of cells and tissues due to trauma or injury as well as cell proliferation leading to regeneration and remodelling. Tissue healing broadly encompasses both wounds that occur due to distinct injury or trauma and events involved in maintaining tissue homeostasis. Tissue regeneration specifically refers to processes involved in the repair and replacement of damaged tissues. Figure created with BioRender.com

Figure 1.2 depicts the proteins involved in bone repair, as an example of a normal healing cascade. In bone repair, major morphogenic factors include angiogenic factors (Ang 1, FGFs, VEGF), which promote vascular network repair, BMPs, which promote osteogenic cell differentiation and mineralization, and RANK and RANKL, which promote bone remodeling. As the soft cartilaginous callus mineralizes and is remodeled, type II and type X collagen are replaced by type I collagen, the predominant ECM molecule in bone.

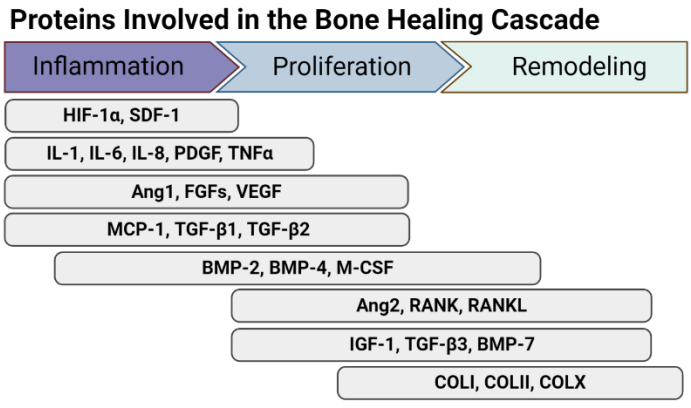


Figure 1.2: Proteins involved in the normal healing cascade specific to bone tissue repair. Successful tissue repair requires the coordinated presentation of multiple proteins. This timeline highlights proteins involved in the healing cascade specific to bone. Proteins are grouped based on time of presentation after injury and approximate phase of healing (inflammation, proliferation, remodelling). Ang: angiopoietin; BMP: bone morphogenetic protein; COL: collagen; FGFs: fibroblast growth factors; HIF: hypoxia inducible factor; IGF: insulin-like growth factor; IL:

interleukin; MCP: monocyte chemoattractant protein; M-CSF: macrophage colony-stimulating factor; PDGF: platelet-derived growth factor; RANK: receptor activator of nuclear factor κB; RANKL: receptor activator of nuclear factor κB ligand; SDF: stromal cell-derived factor; TGF: transforming growth factor; TNF: tumor necrosis factor; VEGF: vascular endothelial growth factor. Figure created with BioRender.com.

Disruption of the normal tissue repair process can be caused by a variety of factors (e.g. severity of injury, systemic disease) and can drastically alter the protein cascade, culminating in tissue injuries that do not heal (Figure 1.3). Tissues with low intrinsic regenerative capacity, such as cardiac tissue, neural tissue, and cartilage, often heal poorly, resulting in impaired function. However, tissues that normally heal readily, such as bone and skin, can also exhibit inadequate regeneration. The severity of the injury is a key factor that can disrupt the normal healing process. Critically-sized defects are tissue defects that are too large to naturally heal without additional intervention.[10–12] In the case of bone, critically-sized defects can cause inadequate hematoma formation or lack of sufficient immune and progenitor cell infiltration, resulting in fracture non-union or delayed union.[6] Critically-sized bone defects often display dysregulated inflammatory protein expression and decreased presence of vital cytokines such as PDGF, VEGF, and TGF-β1, ultimately inhibiting downstream BMP expression and bone formation (Figure 1.3A).[13,14] Significant vascular network damage caused by severe bone injury can prevent initiation of the bone repair process altogether, as the initial platelet plug formation and release of inflammatory mediators (e.g. HIF-1α, PDGF, and interleukins) does not occur (Figure 1.3B).[5] Systemic factors affecting the patient may also diminish the intrinsic regenerative capabilities of injured tissues and the overall healing process. Chronic, systemic diseases such as diabetes can disrupt the normal wound healing cascade by formation of prolonged hypoxic wounds and an impaired immune response.[15] Hypoxic wounds are generally addressed in the normal protein cascade by HIF-1α release; however, in diabetic patients, tissue vascularity is impaired by insufficient levels of growth factors such as HIF-1α and VEGF, which would normally promote vascularization and angiogenesis.[2] In bone repair, diabetes can diminish the initial inflammatory response (e.g. TNFα, PDGF, stromal derived factor-1α (SDF-1α), interleukins) and inhibit angiogenic factor secretion (Ang 1, VEGF, FGFs) – both of which can inhibit overall bone formation and maturation (Figure 1.3C). Taken together, these example scenarios of impaired bone regeneration illustrate that many factors can cause the dysregulation of proteins in the healing cascade and can disrupt the entire process of tissue regeneration.

Similarly, aberrant protein expression caused by severe injuries, poor vascular network support, and chronic diseases can also result in impaired healing in other tissues in the body.

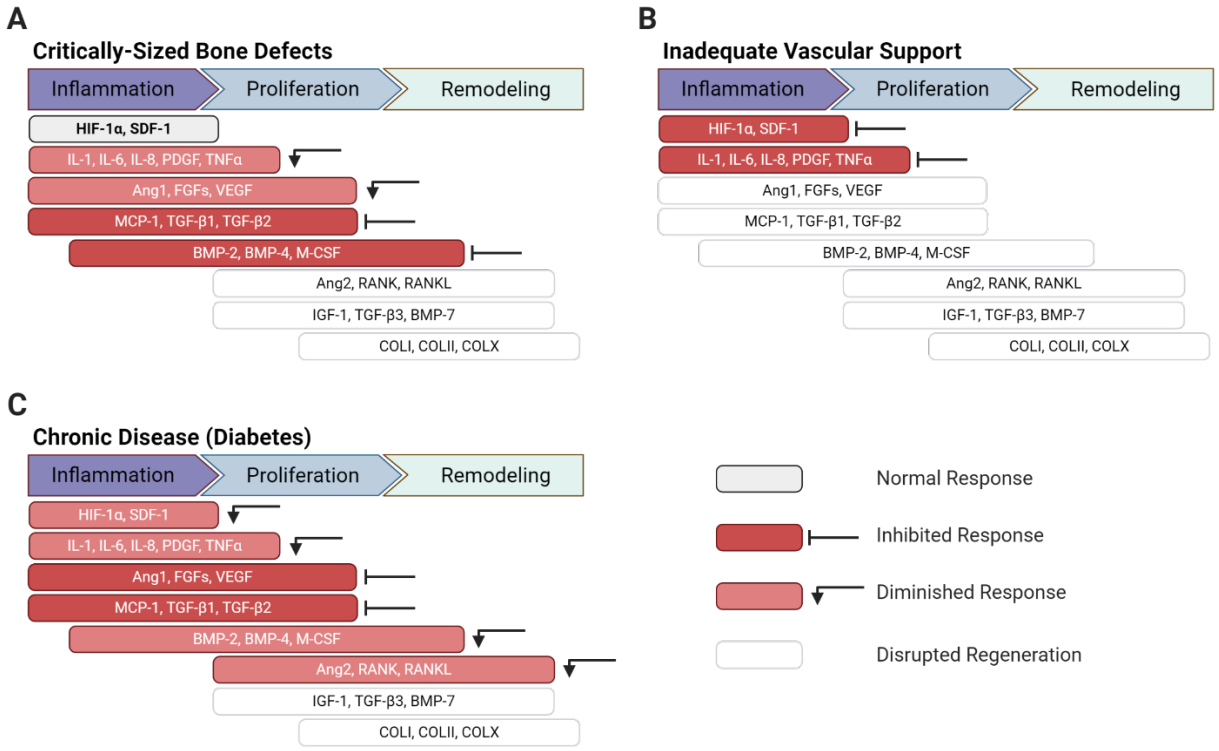


Figure 1.3: Disruption of proteins involved in the bone healing cascade impairs tissue regeneration. A number of complicating factors can dysregulate the normal healing response leading to delayed or incomplete tissue regeneration. (A) In the specific case of bone regeneration, severe, criticallysized defects reduce levels of inflammatory cytokines and angiogenic proteins and inhibit expression of osteogenic proteins. (B) Limited vascular network support inhibits the release of initial chemotactic and inflammatory mediators. (C) Chronic, systemic diseases, such as diabetes, disrupt the expression of numerous inflammatory cytokines and growth factors, while significantly decreasing levels of angiogenic proteins. The colours of the proteins indicate their response: normal response (dark grey, bold font), inhibited response (red), diminished response (light red), disrupted regeneration (light grey, light font). Ang: angiopoietin; BMP: bone morphogenetic protein; COL: collagen; FGFs: fibroblast growth factors; HIF: hypoxia inducible factor; IGF: insulin-like growth factor; IL: interleukin; MCP: monocyte chemoattractant protein; M-CSF: macrophage colony-stimulating factor; PDGF: platelet-derived growth factor; RANK: receptor activator of nuclear factor κB; RANKL: receptor activator of nuclear factor κB ligand; SDF: stromal cell-derived factor; TGF: transforming growth factor; TNF: tumor necrosis factor; VEGF: vascular endothelial growth factor. Figure created with BioRender.com.

Tunable Biomaterial Properties to Enhance Tissue Healing

Restoration of critical proteins involved in healing cascades, such as immunomodulatory cytokines, morphogenic factors, and ECM molecules, may provide the missing link to achieving

functional tissue regeneration in non-healing tissue injuries. Thus, a critical challenge that the field of tissue engineering aims to address is the need for the precise, temporal delivery of proteins. By better understanding how the protein cascade can be disrupted in various situations, new biomaterials can be engineered to effectively augment the healing process.

A number of biomaterials have been developed as therapeutic strategies to overcome disrupted healing cascades and stimulate the repair of injured and diseased tissues. Hydrogels have been extensively investigated for tissue regeneration applications due to their innate hydrophilic characteristic, which makes them suitable delivery vehicles for cells and proteins.[16,17] Hydrogels are 3D networks consisting of various natural and/or synthetic polymers, including alginate,[18] gelatin,[19] hyaluronic acid,[20] polyethylene glycol (PEG),[21] and devitalized or decellularized ECM.[22] Synthetic polymer hydrogels are highly reproducible and can be extensively functionalized for modular addition of proteins, cells, and other bioactive ligands; however, since synthetic polymers are typically biologically inert, multiple functional groups may be required to achieve a desired biological response.[23] In contrast, natural polymer hydrogels are biocompatible, biodegradable, and have cell-adhesive ligands and natural affinities for proteins, but are less reproducible due to batch-to-batch variability that affects material tunability.[24] Hydrogels typically have highly tunable physical characteristics that influence their behavior in the body, such as crosslinking density, polymer molecular weight, mesh size, and stiffness.[25] These physical characteristics can significantly impact therapeutic protein delivery and tissue regeneration. Common protein delivery strategies from hydrogels include encapsulation in a degradable polymer or immobilization using chemical or physical interactions.[26] Encapsulation methods where the protein does not interact with the material (e.g. minimal non-covalent interactions) rely on the crosslinking density and associated pore size of a hydrogel to control protein diffusion from the material and can impede cell migration if the pore size is too small.[27] Protein encapsulation typically provides limited controlled protein release and subsequently exhibits burst release kinetics.[28] Alternatively, protein immobilization strategies using chemical or physical interactions can drastically improve protein retention, stability, and enable controlled delivery.[29] Polymer molecular weight can directly influence cell response due to cell-material interactions and alter the degradation profile of the hydrogel, which can also affect protein delivery and presentation.[30] Hydrogel stiffness can influence cell behavior due to cell

mechanotransduction and alter interactions with the surrounding tissue, especially if the defect is load bearing.[31]

Engineering biomaterials that can adapt to changes in the complex injury environment during tissue repair may augment the healing process and overcome dysregulation of protein presentation in the healing cascade. This review highlights the evolution of the field toward creating biomaterials that precisely control protein delivery and stimulate tissue regeneration using a variety of methods, with a focus on addressing complex and dynamic injury environments. The framework of the following sections explores biomaterial strategies that deliver and present proteins involved in healing cascades, tissue targeting and mimicking strategies, materials that can be triggered by environmental cues, and integrated strategies that leverage multiple biomaterial properties to improve protein delivery. Recommendations for future work and strategies to accelerate biomaterial development conclude the review. Improvements in biomaterial design to better address complex injury environments will ultimately provide a better standard of patient care and expand our understanding of both normal and aberrant tissue repair processes.

Biomaterial Strategies for Protein Delivery and Presentation

Given the importance of coordinated protein expression in tissue repair, a common approach to restore normal healing mechanisms in injured tissues is to deliver exogenous, recombinant proteins to the tissue injury site to introduce or augment a missing biological function. Growth factors that stimulate cell differentiation, vessel formation, and ECM deposition, such as VEGF, BMPs, and FGFs, are often chosen for delivery. The materials chosen as protein delivery vehicles can also significantly impact the efficacy of the treatment by influencing both temporal and spatial protein presentation through interactions between the protein and biomaterial matrix.[32] The chemical and physical properties of biomaterials can be manipulated to control the presentation of various proteins. Extended local presentation of bioactive proteins within injury sites is necessary for lengthy wound healing processes, and numerous biomaterial strategies have been developed to ensure sufficient local protein retention within injury sites (Figure 1.4).

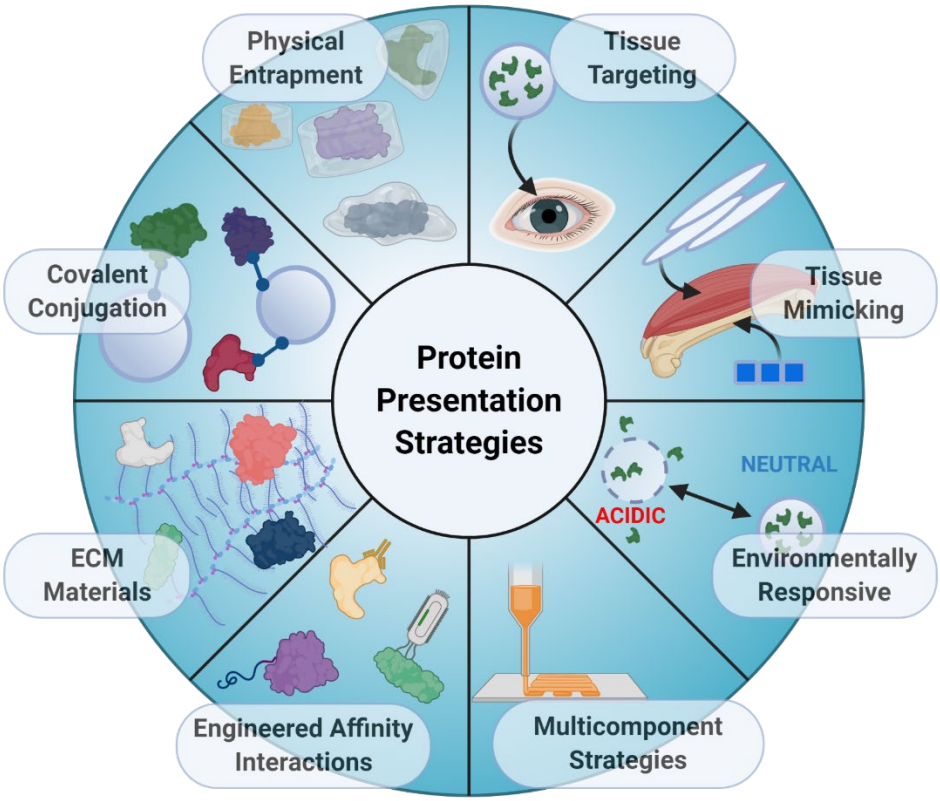


Figure 1.4: Overview of biomaterial strategies for protein presentation. The left side of the wheel identifies several biomaterial strategies for protein delivery and presentation, including the physical entrapment of proteins in hydrogels, covalent conjugation of proteins to materials, use of ECMbased materials with natural affinities for proteins, and engineered affinity interactions using antibodies, peptides, and phage display platforms. The strategies on the right side of the wheel can be broadly categorized as strategies to improve tissue integration, including tissue targeting, tissue mimicking, and environmentally-responsive materials. Multicomponent strategies combine bioengineering techniques, such as 3D printing, with other protein presentation strategies. Figure created with BioRender.com

Physical Encapsulation

Physical encapsulation of proteins, which does not rely on non-covalent or covalent interactions, typically controls protein release through porosity of the matrix (i.e. mesh size) and material degradation kinetics.[33] Physical entrapment of proteins can provide predictable, reproducible protein release in vitro, where the variables affecting protein release can be easily controlled. Hydrogel mesh size and degradation rate are both controlled by polymer molecular weight. In a

study using PEG hydrogels, the release of FGF-2 and BSA was accelerated in hydrogels made from higher molecular weight PEG polymers (4 kDa), which had a larger mesh size and degraded faster than their smaller counterparts (2.5 kDa).[34] Protein release rate following physical encapsulation in a hydrogel is inversely proportional to the size of the payload and directly proportional to the pore or mesh size of the biomaterial.[35,36] The Kloxin group demonstrated that mesh size of a hydrogel could be used to predict release and retention of proteins of different sizes.[36] Using a PEG-based library of materials, they systematically demonstrated that the elasticity and swelling of the material directly correlated to mesh size and that mesh size, in turn, impacted the release of a range of proteins, including aprotinin (7 kDa), myoglobin (17 kDa), bovine serum albumin (BSA) (66 kDa), lactoferrin (77 kDa), and thyroglobulin (663 kDa). Block copolymers can also be manipulated for controlled protein release by modifying the ratio of comonomers, as is typically done with polyesters.[37,38] For example, increasing the ratio of lactic acid to glycolic acid (LA:GA ratio) increases hydrophobicity and reduces the rate of hydrolysis, resulting in nanoparticles that degrade more slowly.[39,40] However, protein activity may potentially be affected by the choice of encapsulating polymer as harsh organic solvents may be required for fabricating polymeric nanoparticles. Despite the ability to tune the release kinetics of encapsulated proteins by changing material properties, physical encapsulation of proteins in biomaterials can often lead to burst release pharmacokinetics in vivo, resulting in rapid diffusion of proteins away from the injury site and reduced therapeutic efficacy.[41] PLGA nanoparticles are commonly used for protein delivery, but have a tendency to exhibit burst release of molecular cargo. Burst release kinetics can be mitigated by encapsulating smaller nanocarriers in larger bulk hydrogels to slow protein diffusion following release from the nanocarrier.[42–44] Pakulska, et al. encapsulated stromal-derived factor-1α (SDF-1α), neurotrophin-3 (NT-3), and brain-derived neurotrophic factor (BDNF) in PLGA nanoparticles which were then suspended in a bulk hyaluronic acid and methylcellulose hydrogel.[44] Similarly, Mancipe Castro, et al. entrapped rhodamine B in PLGA nanoparticles and suspended them in PEG microspheres.[43] Both studies demonstrated that the dual-layer system prevented burst release from PLGA nanoparticles as they degraded. Pakulska, et al. further noted that the method of drug entrapment within the composite material (i.e. encapsulation or adsorption to PLGA) did not significantly impact the release kinetics of the payload.

Covalent Conjugation

Covalently tethering proteins to a biomaterial through irreversible chemical bonds provides increased spatiotemporal control over protein presentation in vivo compared to physical encapsulation.[45,46] Covalent conjugation strategies are valuable in situations where long-term protein presentation is necessary to elicit a sustained cellular response in vivo. Protein immobilization is often achieved using amine-reactive chemistry, which requires an amine group available for nucleophilic attack, or carboxyl-reactive chemistry, which requires a carboxyl group for electrophilic attack. Proteins can be immobilized on polymers such as poly(lactic-co-glycolic) acid (PLGA) via carbodiimide crosslinker chemistry, using N-hydroxysuccinimide (NHS) and 1-Ethyl-3-(3-dimethylaminopropyl)carbodiimide (EDC) coupling.[47] Building upon this approach, Wang, et al. recently demonstrated enhanced retention of VEGF on mussel-adhesion protein (MAP)-coated stents through carbodiimide chemistry.[48] MAP, which is rich in 3,4-dihydroxy-L-phenylalanine (Dopa), has immense cell-adhesive capacity.[49] MAP substrates coated onto a silicon wafer were dip-coated in VEGF, which was immobilized using EDC/NHS chemistry. Substrates containing crosslinked and non-crosslinked MAP, as well as immobilized and free VEGF were tested. The tethered VEGF maintained its bioactivity, resulting in increased spreading of endothelial cells, while crosslinking of the MAP increased its retention on the stent.[48]

Although covalent conjugation of proteins to materials prolongs local protein presentation within an implantation site, this strategy may reduce overall protein bioactivity by causing protein denaturation during processing or interfering with the ability of proteins to interact with cell integrins and receptors.[50–55] For example, modification of collagen I with EDC reduced cell adhesion by inhibiting cationic cell interactions with collagen's integrin binding domains.[50] Moreover, several studies have demonstrated that non-specific, stochastic conjugation of primary amines in proteins using NHS esters can significantly decrease protein bioactivity.[56,57] As a result, site-specific protein modification has recently gained popularity as a method to install functional groups on proteins without decreasing protein bioactivity. Site-specific labeling techniques enable rational placement of functional groups, while avoiding enzymatic and receptor binding sites on proteins. For an in-depth review of methods to achieve site-specific protein modification, we recommend the recent publication of Shadish et al.[58]

Extracellular Matrix-based Materials

ECM molecules that naturally occur within tissues, including glycosaminoglycans (GAGs), collagens, and fibronectin, play a significant role in modulating protein presentation by retaining and releasing a variety of proteins. Morphogenic proteins involved in developmental processes, such as BMPs, TGFs, IGFs, and FGFs, must be presented with precise spatiotemporal control to enable patterning of the developing embryo, and thus retain the ability to interact with multiple ECM molecules.[59–61] The many cationic domains of these proteins, termed "heparin binding proteins," interact with the anionic sulphate groups on a variety of GAGs, but often interact with higher affinity to heparin due to its increased degree of sulfation compared to other GAGs.[62] ECM-based materials use electrostatic payload-vehicle interactions that mimic the natural affinity interactions between proteins and ECM in the body to provide controlled protein delivery. These electrostatic interactions enhance retention of charged biomolecules compared to purely physical encapsulation with minimal protein-material interactions.[63] Heparin binding proteins bind reversibly to biomaterials containing sulphated GAGs (heparin[10,64,65] and chondroitin sulphate[66,67]), non-sulphated GAGs such as hyaluronic acid[68–70], other natural polysaccharides derived from plants and animals (alginate[71] and chitosan[72,73]), and combinations of these polymers.[74–76] Sulphated GAG-based biomaterials interact with a variety of protein partners (heparan sulphate to FGF-2, VEGF-A165, and SDF-1α[65,77]; heparin to BMP-2[78,79]; chondroitin sulphate to TGF-β1 and BMPs[66]). The abundance of heparin and heparan sulphate in both normal and injured tissues strongly suggests that supplementation with GAG-based biomaterials may improve the efficacy of a protein therapy.[65,80]

The protein-material affinity interactions of ECM-based biomaterials were traditionally thought to be difficult to modify, as they involve complex interactions between the repeating units on the ECM molecules and specific tertiary structures of the protein.[62] However, the protein binding properties of GAG-based, electrostatically-driven biomaterials can be tuned by modifying their sulphate content, which changes the electrostatic interactions between the protein and material and subsequently alters protein release from the material.[70,77,81–83] Sulphating non-sulphated molecules such as hyaluronic acid and alginate increases protein retention, while desulphating GAGs such as heparin increases protein release. Sulfation of hyaluronic acid can also slow biomaterial degradation by reducing the availability of octosaccharides necessary for effective

degradation by the enzyme hyaluronidase. Limasale, et al. systematically manipulated the sulfation levels of heparin to assess the effect of sulfation on diffusion rate of proteins from a composite PEG/heparin-based hydrogel (Figure 1.5). They demonstrated precise control over the binding of VEGF-165 to the biomaterial with higher degrees of sulfation leading to increased protein retention. This strategy provided negligible control over the release kinetics of epidermal growth factor (EGF) and VEGF-121, the non-heparin binding isoform of VEGF, due to their low affinity for heparin, while additional heparin-binding proteins such as SDF-1α demonstrated similar, sustained release kinetics to VEGF-165. Although ECM-based biomaterials with affinities for proteins may improve the local retention of specific proteins within injury sites, this does not always translate to improved therapeutic outcomes.[64] Andrews, et al. demonstrated prolonged in vitro retention of BMP-2 in a sulphated GAG-based (chondroitin sulphate) scaffold compared to a collagen scaffold; yet, the overall impact on bone healing was comparable between the scaffolds after 12 weeks.[66] Since protein release is dependent on both the overall degradation rate of the scaffold and the strength of the electrostatic interactions between the protein and material, the slower-degrading collagen matrix with lower BMP-2 affinity likely resulted in similar protein release to the faster-degrading, GAG-based scaffold.

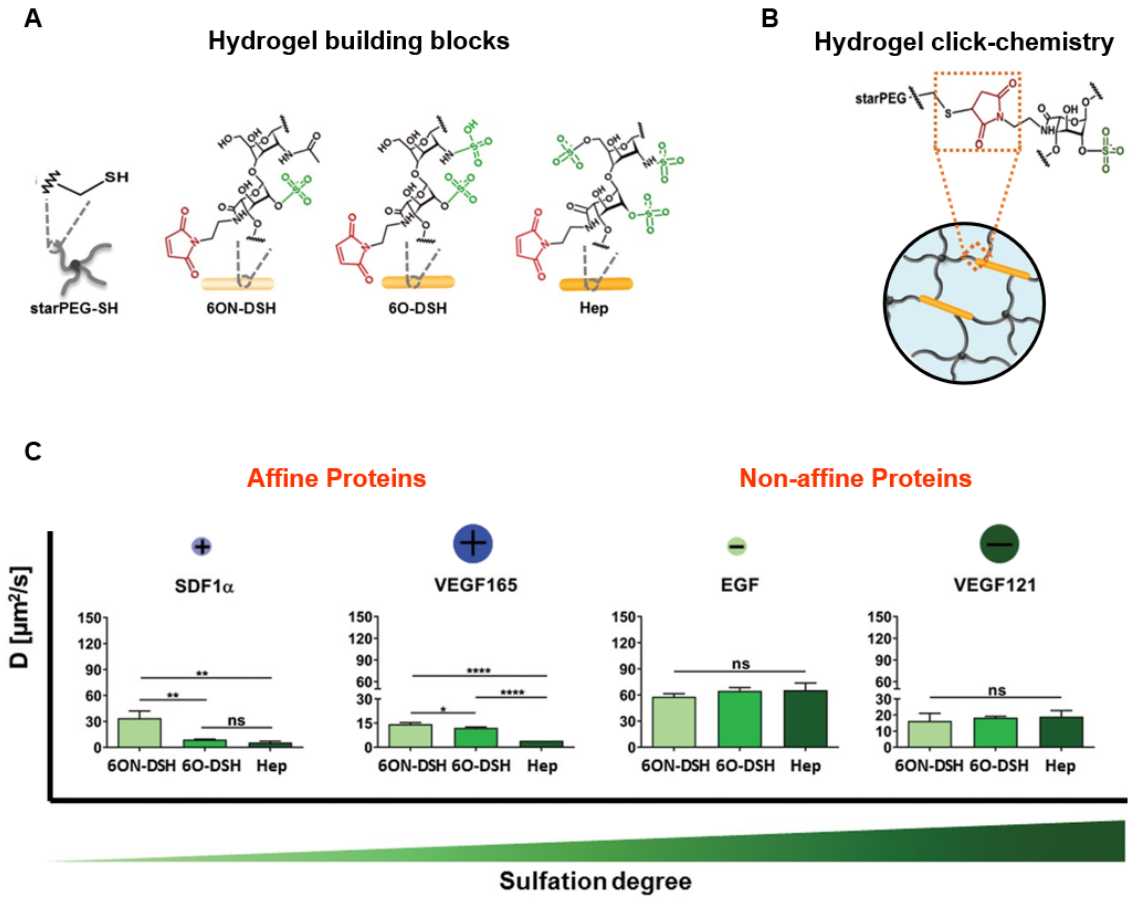


Figure 1.5: Modulation of heparin sulphation degree differentially affects diffusion of proteins from heparin-based hydrogels. (A) Hydrogel building blocks consist of thiol-functionalized starPEG (starPEG-SH) and maleimide-functionalized heparin (Hep) or heparin derivatives with selective degrees of sulphation. (B) Click chemistry creates covalent bonds between the starPEG-SH and maleimide-functionalized heparin and heparin derivatives. (C) Effect of heparin sulphation pattern on the diffusion of heparin affine and nonaffine proteins with heparin-based hydrogels. Heparinbinding proteins SDF-1α and VEGF-165 exhibited slower diffusion in hydrogels containing heparin with a higher degree of sulphation. Conversely, the diffusion of non-heparin-binding proteins EGF and VEGF121 was not affected by degree of heparin sulphation. Diffusion of the proteins through the heparin-based hydrogels was measured using fluorescence recovery after photobleaching (FRAP). "ns" stands for not significant, *p < 0.05, **p < 0.01, ***p < 0.001, and ****p < 0.0001. Reproduced from ref. 77 with permission from Wiley-VCH, copyright 2020

Since many proteins interact with ECM molecules, multiple proteins may interact with the same biomaterial, which may be advantageous for developing strategies to deliver multiple ECM-binding proteins.[84,85] However, the promiscuous binding of heparin and other ECM molecules to a variety of heparin binding proteins can also be disruptive when these biomaterials are delivered in vivo and non-specific, competitive binding to abundant serum proteins can result in accelerated payload release.[86] Thus, caution should be exercised when employing ECM-based biomaterials, which could unintentionally bind additional proteins involved in other cellular

processes, resulting in off-target effects and unpredictable protein release in vivo. Improving the specificity of protein-material interactions may improve the ability of biomaterials to more precisely control protein delivery in vivo and target specific phases of the healing cascade.

Engineered Protein-Material Affinities

More sophisticated affinity interactions have been engineered between proteins and materials to overcome the limited specificity and tunability of natural ECM-based materials. Antibodies specific to proteins of interest can be covalently conjugated[87] or physically adsorbed to biomaterials.[48,88] Alternatively, high affinity molecules can be developed to achieve extremely specific protein-material interactions and can be produced inexpensively compared to antibodies.[89–91] Some notable strategies include peptides that directly bind to the protein of interest,[88,90,92] the synthesis of fusion proteins, consisting of a peptide- or ECM-binding domain and functional protein domain,[91,93–97] and DNA aptamers that contain a protein sequestering component and a cell adhesive component that provides localized cargo release.[98,99] A well-characterized fusion domain used to control protein delivery is the Src homology 3 (SH3) domain, which naturally binds to a variety of short peptide sequences with affinities that enable sustained protein release. The release of SH3 fusion proteins from hydrogels can be mediated by immobilizing high-affinity or low-affinity SH3 binding peptides onto the polymer network. This strategy has been extensively studied for the delivery of fusions of FGF-2,[100] chondroitinase ABC,[57,101,102] ciliary neurotrophic factor,[96] and fibronectin,[103] in both in vitro and in vivo applications. Small antibody-mimetic proteins, such as affibodies have variable regions that can be modified to bind to specific proteins at a broad range of affinities.[104] While they have been primarily used for tissue targeting, recent advances have integrated protein specific affibodies into methylcellulose hydrogels to tune the release of fibroblast growth factor-2 (FGF-2), pigment epithelium growth factor (PEGF), and insulin-like growth factor (IGF).[92,105]

An interesting alternative approach to enhance the therapeutic efficacy of exogenous growth factors is to increase their binding affinity to the target cell population instead of improving their retention within the delivery vehicle. Mochizuki, et al. integrated a syndecan binding peptide into VEGF and the PDGF dimer PDGF-BB.[32] The transmembrane proteoglycan syndecan demonstrated a higher affinity for growth factors expressed with syndecan-binding domains compared to unmodified growth factors and BSA, enabling higher affinity interactions between

the cells and growth factors. This modification resulted in tonic signaling (i.e. continuous, low-intensity signaling) between PDGF and VEGF and their receptors, leading to extended downstream Akt and ERK phosphorylation and enhanced bone regeneration. Tonic signaling is beneficial in the wound healing cascade, as it overcomes the short half-life and loss of bioactivity commonly associated with exogenous protein delivery, though the inability to turn off signaling may cause adverse effects after the natural wound healing process has concluded.[106]

Biomaterials for Endogenous Protein Sequestration

Although protein delivery is a promising strategy to stimulate tissue repair, poor control over protein release kinetics in vivo can reduce the effective protein dose within the injury site, necessitating the use of supraphysiological protein doses to stimulate lengthy healing processes. "Empty" biomaterials can be delivered to sequester endogenous proteins and biomolecules that are involved in tissue repair but are usually present in the body in concentrations that are too low to improve the healing response. This strategy creates a biomolecule depot within the site of interest and mimics how ECM molecules in tissues naturally sequester and present proteins to create morphogen gradients during development and regeneration. Heparin-based and heparin-sequestering biomaterials have been used to amplify the effects of heparin-binding growth factors, such as FGF-2 and IGF binding proteins, within in vitro cell culture environments.[107,108] Crispim, et al. used protein-binding peptides to sequester and present endogenous BMP-2 to promote integration of a ligament graft and endogenous TGF-β1 to improve vascularization and cell recruitment following subcutaneous implantation of polycaprolactone (PCL) films.[88,90] PEG-based biomaterials functionalized with 3-(acrylamido)-phenylboronic acid have been developed to sequester adenosine, a potent signaling molecule, within bone injury sites.[109] Phenylboronic acids are especially useful in sequestration applications because they form dynamic boronate-ester bonds, allowing them to attract many different biomolecules. This functionalized PEG biomaterial has demonstrated utility in both sequestering endogenous adenosine and delivering exogenous adenosine, resulting in improved fracture healing. Moreover, this strategy is responsive to the dynamic injury environment, as adenosine levels within the biomaterial gradually return back to physiological levels during fracture healing.

Multiple Protein Delivery

Since healing is a naturally complex process, requiring many bioactive components, the delivery of multiple proteins involved in tissue repair can lead to more effective healing. Replacing single and dual growth factor delivery strategies with the delivery of more complex combinations of relevant proteins involved in the healing cascade is an emerging focus of protein delivery for tissue repair. Liu, et al. co-delivered stem cells with a "cocktail of growth factors" consisting of IGF-1, HGF, and PDGF-BB for myogenesis, NGF and FGF-2 for neurogenesis, and VEGF for angiogenesis in a hydrogel to assess the impact of multi-protein presentation.[110] The combinations of proteins delivered achieved myogenesis, neurogenesis and angiogenesis; however, multiple growth factor delivery was not drastically better than the presentation of individual growth factors. Although release of these heparin binding proteins was controlled by a heparin-containing hydrogel, regenerative processes typically require sequential presentation and gradients of proteins. Thus, the results observed in this study may be due to the limited ability of the biomaterial to spatially and temporally control protein release. This suggests that the co-delivery of multiple growth factors for tissue repair may require additional focus on sequence and timing of protein delivery in the future.

Several strategies have been developed to achieve sequential protein delivery using several different mechanisms, including material degradation and logic-based systems. These include the use of multi-layered hydrogels containing different proteins in each layer and nanoparticles fabricated by layer-by-layer deposition of proteins and polymers.[111,112] Lee, et al. contained and released VEGF and BMP-4 in a sequential manner by encapsulating BMP-4-containing microparticles within a VEGF-containing hydrogel, resulting in a burst release of VEGF and sustained release of BMP-4. Shah, et al. developed nanolayered constructs containing physiologically relevant amounts of BMP-2 and PDGF-BB in each layer with controlled degradation kinetics, which led to effective bone regeneration over 2 weeks.[113] In these examples, the release kinetics of the proteins were based on material degradation and diffusion kinetics and not in response to specific cues from the surrounding microenvironment. In contrast, logic-based release of proteins can be programmed to respond to microenvironmental cues and external triggers. Several groups have demonstrated control over the release of specific payloads by providing light, pH, or hydrolysis triggers.[114–116] These stimuli enable precise, on-demand protein delivery in vitro, but may be challenging to implement in vivo as the triggers mentioned

are either endogenous stimuli that require many satisfying conditions throughout the body or difficult to systemically administer.

Ultimately, the choice of protein delivery method depends on the duration of protein presentation required and surrounding environment. We have described a myriad of recent advances available to tune protein retention and release from biomaterials in vivo that can be tailored to a variety of injury types and healing scenarios. Tissue repair that requires long-term protein presentation and precise spatial control may benefit from covalent protein immobilization or protein sequestration with high-affinity protein-material binding interactions. Conversely, the delivery of proteins involved in cell recruitment to injury sites may be more effective if rapidly released from biomaterials to promote long range chemotaxis. Finally, sequential protein delivery may be necessary to mimic the phases of the healing cascade (inflammation, proliferation, and remodeling) and can be achieved using composite materials that respond to different stimuli or layer-by-layer protein/polymer deposition.

Strategies to Improve Tissue Integration

We have described a variety of approaches to enhance protein-biomaterial interactions for effective protein delivery. However, there are many other strategies to improve the efficacy of protein delivery for tissue repair that rely on mediating the interactions between the biomaterials and surrounding tissue, including tissue targeting,[117] tissue mimicry,[118] and stimuli-responsive materials. These strategies increase the ability of a biomaterial to respond to changes in the surrounding tissue that occur during injury and healing. Broadly, tissue targeting biomaterials leverage interactions with unique biochemical markers of an injury site to localize therapeutics, tissue mimicking biomaterials aim to optimize the biophysical congruency between the therapeutic system and the injury site, and stimuli-responsive materials respond to internal or external stimuli to trigger protein delivery within the effective therapeutic window. There is often overlap between strategies that enhance protein-biomaterial interactions and tissue targeting, mimicry, and stimuli-responsive material strategies, and the integration of these approaches have led to key developments in the field, which are discussed below.

Tissue Targeting Materials

Biomaterials fabricated with specific ligands or binding partners enable a material delivered locally to bind specifically to a target cell or tissue,[117,119] thereby enhancing local material retention. Biomaterials containing target receptors[63,117] or synthetic peptides[95,119,120] have been fabricated to bind to a variety of tissues. A common approach is to target abundant ECM in the tissue of interest, which has been pursued with both collagen-binding domains for targeting biomaterials to bone,[121] solid tumors,[122] inflammatory sites,[91] and hyaluronic acid-binding domains for targeting tumors[123,124] and cartilage.[46] Directed evolution platforms such as phage display can also be used to evolve peptides or small protein domains that bind strongly to specific tissues. In phage display, bacteriophages express proteins on their surface, enabling sorting and mutagenesis to yield a protein binding partner with specific binding characteristics.[125] Phage display has been used to identify a variety of peptides that bind to cardiac and skeletal muscle[126,127] and the mineral component of bone.[128,129] Binding peptides for specific biomarkers have also been valuable for targeting other tissues, such as the intra-articular spaces within joints, from which drugs are often rapidly cleared. Mancipe Castro, et al. fabricated PEG-based hydrogels with cartilage and synoviocyte targeting peptides, which demonstrated improved bulk material retention in relevant cell lines in vitro and local release of drug in the intra-articular space compared to biomaterials containing non-specific binding domains.[43] HA-based hydrogels have demonstrated efficacy for tumor targeting, as many cancer cells overexpress the CD44 glycoprotein that binds to HA for cell attachment.[82,130] Ding, et al. developed pH-sensitive HA hydrogels that promoted MCF-7 cancer cells binding and endocytosis, allowing the HA hydrogels to disassemble within the low pH environment of the cell (Figure 1.6).[130] This method enabled the intracellular delivery of the otherwise membrane-impermeable protein saporin, which kills cancer cells by inactivating ribosomes. Overall, the use of tissue targeting strategies results in more directed treatment strategies with outcomes that will continue to improve as the specificity and accuracy of the targets increases.

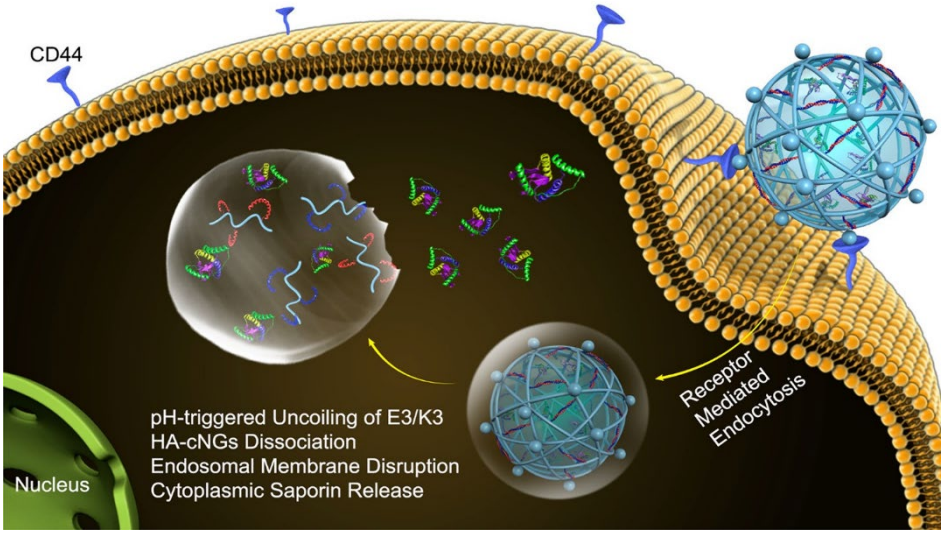


Figure 1.6: Delivery of saporin into MCF-7 breast cancer cells using pH-sensitive hyaluronic acid nanogels. MCF-7 cells overexpress CD44, which has a high affinity for hyaluronic acid (HA). This enables binding and subsequent uptake of the coiled-coil peptide-crosslinked HA nanogels (HAcNGs) by MCF-7 cells. Upon endocytosis, HAcNGs dissociate in the acidic conditions of the endosomes of the cell, due to the pH-sensitive dissociation of the crosslinker, releasing saporin. Reproduced from ref. 127 with permission from the American Chemical Society, copyright 2018.

Tissue Mimicking Materials

Biomaterials that aim to delivery proteins to regenerate tissues with complex architectures may better integrate into surrounding tissues if designed to mimic the physical or biochemical attributes of the surrounding native tissue. In doing so, the biomaterial scaffold can temporarily or permanently contribute to the physiology of the tissue. Engineered tissue scaffolds are often designed to match tissue mechanical properties (e.g. stiffness, strength, elasticity), as a mismatch of mechanical properties can lead to stress shielding,[131] increased fibrosis,[132] or early failure. Alignment of the fibers of the biomaterial is important in the fabrication of biomimetic ligaments[88,118,133,134] and muscles,[135,136] as effective cell growth and tissue function requires matching both native tissue strength and patterning. For example, Zhang, et al. electrospun composite polyethylene terephthalate (PET) and polycaprolactone (PCL) mats and rolled them into cylindrical structures to imitate the braided morphology of the anterior cruciate ligament.[118] BMP-7 was then immobilized on the ends on the graft. The combined strategy of an aligned biomaterial and local protein delivery led to improved calcification and integration of the synthetic ligament into the surrounding bone.

Many native tissues contain gradients, such as cartilage and the osteochondral gradient between cartilage and bone.[137,138] As a result, biomaterial strategies have been developed to create gradients similar to tissues, including layer-by-layer[139–142] and 3D printing[143] strategies. Although there are three distinct layers in cartilage (superficial, middle, and deep zones), the challenge is to build many layers on top of one another to seamlessly transition from one zone to the next. Gegg and Yang developed seven unique biomaterial formulations containing different combinations of chondroitin sulphate and gelatin to mimic the different zones of cartilage.[140] Cells were allowed to proliferate within the hydrogels for 21 days. Using this approach, the group identified the appropriate combinations of concentrations of the two materials to form the intended zones and stacked them, leading to a well-defined cartilage mimetic material. Proteins have also been incorporated into gradient-containing materials. 3D-printed scaffolds were fabricated with gradients of BMP-2 and TGF-β3 to mimic the osteochondral interface and stimulate mesenchymal stem cell differentiation towards osteogenic and chondrogenic lineages, respectively.[144] In this study, growth factor immobilization improved cell differentiation compared to soluble growth factor addition; however, the use of gradients did not promote cell differentiation. In contrast, osteochondral defects treated with a composite material containing BMP-2 in the subchondral layer and IGF-1 in the chondral layer exhibited robust bone repair, but modest cartilage repair.[145] Given that precise protein presentation is necessary to mimic complex tissue interfaces, it is likely that further optimization is needed to create robust osteochondral tissues using gradient protein delivery. As the library of available biomaterials continues to expand, combinations of materials will continue to yield more physiologically relevant tissue mimetics, which will increase our ability to more effectively address site-specific tissue injuries.

Environmentally-Responsive Materials

Stimuli-responsive materials can change properties based on exposure to endogenous cues present in the surrounding microenvironment, such as pH, temperature, reactive oxygen species, or specific enzymes.[146] Integrating components that can be triggered by microenvironmental cues can increase a biomaterial's adaptability to changes in the in vivo environment during tissue repair and provide an additional degree of temporal control over drug/protein release and material behavior. There are numerous types and applications of stimuli-responsive biomaterials. For an in-depth review of both environmentally-responsive and externally-triggered biomaterials

for biomolecule delivery, we recommend the recent publication of Olivia and Almquist.[146] For the purpose of this review, which focuses specifically on biomaterials that address and respond to complex injury environments, we will describe how endogenous triggers in the in vivo environment can induce material changes that modulate drug and protein release.

Thermally-responsive materials provide a means of controlling protein loading and release based on body temperature. Polymers such as poly (N-isopropyl acrylamide) (PNIPAAm) and block copolymers consisting of variations of PEG, polylactic acid (PLA), PCL, and poly (L-lactide) (PLLA) change their conformation from hydrophilic to hydrophobic at a lowest critical solution temperature (LCST), allowing for protein release or sequestration at specific temperatures.[147,148] PNIPAAm is particularly useful in thermally-mediated delivery applications because its hydrophobic/hydrophilic conformation changes are reversible at biologically relevant temperatures. Kim, et al. developed nanoparticles consisting of a thermo-responsive PNIPAAm domain, hydrophobic PLLA domain, and hydrophilic poly (L-lysine) (PLL) domain to deliver nerve growth factor (NGF).[149] PNIPAAm enabled loading of NGF under aqueous conditions and sustained NGF release at 37ºC, above the LCST. The uptake of the nanoparticles into neuroblast-like PC12 cells was also temperature-dependent, with higher uptake above the LCST, which stimulated increased neurite outgrowth. Although these studies were conducted in vitro, the ability of PNIPAAm nanoparticles to exhibit optimal sustained protein release and cellular uptake at physiological temperatures makes them valuable for in vivo therapeutic applications. Other phase changing molecules can also be used to align or open porous channels to allow biomolecule release. Tetradecanol, a fatty alcohol that is solid at 37°C and melts at 39ºC, has been used to provide on-demand, heat-triggered release of doxorubicin in cancer cell cultures.[150] While promising for in vitro use, tetradecanol has not yet been used extensively in vivo.

Targeting chemically unique attributes of injury sites such as pH can enhance site-specific protein delivery while reducing off-target release. Biomaterials can be engineered to respond specifically to the microenvironment of the site of injury or disease,[151] as is often done with the acidic environment of cancer cells.[117,152] pH sensitive vehicles are typically made through the integration of polyelectrolytes, such as phenylboronic acid (PBA),[153–155] due to their ability to change their overall charge at different pH, resulting in triggered release.[117,156,157] Cong, et al. crosslinked chitosan with glycerol 2-phospate disodium to created pH sensitive micelles, which were then dispersed in an alginate hydrogel. The grosup analyzed the release rate of drug in

various pH conditions with different formulations and found that the micelles alone would degrade too quickly while increasing the concentration of alginate surrounding the micelles slowed the release in a controlled fashion.

Additional strategies to create environmentally-responsive materials have also been employed. Biomaterials have been designed to degrade and release molecular cargo in the presence of reactive oxygen species, which are often increased in the initial inflammatory phase of tissue injury.[158] Materials crosslinked using peptide sequences that can be cleaved by enzymes, such as matrix metalloproteinases (MMPs), offer a strategy for triggered protein release that responds to fluctuating MMP expression in the injury environment.[159] These environmentally-responsive materials provide several methods to target a therapeutic to specific injury environments and thus have considerable overlap with tissue targeting strategies.

Collectively, the strategies described here leverage a variety of material properties to enhance material integration into regenerating tissues while providing sustained protein or drug release. Incorporating tissue targeting, tissue mimicking, and environmentally-responsive elements into biomaterial delivery vehicles is a promising approach to enhancing the efficacy of biomaterial-based protein delivery to injured tissues.

Multi-Component Strategies

We have identified a number of strategies to design biomaterials that stimulate tissue repair through delivery of proteins involved in healing cascades. Combining multiple approaches to create complex biomaterials that perform multiple functions can further enhance the ability of biomaterials to respond to environmental changes during tissue injury and repair.

Biomaterials designed to repair tissues with electrical activity (e.g. cardiac, nerve, muscle) can incorporate responsiveness to electrical stimuli to be both tissue mimicking and stimuli-responsive. Conductive biomaterials, such as graphene, carbon nanotubes, gold, polypyrole (PPy), polyaniline (PANI), and poly(3,4-ethylenedioxythiophene) (PEDOT),[135] can respond to electrical stimuli through contraction or expansion and subsequent relaxation, making them prime candidates for muscle mimicry. Graphene, gold, and carbon nanotubes are excellent conductors, but their long-term effects in the body are unknown. Conversely, PPy, PANI, and PEDOT are organic materials, but are not as effective for electrical signal conduction. Conductive materials have been used extensively for scaffolding for regenerating skeletal

muscle[135,160] and cardiac muscle.[161] The Dvir group developed a complex cardiac patch consisting of gold electrodes that could be independently triggered by electrical stimuli to release proteins.[162] 50 μm electrodes were placed in an array, covered in negatively-charged chondroitin sulphate, and electrostatically loaded with positively-charged proteins – lysozyme, a model protein, and SDF-1α, a chemokine that stimulates cell recruitment to sites of myocardial injury. Each node monitored the immediate surrounding electrical activity of the cardiac muscle and, upon sufficient signaling, would release its payload. This strategy enabled both detection and stimulation of electrical signals in cardiomyocytes, as well as on-demand protein release. Future applications of this technology could include additional sensing capabilities and feedback loops that enable remote control over patient cardiac tissue regeneration. Overall, electrically active materials may provide an enhanced ability to restore signaling pathways and re-establish function of electrically active tissues.

Advancements in additive manufacturing have opened additional possibilities for integrated solutions by enabling the fabrication of biomaterials with complex architectures and spatially-defined properties for controlled protein and peptide presentation.[73,143,163,164] This technique is valuable for mimicking tissues that naturally contain gradients, such as cartilage[165] and osteochondral interfaces, or displaying complex architecture, such as vasculature.[166,167] For example, peptide-polymer conjugates can be 3D-printed to control the spatial presentation of cell-adhesive (RGDS) and non-adhesive (RGES) peptides.[165] This strategy achieved precise control over local cell behavior using a single biomaterial scaffold and has future applications in creating complex tissue architectures. Additive manufacturing has also been used to mimic the structure of cortical and cancellous bone. A bioceramic scaffold was 3D-printed to mimic the hierarchical structure of bone, including the Haversian canals present in cortical bone structure.[168] This scaffold fostered proliferation and protein/ECM secretion by co-delivered mesenchymal stem cells, Schwann cells, and endothelial cells and fostered robust integration, bone formation, and revascularization in a rabbit femoral bone defect model. Additive manufacturing can also be combined with protein immobilization to create 3D printing structures that enable spatially localized protein presentation.[169] Subbiah, et al. demonstrated that lithography-based 3D-printing could be used to generate ceramic microcages that could be combined in a modular fashion (Figure 1.7).[170,171] Hydrogels containing a variety of growth factors (VEGF, PDGF, and BMP-2) were loaded into the microcages and combined to modulate

cell behavior both in vitro and in vivo. Together, these studies demonstrate that additive manufacturing can be used to create multifunctional materials with both defined architectures and protein presentation.

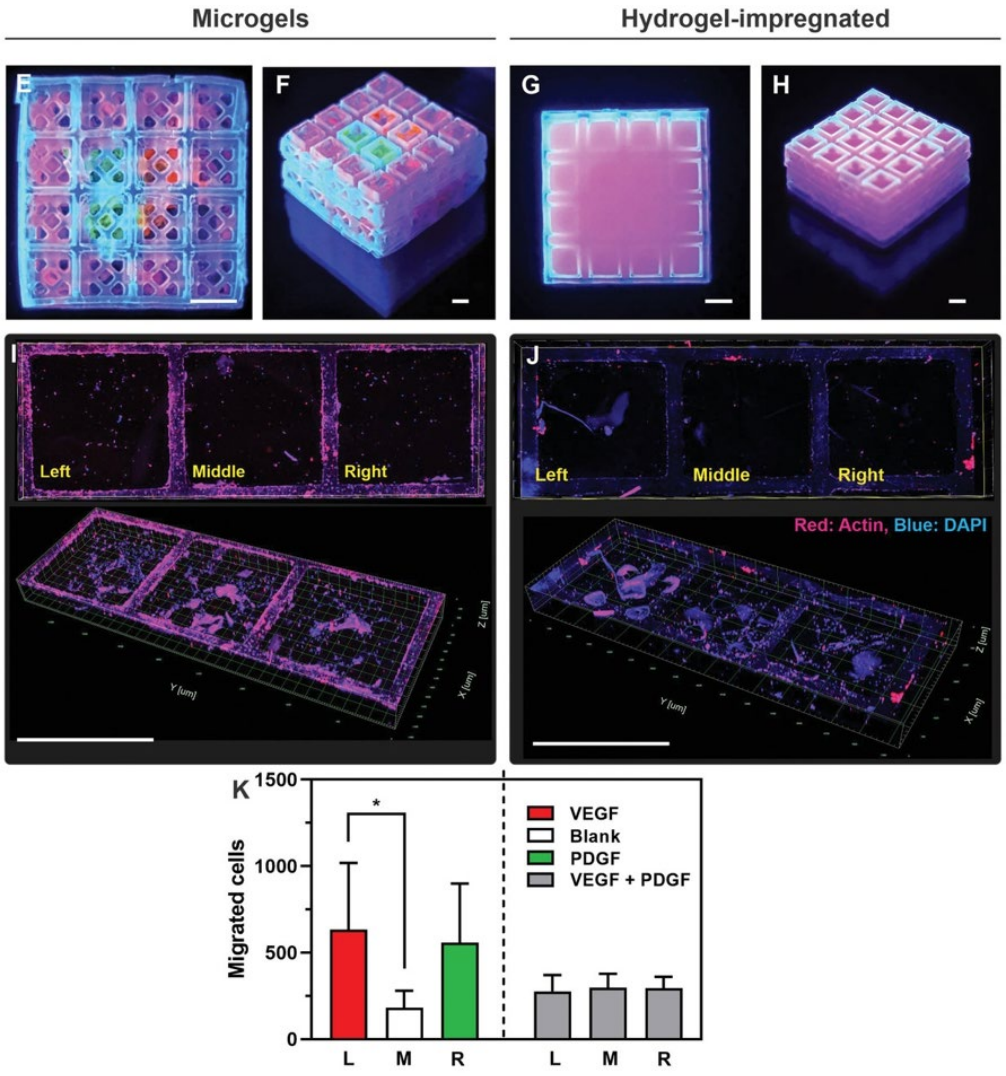


Figure 1.7: Use of 3D-printed, microgel-loaded microcages for protein delivery. (A and B) 3D-printed microcage scaffolds loaded with fluorescently labelled microparticles embedded within microgels, and (C and D) 3D printed microcage scaffolds loaded with fluorescently labelled microparticles within a bulk gelatin methacrylate hydrogel. (E) Directed cell migration achieved by the VEGF-laden microgels (left), no growth factor (middle), and PDGF-laden microgel (right). (F) Non-directed cell migration caused by the bulk hydrogel-impregnated scaffolds. Scale bars: 1.5 mm. Top: 2D view, bottom: 3D view. (G) Quantification of cell migration in each microcage (* $p < 0.05$). Reproduced from ref. 168 with permission from Wiley-VCH, copyright 2020

Current Market-Available Options

The use of therapeutic proteins has exploded in the clinic in the past several decades. By 2017, the FDA had approved a total of 239 proteins and peptides for therapeutic applications.[172] The translation of innovative therapeutic protein strategies to market is challenging due to the complexity of regulatory approval processes. As a result, what is currently available on the market lags behind the recent advances introduced in this review. However, several protein therapeutics used in the clinic today use a biomaterial-based approach for in vivo protein localization. For example, Medtronic produces INFUSE®, which is a bone graft consisting of recombinant human BMP-2 (rhBMP-2) soaked into a collagen sponge, and is used for bone surgery applications such as tibial fractures and spinal fusion. This industry standard uses two of the simpler approaches explored in this review – physical entrapment and an ECM-based biomaterials.[173] Boyne carried out clinical trials for what would become INFUSE® in 1996,[174] with additional trials conducted by Riedel and Valentin-Opran in 1999.[175] After nearly 10 years of clinical studies, the product was approved in the early 2000's by the United States Food and Drug Administration (FDA).[176]

Other tissue healing strategies using allografts and ECM-derived biomaterials are also currently used in the clinic. Although most of these ECM materials provide limited spatiotemporal control over protein retention and release, they retain many functional biological components, such as cells, proteins, and extracellular matrix molecules.[177] Osiris Therapeutics, Inc. produces protein- and cell-rich scaffolds derived from placental membranes for a variety of applications, including dermal tissue,[178] bone, and cartilage repair.[179,180] Preserved placental membranes are also available from other companies for ocular applications.[181,182] However, viable allograft tissue with appropriate properties for tissue healing can be scarce. One strategy to overcome this challenge is to conjugate other biomaterials to allografts to both reduce the amount of foreign tissue required and adjust the mechanical properties of the allograft for specific applications.[183] Although allografts and collagen sponges can be cut to fit the size of the tissue defect, they cannot be easily customized to a predefined structure. The 3D printing strategies described in this review are currently being used by numerous medical device companies to aim to address the specific structural needs of a variety of tissues and organs. Biological structures can be 3D printed with a variety of scaffold materials that enable direct integration of proteins into the

bioprinting ink.[184,185] Although the FDA has yet not cleared the use of 3D bioprinting solutions for whole organ and tissue transplantation, that is a key objective of many of these groups.

Future Outlooks

The strategies described in this review are all at different stages of development, with some being primarily investigated in vitro, some being currently assessed in vivo, and others moving towards clinical translation. Achieving robust tissue regeneration is a complex challenge with no ubiquitous solution; thus, different biomaterial strategies may be required for tissue injuries that alter healing cascades in different ways. The use of high throughput technologies and computational models are recent developments in the field of biomaterials that have the potential to expand our ability to better address the complexity of the wound healing cascade.

Since numerous biomaterial properties (e.g. protein-material affinity, mechanical properties, degradation) interact to influence tissue repair, the ability to generate large numbers of new biomaterial formulations could drastically accelerate progress in the development of biomaterials for tissue regeneration. Recent advances in high throughput screening technologies are expected to enable automated combinatoric synthesis and material discovery. We have recently developed a technique to evaluate protein diffusion through hydrogels using fluorescent proteins loaded into hydrogel-filled capillary tubes.[186] This technique enabled the determination of protein diffusion coefficients using small volumes of proteins and hydrogels and has been adapted for use with both physically and chemically crosslinked hydrogels (PEG, collagen, and alginate). On a larger scale, Xu, et al. used a high throughput liquid handling robot to combine various charged (cationic or anionic poly(oligo ethylene glycol methacrylate) (POEGMA)), uncharged (dextran, carboxymethyl cellulose, and chitosan), thermoresponsive (PNIPAM, POEGMA), non-thermoresponsive, synthetic, and natural precursor polymers.[187] The biomaterials fabricated were then loaded with ovalbumin, as a model protein to evaluate how biomaterial properties affected protein release. Almost 100 unique polymer combinations were made and analyzed, which was a substantial increase in the typical number of biomaterial formulations that can be tested simultaneously. Similarly, Hao, et al. used One Bead One Compound (OBOC) high throughput screening technology to identify high affinity binding ligands for endothelial progenitor cells (EPCs) and endothelial cells (ECs) with minimal affinity for many other biological components.[188] OBOC uses magnetically conjugated target proteins for binding and sorting

through large numbers of peptide sequences, akin to phage sorting.[189] The binding ligands conjugated to small vascular grafts achieved rapid endothelialization in vivo and retained high patency in vivo in a rat carotid bypass model.

High-throughput biomaterial screening can be combined with computational modeling approaches to further expand our ability to screen a vast number of biomaterial properties for tissue regeneration applications. Several studies have demonstrated the utility of statistical optimization techniques, such as design of experiments, to optimize biomaterial properties achieve specific outcomes, such as cell response and gelation kinetics.[190–192] Additionally, we and others have employed computational bio-transport models to predict protein release kinetics from biomaterials and tune biomaterial properties to achieve desired release rates in vitro and in vivo.[10,64,77] Limasale, et al. demonstrated that a reaction-diffusion model could be used to predict the effect of heparin content and sulfation pattern on VEGF release, as well as the spatial distribution of VEGF throughout the hydrogel. Collectively, these examples demonstrate the value of high throughput screening technologies and computational modeling for the rational design of biomaterials for tissue engineering applications. Future work that translates these in vitro results and in silico models into viable predictions for biomaterial behavior within in vivo injury environments has significant potential for improving biomaterials for better therapeutic outcomes.

Conclusions

The complex nature of tissue healing, in which numerous cells, proteins, and matrix molecules participate, is difficult to replicate or restore when normal repair mechanisms are disrupted. Here, we have compiled and reviewed a number of recent advancements in biomaterials for sustained protein delivery, with a focus on strategies that improve the ability of biomaterials to address the complexity of the injury environment during healing. Numerous strategies exist to tailor protein presentation to unique tissue regeneration applications, including covalent and physical entrapment of proteins, the use of ECM-based materials, engineered affinity interactions, environmentally-responsive materials for on-demand protein delivery, and complex fabrication methods to better mimic native tissue architecture. Ultimately, the choice of the most appropriate biomaterial strategy to enable regeneration of a particular tissue rests on gaining a better understanding of how spatiotemporal protein presentation affects healing in that tissue.

With the broad spectrum of engineering tools available to create new biomaterials, we expect that we will be able to both expand our understanding of how proteins influence tissue healing responses and create advanced biomaterials that respond to and integrate into complex injury environments. While many challenges remain in identifying and creating the appropriate material properties to stimulate repair of non-healing tissue defects, emerging interest in designing biomaterials that better integrate and respond to injured tissues is expected to open numerous doors to improved strategies for patient treatment.

Objective

Wound healing is a complex and dynamic process involving the coordinated activity of multiple proteins across three stages: inflammation, proliferation, and remodeling. In the event of traumatic bone fractures, aspects of the healing cascade may be disrupted, leading to non-unions and permanent disability. Current clinical strategies for bone fracture repair deliver the osteogenic growth factor bone morphogenetic protein-2 (BMP-2) in supraphysiological doses. However, large doses lead to non-localized release and ectopic bone growth, and a single exogenous protein fails to mimic the multifaceted nature of wound healing.

The work presented in this thesis aims to address the spatiotemporal limitations of the current BMP-2 delivery vehicles by developing affinity-based protein delivery platforms using affibodies to independently control the release of the anti-inflammatory cytokine interleukin-4 (IL-4) alongside BMP-2 to modulate inflammation and bone regeneration. In this work, we subject a yeast surface display library encoded for affibodies to identify BMP-2- and IL-4-specific affibodies to control the release of proteins. We aim to engineer a affibody-conjugated hydrogel vehicles that can tune the release of two proteins independently by using affibodies of ranging binding affinities, such that low-affinity affibodies release a protein quickly and high-affinity affibodies result in slow and sustained release. Ideally, we would release IL-4 quickly, followed by sustained release of BMP-2.

Overall, this thesis aims to establish a new modality of controlled protein codelivery by leveraging a broad range of protein-specific affinity interactions. Although this project focuses specifically on bone regeneration, this technology could be applied to a plethora of other injuries and conditions, underscoring the potential of affibody-conjugated hydrogels as versatile platforms to emulate natural wound healing cascade and improving bone fracture repair outcomes.

Chapter 2 - Moderate-Affinity Affibodies Modulate the Delivery and Bioactivity of Bone Morphogenetic Protein-2

From Dorogin, J., Hochstatter, H.B., Shepherd, S.O., Svendsen, J.E., Benz, M.A., Powers, A.C., Fear, K.M., Townsend, J.M., Prell, J.S., Hosseinzadeh, P., Hettiaratchi, M.H. 2023. Moderate-Affinity Affibodies Modulate the Delivery and Bioactivity of Bone Morphogenetic Protein-2. *Advanced Healthcare Materials* 12(26): 2300793

Abstract

Uncontrolled bone morphogenetic protein-2 (BMP-2) release can lead to off-target bone growth and other adverse events. To tackle this challenge, we used yeast surface display to identify unique BMP-2-specific protein binders known as affibodies that bound to BMP-2 with different affinities. Biolayer interferometry revealed an equilibrium dissociation constant of 10.7 nM for the interaction between BMP-2 and high-affinity affibody and 34.8 nM for the interaction between BMP-2 and the low-affinity affibody. The low-affinity affibody-BMP-2 interaction also exhibited an off-rate constant that was an order of magnitude higher. Computational modeling of affibody-BMP-2 binding predicted that the high- and low-affinity affibodies bind to two distinct sites on BMP-2 that function as different cell-receptor binding sites. BMP-2 binding to affibodies reduced expression of the osteogenic marker alkaline phosphatase (ALP) in C2C12 myoblasts. Affibody-conjugated polyethylene glycol-maleimide hydrogels increased uptake of BMP-2 compared to affibody-free hydrogels, and high-affinity hydrogels exhibited lower BMP-2 release into serum compared to low-affinity hydrogels and affibody-free hydrogels over four weeks. Loading BMP-2 into affibody-conjugated hydrogels prolonged the ALP activity of C2C12 myoblasts compared to soluble BMP-2. This work demonstrates that affibodies with different affinities can modulate BMP-2 delivery and activity, creating a promising approach for controlling BMP-2 delivery in clinical applications.

Introduction

Bone morphogenetic protein-2 (BMP-2) is an integral protein for bone and cartilage repair.[193,194] It has chemotactic properties that aid in the recruitment of osteoblasts and mesenchymal stromal

cells,[195–197] as well as morphogenic properties that differentiate mesenchymal stromal cells towards osteogenic phenotypes.[193,198] Because of its ability to promote bone formation, BMP-2 has been used clinically as a bone graft substitute that is delivered from an implanted absorbable collagen sponge.[194,199] However, the absorbable collagen sponge relies primarily on weak electrostatic interactions to physically entrap BMP-2, giving it a limited ability to retain BMP-2 compared to other materials.[200,201] Uncontrolled release of BMP-2 from collagen sponges has led to reduced efficiency of BMP-2-mediated osteogenesis[202] and numerous adverse effects, including soft tissue inflammation and ectopic bone formation.[64,194,203] Consequently, there is significant interest in developing methods to improve control over BMP-2 delivery to improve the efficacy and reduce the side effects of clinical bone regeneration therapies.

Methods to control protein release from biomaterial delivery vehicles include physical modifications such as changing the porosity or degradation rate of the delivery vehicle[204,205] and chemical modifications such as tethering proteins directly to the delivery vehicle.[206] While promising under certain conditions, these techniques often result in burst release kinetics, unpredictable protein release rates within complex *in vivo* environments, and inconsistent loading of the protein therapeutic, contributing to insufficient localization of the protein in the intended site and poor healing outcomes.[86] Although chemical conjugation of therapeutic proteins to biomaterials can reduce the likelihood of burst release and prolong protein presentation within the site of interest,[207] it can also interfere with protein-receptor binding, potentially altering the biological function of the therapeutic protein and resulting in reduced protein bioactivity.[50,52,54] To better address the need for controlled protein delivery, we and others have fabricated biomaterial delivery vehicles from extracellular matrix molecules, such as heparin[208,209] and fibronectin[210] with intrinsic affinity interactions for therapeutic proteins in an effort to provide sustained protein delivery without directly conjugating the protein to the delivery vehicle.[64,77,82] Affinity-mediated protein release relies primarily on the equilibrium dissociation constant (K_D) between the protein and material to control the rate of protein release.[211] These reversible interactions provide prolonged protein presentation within the site of biomaterial implantation that mimics that of the extracellular matrix. Building upon this work, additional affinity interactions for therapeutic proteins have also been engineered using various types of affinity molecules, including antibodies,[212] antibody fragments,[199] peptides,[88,213] and aptamers.[214]

A challenge remains in finding ideal candidates to engineer suitable protein-material interactions for affinity-based release. Heparin-containing delivery vehicles have an intrinsic affinity for BMP-2 and the ability to retain BMP-2 at the site of injury[199,215]; however, heparin interacts with a plethora of other proteins and extracellular matrix molecules via electrostatic and hydrophobic interactions,[216] making it difficult to predict the behavior of the delivery vehicle in complex *in vivo* environments that contain numerous serum-borne proteins. While antibodies are highly specific protein binders with high affinities for their targets, they are expensive to produce and bulky, which hinders the integration of sufficient quantities of antibodies into a delivery vehicle. [217] [218] Conversely, aptamers, peptides, and antibody fragments are smaller and less expensive to produce, but may suffer from lower specificity and/or weaker affinities for their respective proteins due to either smaller interfaces of interaction[219,220] or non-specific targeting domains such as the heparin-binding domain.[216,221] To overcome these challenges, directed evolution has recently been used to identify highly specific protein binders that are easy to produce and conjugate to biomaterials.[222] For instance, a large yeast surface display library containing ~10^8 unique protein binders was subjected to directed evolution to identify highly specific protein binding partners that were integrated into methylcellulose and hyaluronic acid hydrogels to tune the delivery rates of several growth factors.[92,105] Similarly, directed evolution of a phage display library of random 7-mer peptides identified several binding peptides for integration into polyethylene glycol (PEG)-based hydrogels for controlled release of neurotrophin-3. [223]

We were particularly interested in applying this directed evolution approach to affibodies, which are a class of small, α-helical, antibody-mimetic proteins that can be engineered to bind to a target protein of interest.[104,224] Affibodies are currently being tested clinically and preclinically as targeting agents for $HER2^+$ breast cancer cells,[225,226] and for the detection of other biological markers, such as CD69 cell markers for early detection of activated immune cells[227] and vascular endothelial growth factor receptor-2 (VEGFR2) expression for analyzing angiogenesis signaling pathways.[228] Moreover, affibodies have also recently been used to tune the release of fibroblast growth factor-2 (FGF-2),[92] insulin-like growth factor-1 (IGF-1), and pigment epithelium-derived factor (PEDF).[105] Their clinical benefit is derived from their relatively stable structure under physiological conditions, the diversity of proteins to which they can bind, and the ability to modify their binding affinity by changing 13 to 17 amino acids at the binding interface between the affibody and target protein.[104,229] However, the tunability of affibody affinity is underutilized,

as affibody affinity has thus far only been maximized for targeting endogenous protein species without considering the use of multiple affibodies displaying a range of moderate affinities for tuning the delivery rates of exogenous proteins. While typical affinity binders generated via directed evolution target strong interactions with equilibrium dissociation constants in the picomolar range,[230] we were interested in moderate affinity interactions with equilibrium dissociation constants in the nanomolar range to enable controlled protein release. We hypothesized that using affibodies with different affinities for a protein of interest would allow us to tune the amount and rate of protein released from a hydrogel delivery vehicle.

In this work, we identified BMP-2-specific affibodies with a range of affinities for BMP-2 from a yeast surface display library containing 10^8 affibody variants and used these affibodies to tune BMP-2 release from a polyethylene glycol-maleimide (PEG-Mal) hydrogel that could be prepared and used in a similar manner to the clinically used implantable collagen sponge. This project aimed to satisfy two primary objectives: first, identifying multiple BMP-2-specific affibodies that minimally interact with other proteins involved in the tissue healing cascade; and second, using BMP-2-specific affibodies with significantly different equilibrium dissociation constants to tune the release kinetics of BMP-2. We identified two unique, BMP-2-specific affibodies that did not interact with several other key proteins in the bone healing cascade: vascular endothelial growth factor (VEGF), interleukin-4 (IL-4), or granulocyte macrophage colony stimulating factor (GM-CSF). We used computational modeling to predict the binding interface between the affibodies and BMP-2, revealing that the high-affinity binder may bind BMP-2 at a different interface than the low-affinity binder. We found that BMP-2 bound to affibodies demonstrated diminished osteogenic properties *in vitro*. The integration of the affibodies into PEG-Mal hydrogels slowed the release of BMP-2, with the high-affinity binder reducing BMP-2 release to a greater extent than the low-affinity binder. Overall, this work established the use of affibody-containing delivery vehicles to tune the release rate of BMP-2 with the potential to improve clinical BMP-2 delivery strategies for healing traumatic skeletal injuries.

Results and Discussion

Magnetic-Activated Cell Sorting Depleted Over 99% of the Yeast Display Library Diversity

Four rounds of magnetic-activated cell sorting (MACS) were performed to enrich for BMP-2-binding affibodies within the yeast surface display library (Figure 2.1A). Each round of MACS consisted of two negative magnetic bead sorts to remove non-specific protein binders[92,105,231,232] and one positive magnetic bead sort using beads conjugated with BMP-2 to enrich for yeast displaying BMP-2-specific affibodies. Following each round of MACS, yeast from each bead sort were plated on selective growth plates to count the number of colonies that bound to the negative beads and BMP-2-conjugated beads.

The new yeast library diversity after each round of MACS was estimated by counting the number of colonies grown on the BMP-2 plates, while the ratio of positive-to-negative binders was calculated by dividing the number of colonies grown on the BMP-2 plates by the sum of colonies grown on the negative plates. Figure 2.1B demonstrates how each round of MACS enriched BMP-2 specific affibodies (blue bar graph) while reducing the total yeast library diversity (i.e., number of unique variants) (orange line plot). After four rounds of MACS, the library diversity was reduced by over 99%, and the number of BMP-2-specific affibodies was estimated to account for approximately 89% of the remaining library.

Fluorescence-Activated Cell Sorting Identified BMP-2-Specific Affibodies

Following four rounds of MACS, fluorescence-activated cell sorting (FACS) was performed on the enriched yeast library, which was gated into populations corresponding to different affinity ranges for BMP-2 binding. Yeast were incubated in 0.1 mg mL^{-1} bovine serum albumin (BSA) in phosphate buffered saline (PBS) (i.e., PBSA) without fluorescent tags or proteins (cells-only control) (Figure 2.1C), with a mouse anti-c-myc antibody (αCMYC, 9E10) to assess affibody expression levels by binding to the N-terminal c-myc epitope (Figure 2.1D), or with both αCMYC and biotinylated BMP-2 (bBMP) to assess BMP-2 binding to displayed affibodies (Figure 2.1E). Except for the cells-only control, all yeast were incubated with secondary fluorescent tags that bound specifically to αCMYC (AlexaFluor 647 goat anti-mouse conjugate; AF647) or bBMP (AlexaFluor 488 streptavidin conjugate; AF488). AF647+/AF488+ yeast cells

were gated using two gating approaches and collected (Figure S1). At least 10,000 yeast cells were collected from each gate during FACS in an effort to capture all unique affibody sequences from each gate.

Following FACS, yeast from each gate were plated onto selective growth plates and allowed to form discernable colonies that each contained a single affibody sequence (i.e., monoclonal yeast). Three colonies from each gate were grown in growth media for a total of 21 yeast clones. Sanger sequencing of plasmid DNA revealed 11 unique affibody sequences.

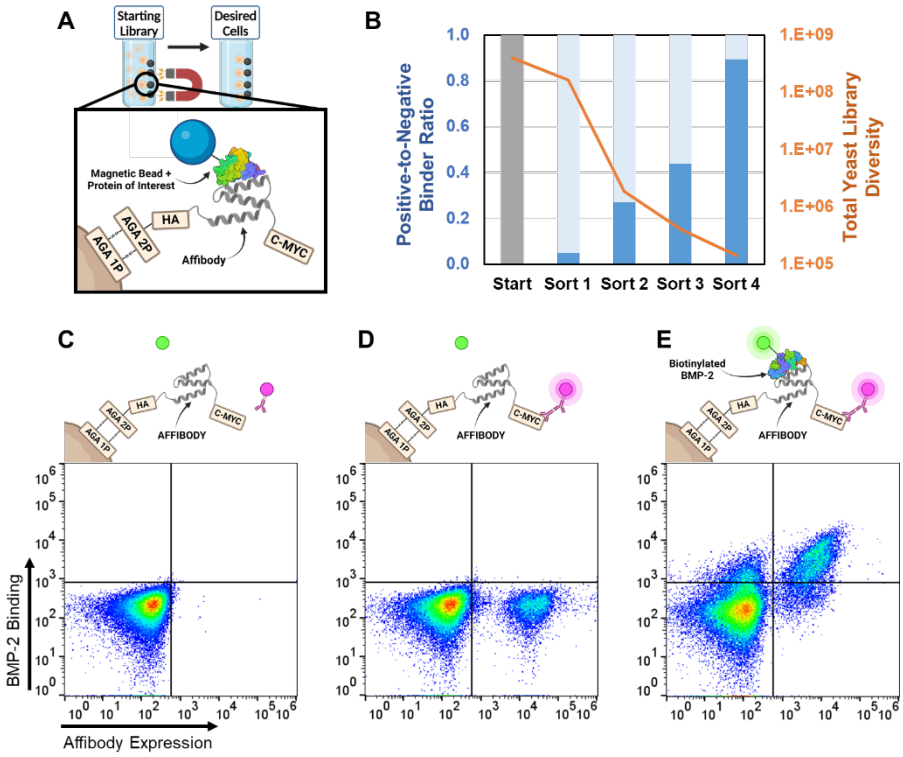


Figure 2.1: Identification of BMP-2-specific affibodies using cell sorting of a yeast surface display library. A-B) Magnetic activated cell sorting. A) Schematic of MACS. Yeast induced to express surface-displayed affibodies were incubated with magnetic beads coated with tris or bovine serum albumin (BSA) for negative bead sorts or BMP-2 for positive bead sorts. Yeast that did not bind to the negative sort beads were transferred to a tube containing the BMP-2 beads. Yeast that bound to the BMP-2 beads were collected and expanded for the next round of cell sorting. B) Diversities of the sorted yeast libraries obtained after each round of MACS. Left y-axis (blue bar graph) depicts approximate ratio of BMP-2-specific to non-specific binders (i.e., positive-to-negative binder ratio). Right y-axis (orange line graph) depicts the diversity of the yeast library after each round of MACS. C-E) FACS plots and corresponding cell labeling diagrams. Yeast were incubated with secondary fluorescent tags that bound specifically to αCMYC for affibody expression or bBMP. C) Secondary fluorescent tag control, in which no affibody expression or bBMP-2 binding is measured. D) In the presence of αCMYC, affibody expression is observed as a rightward shift. E) In the presence of αCMYC and bBMP-2, affibody expression is observed as a rightward shift, and binding of bBMP-2 to displayed affibodies results in a shift upward along the y-axis. Gating was performed based on positive bBMP-2 binding and affibody expression (upper right quadrant).

Characterization of BMP-2 Binding to Monoclonal Yeast Affibodies

Binding affinities between BMP-2 and BMP-2-specific affibodies were assessed on yeast using flow cytometry. Similar to FACS, monoclonal affibody-displaying yeast were incubated in either PBSA, αCMYC and secondary solution, or αCMYC with a range of bBMP concentrations (0.5-1000 nM) and secondary solution (AF647 and AF488 for affibody expression and bBMP-2 binding, respectively). At each concentration of bBMP, the fraction of displayed affibodies that were bound to BMP-2 was determined by dividing the top right quadrant (AF647+/AF488+) by the right half of the graph (AF647+). With increasing bBMP-2 concentrations, more cells were labeled with AF488, resulting in an upward shift of the population that indicated increased bBMP-2 binding (Figure 2.2A-D). Binding affinity was assessed by plotting the fraction of bBMP-2 bound over the bBMP-2 concentration range (Figure 2.2E). Monoclonal yeast that demonstrated a greater bBMP-2 binding had higher affinities for BMP-2.[233] Equilibrium dissociation constants (K_D) were calculated by performing a nonlinear regression on bBMP-2 binding to affibody-displaying yeast at varying bBMP-2 concentrations (Figure 2.2E,F). We quantified the affinities of all 11 unique clones that bound to BMP-2 (Figure S2A) and chose two unique clones to assess further. These clones displayed significantly different affinities for BMP-2 and will be identified hereafter as high-affinity (K_D = 1.95±0.14 nM) and low-affinity (K_D = 61.82±9.38 nM) BMP-2-binding affibodies. The affinities between the other affibodies and BMP-2 were found to be within the range of the equilibrium dissociation constants of the high- and low-affinity affibodies. The quantity of surface-displayed affibodies may have affected the perceived affinity between the affibodies and BMP-2 by altering the ratio between the proteins and the protein–binding partners.[233] The average AF647+ fluorescence signal, indicative of affibody expression, was similar between the high- and low-affinity affibodies at each BMP-2 concentration, confirming a comparable number of affibodies displayed on the surface of each monoclonal yeast species (Figure S2B).

Specificity of the high- and low-affinity affibodies for BMP-2 was also assessed using flow cytometry. Several other proteins involved in the bone healing cascade were chosen to investigate specificity of the BMP-2 affibodies. Monoclonal affibody-displaying yeast were incubated with PBSA, αCMYC and secondary solution, or αCMYC with 1000 nM of biotinylated vascular endothelial growth factor (bVEGF), biotinylated interleukin-4 (bIL-4), or

biotinylated granulocyte-macrophage colony stimulated factor (bGM-CSF) and secondary solution. All affibodies exhibited negligible binding to bVEGF, bIL-4, and bGM-CSF, suggesting that these affibodies were specific to BMP-2 (Figure 2.2G, H).

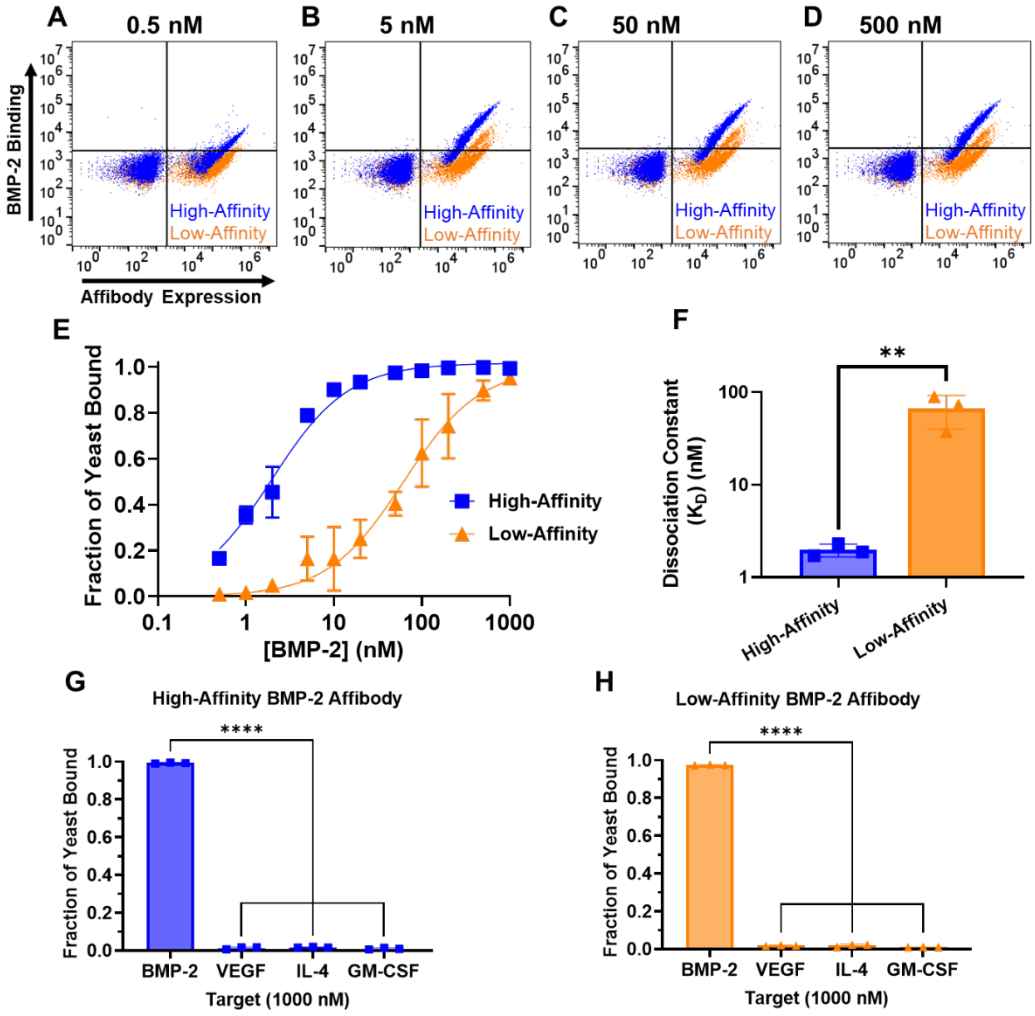


Figure 2.2: Identification and characterization of yeast-displayed BMP-2-specific affibodies. Affibody binding to BMP-2 and off-target proteins was determined using flow cytometry. Flow cytometry plots of affibodies binding to bBMP-2 at A) 0.5 nM of bBMP-2, B) 5 nM of bBMP-2, C) 50 nM of bBMP-2, and D) 500 nM of bBMP-2. E) Fraction of yeast binding to bBMP-2 as a function of bBMP-2 concentration ranging from 0.5-1000 nM. Non-linear regression was performed to determine equilibrium dissociation constants (K_D). Curves were identified as statistically significantly different from each other by two-way ANOVA, Tukey's post-hoc test. n=3, $p<0.01$. F) Equilibrium dissociation constants (K_D) of the two unique affibodies. Statistical significance was determined using one-way ANOVA with Tukey's post-hoc test. n=3, ** $p<0.01$. G-H) BMP-2-specific affibodies do not bind to other recombinant proteins of interest. G) High-affinity and H) low-affinity affibodies were incubated with 1000 nM of bBMP-2, bVEGF, bIL-4, or bGM-CSF. Statistical significance was measured using one-way ANOVA and Tukey's post-hoc test. n=3, **** $p<0.0001$.

Collection and Characterization BMP-2-Specific Affibodies

Sequences for the high- and low-affinity affibodies modified with a 6-histidine (His-tag) for protein collection[105,234,235] and a N-terminal cysteine for bioconjugation[236–238] were ligated into a pET28b+ expression vector, which was transformed into chemically competent BL21 *E. coli* for protein expression. Soluble protein was collected using benchtop immobilized metal affinity chromatography (IMAC) with cobalt-nitrilotriacetic acid beads.[234] Approximately 10 mg of pure soluble affibodies were collected from each liter of *E. coli* culture.

Sodium dodecyl sulfate polyacrylamide gel electrophoresis (SDS-PAGE) (Figure 2.3A) and native ion mass spectrometry (NIMS) (Figure S3) were used to determine the size of the affibodies. SDS-PAGE of purified affibodies (150 μM in tris, pH 8) revealed thick bands visible between the 5 kDa and 11 kDa rungs of the control ladder at the approximate expected sizes of the two affibodies (7308 Da and 7414 Da for the high- and low-affinity affibodies, respectively) without any other noticeable bands. Native ion mass spectrometry (NIMS) of affibodies (20 μM in 0.2 M ammonium acetate, pH 7.52) demonstrated a dominant high-affinity affibody peak corresponding to the expected mass of 7308 Da with other well-populated peaks associated with sodium and potassium adducts, the possible formation of a cysteic acid or piperidine on the C-terminal,[239] and glutamylation of the N-terminal cysteine. The low-affinity affibody displayed a small peak at the expected mass of 7414 Da and had prominent peak shifts associated with the formation of a dehydroalanine,[240] a 32 Da shift attributed to a trisulfide bond,[241] an additional shift associated with a piperidine formation on the terminal cysteine,[239] and another prominent peak shift (161 Da) attributed to a carboxymethyl cysteine or carboxymethyl cystenyl.[242] These data suggest that these affibodies may readily undergo post translational modifications and that the low affinity affibody may undergo extensive post-translational modification. However, these modifications mainly affect the terminal cysteine, which may affect chemical conjugation of the affibody to biomaterials, but are not expected to affect affibody binding affinity for BMP-2.[239]

Circular dichroism was used to determine the secondary structure of the affibodies.[243] Affibodies were diluted to concentrations between 17-30 μM in 5 mM tris pH 6.92, which was a pH equidistant from each of their isoelectric points. Both affibodies exhibited characteristic α-helical profiles, including troughs at 208 nm and 222 nm and a peak at 195 nm,[92,243] confirming the secondary structure of the affibodies in their soluble state (Figure 2.3B).[244]

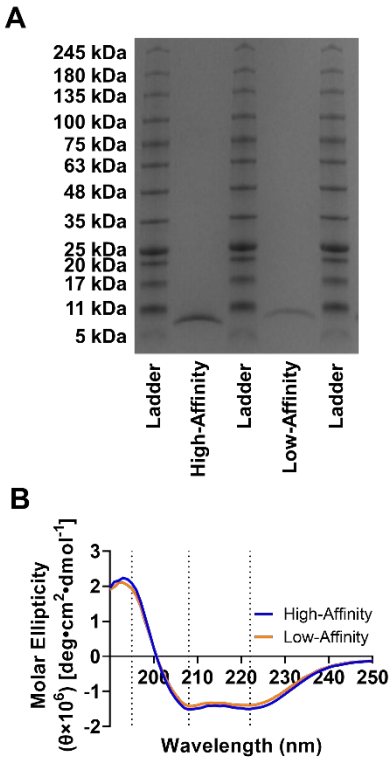


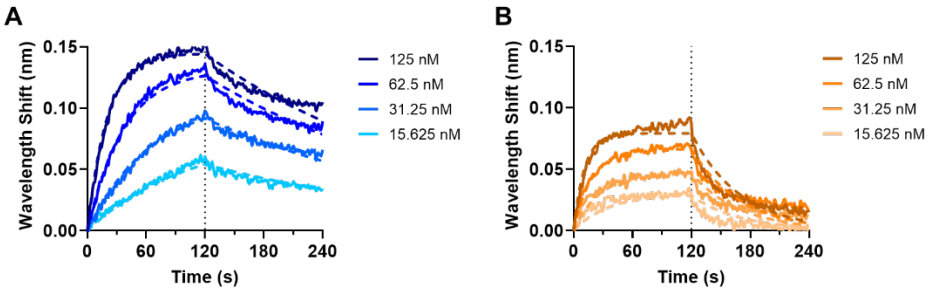
Figure 2.3: Soluble affibody characterization. A) SDS-PAGE of high- and low-affinity BMP-2-specific affibodies with a 5-245 kDa ladder. Samples were run at concentration of 150 µM. Expected molecular weights of the high- and low-affinity affibodies were 7308 Da and 7414 Da, respectively. B) Circular dichroism spectra of affibodies displayed in molar ellipticity. Affibodies were diluted to a concentration between 17-30 µM in 5 mM tris pH 6.92 and loaded into a quartz cuvette with 1 mm path length. Circular dichroism and high-tension voltage were measured over a wavelength range of 190-250 nm, and the circular dichroism output was adjusted for protein concentration and molecular weight.

Characterization of Soluble Affibody-BMP-2 Binding Interactions

The binding interaction between the soluble high- and low-affinity affibodies and BMP-2 were characterized using biolayer interferometry (BLI). Streptavidin-coated BLI probes were coated with 25 nM bBMP-2 in PBS with 0.05% Tween-20® (PBST), followed by association of 0-125 nM of the purified soluble affibody in PBST for 120 seconds and dissociation in PBST for 120 seconds (Figure 4A, B). BLI enabled the determination of the dissociation rate constant (k_{off}), association rate constant (k_{on}), and overall equilibrium dissociation constant (K_D) of each binding interaction. The equilibrium dissociation constants of the high- and low-affinity affibodies for BMP-2 were determined to be 10.7 nM and 34.8 nM, respectively (Figure 4C). The k_{off} of the low-affinity affibody was an order of magnitude higher than that of the high-affinity affibody, and the low-affinity affibody completely dissociated from the bBMP-2. While evaluating BMP-

2-affibody binding on the surface of the yeast provided some insight to the binding strength of the affibody, it was more representative of the avidity (i.e., total binding strength) rather than affinity of the individual affibodies and did not provide information about the association and dissociation rates of the binding interaction.[233] As such, BLI provided a more representative measurement of affibody affinity for BMP-2 when integrated into hydrogels.

BLI was also performed using streptavidin-coated probes coated with 25 nM of bVEGF, bIL-4, or bGM-CSF followed by association and dissociation of 0-125 nM of high- and low-affinity affibody in PBST (Figure S4). There was no noticeable binding response to VEGF and GM-CSF, and only a minimal binding response to IL-4, suggesting that the affibodies do not bind to VEGF or GM-CSF and bind minimally to IL-4 when compared to BMP-2. Overall, these results suggested that the soluble affibodies specifically bind to BMP-2 and that the high-affinity affibody has a stronger interaction with BMP-2 compared to the low-affinity affibody.



C

	k_{on} ($M^{-1}s^{-1}$)	k_{off} (s^{-1})	K_D (M)
High-Affinity Affibody	$3.70 \pm 0.03 \times 10^{5}$	$3.97 \pm 0.02 \times 10^{-3}$	1.07×10^{-8}
Low-Affinity Affibody	$5.75 \pm 0.13 \times 10^{5}$	$2.00 \pm 0.01 \times 10^{-2}$	3.48×10^{-8}

Figure 2.4: Binding interactions of soluble affibodies with BMP-2 measured by biolayer interferometry. All samples were diluted in PBST. Streptavidin probes were loaded with 25 nM of bBMP-2 for 120 seconds. Bound protein was allowed to associate with 0-125 nM high-affinity affibody(A) and low-affinity affibody (B) for 120 seconds followed by dissociation into PBST for 120 seconds. Association and dissociation rate constants as well as overall equilibrium dissociation constants were obtained using a 1:1 global curve fitting of the data. Raw data is displayed with solid lines, and fitted data is displayed as dotted lines. C) Table of association and dissociation rate constants and overall equilibrium dissociation constants of high- and low-affinity affibodies.

Computational Predictions of Affibody Binding to BMP-2

The computational tools AlphaFold 2, ZDOCK, and Rosetta were used to predict the site of interaction between each affibody and BMP-2. AlphaFold predicted the folded structures of the affibodies with high confidence (predicted local distance difference test score >95 for most of the predictions).[245–250] Predicted affibody structures were energetically minimized using a protocol in Rosetta.[251–253] These structures were then docked to BMP-2 using the ZDOCK algorithm.[254] The top-ranked conformations for each affibody-BMP-2 complex were visualized in Pymol (Figure 2.5A).[255] The high-affinity affibody was predicted to interact with BMP-2 at the binding site commonly referred to as the "wrist," while the low-affinity affibody was predicted to bind to a different site of BMP-2 known as the "knuckle."[193,256] Electrostatic interactions were defined as polar contacts between BMP-2 and each respective affibody. Hydrophobic interactions were defined as hydrophobic amino acids of BMP-2 less than 3.5 Å away from each affibody, which structurally contributed to the formation of a hydrophobic pocket. Interfacial calculations suggested that the interactions between the high-affinity affibody and BMP-2 were governed by multiple hydrophobic and electrostatic intermolecular interactions with BMP-2 at the wrist binding site, whereas the low-affinity affibody interacted with the knuckle binding site of BMP-2 primarily through electrostatic interactions (Figure 2.5B).[257,258] In comparison to collagen which has been shown to have a >500 nM equilibrium dissociation constant with BMP-2,[259] the affibody-based electrostatic interactions with BMP-2 are an order of magnitude stronger. Furthermore, collagen interacts with many different biomolecules, making its interaction with BMP-2 less specific than the BMP-2-affibody interactions and potentially less controllable in complex in vivo environments.[259,260]

The BMP-2 wrist binding epitope has been recognized as the binding site for BMP receptor type-1A (BMPR1A), with which the growth factor makes a relatively strong binding interaction($K_D \approx$ 0.7 nM),[261] while the knuckle is a relatively weak binding site for BMP receptor type II (BMPR-II) ($K_D \approx$ 100 nM).[193,262] BMP-2-induced osteogenesis occurs in skeletal myoblasts and mesenchymal stromal cells when a BMP-2 dimer interacts with a cell membrane-bound hetero-tetramer formed from two BMPR1A and two BMPR-II[193,256,263,264] We hypothesized that binding of the affibody to BMP-2 at higher affinities than its receptors could potentially interfere with BMP-2-receptor binding, subsequently inhibiting BMP-2-induced osteogenesis. We also hypothesized that increasing the quantity of affibody present in solution would shift the

dynamics of receptor binding, resulting in a concentration-dependent inhibition. To test these hypotheses *in vitro,* we used the C2C12 immortalized murine skeletal myoblast cell line, which has been shown to express markers of early osteogenic differentiation, such as alkaline phosphate (ALP) activity, in the presence of BMP-2 in a dose-dependent manner.[262,265,266]

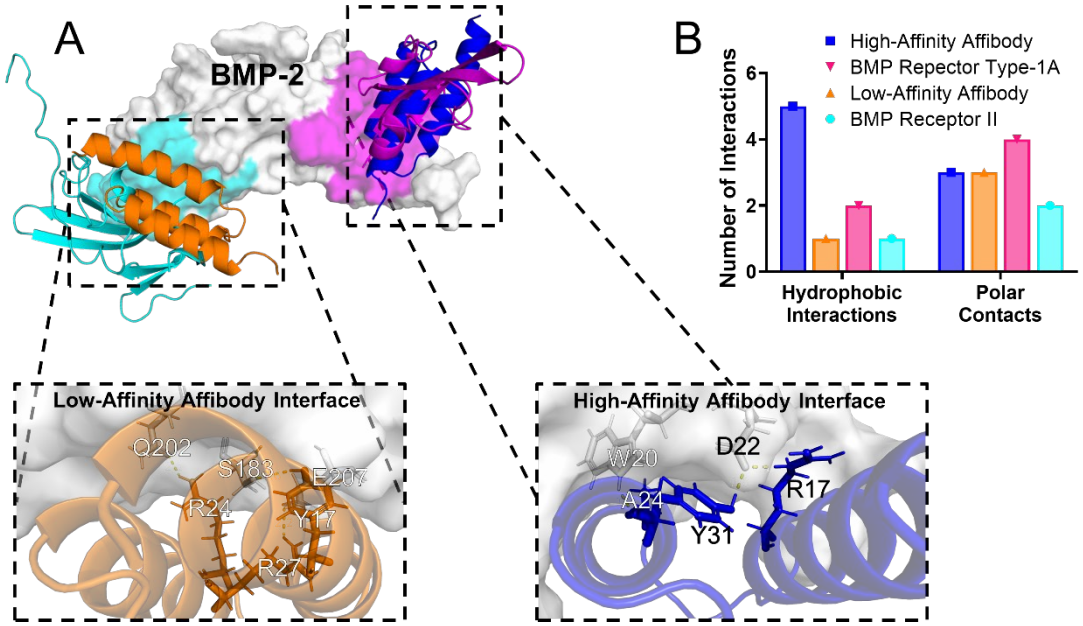


Figure 2.5: Computational predictions of BMP-2 binding with affibodies or BMP receptors. A) Visual representation of docking of affibodies and receptors to BMP-2 in Pymol. High-affinity affibody (blue) overlaps with the docking interface of BMPR-1A (magenta), and low-affinity affibody (orange) overlaps with the docking interface of BMPRII (cyan). Predicted affibody structures were docked to BMP-2 using ZDOCK. B) Characteristic binding interactions of affibodies and BMP receptors to BMP-2. The high-affinity affibody docks to BMP-2 in the binding epitope known at the "wrist" using 3 polar contacts and 5 hydrophobic interactions. The low-affinity affibody docks to BMP-2 at the binding epitope called the "knuckle" with 3 polar interactions and one weak hydrophobic pocket. The wrist traditionally binds BMPR-1A (PDB: 1REW) and the knuckle traditionally binds with BMPR-II (PDB: 7PPA).

Affibodies Do Not Impact C2C12 Cell Viability or Proliferation

The cytocompatibility of the soluble BMP-2-specific affibodies was assessed using C2C12 cells. Soluble high- and low-affinity affibodies were added to C2C12 cultures at final concentrations of 10 nM, 20 nM, 40 nM, 80 nM, or 800 nM. After incubation for 72 h, cells were stained with calcein AM and ethidium homodimer-1 to quantify live and dead cells, respectively, and imaged (Figure 2.6A-C). Cell viability was calculated by dividing the number of living cells by the total number of cells (Figure 2.6), and total cell count was calculated by averaging the number of live cells in each image (Figure 2.6E). C2C12 viability was not negatively impacted by the

introduction of any concentration of affibodies. The total viable cell count was also largely unaffected by the various concentrations of the affibodies. Although treatment with 80 nM of low-affinity affibody increased cell number, the lack of discernable pattern suggested that cell proliferation was not affected by the affibodies.

Affibody-BMP-2 Binding Reduces Alkaline Phosphatase Activity of C2C12 Cells

ALP activity, which is an indicator of early osteogenic differentiation,[267,268] was used to assess the impact of affibodies on BMP-2 bioactivity. 20 nM of BMP-2 with or without different concentrations of soluble high- or low-affinity affibodies were added to C2C12 cultures sequentially for the "uncomplexed" treatment groups (affibodies first, incubated for 45 minutes, followed by BMP-2) or as a premixed solution (45 minutes of mixing to ensure adequate time for interaction) for the "complexed" treatment groups. After 72 h, cells were lysed and their ALP activity was quantified by a colorimetric change caused by the ALP-induced catalysis of p-nitro phenyl phosphate to p-nitrophenol.[269] ALP activity was normalized to the total amount of double-stranded DNA present in each cell culture. Treatment with both uncomplexed and complexed BMP-2 and affibodies was performed to compare the different states in which BMP-2 may be presented in clinical applications. Traditionally, BMP-2 is soaked into a collagen sponge prior to delivery to a bone defect,[270] resulting in some burst release of protein and some long-term retention of BMP-2 within the scaffold. In the absence of a hydrogel or other delivery vehicle, the uncomplexed treatment group represented the released BMP-2, which would interact with cells outside of the scaffold, while the complexed treatment group represented the BMP-2 that would remain bound to the affibodies within the delivery vehicle and would interact with cells that migrate into the scaffold.[215,271] Figure 2.6F depicts the normalized ALP activity for the experimental groups using 20 nM affibody concentrations (1:1 ratio of BMP-2 to affibody). Figure S5 depicts additional affibody concentrations (10-1000 nM), which resulted in ALP activity that followed similar trends. No significant differences were observed between ALP activity induced by high- and low-affinity affibody-BMP-2 treatment groups. In the absence of BMP-2, no ALP activity was observed, regardless of affibody presence. In the presence of BMP-2 alone, normalized ALP activity was 37.9 ± 12.5 nmol pNPP μg^{-1} dsDNA min^{-1}, indicative of early osteogenic differentiation of the C2C12 cells.[265] For the uncomplexed approach, the affibodies caused an insignificant reduction in ALP activity. For all of the complexed treatment

groups, ALP activity was significantly reduced compared to BMP-2 treatment and the uncomplexed treatment groups. These results suggest that affibody binding to BMP-2 may have inhibited some of the function of BMP-2 or inhibited its interaction with the requisite tetramer complex of membrane-bound BMP receptors,[193,256] supporting the computational docking simulations. Our BLI data (Figure 2.4) suggested that some portion of the BMP-2 remained bound to the high-affinity affibody for an extended period, potentially exceeding the 72 h incubation period. Even though our BLI data indicated that the low-affinity binder allows for complete dissociation of the BMP-2, the low-affinity binder has a greater affinity for the knuckle than BMPR-II. Since optimal BMP-2 activity requires a tetramer of two BMPR-1A and two BMPR-II,[262] disruptions to the binding interactions between BMP-2 and either BMP receptor on the C2C12 cells may have restricted the induction of ALP activity in C2C12 cells.

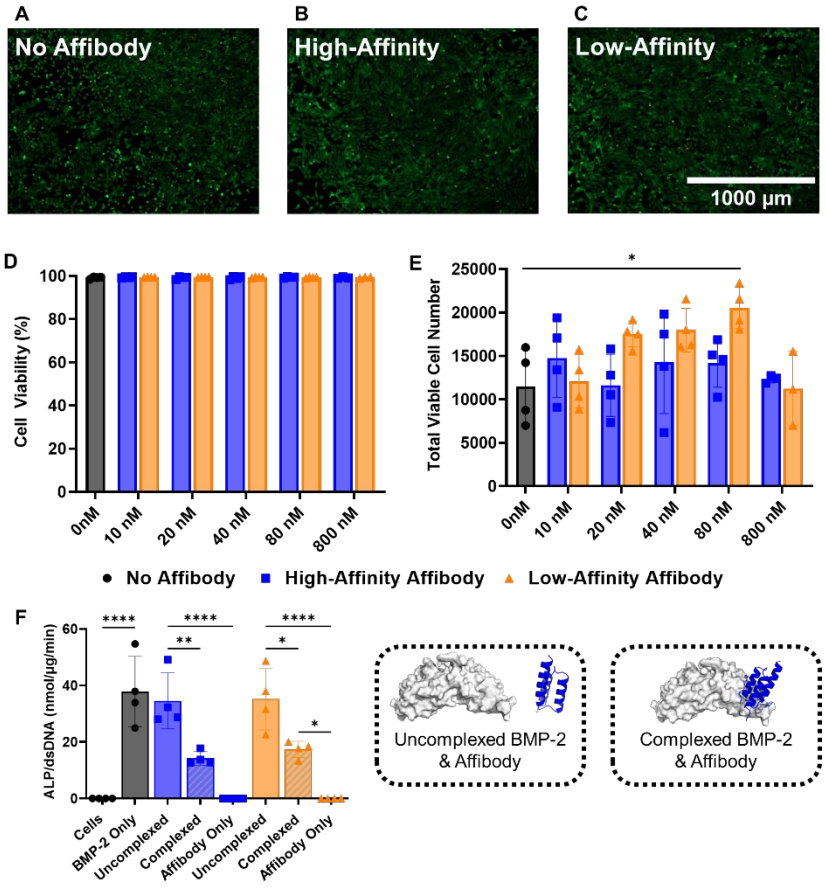


Figure 2.6: Effects of BMP-2 affibodies on viability, growth, and alkaline phosphate activity of C2C12 skeletal myoblasts. A-E) Cytocompatibility of high- and low-affinity affibodies with C2C12s. Cells were seeded at a density of 2000 cells cm^{-2} and incubated with 0-800 nM soluble affibody in growth media for 72 h. Cells were stained with

calcein AM (live cells; green) and ethidium homodimer (dead cells; red) and imaged. A-C) Representative photos of stained cell culture wells containing C2C12 cells and A) no affibodies, B) 20 nM high-affinity affibodies, and C) 20 nM low-affinity affibodies. Scale bar = 1000 μm. D) Percent cell viability as a function of affibody concentration. E) Total viable cell number as a function of affibody concentration. Statistical significance determined by two-way ANOVA and Dunnett's post-hoc test, n=4, * $p<0.05$. F) Effects of BMP-2 and BMP-2-specific affibodies on alkaline phosphatase activity of C2C12 cells. C2C12 cells were seeded at a density of 62,500 cells cm^{-2} and allowed to adhere for 6 h in growth media. Media was then replaced with low serum media containing premixed affibody (20 nM) and BMP-2 (20 nM) (complexed) or low serum media containing 20 nM soluble affibody with 20 nM of BMP-2 added 45 minutes later (uncomplexed). The cells were cultured for 72 h and then lysed for quantification of ALP activity and double stranded DNA content. Statistical significance was determined by one-way ANOVA and Tukey's post-hoc test. n=4, * $p<0.05$, ** $p<0.01$, *** $p<0.001$, **** $p<0.0001$. Complexed and uncomplexed affibody-BMP-2 structures were obtained from computational predictions.

Synthesis of Affibody-Conjugated Poly(Ethylene Glycol)-Maleimide Hydrogels

Affibody-conjugated PEG-Mal hydrogels were fabricated to assess the effect of affibody affinity on BMP-2 release from a hydrogel delivery vehicle that could be implanted similarly to the industry-used absorbable collagen sponge. 100 μL 5 w/v% PEG-Mal hydrogels containing 1.92 nmol of either high- or low-affinity BMP-2-specific affibodies were synthesized by mixing PEG-Mal with soluble affibody, where the C-terminal cysteines of the affibodies spontaneously reacted with available maleimides through a thiol-maleimide addition to form an affibody-conjugated PEG-Mal intermediate.[272] The remaining maleimides were then crosslinked using dithiothreitol (DTT) to form hydrogels (Figure 2.7A).[237] To confirm the conjugation of the affibodies to the maleimide groups, the intermediate solutions of affibody-PEG conjugates were passed through a 10 kDa molecular weight cut-off filter to separate unconjugated affibodies, and the flowthrough was subjected to SDS-PAGE. The unconjugated affibody solutions that were used underwent the same filtration and SDS-PAGE to compare the inputs and outputs of the reaction (Figure S6). The presence of affibodies in the pre-conjugation lanes indicated the affibodies readily pass through the filter pores. However, upon conjugation to a 20 kDa 4-arm PEG-Mal, the affibodies were no longer able to pass through the filter. The absence of a band indicated that most of the affibodies reacted with the maleimide groups and an undetectable amount of free affibodies was retained in the PEG-Mal + affibody intermediate conjugate. [273]

Encapsulation and Controlled Release of BMP-2 from Affibody-Conjugated PEG-Mal Hydrogels

To assess the impact of affibodies on BMP-2 encapsulation, 100 μL 5 w/v% PEG-Mal hydrogels containing no affibodies, low-affinity affibodies, or high-affinity affibodies were loaded with 100 ng of BMP-2 (3.85 pmol, 500x molar equivalents of affibody to BMP-2) in PBSA overnight. The next day, the hydrogels were washed in PBSA to remove unencapsulated BMP-2 and minimize variability in BMP-2 uptake. Although the timeframes are different, this method of absorbing BMP-2 into prefabricated PEG-Mal hydrogels encapsulation is similar to the clinical method procedure of absorbing BMP-2 into collagen sponges before implantation in the patient.[270] BMP-2 content in the washes and the original BMP-2 solution were quantified using enzyme-linked immunosorbent assay (ELISA). The affibody-conjugated hydrogels demonstrated a significantly higher BMP-2 encapsulation efficiency than hydrogels without affibodies (Figure 2.7B). The high-affinity hydrogel demonstrated an encapsulation efficiency of 83.0 ± 1.98%, which was higher than that of the low affinity hydrogel, which was 68.4 ± 4.90%.

After removing the unbound BMP-2 from the hydrogels, the hydrogels were suspended in either PBSA or PBS containing 10% fetal bovine serum (FBS) to study the effect of the surrounding environment on BMP-2 release. The saline solution was used to reduce the number of variables that could affect the release, while the serum solution, which contains a variety of lipids proteins, enzymes, and other constituents, was used to more accurately mimic the *in vivo* environment.[274–276] Aliquots of the supernatant were collected over four weeks, analyzed by BMP-2 ELISA, and graphed as cumulative release as a percentage of BMP-2 encapsulated (Figure 2.7C,D). At the conclusion of the experiment, all PEG hydrogels were still intact and did not exhibit notable degradation, which is comparable similar to other PEG-based hydrogels crosslinked via Michael-type addition[277] No significant differences were observed between BMP-2 released into saline from any of the hydrogel groups. In contrast, the high-affinity affibody hydrogels demonstrated significantly slower BMP-2 release into serum than the no affibody and low-affinity affibody hydrogels at all timepoints after 15 minutes. The total amount of BMP-2 released from the high-affinity hydrogels was lower than that of the no affibody and low-affinity affibody hydrogels. These results corroborated the affibody-BMP-2 binding interaction data from BLI that demonstrated complete dissociation of BMP-2 from the low-affinity affibody, but incomplete

dissociation of the BMP-2 from the high-affinity affibody. All hydrogel groups exhibited a plateau in BMP-2 release after approximately one week that was lower than the total amount of BMP-2 loaded into the hydrogel, which is a common observation for protein release vehicles.[214,278,279] This could be attributed to the establishment of a protein concentration equilibrium between the hydrogel and its surrounding environment, as well as protein aggregation and conformational changes that reduced protein detection by ELISA.[280–283] BMP-2 has been shown to aggregate at physiological pH, even with the addition of stabilizing agents such as BSA and salts.[284,285]

The effective diffusivity (i.e., release rate) of the BMP-2 from the hydrogels was calculated using a Fickian diffusion model,[286] from the slope of the linear portion of a curve comparing M_t/M_∞ and root time ($s^{1/2}$), where M_t was the cumulative BMP-2 released at time t, and M_∞ was the cumulative BMP-2 released at the end of the experiment, when a plateau in protein release had been reached. The effective BMP-2 diffusivity of the no affibody hydrogel was unaffected by the different media for release, likely because PEG demonstrates limited protein adsorption, resulting in nonspecific BMP-2 adsorption into the hydrogel.[287] Conversely, the effective BMP-2 diffusivity of the high-affinity affibody hydrogel was higher in serum compared to saline (Figure 2.7E). The low-affinity hydrogel did not demonstrate significantly different BMP-2 release compared to any other group. Increased BMP-2 release in serum compared to saline may be due to the presence of proteases that may have affected protein binding and stability or lipids that may have affected the hydrophilic/lipophilic balance of the release media, potentially interfering with the hydrophobic interactions between the high-affinity affibody and the BMP-2.[288] However, since the low-affinity affibody was predicted to interact with BMP-2 primarily via electrostatic interactions, these interactions may not have been largely affected by the components of serum. Although the diffusion rate of BMP-2 from hydrogels containing the high-affinity affibody was lower than that of hydrogels containing low-affinity affibodies in saline, there was no difference in cumulative BMP-2 release. Conversely, the presence of proteins and lipids in serum-containing release media introduced additional protein-protein and protein-lipid interactions, which significantly increased the diffusion rate of BMP-2 from hydrogels containing the high affinity-affibody. This result demonstrates that, depending on the nature of the affinity interaction, the presence of serum in the release media can increase the dissociation constant of the interaction and shift the equilibrium concentrations of bound and unbound

protein, in turn increasing cumulative protein release. In saline alone, these interactions would not be affected. Thus, affinity-based protein release experiments should be carried out in release media with and without serum to more effectively predict the mass transport in various *in vitro* and *in vivo* environments.

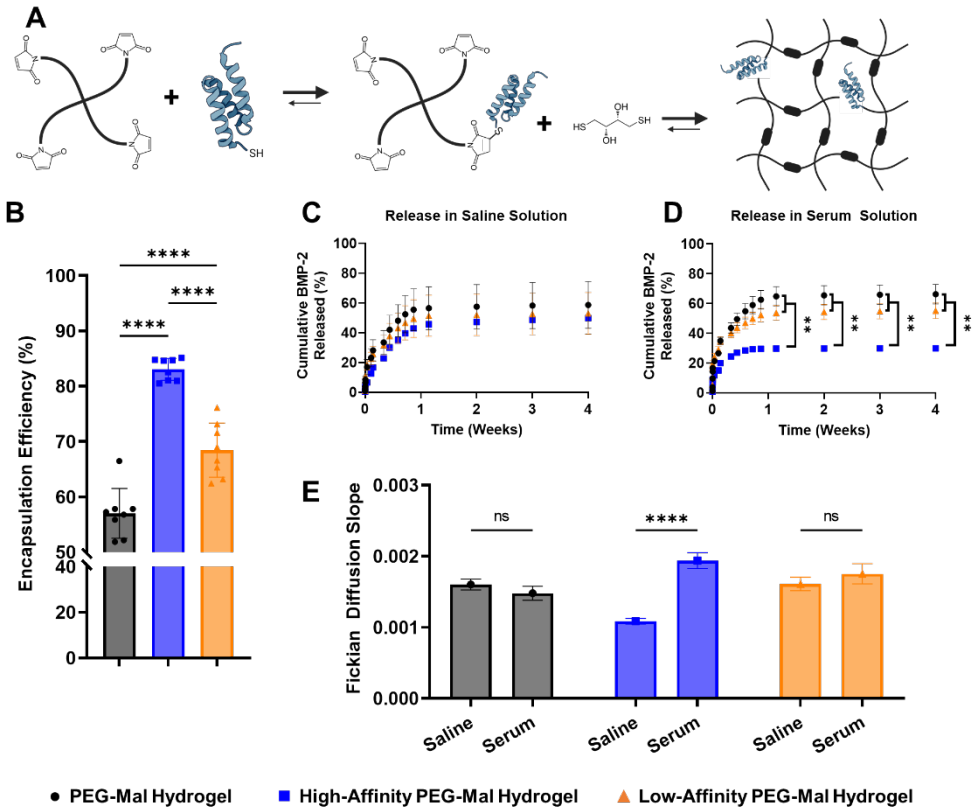


Figure 2.7: Release of BMP-2 from affibody-conjugated PEG-Mal hydrogels. A) Synthesis schematic for affibody-conjugated PEG-Mal hydrogels. 4-arm PEG-Mal (20 kDa) underwent a thiol-maleimide Michael addition with the terminal cysteines of the high- or low-affinity affibodies in PBS pH 6.92. The remaining unreacted maleimide groups of the intermediate complex were crosslinked with DTT in PBS pH 6.92 to form a hydrogel. PEG-Mal hydrogels containing no affibody, low-affinity affibody, or high-affinity affibody were loaded with 100 ng of BMP-2. B) Encapsulation efficiency of affibody-conjugated PEG-Mal hydrogels. One-way ANOVA and Tukey's post-hoc test. n=8, **** $p<0.0001$. C, D) Cumulative BMP-2 release from affibody-conjugated PEG-Mal hydrogels measured over a 4-week period using ELISA. BMP-2 was released into either (C) saline solution or (D) 10% serum solution. Two-way ANOVA and Tukey's post-hoc test. n=4. * $p<0.05$, ** $p<0.01$. E) Fickian diffusion rates of BMP-2 release from PEG-Mal hydrogels observed in the linear region of release in serum and saline solutions. One-way ANOVA and Tukey's post-hoc test. n=4 **** $p<0.0001$.

BMP-2 Bioactivity upon Release from Affibody-Conjugated PEG-Mal Hydrogels

To determine whether BMP-2 bioactivity was preserved upon release from affibody-conjugated PEG-Mal hydrogels, ALP activity assays were performed on C2C12 cells using BMP-2 released from the hydrogels over a 7-day period. 200 µL 5 w/v% PEG-Mal hydrogels containing no

affibody, low-affinity affibodies, or high-affinity affibodies were loaded with 200 ng of BMP-2. The hydrogels were then submerged in 1 mL of low serum media, and aliquots were taken immediately and after 1, 2, 3, 5, and 7 days. Fresh media was replenished at each timepoint. The BMP-2 content of each aliquot was quantified using ELISA (Figure 2.8A). To evaluate ALP induction, C2C12 cells were seeded as described above, resuspended in 180 µL of the aliquots containing released BMP-2 from each timepoint, and incubated for 72 h in 37 °C. ALP activity was quantified, normalized to dsDNA, and plotted as a function of time (Figure 2.8B).

Initially, the high-affinity affibody hydrogels bound more BMP-2, reducing the amount of BMP-2 present in solution at 0 h compared to the no affibody and the low-affinity affibody hydrogels (Figure 2.8A); these data reflect the encapsulation efficiency results (Figure 2.7E), which demonstrate that high-affinity affibody hydrogels encapsulated more BMP-2. As such, the no affibody and low-affinity affibody hydrogels released between 10-20 ng of BMP-2 at 0 h compared to the high-affinity affibody hydrogels, which released less than 5 ng of BMP-2. At all of the timepoints, the high-affinity affibody hydrogels released significantly less BMP-2 than the no affibody and low-affinity affibody hydrogels. Consequently, the ALP activity induced by BMP-2 released from the high-affinity affibody hydrogels was lower than that of the no affibody and low-affinity affibody hydrogels. Cumulative BMP-2 release was also quantified (Figure S7), which demonstrated a similar release profile to the BMP-2 release into 10% serum (Figure 2.7D), suggesting that the inclusion of serum, even at low concentrations, affected the protein release kinetics of the affibody-conjugated hydrogels.

ALP activity was normalized to the amount of BMP-2 released at each timepoint for each hydrogel in order to determine if the osteogenic function of BMP-2 changed over time (Figure 2.8C). Overall, the specific bioactivity of the BMP-2 decreased over time, which was likely due to denaturation of the protein at 37 °C.[289] To determine the overall osteogenic effect of the BMP-2 over time, the area under the curve of the normalized ALP activity was calculated (Figure 2.8D). The use of any hydrogel delivery vehicle increased and prolonged the total effect of the BMP-2 on the C2C12 cells, consistent with other studies.[208,290] The use of the high-affinity affibody hydrogels resulted in lower total BMP-2 activity, which may have been due to the extended binding of the BMP-2 to the affibodies and retention within the hydrogels. While the binding of the high-affinity affibody to BMP-2 explains the retention of the protein in the PEG-Mal hydrogels, it does not explain the decreased ALP activity of the C2C12 cells, as the

hydrogels never directly interacted with the cells. However, indirect introduction of BMP-2 to cells *in vitro* may not accurately reflect the *in vivo* environment.[291] The early release of BMP-2 from the no affibody hydrogel and low-affinity affibody hydrogel resulted in more bioactive BMP-2 compared to the high-affinity affibody hydrogels, leading to higher overall BMP-2 activity. While some other affinity peptides and extracellular matrix molecules such as heparin have demonstrated a stabilizing effect on their target proteins,[92] our affibody-conjugated hydrogels did not exhibit this capacity with BMP-2 and C2C12 cells. Although heparin and heparin-based biomaterials can prolong the bioactivity of BMP-2,[64,208,292] heparin's interactions with numerous other heparin-binding proteins such as VEGF, fibroblast growth factors, and platelet-derived growth factor can lead to unpredictable protein release rates, unexpected protein sequestration, and unanticipated biological effects in complex in vivo environments where many growth factors are present. Furthermore, the optimal BMP-2 dose for bone regeneration depends on numerous factors, including the size of injury, age of the patient/animal, presence of any comorbidities, and species, as apes, humans and rats have all been shown to require different BMP-2 doses for effective bone regeneration.[194] The advantage of our approach is that the binding interactions of affibody-containing hydrogels are specific and tunable, making it easier to engineer materials that specifically perform their intended functions.

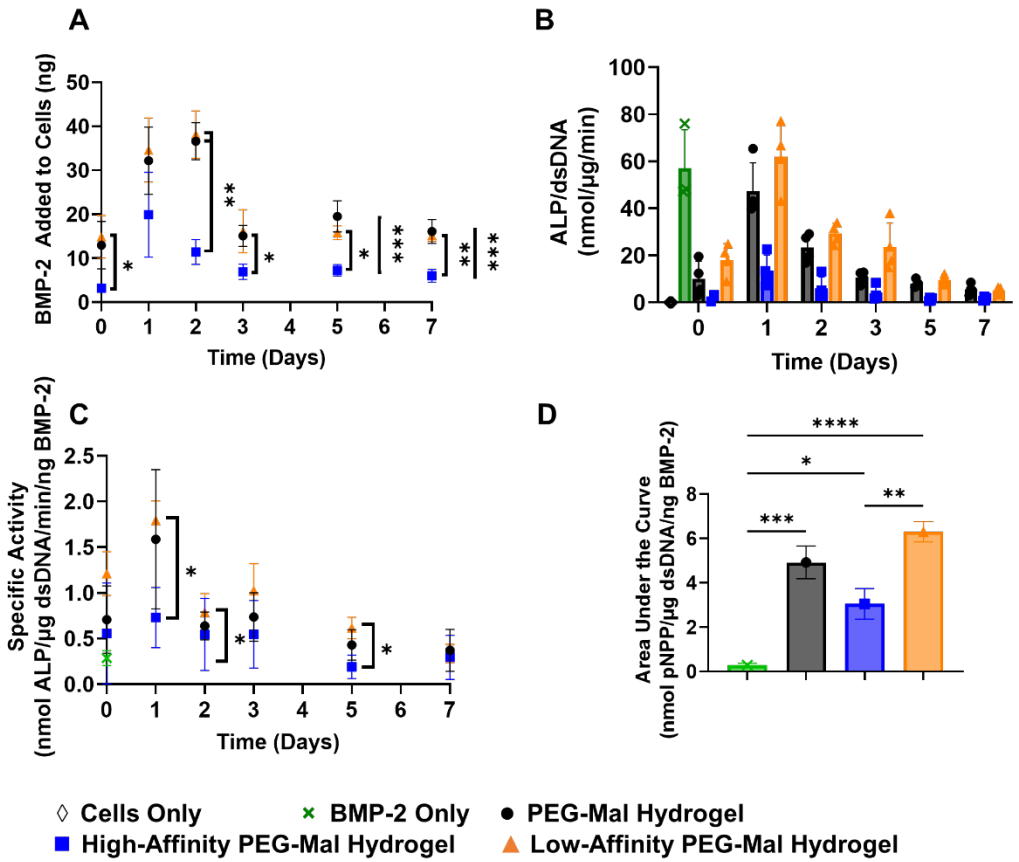


Figure 2.8: ALP activity of C2C12 cells as a function of BMP-2 release from affibody-conjugated PEG-Mal hydrogels. PEG-Mal hydrogels containing no affibody, low-affinity affibody, or high-affinity affibody were loaded with 200 ng of BMP-2. The hydrogels were submerged in low serum media, and aliquots of the media were removed and replenished with fresh media over 7 days. A) Amount of BMP-2 added to C2C12 cells from each timepoint was quantified by BMP-2 ELISA. Two-way ANOVA and Tukey's post-hoc test. n=4, * $p<0.05$, ** $p<0.01$, *** $p<0.001$. B) ALP activity of C2C12 myoblasts normalized to double-stranded DNA content of the cell cultures. 180 µL of media from each timepoint of BMP-2 release were added to C2C12 cells seeded at 62,500 cells cm^{-2} and allowed to incubate for 72 h at 37 °C, after which ALP activity was quantified and normalized to dsDNA. C) ALP activity of BMP-2 normalized to the amount of BMP-2 in solution at each timepoint. Two-way ANOVA and Tukey's post-hoc test. n=4, * $p<0.05$. D) Area Under the Curve (AUC) of the normalized ALP activity from (C) for each PEG-Mal hydrogel and the soluble BMP-2 control. One-way ANOVA, post-hoc Tukey multiple comparisons. n=4, * $p<0.05$, ** $p<0.01$, *** $p<0.001$, **** $p<0.0001$.

.

Conclusion

Improving the sustained delivery of BMP-2 is especially important given its clinical relevance in bone regeneration. However, designing a delivery vehicle that provides tunable protein release with the high specificity required to achieve controlled delivery in complex environments is challenging. Here, we used yeast surface display to identify unique affibodies that demonstrate highly specific BMP-2 binding with different affinities. Biolayer interferometry of soluble

affibodies revealed that the high-affinity affibody remained bound to BMP-2 for a longer period of time compared to the low-affinity affibody, which allowed for faster dissociation. Computational protein modeling predicted that the low-affinity affibody would bind to the knuckle epitope of BMP-2 while the high-affinity affibody would bind at the wrist epitope – the sites of two different BMP receptors. Affibody-BMP-2 binding inhibited ALP activity of C2C12 myoblasts, which is induced by BMP-2 binding at the wrist/knuckle to the BMPR-1A and BMPRII receptors, respectively, reinforcing the idea that the affibodies bind to the sites of receptor binding. Conjugation of either type of affibodies into PEG-Mal hydrogels increased the amount of BMP-2 encapsulated in the hydrogels, reflecting the similar association rates of the affibodies determined through BLI. Although no differences in protein release were observed in saline, conjugating the high-affinity affibody into PEG-Mal hydrogels reduced BMP-2 release from hydrogels exposed to an *in vivo*-mimicking environment, further reflecting the dissociation rates observed in BLI. Furthermore, all hydrogels released bioactive BMP-2 for seven days that induced ALP activity in C2C12 cells.

Overall, our findings demonstrate the promise of using affibodies in hydrogels for controlling BMP-2 bioactivity and release and encourage future studies investigating affibody-mediated delivery of BMP-2 in preclinical bone regeneration models. Our computational modeling results highlight the potential importance of determining where on the protein an affinity binder may bind as a method of understanding and controlling the activity of a protein. The ability to identify protein binders that impact protein bioactivity may have implications for providing spatiotemporal control over protein activity. Unlike other affinity-based delivery systems that rely on protein-material interactions that may be nonspecific and unpredictable in *in vivo*-mimicking environments, BMP-2-specific affibodies may provide the specificity necessary to more precisely tune protein release *in vivo* and enable the delivery of multiple proteins simultaneously with individually tunable release kinetics in the future. Because these affibodies contain a C-terminal cysteine for site-specific bioconjugation, they can be conjugated to a variety of other biomaterials with additional functionality, including injectable, degradable, and stimuli-responsive hydrogels, thereby increasing the versatility of this approach.[92,114,293,294]

Acknowledgements

This work was supported by a grant from the Collins Medical Trust, an R21 Trailblazer Award from the National Institutes of Health (R21EB032112), and a Discovery Award from the Department of Defense's Peer-Reviewed Medical Research Program (W81XWH2210700). JD is supported by a doctoral-level post-graduate scholarship (PGS-D) from the Natural Sciences and Engineering Research Council (NSERC) of Canada. HBH was partly supported by the University of Oregon Summer Program for Undergraduate Research (SPUR). We would like to thank Professor Benjamin Hackel for the generous donation of the naïve affibody-expressing yeast surface display library. We would like to thank Professor Mike Harms and Jonathan Muyskens for advice and use of the Jasco J-815 circular dichroism spectropolarimeter, and Professor Calin Plesa and Samuel Hinton for advice and use of the Applied Biosystems Thermocycler and Azure Biosystems Imager. We would also like to thank Andrew Swansiger for preliminary work on mass spectrometry analysis of the affibodies. Finally, we would like to thank members of the Hettiaratchi lab for their thoughtful review of this manuscript. Figures were created using BioRender.com.

Materials and Methods

Protein Modifications

Recombinant human BMP-2 (Medtronic, R&D Systems) was biotinylated using EZ-Link™ Sulfo-NHS-Biotin (Thermo Fisher) per the manufacturer's protocols. Briefly, a 10 mM solution of sulfo-NHS-biotin in water was prepared, and 20 molar excess of sulfo-NHS-biotin was added to a 0.5 mg mL^{-1} solution of BMP-2 (Medtronic) in phosphate buffered saline (Fisher Scientific; PBS). The reaction was carried out for 2 hours at 4 °C, and the biotinylated product (bBMP-2) was eluted into PBS using 7 kDa Zeba Spin Desalting Column (Thermo Fisher). Biotinylation was confirmed using a Pierce™ Biotin Quantitation Kit (Thermo Fisher).

Yeast growth and induction

The naïve affibody-expressing yeast surface display library used in this paper was generously donated by Dr. Benjamin Hackel. This EBY100 strain of *Saccharomyces cerevisiae* contains the pCT surface display vector for galactose-inducible surface protein expression of roughly 4×10^8 unique affibody sequences.[104]

Yeast were grown in selective growth media (16.8 g sodium citrate dihydrate (, 3.9 g citric acid, 20.0 g dextrose, 6.7 g yeast nitrogen base, 5.0 g casamino acids, 1 mg ciprofloxacin and 100 mg ampicillin in 1 L reverse osmosis (RO) water) in an Innova44 shaking incubator (Innova) at 37 °C for 20 hours to a concentration between 5-10×10^7 cells mL^{-1}, after which 10× library diversity was transferred into selective induction media (10.2 g sodium phosphate dibasic heptahydrate, 8.6 g sodium phosphate monobasic monohydrate, 19.0 g galactose, 1.0 g dextrose, 6.7 g yeast nitrogen base, 5.0 g casamino acids, 1 mg ciprofloxacin and 100 mg ampicillin in 1 L RO water) to induce affibody expression in a shaking incubator at 37 °C for 20 hours.

Surface protein expression was confirmed by flow cytometry. 1×10^6 cells were aliquoted into tubes labeled cells only, secondary only, and c-myc + secondary. Each tube was washed and resuspended in 50 µL of PBS + 0.1% BSA (PBSA). 1.25 µL of anti-c-myc mouse monoclonal antibody (αCMYC, 9E10; BioLegend) were added to the c-myc + secondary tube. The tubes were rotated at 4 °C for 30 minutes. All tubes were washed again and resuspended in 50 µL of PBSA. 0.625 µL of goat anti-mouse IgG-AlexaFluor™ 488 secondary antibody (Thermo Fisher; AF488) were added to the secondary only and c-myc + secondary tubes. All tubes were rotated for 30 minutes in the dark at 4 °C. All tubes were washed twice and resuspended in 200 µL PBSA. Flow cytometry was performed using an Accuri™ C6 Plus Flow Cytometer with 96-well plate autosampler (Becton Dickinson).

Magnetic Activated Cell Sorting

Magnetic-activated cell sorting (MACS) was performed to enrich for BMP-2-binding affibodies within the yeast surface display library. One round of MACS consisted of two negative bead sorts and one positive bead sort. Negative bead sorts were performed using carboxylic acid magnetic beads (COOH beads) conjugated with either tris or BSA, which removed non-specific binders.[92,105,231,232] The positive bead sorts consisted of COOH beads conjugated with BMP-2 to enrich for yeast displaying BMP-2-specific affibodies. To prepare the beads, 2 µL of COOH beads (Invitrogen™ Dynabeads™ M-270 Carboxylic Acid) were rotated with 100 µL of cold 0.05 M NaOH for 10 minutes and then exposed to a magnetic field for 2 minutes so that a magnetic bead pellet formed at the wall of the tube. The NaOH was carefully removed to avoid disturbing the pellet, and the beads were then resuspended in 100 µL of cold water and rotated for 10 minutes. The beads were then resuspended and rotated in 100 µL of 50 mg mL^{-1} solution

of 1-Ethyl-3-(3-dimethylaminopropyl)carbodiimide (EDC) in water for 30 minutes. The EDC solution was removed, and the beads quickly rinsed with cold water and resuspended in 100µL of 0.1 M MES buffer pH 5 followed by either 500 µL of PBSA, 500 µL of 0.05 M tris pH 7.4, or 33 pmol of carrier-free BMP-2 (R&D Biosystems) in water and rotated for 30 minutes. The reaction was terminated using the 0.05 M tris pH 7.4, and the beads were washed and resuspended in a solution of PBSA and stored on ice until needed.

10x library diversity was washed in PBSA to remove the induction media and resuspended in BSA-conjugated COOH bead solution. The yeast and beads were rotated at 4 °C for 2 hours and then exposed to a magnetic field. The unbound solution was gently removed and transferred to a tube containing tris-conjugated magnetic beads. The rotation and exposure were repeated as above, and the unbound solution was transferred to a tube with the BMP-2-conjugated magnetic beads and rotated once again for 2 hours. After exposure to the magnetic field, the unbound solution was removed, and the magnetic beads were resuspended in PBSA. 10 µL of 100x and 2000x diluted BSA, tris, and BMP-2-conjugated beads were plated on selective growth plates (16.8 g sodium citrate dihydrate, 3.9 g citric acid, 16 g bacto agar, 20 g dextrose, 6.7 g yeast nitrogen base, 5 g casamino acids, RO water, autoclaved and poured into petri dishes). Plates were incubated at 30 °C for 36 h, and colonies were counted to determine the ratio of positive-to-negative binders and new library diversity. The updated library diversity was estimated by Equation 2.1, and the new diversity was used to determine the number of yeast used for subsequent sorts.

Equation 2.1: Library diversity estimation as a function of CFUs, dilution, and culture volume

$$Library\ Diversity = \left(\frac{CFU}{plate}\right) * (dilution\ factor) * \left(\frac{total\ volume\ of\ undiluted\ positve\ sort}{10\mu L}\right)$$

Fluorescence-Activated Cell Sorting

Fluorescence-activated cell sorting (FACS) was performed on the enriched yeast library after MACS to separate yeast into populations corresponding to approximately different affinity ranges for BMP-2 binding. 40×10^6 induced yeast cells were aliquoted into tubes labeled cells only, secondary only, c-myc, and c-myc + bBMP-2, and washed in PBSA. The cells only, secondary only and c-myc tubes were resuspended in 50 µL PBSA. The c-myc + bBMP-2 tube

was resuspended in 50 µL of 1 µM bBMP-2 in PBSA. 1.25 µL of αCMYC were also added to the c-myc and c-myc + bBMP-2 tubes. All tubes were rotated at 4 °C for 1 h and then washed with PBSA. Except for the cells-only control, all tubes were incubated with 50 µL of secondary fluorescent solution (10.4 µL of 333 nM goat anti-mouse IgG AlexaFluor™ 647, 3.25 µL of AlexaFluor™ 488 streptavidin conjugate, 187 µL PBSA). The tubes were all rotated at 4 °C for 30 minutes and washed 2 times in 500 µL of PBSA. The yeast were suspended in 1000 µL PBSA and sorted by a SH800 Cell Sorter (Sony Biotechnology). At least 10,000 cells were obtained from each gate. Following FACS, yeast from each collected gate were grown in selective growth media at 30 °C to an approximate concentration of 10^7 cells mL^{-1},plated onto selective growth plates, and incubated for 24-36 hours in 30 °C.

Gene Sequencing of Monoclonal Affibody Yeast

Individual colonies from FACS-sorted yeast plates were selected and expanded in yeast growth media to a cell density of 10^7 cells mL^{-1}. The yeast plasmids were isolated using Easy Yeast Plasmid Isolation Kit (Clontech) per the manufacturer's instructions. The affibody sequences from the plasmids were amplified by PCR in an Applied Biosystems Thermocycler (Fisher Scientific) using HiFi PCR Premix (CloneAmp) and forward primer (*5'-CCCTCAACAACTAGCAAAGG-3'*) and reverse primer (*3'-ATGTGTAAAGTTGGTAACGGAACG-5'*) for 35 cycles and purified using a DNA Clean and Concentrator Kit (ZymoGen). The purified products were submitted for Sanger Sequencing to GeneWiz® (Azenta Life Sciences).

Monoclonal Affibody Yeast Characterization

The binding affinity of each unique affibody for BMP-2 was characterized using flow cytometry. Samples were prepared similarly to the FACS procedure with the following differences: $1x10^6$ induced cells were used in each tube instead of 40×10^6 cells, c-myc + bBMP-2 tubes were prepared with bBMP-2 concentrations ranging from 0.5-1000 nM, and each tube was resuspended in 200 µL of PBSA and transferred to a 96-well plate. Flow cytometry was performed on bBMP-2-containing samples in triplicate. Cells were analyzed using Accuri™ C6 Plus Flow Cytometer with 96-well plate autosampler (Becton Dickinson).

To quantify the equilibrium dissociation constant (K_D) of affibody-BMP-2 binding, the ratio of AF647+/AF488+ cells to AF647+ cells was calculated at each bBMP-2 concentration and plotted against protein concentration. Nonlinear regression was performed, in which the equilibrium dissociation constant was the inflection point of the curve.
Specificity of the affibodies to BMP-2 was confirmed using flow cytometry in a similar manner, except that 1 μM solutions of bVEGF (R&D Biosystems), bIL-4 (Acro Biosystems), and bGM-CSF (Acro Biosystems) were used.

Transformation of BMP-2-Specific Affibodies into *E. coli*

pET28b+ expression vectors containing sequences for each of the unique BMP-2-specific affibodies modified with a methionine at the N-terminus and a 6-His-tag and cysteine at the C-terminus were prepared by GenScript. The pET28b+ vector confers kanamycin resistance and uses an isopropyl ß-D-1-thiogalactopyranoside (IPTG)-inducible T7 promoter for protein expression. Vectors were transformed into BL21 chemically competent E. coli (New England BioLabs) per the manufacturer's protocols. 100 μL of transformed *E. coli* were plated on kanamycin selective growth plates (10 g yeast extract, 20 g bacto peptone, 20 g dextrose, 16 g bacto agar, 50 mg kanamycin sulfate, 1 L RO water) and incubated at 37 °C for 24 h. Colonies were selected and expanded in 20 mL Luria-Bertani (LB) broth (Thermo Fisher) supplemented in 20 μL of 50 mg mL^{-1} of kanamycin sulfate in water until an optical density at 600 nm (OD600) of 0.8 was reached. 4 mL of the culture were lysed and used to obtain plasmid DNA for sequence confirmation (Plasmid Miniprep Kit; Zymo Research), and the remaining volume was split in half, in which one half was induced with 10 μL of IPTG 0.5 M and incubated further for 4 hours at 37 °C, and the other half was refrigerated at 4 °C. The induced and uninduced E. coli were lysed using Bug Buster Protein Extraction Agent (Millipore Sigma) and centrifuged to separate the soluble proteins and the lysate. The soluble proteins were prepared for SDS-PAGE by diluting 18 μL of sample in 6 μL Laemmli buffer (BioRad) supplemented with 10 v/v% β-mercaptoethanol (BioRad) and heated for 5 minutes at 90 °C. The sampled were loaded into a 4-20% Mini-PROTEAN® TGX™ Precast Protein Gel (BioRad), run under denaturing conditions at 200 V for 35 minutes, stained with Coomassie blue dye, and imaged on an Azure 200 Gel Imager (Azure Biosystems, Inc.).

Collection and Purification of Soluble BMP-2-Specific Affibodies

Transformed E. coli were grown in 20 mL LB broth supplemented with kanamycin to a 0.5 mM concentration and incubated overnight at 37 °C. The contents were then transferred into 1.8 L of Terrific Broth (TB) supplemented with kanamycin to 0.5 mM and 500 µL of anti-foam 204 (Thermo Scientific) and cultured at 37 °C in a LEX-10 bioreactor (Epiphyte3). When the OD600 reached approximately 1.4, 1.8 mL of 0.5 M IPTG was added to the growth vessel to obtain a final concentration of 0.5 µM, and the temperature was reduced to 18 °C for 18 hours for induction of protein expression. After 18 hours, the culture was centrifuged for 20 minutes at 4 °C at 6000 RPM, and the cell pellet was removed and transferred to two 50 mL conical tubes. Binding buffer (50 mL of 1 M tris pH 7.5, 100 mL of 5 M NaCl, 5 mL of 1 M imidazole, and 845 mL RO water) supplemented with 75 mg of tris(2-carboxyethyl)phosphine hydrochloride (TCEP; GoldBio) was added to the cell pellet to a volume of 35 mL and lysed using a probe sonicator (Fisher Scientific) for 5 minutes in an ice bath. The sonicated product was centrifuged at 13,000 rcf for 30 minutes at 4 °C. The supernatant was transferred to a 50 mL conical tubes along with 3.6 mL of Nickel-NTA Agarose Beads (GoldBio; Nickel beads) and rotated at 4°C for 45 minutes. The supernatant was then transferred to a Econo-Column® chromatograph column (Biorad), washed with 50 mL of wash buffer (50 mL of 1 M tris pH 7.5, 100 mL of 5 M NaCl, 30 mL of 1 M imidazole, and 820 mL RO water) supplemented with 125 mg of TCEP followed by with 50 mL of wash buffer without TCEP, and eluted into 10 mL of elution buffer (50 mL of 1 M tris pH 7.5, 100 mL of 5 M NaCl, 250 mL of 1 M imidazole, and 600 mL RO water). The collected solution was then buffer-exchanged into 0.5 M Tris pH 8 using a 3 kDa molecular weight cut-off (MWCO) centrifuge filter (Millipore) and frozen at -80 °C until further use. SDS-PAGE was used to determine purity of the affibody at each step. UV-vis spectroscopy (Implen NP80) at 280 nm was used to determine the final concentration of the affibodies.

Circular Dichroism of Pure and Soluble Affibodies

A Jasco J-815 circular dichroism spectropolarimeter (CD Spec; JASCO) was used to characterize the secondary protein structure of the affibodies. Purified affibody was buffer exchanged into PBS pH 6.92 using Zeba columns and diluted to a concentration below 50 µM. The protein was loaded into a quartz cuvette with 1 mm path length and placed in the CD Spec. The circular

dichroism value and the high-tension voltage were collected over a wavelength range of 190-250 nm. The circular dichroism was converted to molar ellipticity using the molecular weight and concentration of each affibody (Equation 2.2).

Equation 2.2: Unit conversion from mdegrees to molar ellipticity

$$\Theta = \frac{m^\circ * M}{10 * L * C}$$

Native Ion Mass Spectrometry of Pure and Soluble Affibodies

A Waters Synapt G2S*i* mass spectrometer, calibrated with CsI cluster ions, was used to characterize the purity and mass of the collected affibodies. For each affibody, 1 mL of approximately 0.1 mg mL^{-1} was buffer-exchanged into 200 mM ammonium acetate pH 7.52 via 6 kDa molecular weight cut-off Micro Bio-Spin 6 Columns (BioRad) and diluted to approximately 20 µM. Mass spectra were collected over 1-5 minutes using nano-electrospray ionization at a capillary voltage of 0.7-1.0 kV. Samples were deconvolved in UniDec[295] using charge states 3 to 7 and an output mass range of 5,000-9,000 Da.

Characterizing Binding Interactions of Pure and Soluble Affibodies via BioLayer Interferometry

The binding interaction between BMP-2 and each soluble affibody was measured using a Gator® Plus biolayer interferometer (BLI; Gator Bio). Biotinylated BMP-2 was buffer-exchanged into PBS and diluted to 25 nM in PBS with 0.05% Tween20 (PBST; Thermo Fisher). Each soluble affibody was also buffer-exchanged into PBS and diluted to concentrations between 0-125 nM in PBST. Streptavidin-coated BLI probes (Gator Bio) were pre-soaked in 250 µL PBST for 45 minutes. The probes were then baselined with 200 µL PBST for 300 seconds and loaded with bBMP-2 for 90 seconds or until the wavelength shift plateaued. A new baseline was established using 200 µL PBST for 90 seconds, followed by 300 seconds of association with 200 µL of the various concentrations of affibody and dissociation for 300 seconds in 200 µL PBST. The association and dissociation data for the first 120 seconds were used to avoid confounding nonspecific binding interactions. One probe was loaded with bBMP-2 and no affibodies and

another probe was loaded with 125 nM of affibody and no bBMP-2 for use as a reference probe and to quantify nonspecific binding to the probes, respectively.

Computational Prediction of Binding Interaction Between BMP-2 and Pure Affibodies

The high- and low-affinity affibody sequences were input into AlphaFold2,[250] which outputs high-ranking protein structures and their corresponding prediction confidence as determined by AlphaFold2's deep learning network. The five highest ranked affibody structure prediction models for each unique affibody sequence were energetically minimized using Rosetta build 314.[245–248,250–253] Specifically, we used a full-atom refinement application called Relax which samples backbone and sidechain conformations to make local optimizations to the protein structure based on physics and heuristics-based weighted calculations.[252,257,296] Furthermore, the Relax protocol constrains the minimization movements to input structure, thereby biasing the refinements to the AlphaFold2 structure predictions. The affibody binding sites and orientations to target protein BMP-2 (PDB ID: 3BMP) were then modeled using the publicly available web server for ZDOCK, a docking application which approximates global binding.[254] The ten most probable affibody-BMP-2 complexes determined in the ZDOCK 3.0.2 algorithm for each sequence were similarly relaxed with Rosetta. To characterize the predicted interactions from ZDOCK, we performed interface analysis using PyMOL.[255] The x-ray crystallography structure of BMP Receptor Type-1A was used as present in the RSCB protein databank (PDB: 1REW). The AlphaFold2- Multimer tool was also used to predict the docking of BMP Receptor II (BMPR-II) using PDB: 7PPA onto BMP-2 using PDB: 3BMP.[297,298]

Cell Culture

High glucose Dulbecco's modified eagle medium (DMEM; Gibco) was supplemented with fetal bovine serum (FBS; Bio-techne) to either 1 v/v% or 10 v/v% to create low serum or high serum medium, respectively. Both media were supplemented with 1 mL of penicillin-streptomycin solution (Millipore Sigma) containing 10,000 U mL^{-1} penicillin and 10,000 μg mL^{-1} streptomycin. C2C12 immortalized murine skeletal myoblasts (CRL-1772; ATCC) were maintained in high serum medium, detached and passaged using 0.25% trypsin-EDTA (Lonza),

and reseeded into T75 flasks (NEST Scientific) at a density of 2,500 cells cm^{-2}. Cell number and viability were quantified using a Countess II Automated Cell Counter (Invitrogen).

C2C12 Cytocompatibility Assay for Affibodies

C2C12 myoblasts were seeded onto a 96-well plate at a concentration of 2000 cells cm^{-2} in 180 µL of high serum medium and allowed to adhere for 6 h. Affibodies were buffer-exchanged into PBS using 7 kDa Zeba columns, sterile-filtered through 0.22 □m filters, and diluted in sterile Dulbecco's PBS. Affibodies were added to the cell culture wells at final concentrations of 10 nM, 20 nM, 40 nM, 80 nM, or 800 nM and incubated for 72 h. The cells were washed with PBS and stained for 30 minutes at 37 °C with fresh high serum medium containing 4 mM Calcein AM (Fisher Scientific) and 2 mM ethidium homodimer-1 (Santa Cruz Biotechnology) to quantify the number of live and dead cells, respectively. Cells were imaged using a LionHeart FX automated microscope (BioTek). The number of live and dead cells were quantified using a custom script developed for Python. Cell viability was calculated by dividing the number of living cells by the total number of cells.

C2C12 Alkaline Phosphatase Activity Assay

C2C12 myoblasts were seeded onto a 96-well plate at a concentration of 62,500 cells cm^{-2} in 200 µL of high serum medium and allowed to adhere for 6 h, after which the cells were washed with PBS and resuspended in 100 µL of low serum media containing the different treatments. Affibodies were buffer-exchanged into PBS using 7 kDa Zeba columns, sterile-filtered through 0.22 µm filters, and diluted in PBS to concentrations of 10 nM, 20 nM, 40 nM, 80 nM, and 1000 nM. Sterile carrier-free recombinant human BMP-2 (R&D Biosystems) was diluted to 20 nM in PBS. 20 nM of BMP-2 and/or 10 nM, 20 nM, 40 nM, 80 nM, or 1000 nM of affibodies were added sequentially for the "uncomplexed" treatment groups or as a premixed solution for the "complexed" treatment groups as described above. After 72 h, the cells were lysed with Cellytic M (Millipore Sigma), and their ALP activity was quantified and normalized to the total amount of double stranded DNA (dsDNA) present in each well.[269] For the ALP colorimetric assay, 50 µL buffer solution consisting of equal volumes of 1.5 M 2-amino-2methyl-1-propanol solution pH 10.25, 20 mM p-nitrophenyl phosphate solution, and 10 mM $MgCl_2$ hexahydrate solution

were mixed with 50 µL of lysed cells and incubated in the dark for 20 minutes before the absorbance of the solutions was read at 405 nm (Synergy Neo2, Biotek). The colorimetric change in the solutions was converted to p-nitrophenol concentration using a calibration curve of 0-0.8 µmol mL^{-1} 4-nitrophenol solution (Millipore Sigma). The QuantiFluor dsDNA System (Promega) was used for dsDNA quantification. The ALP activity in each well was normalized to the dsDNA content to account for variability in cell number between samples.

Synthesis of Affibody-Conjugated Poly(Ethylene Glycol)-Maleimide Hydrogels

Affibodies were buffer-exchanged into PBS pH 6.92 using 7 kDa Zeba columns. A 16.7 w/v% solution of 20 kDa 4-arm PEG-Mal (Laysan Bio) in PBS pH 6.92 was prepared. 30 µL of PEG-Mal solution was mixed with 1.92 nmol of affibody in 30 µL PBS pH 6.92 or with 30 µL of PBS pH 6.92 for the negative control. The solution was rotated for 1 hour at room temperature for affibody conjugation. 40 µL of DTT (GoldBio) solution (1.93 mg mL^{-1} in PBS pH 6.92) was added to each tube containing PEG-Mal and rotated at room temperature for 30 minutes to form 100 µL 5 w/v% PEG-Mal hydrogels with/without 1.92 nmol of affibodies.[237,273] The hydrogels were washed three times with 500 µL of PBS for 6 h to remove unreacted DTT and affibody. To maintain sterility for sterile hydrogels, the PEG-Mal, DTT, and PBS solutions were sterile-filtered with a 0.22 µm syringe filter and handled in a biosafety cabinet prior to mixing and crosslinking.

Encapsulation and Controlled Release of BMP-2 from Affibody-Conjugated PEG-Mal Hydrogels

100 µL 5 w/v% PEG-Mal hydrogels were prepared without affibody and with each of the two unique BMP-2 affibodies as described above. After purification, the PBS supernatant was removed and 20 µL of 5 µg mL^{-1} BMP-2 in PBSA were pipetted onto each hydrogel. The tubes were rotated at 4 °C for 12 h to allow BMP-2 to infiltrate the hydrogels. The hydrogels were washed with PBSA twice. 880 µL of PBSA was added to each hydrogel for a total tube volume of 1 mL. The hydrogels were placed at 37 °C and timepoints were collected by removing 200 µL of supernatant from the tube and replenishing it with fresh PBSA. BMP-2 in the washes and collected timepoints was quantified using a Human BMP-2 DuoSet ELISA kit (R&D

Biosystems). For BMP-2 release into serum, 10 v/v% of FBS in PBS was used as the solution for time 0 and onward.

Encapsulation efficiency was calculated by comparing the total amount of BMP-2 collected from each hydrogel in wash 1 and wash 2 with the total amount of BMP-2 added to the hydrogel. Cumulative release at each timepoint was calculated by dividing the total amount of BMP-2 collected from each hydrogel by the amount of BMP-2 encapsulated in each hydrogel. The effective diffusivity (i.e., release rate) of the BMP-2 from the hydrogels was calculated using a Fickian diffusion model from a thin polymeric sheet in a pseudo-infinite surrounding volume.[286]

Chapter 3 BMP-2 Bioactivity Upon Release from Affibody-Conjugated PEG-Mal Hydrogels

200 µL sterile PEG-Mal hydrogels without affibody (PEG-Mal control hydrogel) or with each affibody (affibody-conjugated PEG-Mal hydrogels) were prepared in a biosafety cabinet as described above by doubling the quantities of all reagents in each hydrogel. 10 µg mL^{-1} of sterile BMP-2 in low serum media was added to each hydrogel and rotated overnight at 4 °C to allow the BMP-2 infiltrate the hydrogels. 800 µL of low serum media was added to each hydrogel formulation and incubated at 37 °C. 230 µL of the supernatant were collected and replenished with fresh low serum media at 1, 2, 3, 5 and 7 days.

Meanwhile, C2C12 myoblasts were cultured as described above. After all of the timepoints were collected, the cells were washed and detached with 0.25% trypsin-EDTA, and the wells of a 96-well plate were seeded with 62,500 cells cm^{-2} in 200 µL of high serum medium for 6 h to adhere. The medium was then removed, the cells were washed with PBS, and 200 µL of each collected timepoint was added to the cells for 72 h. ALP activity was quantified as described above. The remaining 30 µL of each collected sample were used to quantify the amount of BMP-2 added to each well using BMP-2 ELISA. ALP activity was normalized to dsDNA and the amount of released BMP-2 added to each well. Area under the curve was calculated for each group as the sum of normalized activity for the duration of the experiment.

Statistical Analysis

All data pre-processing was performed using GraphPad Prism 9.5.1, except flow cytometry data which was prepared using FlowJo 10.8.1, biolayer interferometry preparation and curve fitting which was prepared using GatorOne 2.10, and protein structural presentation which was prepared using PyMOL 4.6.0. All relevant data are reported as means +/- standard deviation with

sample sizes indicated in the figure caption. All statistical methods used to assess significant differences and applicable post-hoc tests are reported in figure captions.

Figure 2: E) Significance determined by two-way ANOVA, Tukey's post-hoc test. * $p<0.01$. F) Significance determined by one-way ANOVA with Tukey's post-hoc test. n=3, ** $p<0.01$. G-H) Significance determined by one-way ANOVA and Tukey's post-hoc test. n=3, **** $p<0.0001$.

Figure 6: D,E) Significance determined by two-way ANOVA and Dunnett's post-hoc test, n=4, * $p<0.05$. F) Significance determined by one-way ANOVA and Tukey's post-hoc test. n=4, * $p<0.05$, ** $p<0.01$, *** $p<0.001$, **** $p<0.0001$.

Figure 7: B) Significance determined by one-way ANOVA and Tukey's post-hoc test. n=8, **** $p<0.0001$. C, D) Significance determined by two-way ANOVA and Tukey's post-hoc test. n=4. * $p<0.05$, ** $p<0.01$. E) Significance determined by one-way ANOVA and Tukey's post-hoc test. n=4 **** $p<0.0001$.

Figure 8: A) Significance determined by two-way ANOVA and Tukey's post-hoc test. n=4, * $p<0.05$, ** $p<0.01$, *** $p<0.001$. C) Significance determined by two-way ANOVA and Tukey's post-hoc test. n=4, * $p<0.05$. D) Significance determined by one-way ANOVA, post-hoc Tukey multiple comparisons. n=4, * $p<0.05$, ** $p<0.01$, *** $p<0.001$, **** $p<0.0001$.

For all data, the use of one-way ANOVA was chosen for a single variable of comparison. For all two-way ANOVA, multiple variables were compared. Tukey post-hoc tests were performed to compare the significance of all groups between each other. Dunnett post-hoc tests were performed to compare the significance of all data to a control group.

All statistical analyses were performed using GraphPad Prism 9.5.1. All data are reported as means +/- standard deviation.

Chapter 3 - Recombinant and Synthetic Affibodies Function Comparably for Modulating Protein Release

From Dorogin, J., Benz, M.A., Moore, C.J., Benoit, D.S.W., Hettiaratchi, M.H. 2024. Recombinant and Synthetic Affibodies Function Comparably for Modulating Protein Release. *Cellular and Molecular Bioengineering* 17(4): 305-312.

Abstract

Purpose

Affibodies are a class of versatile affinity proteins with a wide variety of therapeutic applications, ranging from guided contrast agents for imaging to cell-targeting therapeutics. We have identified several affibodies specific to bone morphogenetic protein-2 (BMP-2) with a range of binding affinities and demonstrated the ability to tune release rate of BMP-2 from affibody-conjugated poly(ethylene glycol) (PEG) hydrogels based on affibody affinity strength. In this work, we compare the purity, structure, and activity of recombinant, bacterially-expressed BMP-2-specific affibodies with affibodies synthesized via solid-phase peptide synthesis.

Methods

High- and low-affinity BMP-2-specific affibodies were recombinantly expressed using BL21(DE3) *E. coli* and chemically synthesized using microwave-assisted solid-phase peptide synthesis with Fmoc-Gly-Wang resin. The secondary structures of the affibodies and dissociation constants of affibody-BMP-2 binding were characterized by circular dichroism and biolayer interferometry, respectively. Endotoxin levels were measured using chromogenic limulus amebocyte lysate (LAL) assays. Affibody-conjugated PEG-mal hydrogels were fabricated and loaded with BMP-2 to evaluate hydrogel capacity for controlled release, quantified by enzyme-linked immunosorbent assays (ELISA).

Results

Synthetic and recombinant affibodies were determined to be α-helical by circular dichroism. The synthetic high- and low-affinity BMP-2-specific affibodies demonstrated comparable BMP-2-

binding dissociation constants to their recombinant counterparts. Recombinant affibodies retained some endotoxins after purification, while endotoxins were not detected in the synthetic affibodies. High-affinity affibody-conjugated hydrogels reduced cumulative BMP-2 release compared to the low-affinity affibody-conjugated hydrogels and hydrogels without affibodies.

Conclusions

Synthetic affibodies demonstrate comparable structure and function to recombinant affibodies, while reducing endotoxin contamination and increasing product yield, indicating that solid-phase peptide synthesis is a viable method of producing affibodies for controlled protein release and other applications.

Keywords: Affibody, BMP-2, peptide, Solid-phase peptide synthesis, recombinant protein expression, hydrogel

Introduction

Affibodies are a class of versatile antibody-mimetic proteins that can be engineered to bind with high specificity and tunable affinity to various targets, enabling their use in numerous biomedical applications, including contrast agents for medical imaging and affinity-mediated protein delivery vehicles.[92,224,225,299] Recently, we identified several affibodies that specifically bind to bone morphogenetic protein-2 (BMP-2) with a range of affinities and used these affibodies to tune the release of BMP-2 from affibody-conjugated poly(ethylene glycol) hydrogels based on the strength of the affibody-BMP-2 affinity interaction.[300] In this work, high-affinity and low-affinity BMP-2 affibodies were expressed recombinantly in BL21(DE3) *E. coli*. However, bacterial protein expression can result in contamination with endotoxin, a bacterial membrane component, leading to inflammation and activation of the innate immune system in vivo.[301,302] Thus, reducing endotoxin levels in affibodies could improve their utility in biomedical applications.

Common approaches to reducing endotoxin contamination include post-processing recombinant proteins with endotoxin removal columns[303–305] and phase separation methods,[303,306] using low endotoxin bacterial expression systems and mammalian cell lines to minimize levels of

endotoxin expressed,[235,307–309] and solid-phase protein synthesis (SPPS).[310] While recombinant protein expression is optimized for the expression system (i.e., BL21 E. coli) to ensure protein expression and proper folding, the yield can be quite low. Conversely, the higher mass yields associated with SPPS do not guarantee proper protein folding and require multiple purification steps. Further, SPPS synthesis efficiency decreases with larger peptide and protein sequences.[311,312] As a result, recombinant and synthetic proteins functions may differ slightly. In this work, we compare the yield, endotoxin levels, secondary structure, and affinity binding interactions of recombinant and synthetic affibodies to determine whether synthetic BMP-2-specific affibodies can substitute recombinant affibodies for controlled BMP-2 delivery.

Methods and Results

Unless otherwise specified, all chemicals were purchased from Fisher Scientific.

Bacterial expression and purification of recombinant affibodies

Recombinant affibodies were expressed in *E. coli* and purified as previously described.[300] Briefly, pET28b+ vectors for isopropyl β-D-1-thiogalactopyranoside (IPTG (Thermo Scientific))-inducible protein expression were constructed with high- or low-affinity BMP-2-specific affibody sequences modified with a C-terminal hexahistidine tag for immobilized metal affinity chromatography and cysteine for bioconjugation. Plasmids were transformed into BL21 *E. coli*, and sequences were verified using Sanger sequencing (Azenta Life Sciences). *E. coli* were expanded in 20 mL of Lysogeny Broth overnight at 37 °C, and then further expanded in 1.8 L of Terrific Broth (Research Products International) at 37 °C with air sparging in a bioreactor (LEX-10, Epiphyte3) for 3-4 hours until the optical density of the culture at 600 nm reached approximately 0.8-1.2 absorbance units. Protein expression was induced with IPTG at 18 °C for 20 hours. The cells were lysed by sonication in 50 mM Tris buffer pH 7.5 supplemented with 500 mM NaCl, 5 mM imidazole (Sigma Aldrich), and 75 mg of tris(2-carboxyethyl)phosphine (TCEP (GoldBio)) to prevent oxidation of the cysteines and then centrifuged (13,000 RCF for 30 minutes). The supernatant was mixed with cobalt-nitrilotriacetic acid (Co-NTA (GoldBio)) beads for 1 hour and washed with 100 mL of 50 mM tris buffer containing 500 mM NaCl and 30 mM imidazole. The affibodies were eluted into 50 mM tris buffer pH 7.5 containing 500 mM NaCl and 250 mM imidazole and buffer-exchanged into phosphate-buffered saline (PBS). The

affibodies were further purified by size exclusion chromatography (BioRad NGC with Enrich SEC 70, 10/300 mm column), concentrated to 0.5-2 mg/mL, and stored frozen at -20 °C.

Synthesis and purification of synthetic affibodies

Synthetic affibodies modified with a penultimate cysteine and a C-terminal glycine were prepared by SPPS on Fmoc-Gly-Wang resin (CEM Corporation) (0.602 mmol/g loading) using a CEM Liberty Blue 2.0 microwave peptide synthesizer (CEM Corporation). 0.2 M amino acid (CEM Corporation), 10% v/v pyrrolidine (Sigma Aldrich) deprotection, 1 M N,N'-diisopropylcarbodiimide (DIC) (Oakwood Chemical), and 1 M Oxyma (CEM Corporation) solutions were prepared in DMF. Affibodies were cleaved and deprotected by vacuum-filtering the resin, washing with dichloromethane twice, and resuspending in the cleavage cocktail (1:1:1:1:36 ratios of ddH_2O, triisopropyl silane (Oakwood Chemical), 2,2'-(Ethylenedioxy)diethanethiol (Tokyo Chemical Industry), thioanisole (Oakwood Chemical), trifluoroacetic acid (TFA) (Oakwood Chemical)) for 40 minutes at 42 °C[313]. The solution was vacuum filtered and the filtrate was purified via precipitation and three rounds of centrifugation (1200 RCF for 5 minutes) using -20 °C diethyl ether. The resultant slurry was dried overnight in a vacuum desiccator and transferred to -20 °C for storage. The crude products were purified by high-performance liquid chromatography (HPLC; CEM Prodigy using 19 x 150 mm C18 Waters column) by running a 15-75% acetonitrile gradient in ddH_2O with 0.1% v/v TFA. The purified products were lyophilized and stored at -20 °C.

Characterization of synthetic and recombinant affibodies

Affibody molecular weights were confirmed using matrix-assisted laser desorption/ionization time of flight (MALDI-TOF) mass spectrometry (Bruker Smart LS). A matrix solution of 10 mg/mL α-cyano-4-hydroxycinnamic acid (Sigma Aldrich) in 0.1% v/v TFA and 50% v/v acetonitrile in ddH_2O was prepared, and equal parts matrix and sample in 3% v/v acetonitrile in ddH_2O were deposited on a MALDI target plate.

The secondary structure of the affibodies was measured using circular dichroism (CD) spectrophotometry (Jasco J-815). Affibodies were reconstituted in 10 mM tris buffer, pH 8 and loaded into a quartz cuvette (Starna Cell Corp.) with a 1 mm path length. Circular dichroism

spectra were obtained over 190-250 nm and normalized to mean residue molar ellipticity (Equation 2.2).[243,314,315]

The kinetics of BMP-2-affibody binding were measured by biolayer interferometry (BLI; Gator Bio). Streptavidin-coated probes were loaded with 25 nM of biotinylated BMP-2 (Medtronic, biotinylated in-house using EZ Link NHS-Biotin (Thermo Fisher) per manufacturer's protocols)) in PBS with 0.05% Tween 80 (PBST) and then allowed to associate to and dissociate from 31.25-125 mM of affibody in PBST for 60 seconds each. The dissociation constants (K_D), on-rate constants (k_{on}), and off-rate constants (k_{off}) were calculated for each affibody-BMP-2 binding pair by curve fitting the wavelength shifts using a 1:1 Langmuir isotherm binding model.

Endotoxin removal and quantification of synthetic and recombinant affibodies

Pierce High Capacity Endotoxin Removal Spin Columns (Thermo Fisher Scientific) were used to remove lipopolysaccharides (LPS), the prominent endotoxin contaminant, from the affibodies. Columns were regenerated and equilibrated using Endotoxin-Free Dulbecco's PBS (Millipore Sigma) according to the manufacturer's instructions. Endotoxin levels in each synthetic and recombinant affibody, before and after endotoxin removal, were quantified using the ToxinSensor Chromogenic LAL endotoxin assay kit (GenScript) according to the manufacturer's instructions. The endotoxin concentration in each sample was determined using a standard curve ranging from 0.1 to 1 endotoxin units (EU)/mL constructed from known amounts of *E. coli* endotoxin, wherein 1 EU corresponds to approximately 0.1-0.2 ng of endotoxin.

BMP-2 release from hydrogels conjugated with synthetic and recombinant affibodies

Affibody-conjugated PEG-mal hydrogels were synthesized as previously described.[237,300] Briefly, PEG-maleimide (Laysan Bio) and affibodies (recombinant high-affinity, recombinant low-affinity, synthetic high-affinity, or synthetic low-affinity) were each dissolved in PBS pH 6.9 and rotated for 30 minutes at room temperature to form PEG-affibody intermediates. 70 µL aliquots of intermediate solutions were transferred into 2 mL microcentrifuge tubes, mixed with 30 µL dithiothreitol (DTT) (GoldBio) dissolved in PBS pH 6.9, and allowed to crosslink for 30 minutes at room temperature to form 100 µL hydrogels with 2 nmol of BMP-2-specific

affibodies. Unreacted DTT was removed from the hydrogels by washing with fresh PBS 3 times over 36 hours.

Hydrogels were loaded with 100 ng of BMP-2 (3.85 pmol; 500:1 affibody-to-BMP-2 molar ratio) for 3 hours at 4 °C. The remaining loading solution was removed, and BMP-2 concentration was measured using ELISA to calculate initial BMP-2 encapsulation. Hydrogels were submerged in 900 μL of 0.1% w/v bovine serum albumin (BSA) in PBS. BMP-2 release was measured over 2 weeks by collecting 200 μL aliquots of the supernatant periodically and measuring BMP-2 concentration using ELISA. To compare release rates, the slopes of the linear portion of each hydrogel release profile, corresponding to the Fickian diffusion model, were calculated and compared, as previously described.[299,300]

Results

Recombinant and synthetic affibodies display similar characteristics

Recombinant expression of BMP-2-specific affibodies in *E. coli* resulted in a yield of approximately 20 mg of purified affibodies from a single 1.8 L culture. SPPS production of affibodies resulted in a yield of approximately 100 mg of purified affibodies from a single 0.1 mmol reaction. MALDI was used to determine the molecular weights of the affibodies. All affibodies displayed single peaks at the expected molecular weights, indicating high purity. The recombinant high-affinity affibody displayed a narrow peak at 7277 Da (-34 Da shift associated with dehydroalanine modifications),[240] and low-affinity affibody displayed a broader peak at 7627 Da (+213 Da shift associated with myristoilation[316]) (Figure 3.1A). We have previously reported the presence of these adducts in recombinantly expressed BMP-2-specific affibodies.[300] The synthetic affibodies both displayed narrow peaks, with the high-affinity affibody displaying a peak at 6544 Da (+2 Da shift associated with reduction of cystine[317]) and the low-affinity affibody displaying a peak at 6650 Da (+2 Da shift associated with reduction of cystine[317]) (Figure 3.1B). The lower molecular weights of the synthetic affibodies compared to the recombinant affibodies were due to the absence of the hexahistidine tag used in recombinant protein purification.

All affibodies displayed characteristic α-helical CD spectra with troughs at 222 nm and 208 nm, and a peak at 193 nm (Figure 3.1C).[243] The increase in molar ellipticity of the synthetic

affibodies compared to the recombinant affibodies could be attributed to either the absence of the hexahistidine tag in the synthetic product or the presence of LPS in the recombinant product, as hexahistidine tags do not typically contribute to the α-helicity and reduce the mean residue secondary structure,[318] while LPS can affect protein folding.[306,319,320] Greater chirality is associated with tighter folded α-helices.[315,321]

BLI demonstrated no significant differences between the BMP-2-affibody dissociation constants displayed by the recombinant and synthetic affibodies, indicating that these affibodies functioned similarly as binding proteins (Figure 3.1D). As expected, the synthetic high-affinity affibody displayed a significantly lower dissociation constant (i.e., higher BMP-2 binding affinity) than the synthetic low-affinity affibody. Complete dissociation of BMP-2 from the affibody was observed for the low-affinity affibody but not for the high-affinity affibody.

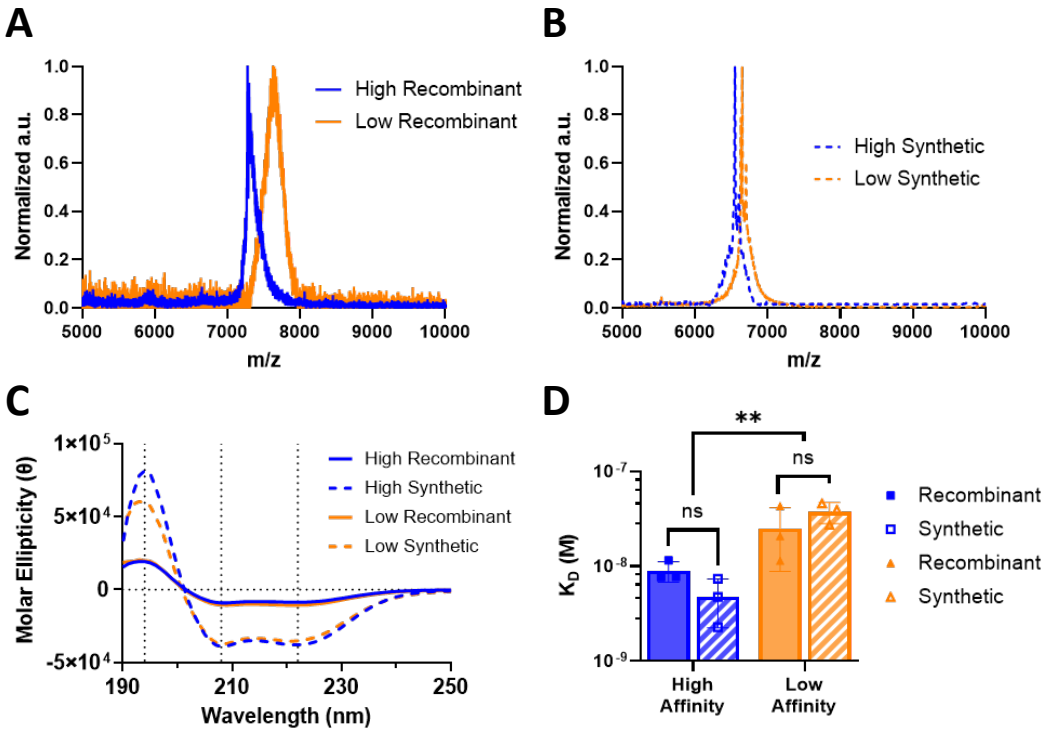


Figure 3.1: Properties of recombinant and synthetic affibodies. A,B) MALDI spectra of (A) recombinant and (B) synthetic affibodies. A single prominent peak was present in each sample at the expected masses. C) Circular dichroism spectra of affibodies, depicting α-helical secondary structures. D) Equilibrium dissociation constants (K_D) of affibodies measured by biolayer interferometry. Statistical significance was determined using two-way ANOVA with Tukey post-hoc test. n=3; ns – not significant, ** $p<0.01$ as indicated.

Synthetic affibodies contain fewer endotoxins than recombinant affibodies

Endotoxin content of the affibodies was measured before and after endotoxin removal via spin columns (Figure 3.2). The United States Food and Drug Administration (FDA) permits up to 0.5 EU/mL in medical devices.[302] The recombinant affibodies contained more than the permissible amount of endotoxin, before and after treatment with the endotoxin removal columns. The endotoxin levels of the recombinant affibodies were significantly higher than those in synthetic affibodies, which were below the levels permissible by the FDA. These results were as expected since the recombinant affibodies were in close contact with bacterial lysate during purification, while the synthetic affibodies had no exposure to bacteria. Furthermore, endotoxins have high affinities towards metals such as nickel and cobalt which are used in protein collection, resulting in larger quantities of endotoxins requiring purification.[319] Additionally, LPS binds to histidines which are present both during protein collection and during endotoxin removal, posing additional challenges for purifying recombinant proteins. [319] It is possible to overcome this challenge by modifying the affibody sequence to include protease cleavable sequences to remove the HisTag during purification.[322] However, the removal of histidine tags may not result in complete removal of endotoxins.[319]

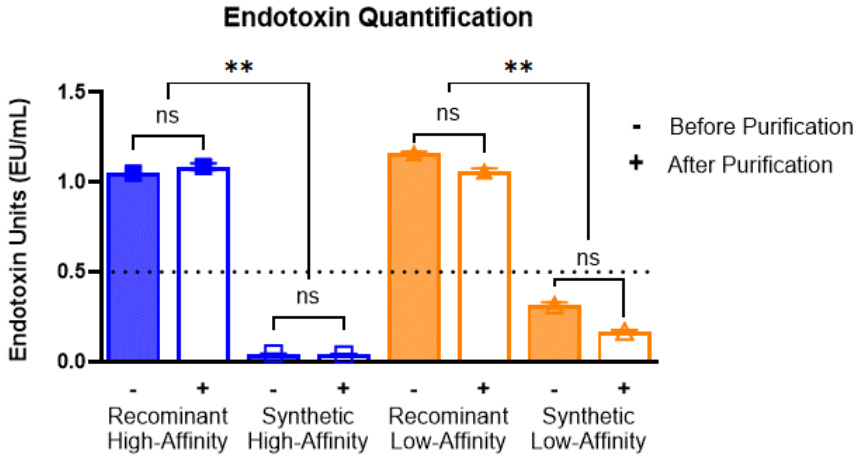


Figure 3.2: Endotoxin levels of recombinant and synthetic affibodies before and after endotoxin removal using spin columns. Endotoxin levels were measured using a chromogenic LAL endotoxin assay. Dotted line indicates the FDA approved limit for endotoxins in medical devices of 0.5 EU/mL. Statistical significance was determined using two-way ANOVA with Tukey post-hoc test. n=3; ns – not significant, ** $p<0.01$ as indicated.

Recombinant and synthetic affibodies similarly control BMP-2 encapsulation and release

PEG-mal hydrogels were synthesized without affibodies or with recombinant high-affinity, recombinant low-affinity, synthetic high-affinity, or synthetic low-affinity affibodies for BMP-2 encapsulation and release (Figure 3.3A). Hydrogels containing high-affinity affibodies demonstrated a higher BMP-2 encapsulation efficiency (Figure 3.3B) and lower cumulative BMP-2 release (Figure 3.3C) than the PEG and low-affinity affibody hydrogels. There were no significant differences in BMP-2 encapsulation and release between recombinant and synthetic affibodies for either the high-affinity or low-affinity affibodies. The slopes of Fickian diffusion determined using the linear portion of each hydrogel release profile were significantly lower for both the recombinant and synthetic high-affinity affibody-conjugated hydrogels compared to the low-affinity and affibody-free hydrogels, indicating a lower effective BMP-2 diffusivity in these systems. No significant differences between the synthetic and recombinant affibodies were observed in Fickian diffusion slopes (Figure 3.3D). These results were consistent with our previously published work using recombinantly expressed affibodies.[300] The cumulative release of the low-affinity affibody-containing hydrogels and hydrogels without affibodies plateaued at similar amounts after 7 days, which was anticipated by the BLI data that showed the complete dissociation of BMP-2 from the low-affinity affibody but not the high-affinity affibody.

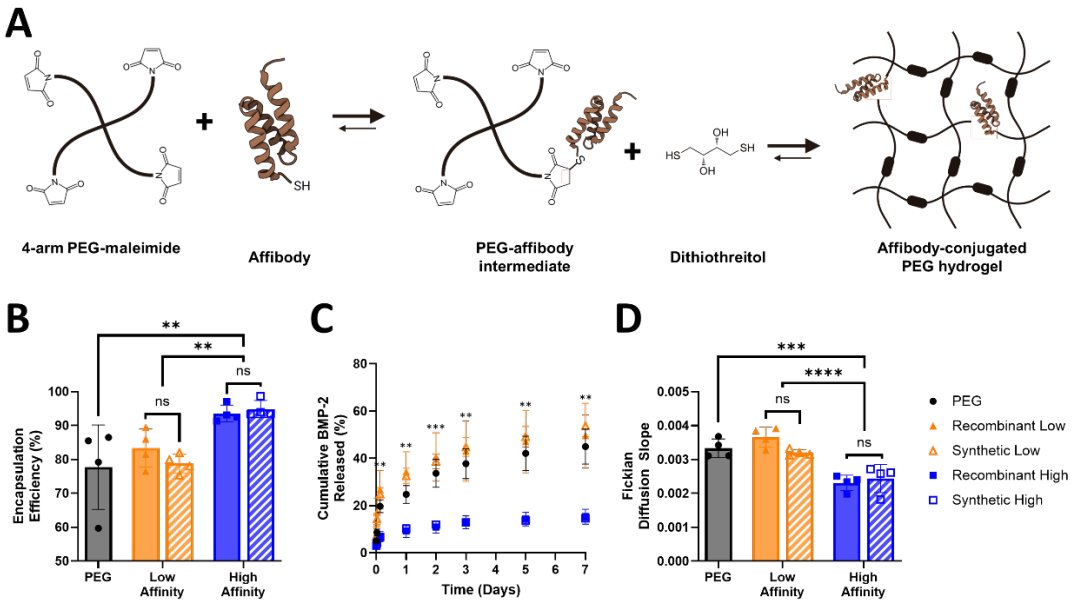


Figure 3.3: Encapsulation and cumulative release of BMP-2 from affibody-conjugated hydrogels. A) Synthesis schematic of affibody-conjugated PEG hydrogels. B) High-affinity affibody-conjugated hydrogels encapsulated more BMP-2 than low-affinity affibody and affibody-free hydrogels. C) High-affinity affibody-conjugated hydrogels released significantly less BMP-2 compared to low-affinity affibody and affibody-free hydrogels. D) Fickian diffusion rates. High-affinity affibody-conjugated hydrogels had a significantly slower Fickian diffusion rate compared to low-affinity and affibody-free hydrogels. Statistical significance was determined using 2-way ANOVA with Tukey post-hoc test. n=4; ns – not significant, ** $p<0.01$, *** $p<0.001$, **** $p<0.0001$; for panel B asterisks represent significance between the the high-affinity formulations and the PEG and low-affinity formulations.

Discussion

Affibodies are versatile affinity-binding proteins that can be produced using recombinant protein expression or SPPS and can be used for various biomedical applications.[224,227,323,324] Recent advances have enabled recombinantly expressed affibodies for controlled protein delivery using hydrogels.[92,299,300] Here, we demonstrated that BMP-2-specific affibodies produced via SPPS have comparable structure and function to affibodies expressed recombinantly in *E. coli.* Recombinant and synthetic affibodies share characteristic α-helical folding, similar dissociation constants for affibody-BMP-2 binding, and the ability to retain and release BMP-2 from PEG-mal hydrogels. Notable differences include lower molecular weights for the synthetic affibodies, which were engineered without hexahistidine tags, and could be leveraged for higher degrees of hydrogel modification, different magnitudes in circular dichroism signal, which could be representative of greater chirality in the synthetic affibodies, and lower endotoxin levels in the synthetic affibodies compared to their recombinant equivalents. These data suggest that synthetic and recombinant affibodies behave similarly in controlled BMP-2 release applications.

Although affibodies are typically expressed recombinantly in *E. coli*, SPPS may provide several advantages over recombinant protein expression. As noted in this work, recombinant expression of affibodies through an *E. coli* expression system yielded high levels of endotoxin contamination. Even after endotoxin removal, recombinant affibodies contained significantly higher endotoxin levels than synthetic affibodies, motivating the use of SPPS for affibody production for applications that eventually require in vivo use. Furthermore, SPPS has a high product yield and eliminates the risk of introducing other contaminating bacterial proteins into the product. Conversely, generating synthetic affibodies requires extensive infrastructure for SPPS that may not be readily available to all research groups. Generally, larger products also become more challenging to prepare by SPPS due to the stepwise growth of each product by chemical reaction. In certain cases, it may be advantageous to initially screen several affibodies

generated recombinantly before using SPPS to make large quantities of a single affibody. Ultimately, this work reveals that recombinant and synthetic affibodies share comparable structure and function, demonstrating that these methods could be used interchangeably depending on the application and reaffirming the robust nature of these affibody molecules.

Acknowledgements:

We are grateful for funding from the National Institutes of Health (R35-GM147507), and the Department of Defense's Peer-Reviewed Medical Research Program (W81XWH2210700) . JD is supported by a doctoral-level post-graduate scholarship (PGS-D) from the Natural Sciences and Engineering Council of Canada. MAB was supported by the Knight Campus Undergraduate Scholars Program. A list of affibody sequences used in this work can be found at: https://github.com/hettiaratchi-lab/Affibody-Sequences

Statement of Declaration

JD and MHH are authors on a pending patent application encompassing some of this work

Chapter 4 - Identification and Characterization of Interleukin-4-Specific Affibodies for Modulating Macrophage Polarization

The transformation procedure of IL-4-specific affibodies described in this chapter was developed Henry Hochstatter. Morrhyssey Benz contributed substantially to the identification, Sanger sequencing, transformation, expression, and purification of the affibodies. Morrhyssey also contributed to some of the affibody characterization and controlled release experiments. Morrhyssey Benz and David Frey performed some of ther THP-1 troubleshooting described in this chapter. I was the primary contributor to the magnetic and fluorescence activated cell sorting, gene sequencing, affibody characterization, computational predictions, in vitro THP-1 experiments, controlled release, and did all of the writing.

Introduction

The inflammatory response is a fundamental defense mechanism that protects the body from infection, injury, and other harmful stimuli.[325] It involves a highly coordinated interplay of immune cells and signaling molecules to manage repair processes. Macrophages are versatile immune cells derived from monocytes that play an integral role within this cascade.[326] They are recruited to sites of inflammation, where they perform essential functions, including pathogen clearance, antigen presentation, and the secretion of pro-inflammatory and anti-inflammatory cytokines.

Macrophages can differentiate into distinct phenotypes depending on the local microenvironment and cues they receive. Broadly, macrophages are classified as classically activated macrophages (M1) and alternatively activated macrophages (M2), which are further subcategorized as M2 a, b, c, d.[327–329] M1 macrophages are induced by pro-inflammatory signals, such as granulocyte macrophage colony stimulating factor (GM-CSF), interferon-gamma (IFN-γ) and lipopolysaccharide (LPS), and are characterized by their ability to produce inflammatory mediators, including tumor necrosis factor-alpha (TNF-α).[329] M2 macrophage subtypes play critical roles in injury resolutions, with M2a macrophages being the most commonly studied subtype associated with anti-inflammatory and wound healing functions arising in response to anti-inflammatory cytokines such as interleukin-4 (IL-4) and interleukin-13 (IL-13).[329,330] While

all M2 subtypes produce mediating cytokines such as interleukin-10 (IL-10), their activation pathways and functions are diverse. M2c is functionally similar to M2a and plays a role in phagocytosis and tissue remodeling, while M2b and M2d are involved in immune regulation of tumors.[330] These dynamic differentiation pathways play a pivotal role in ensuring tissue homeostasis and enable macrophages to participate in the initiation and resolution of inflammatory responses.

In vitro assays are an effective approach to study macrophage activity and response to various stimuli. There are several different cells which are commonly used, each with distinct advantages and limitations. Primary human peripheral blood mononuclear cells (PBMCs) are widely considered the gold standard due to their physiological relevance, as they closely mimic *in vivo* macrophage behavior, polarization and plasticity.[331] However, they require donor blood, are subject to donor variability, and have a limited lifespan in culture. Mouse bone marrow-derived macrophages (BMDMs) offer a more controlled genetic background and are commonly used in preclinical research but may not fully replicate human macrophage responses.[332] Alternatively, immortalized cell lines such as THP-1 and RAW 264.7 provide a more accessible and reproducible system.[333] RAW 264.7 cells, derived from murine macrophages, are easy to culture and highly responsive to stimuli but lack key polarization markers. THP-1 cells, a human monocytic leukemia cell line, can be differentiated into macrophage-like cells using phorbol 12-myristate 13-acetate (PMA) and are widely used for polarization studies.[334] While they do not fully replicate primary macrophage functionality, their ease of use, reproducibility, and clear polarization responses make them a good choice for proof-of-concept studies on simple macrophage polarization.

Traumatic injuries and chronic diseases may lead to dysregulation of the inflammatory process, and disrupt the body's innate capacity to heal.[335,336] Indeed, bone regeneration following trauma can be predicted by assessing the presence or absence of specific immunomodulatory cytokines interleukin-1 receptor antagonist (IL-1RA), IL-10, and transformation growth factor-β (TGF-β), IL-6 and IL-13.[337,338] Thus, developing therapeutics to effectively modulate or re-establish the inflammatory response would be valuable for improving healing outcomes and easing healthcare burdens. Some potential treatments for these dysregulations include delivering cytokines, antibodies and small molecules to either suppress the immune response[339] or re-establish homeostasis,[340,341] or alternatively to deliver cells overexpress cytokines such as IL-4 to manage

inflammation and tune bone resorption.[342] Yet, dosing in such dynamic injury environments poses a challenge, as the immune response in traumatic injuries is both spatially and temporally regulated. Systemic upregulation of macrophages may lead to additional complications. For instance, an overexpression of pro-inflammatory macrophages are a hallmark of rheumatoid arthritis and inflammatory bowel disease, while an overexpression of anti-inflammatory macrophages lead to allergic dermatitis, allergic asthma, and more.[327]

IL-4 is a particularly dynamic cytokine that plays a pivotal role in regulating the immune response, cellular permeability, and bone homeostasis.[343] IL-4 promotes a shift toward a Th2 immune response and suppressing the production of pro-inflammatory cytokines, such as IL-1β and TNF-α, by macrophages and other immune cells. IL-4 also modulates endothelial cell permeability by influencing endothelial and epithelial barrier function,[344] primarily through the upregulation of tight junction proteins and suppression of factors that increase vascular leakage. In bone biology, IL-4 exerts dual effects: it inhibits osteoclastogenesis by downregulating receptor activator of nuclear factor κ-B ligand (RANKL) expression[345] and pro-osteoclast factors such as TNF-α, and IL-6[346] while enhancing osteoprotegerin production[347], thus reducing bone resorption. Simultaneously, promotes the osteogenic differentiation of bone mesenchymal stem cells (BMSCs) by activating TGF/Smad pathways in BMSC co-cultures with macrophages. Collectively, these diverse functions underscore IL-4's critical role in maintaining tissue integrity and regenerating functional bone after injury.

To address the challenge of regulating the localized inflammatory response after traumatic injury, we propose a system for localized and tunable cytokine delivery. Our aim is to innovate upon literature that has delivered IL-4 from biomaterials to tune macrophage polarization.[340,348] Affinity-based interactions[211] could be used to ensure the temporally relevant presentation of IL-4, and the spatial aspect would be addressed with bulk hydrogels. We have previously described the process of identifying and characterizing affibodies, a class of small antibody-mimetic proteins,[349] for the delivery of bone morphogenetic protein-2 (BMP-2), and demonstrated the ability to tune the release rate of BMP-2 by controlling the affibodies' binding strengths or equilibrium dissociation constants.[350] Affibodies were also shown to mediate BMP-2-induced alkaline phosphatase (ALP) cellular activity. Taken together, an IL-4-specific affibody-conjugated hydrogel could be used to spatiotemporally deliver the anti-inflammatory cytokine and modulating the immune response.

In this chapter, we subject a yeast surface display library encoded for affibodies to magnetic activated cell sorting (MACS) and fluorescence activated cell sorting (FACS) to identify IL-4-specific affibodies. We use computational docking algorithms to predict the docking sites of IL-4 affibodies with IL-4 and rationalize/predict cellular functions. We use immortalized THP-1 monocyte-like cells to observe macrophage polarization towards the M1 or M2 phenotypes. The IL-4 affibodies are conjugated to poly(ethylene glycol)-maleimide (PEG-mal) hydrogels to tune the release of IL-4.

Materials and Methods

Yeast growth and induction

A naïve affibody-expressing yeast surface display library containing 4×10^8 unique affibody sequences was donated by Dr. Benjamin Hackel.[104] Yeast were cultured in growth media and induced in induction media as described previously. Briefly, yeast were grown in selective growth media at 37 °C for 20 hours to approximately 5×10^7 cells mL^{-1}, after which 10× library diversity was transferred into selective induction media to induce affibody expression in a shaking incubator at 37 °C for 20 hours.

Affibody Identification from yeast surface display (MACS)

The yeast surface display library was subjected to magnetic-activated cell sorting (MACS) using surface-modified carboxylic acid magnetic beads (COOH beads) (Invitrogen) to enrich for IL-4-binding affibodies. Each round of MACS consisted of two negative bead sorts and one positive bead sort, as described.[350] Negative bead sorts were performed with either tris- or bovine serum albumin- (BSA-) (Thermo Fisher) conjugated COOH beads to remove non-specific binders,[92,105,231,232] and the positive bead sorts consisted of IL-4-conjugated COOH beads to enrich for yeast displaying IL-4-specific affibodies. COOH bead bioconjugation was performed by rotating 2 µL of COOH beads with 100 µL of cold 0.05 M NaOH (Thermo Scientific), followed by purification through exposure to a magnetic field and supernatant removal. Beads were washed in 100 µL of cold water to remove NaOH and resuspended in 100 µL of 50 mg/mL solution of 1-Ethyl-3-(3-dimethylaminopropyl)carbodiimide (EDC) (G Biosciences) in water for 30 minutes. The EDC solution was removed, the beads were quickly rinsed with cold water and

resuspended in 100µL of 0.1 M MES buffer pH 5 and either 500 µL of 1 mg/mL BSA in PBS pH 7.4 (PBSA), 500 µL of 0.05 M tris pH 7.4, or 33 pmol of IL-4 (Peprotech, Inc.) in water to conjugate BSA, tris, or IL-4 to the beads, respectively. After 30 minutes, the reaction was terminated with 0.05 M tris pH 7.4. The beads were washed twice using magnet purification and resuspended in a solution of PBSA and stored on ice until needed.

Induced yeast were washed in PBSA to remove the induction media and 10× diversity was incubated in BSA-conjugated COOH bead solution for 2 hours at 4 °C. Beads were exposed to a magnetic field, and the unbound yeast solution was gently removed and transferred to a tube containing tris-conjugated magnetic beads for 2 hours of incubation at 4 °C. The magnet exposure was repeated, and the unbound yeast solution was transferred to a tube containing IL-4-conjugated magnetic beads for 2 hours. After exposure to the magnetic field, the magnetic beads kept and were resuspended in PBSA. 10 µL of 100x and 2000x diluted BSA, tris, and BMP-2-conjugated beads were plated on selective growth plates for 36 hours at 30 °C. The ratio of positive-to-negative binders and new library diversity was determined by counting the colony forming units (CFUs). The updated library diversity was estimated using Equation 2.1[350] and the new diversity was used to determine the number of yeast used for subsequent sorts.

Binding Checks and Fluorescence Activated Cell Sorting

Yeast populations were subjected to flow cytometry to determine both the degree of affibody expression on the yeast surface as well as the degree of protein-binding to the expressed affibodies. 1×10^6 induced yeast cells were aliquoted into tubes labeled cells only, secondary only, c-myc, and c-myc + bIL-4, and washed in PBSA. The cells only, secondary only and c-myc tubes were resuspended in 50 µL PBSA. The c-myc + bIL-4 tube was resuspended in 50 µL of 1 µM biotinylated IL-4 (bIL-4) (Acro Biosciences) in PBSA. 1.25 µL of anti-c-myc mouse monoclonal antibody 9E10 (αCMYC) (BioLegend) was added to the c-myc and c-myc + bIL-4 tubes. All tubes were rotated at 4 °C for 90 minutes and then washed with PBSA. Except for the cells-only control, all tubes were incubated with 50 µL of a secondary fluorescent solution containing 17.3 nM goat anti-mouse IgG AlexaFluor™ 647 (Invitrogen), 1.625 µg of AlexaFluor™ 488 streptavidin conjugate (Invitrogen) in PBSA for 30 minutes at 4 °C and washed 2 times in 500 µL of PBSA. The yeast were suspended in 200 µL PBSA and analyzed by flow cytometry using a BD C6 Plus Flow Cytometer with 96-well plate autosampler (Becton

Dickinson). The "cells only" only tubes were used to establish a gate for yeast singlets, characterized as a cells with approximately a 1:1 forward scatter area-to-forward scatter height ratio.[351] The secondary solution was used to establish the quadrant gating for AF488 and AF647 fluorophores; AF647+ cells were affibody expressing yeast, and AF488+/AF647+ cells were IL-4-specific affibodies.

After 4 rounds of MACS, fluorescence-activated cell sorting (FACS) was performed on the enriched yeast library, as described previously.[350] 40×10^6 induced yeast cells were aliquoted into tubes labeled cells only, secondary only, c-myc, and c-myc + bIL-4, and washed in PBSA. The cells only, secondary only and c-myc tubes were resuspended in 50 µL PBSA. The c-myc + bIL-4 tube was resuspended in 50 µL of 1 µM biotinylated IL-4 (bIL-4) (Acro Biosciences) in PBSA. 1.25 µL of anti-c-myc mouse monoclonal antibody 9E10 (αCMYC) (BioLegend) was added to the c-myc and c-myc + bIL-4 tubes. All tubes were rotated at 4 °C for 90 minutes and then washed with PBSA. Except for the cells-only control, all tubes were incubated with 50 µL of a secondary fluorescent solution containing 17.3 nM goat anti-mouse IgG AlexaFluor™ 647 (Invitrogen), 1.625 µg of AlexaFluor™ 488 streptavidin conjugate (Invitrogen) in PBSA for 30 minutes at 4 °C and washed 2 times in 500 µL of PBSA. The yeast were suspended in 1000 µL PBSA and sorted by a SH800 Cell Sorter (Sony Biotechnology). Cells were collected from the 488+/647+ quadrant. Following FACS, yeast were grown in selective growth media at 30 °C to an approximate concentration of 10^7 cells mL^{-1}, induced, and subjected to a second round of FACS for further enrichment. During the second round of FACs, the 488+/647+ quadrant was further divided into 4 gates corresponding to 4 distinct yeast populations, and at least 7000 cells were collected from each population. The collected cells from each gate was individually grown and induced as above, and subjected to a binding check. Subsequent FACS was performed on gates 2 and 3 to further enrich for IL-4-specific affibodies. Yeast from each collected gate were grown in selective growth media, plated onto selective growth plates, and incubated for 24-36 hours in 30 °C.

Gene Sequencing

Individual colonies from FACS-sorted yeast plates were selected and expanded in yeast growth media to a cell density of 10^7 cells mL^{-1}. The yeast plasmids were isolated using Easy Yeast Plasmid Isolation Kit (Clonetech) per the manufacturer's instructions, and affibody sequences

from the plasmids were amplified by PCR (Fisher Scientific) using HiFi PCR Premix (CloneAmp) and forward primer (*5'-CCCTCAACAACTAGCAAAGG-3'*) and reverse primer (*3'-ATGTGTAAAGTTGGTAACGGAACG-5'*) (IDT). The product was purified using a DNA Clean and Concentrator Kit (ZymoGen). The purified products were submitted for Sanger Sequencing.

Monoclonal Yeast Characterization

Binding affinity of each yeast surface displayed affibody for IL-4 was characterized by flow cytometry. $1x10^6$ induced cells were prepared as for the binding checks, but with a range of bIL-4 concentrations (0.5-5000 nM). Cells were suspended in 200 µL of PBSA and transferred to a 96-well plate in triplicates. Cells were analyzed using Accuri™ C6 Plus Flow Cytometer. Equilibrium dissociation constants of IL-4-affibody binding were calculated as described previously.[350] Fractional protein binding was determined as the ratio of AF647+/AF488+ cells to AF647+ cells. A nonlinear regression for one site binding saturation was performed on the fractional binding vs. protein concentration.

Transformation of IL-4-Specific Affibodies into E. coli

IL-4-specific affibody sequences were modified with a penultimate C-terminal hexahistidine tag for protein purification and a C-terminal cysteine for bioconjugation. Modified affibody sequences were transformed into E. coli using a digestion and ligation protocol optimized in-house for affibody transformation.[352] gBlock double stranded DNA (dsDNA) fragments (Integrated DNA Technologies; IDT) were codon-optimized for expression in *E. coli*. BL21 (DE3) *E. coli* containing a pET-28b(+) vector (New England BioSciences; NEB) were cultured overnight at 37 °C in Luria-Bertani (LB) (Affymetrix) media with 50 µg/mL kanamycin sulfate, followed by plasmid extraction using Plasmid Miniprep Kit (Monarch Biosciences), per the manufacturer's protocols. The 1000 ng each IL-4-specific gBlocks and the pET-28b(+) vectors were individually digested with 5 µL of rCutSmart buffer (NEB) and 1 µL each of NCoI-HF and XhoI endonucleases (NEB) at 37 °C for 1.5 hours, followed by heat inactivation at 80 °C. The reactions were purified using a DNA Clean and Concentrator 5x kit (Zymo Research), per manufacturer's protocols, followed by agarose gel electrophoresis using a 1.8 % w/v gel at 80 V for 40 minutes. The digested vector and insert were carefully extracted from the gel using

sterilized razors and DNA Gel Extraction Kit (NEB), and purified by drop dialysis. Digested pET-28b(+) vector and gBlocks were mixed with T4 DNA ligase buffer and enzyme (NEB) and incubated overnight at 16 °C, followed by heat inactivation at 65 °C. Ligated affibody DNA sequences were transformed into BL21 (DE3) competent *E. coli* via heat shocking per the manufacturer's protocols. 100 µL of the transformed products were seeded onto kanamycin selective growth plates (10 g yeast extract, 20 g bacto peptone, 20 g dextrose, 16 g bacto agar, 50 mg kanamycin sulfate, 1 L RO water) and incubated for 16 h at 37 °C. Individual colonies were cultured in LB media with 50 µg/mL kanamycin sulfate. Upon reaching an optical density at 600 nm (OD600), 4 ml of each culture were collected and subjected to plasmid extraction using Plasmid MiniPrep Kit (Zymo Research) for subsequent whole plasmid sequencing (Genewiz). Cultures were expanded further in LB and stored in 25% (v/v) glycerol in LB at -80 °C.

Collection and Purification of Soluble affibodies

Transformed E. coli containing IL-4 affibodies were collected and purified as described previously.[350] Transformed E. coli were incubated in 20 mL LB broth with 0.5 mM kanamycin overnight at 37 °C. The culture was transferred into 1.8 L of Terrific Broth (TB) (Affymetrix) with 0.5 mM kanamycin and 500 µL of anti-foam 204 (Thermo Scientific) and cultured at 37 °C in a LEX-10 bioreactor (Epiphyte3) to an OD600 of 1.4. 1.8 mL of IPTG was added to the culture growth vessel to obtain a final concentration of 0.5 µM, and the temperature was reduced to 18 °C for 18 hours for induction of protein expression. The culture was centrifuged for 20 minutes at 4 °C at 6000 RPM, and the cell pellet was split and transferred to two 50 mL conical tubes. Each pellet was resuspended in binding buffer (50 mL of 1 M tris pH 7.5, 100 mL of 5 M NaCl, 5 mL of 1 M imidazole, and 845 mL RO water) supplemented with 75 mg of tris(2-carboxyethyl)phosphine hydrochloride (TCEP) (GoldBio) to a volume of 35 mL and lysed using a probe sonicator (Fisher Scientific) for 7.5 minutes in an ice bath (10 seconds on, 30 seconds off, 55% probe amplitude). The sonicated product was centrifuged at 13,000 rcf for 30 minutes at 4 °C, and the supernatant was transferred to a 50 mL conical tubes with 3.6 mL of Nickel-NTA Agarose Beads (Nickel beads) (GoldBio) and agitated at 4°C for 45 minutes. The supernatant was transferred to a Econo-Column® chromatograph column (Biorad), washed with 50 mL of wash buffer (50 mL of 1 M tris pH 7.5, 100 mL of 5 M NaCl, 30 mL of 1 M imidazole, and 820 mL RO water) supplemented with 125 mg of TCEP followed by with 50 mL of wash buffer

without TCEP, and eluted into 15 mL of elution buffer (50 mL of 1 M tris pH 7.5, 100 mL of 5 M NaCl, 250 mL of 1 M imidazole, and 600 mL RO water). The collected solution was buffer-exchanged into 0.5 M Tris pH 8 using a 3 kDa molecular weight cut-off (MWCO) centrifuge filter (Millipore) and frozen at -20 °C until further use.

Synthetic affibody synthesis

Synthetic IL-4 affibodies were prepared using Fmoc synthesis as described previously.[353] IL-4-specific affibody sequences were modified to include a penultimate cysteine and a C-terminal glycine, and prepared by solid-phase peptide synthesis (SPPS) on Fmoc-Gly-Wang resin (CEM Corporation) with a 0.602 mmol/g loading capacity using a CEM Liberty Blue 2.0 microwave peptide synthesizer (CEM Corporation). 0.2 M amino acid (CEM Corporation), 10% v/v pyrrolidine (Sigma Aldrich) deprotection, 1 M N,N'-diisopropylcarbodiimide (DIC) (Oakwood Chemical), and 1 M Oxyma (CEM Corporation) solutions were prepared in DMF. Resin-bound affibodies were washed with dichloromethane twice, and resuspended in a cocktail containing 1:1:1:1:36 ratios of ddH_2O, triisopropyl silane (Oakwood Chemical), 2,2'-(Ethylenedioxy)diethanethiol (Tokyo Chemical Industry), thioanisole (Oakwood Chemical), trifluoroacetic acid (TFA) (Oakwood Chemical) for 40 minutes at 42 °C[313] for cleavage. The solution was vacuum filtered, and the filtrate was purified via precipitation and three rounds of centrifugation (1200 RCF for 5 minutes) using -20 °C diethyl ether. The resultant slurry was dried overnight in a vacuum desiccator and transferred to -20 °C for storage.

To purify the products, the crude product pellets were dissolved in a 30 % w/v acetonitrile in water solution with 0.1% v/v TFA, and subjected to high-performance liquid chromatography (HPLC) (CEM) using 19 x 150 mm C18 Waters column by running a 40-75% acetonitrile gradient in ddH_2O with 0.1% v/v TFA. The prominent peaks of each run were collected in a 50 mL conical tube, frozen at -80 °C, lyophilized at -104 °C and 50 mTorr for 24 hours using a benchtop lyophilized (SP Scientific) and stored at -20 °C until used.

Characterization of affibodies

Affibodies were characterized for their size, secondary structure, and IL-4-binding interactions, utilizing techniques described previously.[353] Affibody molecular weights were confirmed using

sodium dodecyl sulfate polyacrylamide gel electrophoresis (SDS-PAGE) and matrix-assisted laser desorption/ionization time of flight (MALDI-TOF) mass spectrometry. For SDS-PAGE, 18 μL of 1 mg/mL affibody in 0.5 M Tris pH 8 was diluted with 6 μL of Laemmli buffer (BioRad) supplemented with 10 v/v% β-mercaptoethanol (BioRad) and heated for 5 minutes at 90 °C. The samples were loaded into a 4-20% Mini-PROTEAN® TGX™ Precast Protein Gel (BioRad), run under denaturing conditions at 200 V for 35 minutes, stained with Coomassie blue dye, and imaged on an Azure 200 Gel Imager (Azure Biosystems, Inc.).[350] For MALDI, 1 μL of 1 mg/mL affibody in 0.5 M Tris buffer pH 8 was deposited onto a MALDI stainless steel target plate (Bruker) with 1 μL of matrix solution consisting of 10 mg/mL α-cyano-4-hydroxycinnamic acid (Sigma Aldrich) in 0.1% v/v TFA and 50% v/v acetonitrile in ddH_2O. The products were analyzed on a MALDI Smart LS system (Bruker) using 200 event counts and fitted to a 3-20 kDa protein standard (Bruker). Baseline noise was background subtracted in the Bruker software. The secondary structure of the affibodies was measured using circular dichroism (CD) with a J-815 (Jasco) spectropolarimeter. Affibodies were buffer exchanged or reconstituted in 10 mM tris buffer, pH 8 and their concentrations were adjusted to approximately 0.5 mg/mL. 200 μL of the affibody solution was loaded into a quartz cuvette (Starna Cell Corp.) with a 1 mm path length. Circular dichroism spectra were obtained over 190-250 nm and normalized to mean residue molar ellipticity using Equation 2.2.[243,314,315]

The kinetics of IL-4-affibody binding were measured by biolayer interferometry (BLI) (Gator Bio). Streptavidin-coated probes (SAXT probes) were loaded with 1 nM of biotinylated IL-4 (Acro Biosystems) in PBS with 0.05% Tween 80 and 2 mg/mL BSA (Buffer solution), quenched with 20 μg/mL biocytin (Caymen Chemicals) in buffer solution, and then allowed to associate to and dissociate from 15.6-4000 nM of affibody in buffer solution for 120 seconds each. The dissociation constants (K_D), on-rate constants (k_{on}), and off-rate constants (k_{off}) were calculated for each affibody-BMP-2 binding pair by curve fitting the wavelength shifts using a 1:1 Langmuir isotherm binding model.

Computational Predictions of binding

Affibodies were folded and docked to IL-4 using the AlphaFold2 multimer protocol.[250] Affibody sequences and the IL-4 residue sequences were input into AlphaFold2 and recycled 3 times. To perform interface analysis, the highest ranked predictions were loaded into PyMol alongside the

X-ray crystallography structures of human IL-4 (1HIK)[354] and the IL-4-to-IL-4 receptor-α complex (PDB: 1IAR).[355] The docked predictions and the x-ray crystallography structures were structurally aligned using the IL-4 coordinates, and the affibodies and receptors were extracted from their respective object. The polar contacts of IL-4 and the affibodies and receptor complexes within 4 Å were identified to determine steric hinderance.

Monocyte Cell culture

The immortalized monocyte-like cell line THP-1 was used to study the effects of IL-4 delivery and affibody activity on macrophage function.[356] THP-1 cells (ATCC) were cultured in T75 flasks in media containing 10 %v/v heat inactivated FBS (Cytiva) (base media) and 0.05 mM 2-mercaptoethanol (βME) (Gibco) and maintained at a concentration of 2-4×10^5 cells/mL at 37 °C and 5 %CO2. Additional media was added every 2-3 days, and replaced entirely once every 7 days, per manufacturer's protocols.

Polarization assays

To determine the effects of affibodies on macrophage polarization, THP-1 cells were differentiated into M0 macrophage-like cells, and then incubated with various polarizing factors.[334] THP-1 monocytes were seeded in 24-well plates at 1×10^5 cells/cm^2 in base media supplemented with 20-100 ng/mL phorbol 12-myristate 13-acetate (PMA) for 48-72 hours to differentiate into M0 macrophage-like cells. After the differentiation period, cells were incubated with base media as the negative control, base media with either 100 ng/mL of lipopolysaccharide (LPS) (Millipore Sigma) and 20 ng/mL of interferon-γ (IFN-γ) (Peprotech) or with 50 ng/mL granulocyte macrophage colony stimulating factor (GM-CSF) (Peprotech) to polarize the cells to the M1 phenotype, base media supplemented with 20 ng/mL IL-4 and 50 ng/mL macrophage colony stimulating factor (M-CSF) (Peprotech) to polarize the cells to M2, base media supplemented with affibody alone (2 – 1000 nM (1-500 times molar equivalents of IL-4)) to determine the effects of soluble affibody, or base media supplemented with affibody that has been previously mixed with 20 ng/mL IL-4 to form a complex to determine if the affibodies interfere with macrophage polarization. All groups were incubated at 37 °C for 72 hours, and further processed and analyzed as described below.

Cells were visually inspected using microscopy and immunocytochemistry (ICC). Cells were centrifuged at 200 RCF for 5 minutes and washed with warm PBS to remove media. Cells were briefly fixed using 4% formalin (Gibco) for 30 minutes at room temperature, and excess fixative was washed away with PBS. 0.75 w/v% glycine in water solution was briefly added to the cells to neutralize excess aldehydes, and then washed with PBS. Cells were incubated in a permeabilization buffer consisting of 0.15 %v/v Triton-X (Millipore Sigma) and 5 %v/v goat serum (Gibco) in PBS for 1 hour at room temperature. Permeabilization buffer was removed, and cells were incubated with a primary staining solution consisting of 50 %v/v permeabilization buffer in PBS supplemented with DAPI (Fisher scientific), inducible nitric oxide synthase (iNOS) rabbit anti-mouse polyclonal antibody (Thermo Fisher Scientific), and arginase-1 (ARG-1) mouse anti-mouse monoclonal antibody (Proteintech) for 2 hours at 4 °C away from light. The solution was washed twice with PBS, and cells were incubated in secondary staining solution consisting of 50% v/v permeabilization buffer in PBS supplemented with Goat anti-mouse IgG AlexaFluor 488 (Thermo Fisher) and Goat anti-rabbit Alexa Fluor 594 conjugate (Thermo Fisher) for 2 hours at room temperature away from light. Cells were washed twice with PBS to remove excess staining, and imaged using a BioTek Lionhear Imager (Agilent) with DAPI, green fluorescent protein, and orange fluorescent protein filters.

A sacrificial group of THP-1 cultures with or without PMA was collected to confirm the differentiation of THP-1s to M0 macrophage-like cells, and assessed by flow cytometry.[357] Cells were washed with warm PBS to remove any media, and incubated in PBS supplemented with AlexaFluor 488 – Anti-CD68 antibody (Abcam) and propidium iodide (BioLegend) at the manufacturer's recommended concentrations for 30 minutes at 37 °C. Cells were washed twice with warm PBS, and then detached from the well plates using 200 µL cold PBS. Samples were analyzed using a BD C6 Plus Flow Cytometer. Unstained cells were used to identify the cell population; undifferentiated stained cells were used to set the bounds for the AF 488 and propidium iodide fluorescent signals. The mean residue fluorescence was used to confirm cell differentiation.

Phenotype-specific cytokine production in culture media was quantified by enzyme-linked immunosorbent assay (ELISA).[334,358] After 72 hours of incubation with various polarization treatments, 250 µL of media were collected and analyzed with tumor necrosis factor-α (TNF-α) ELISA (R&D Biotechne) and interleukin-10 (IL-10) ELISA (R&D Biotechne) per the

manufacturer's protocols. Undifferentiated cells were used as the baseline for fold-change calculations.

Gene expression was quantified using reverse transcription-quantitative polymerase chain reaction (RT-qPCR). First cell RNA was extracted by washing and detaching the cells with ice cold PBS, followed by incubation with RNA lysis buffer (Zymo Research) for 10 minutes. The RNA was extract from the lysate using a RNA Miniprep kit (Zymo research), amending the manufacturer's instructions to use molecular biology grade ethanol (Thomas Scientific) and perform 3 washing steps with RNA wash buffer instead of 2 washing steps. The product was collected into 32 µL nuclease- and RNAse-free water. The RNA concentration and purity were determined using UV-Vis spectrophotometry (Implen). Complimentary DNA (cDNA) synthesis was performed on the RNA products using LunaScript RT SuperMix Kit (New England Biosciences) per the manufacturer's protocols. For consistency, all syntheses were performed with 100 ng of RNA. RT-qPCR was performed in a CFX96 Opus (BioRad) by combining PerfeCTa SYBR Green SuperMix Low Rox (QuantaBio), the cDNA product, forward and reverse primers, and water to 20 µL per the manufacturer's protocols. The analyzed genes were GAPDH for housekeeping, TNF-α, iNOS, and matrix metalloproteinase-2 (MMP-2) for M1 gene quantitation, IL-10, ARG-1, and CD163 for M2 gene quantitation, and CD68 to confirm monocyte-to-macrophage differentiation. The change in threshold cycle (ΔC_t) was used to compare the presence of a particular gene in relation to the housekeeping gene, and $\Delta\Delta C_t$ quantified the difference between the control (M0) and the polarized samples. Relative gene expression was calculated using the CFX Maestro software (BioRad) by normalizing each gene to GAPDH using Equation 4.1.

Equation 4.1: Gene expression as a function of change in threshold cycles

$$Gene\ expression = 2^{-\Delta\Delta C_t}$$

Synthesis of hydrogels and controlled release

100 µL 5 w/v% affibody-conjugated polyethylene glycol (PEG) hydrogels were synthesized as described.[237,300] Briefly, 20 kDa, 4-arm PEG-maleimide (Laysan Bio), and recombinant high- or low-affinity IL-4- specific affibodies were each dissolved in PBS pH 6.9 and mixed for 30 minutes at room temperature to form PEG, and PEG-affibody intermediates. The intermediate

solutions were crosslinked in 2 mL centrifuge tubes by combining with dithiothreitol (DTT) (Gold Biotechnology) dissolved in PBS pH 6.9 and reacting the solutions for 30 minutes at room temperature. Each hydrogel contained 500 times molar excess of affibody compared to the amount of IL-4 loaded. Unreacted DTT was removed from the hydrogels prior to loading with IL-4 by submerging the hydrogels in 1 mL of PBS and exchanging 3 times with fresh PBS every 12 hours. To maintain sterility for sterile hydrogels, the PEG-Mal, DTT, and PBS solutions were sterile-filtered with a 0.22 μm syringe filter and handled in a biosafety cabinet prior to mixing and crosslinking.

IL-4 encapsulation and controlled release was performed as described previously.[300,353] After purification, supernatant was aspirated from the hydrogels, and 20 μL of 5 μg/mL of IL-4 (100 ng total) were dispensed onto each hydrogel. The hydrogels were rotated overnight at 4 °C to allow the IL-4 to diffuse into the hydrogel. The 200 μl of PBSA were added to the hydrogels and immediately removed to determine the encapsulation efficiency. PBSA was added to the hydrogels to a total volume of 1 mL, and 200 μL aliquots were collected and replenished with fresh supernatant for 1 week. Encapsulation efficiency and protein release were measured by IL-4-specific ELISA (R&D Biotechne).

Results

Identification of IL-4-specific affibodies using magnetic and fluorescence activated cell sorting

To identify IL-4-specific affibodies, a yeast surface display library containing 4×10^8 unique affibody sequences was subjected to MACS and FACS. After 4 rounds of MACS, the library diversity was reduced to approximately 1.07×10^6 sequences (Figure 4.1A). The post-MACS library was further depleted using FACS, and 4881 AF647+/AF488+ cells were collected. The collected cells were expanded, induced, and characterized with a binding check by flow cytometry. Due to low IL-4-binding, an additional round of MACS was performed, followed by a subsequent round of FACS. In the second FACS, the AF488 signal had a greater shift upward, and cells were collected into 4 gates corresponding to 4 distinct populations (Figure 4.1B). Upon growth and induction, an additional binding check was performed. The yeast in Gate 1 did not efficiently induce and were thus discarded from future characterization. The cells in Gates 2 and

3 showed promise due to their increase in total AF488+ signal and were further investigated. The cultures from Gates 2 and Gates 3 were subject to one additional round of FACS with more stringent AF488 gates to AF488+/AF647+ cells and increase the chances of finding IL-4-specific affibody sequences. When comparing the. The enrichment was successful, as the number of AF488+/AF647+ events increased between FACS2 and FACS3 for both Gate2 and Gate 3 (Figure 4.1C,D), although there was no substantial difference in the IL-4 binding signal. Individual colonies from the post FACS3 Gates 2 and 3 were grown, induced, and subjected to a binding check and concurrently prepared for Sanger sequencing. Two unique IL-4-specific affibodies (Affibody_1 and Affibody_2) were identified by binding checks with 1000 nM bIL-4 (Figure 4.1E) as well as one truncated affibody that only contained 52 amino acids instead of 58 amino acids. This product was an unexpected mutant and not further investigated, although this specific sequence was previously discovered by another lab member when searching for GM-CSF-specific affibodies.

Flow cytometry was used to predict the binding strengths of the IL-4 affibodies. Cells were characterized by flow cytometry. Affibody fraction binding to IL-4 was calculated by dividing the top right quadrant (AF647+/AF488+) by the right half of the plot (AF647+), and was plotted against bIL-4 concentration (Figure 4.1F). Unfortunately, Beyond 500 nM, affibody binding unexpectedly decreased, resulting in inconclusive dissociation constant quantification.

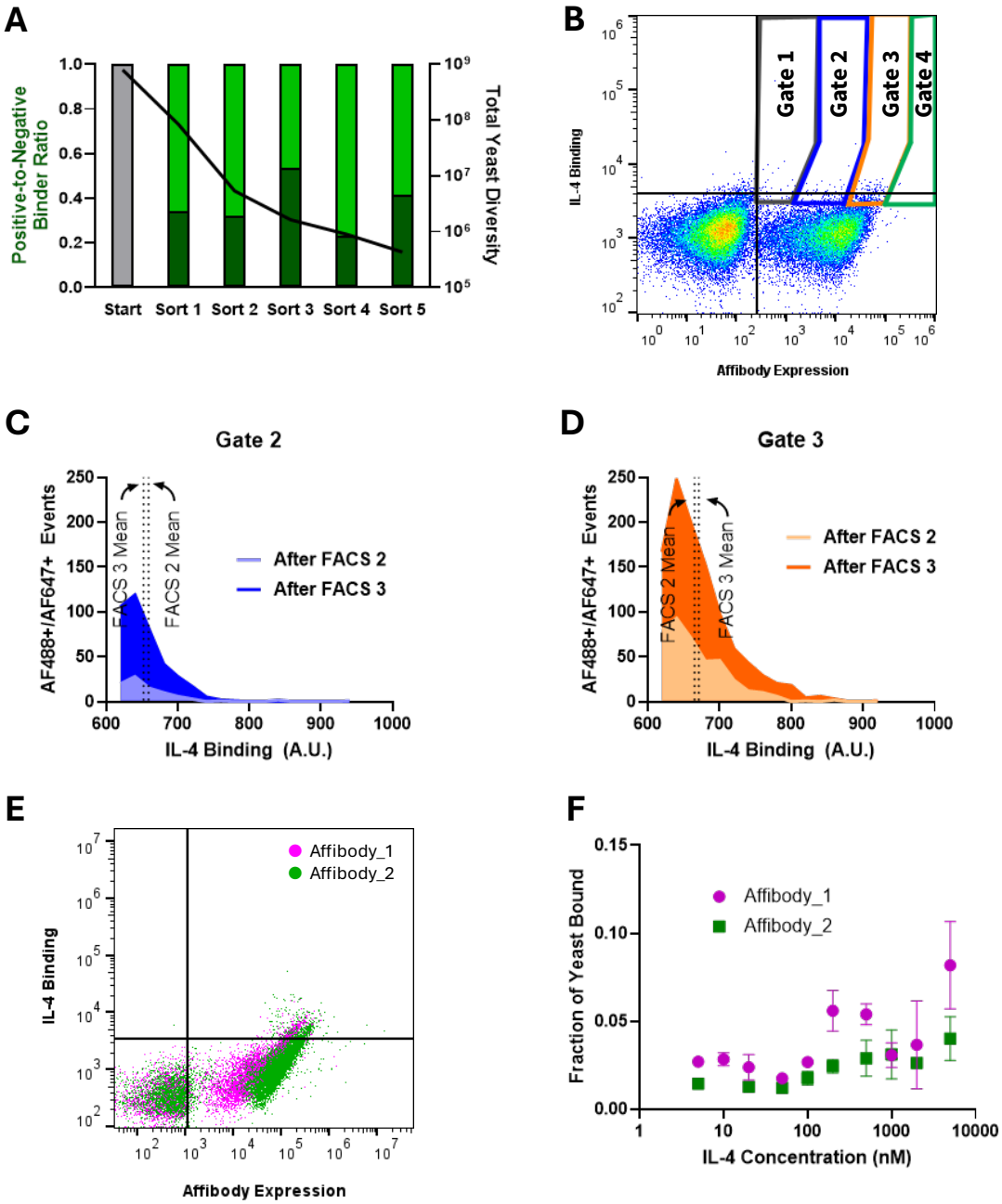


Figure 4.1: Identification of IL-4-specific affibodies. A) Diversity of sorted yeast library obtained after each round of MACS. Left y-axis (green bar graph) depicts approximate IL-4-positive-to-IL-4-negative ratio. Right y-axis (line graph) indicates the total number of IL-4-positive yeast after each round of MACS. B) Gating strategy for yeast during FACS 2. C,D) Binding. C,D) Enrichment of AF488+/AF647+ cells in Gate 2 (C) and in Gate 3 (D) using an additional round of FACS (FACS 3). E) Binding check of monoclonal yeast after FACS 3 encoded for potential affibodies named Affibody_1 (magenta) and Affibody_2 (green). F) Fraction of yeast binding to bIL-4 as a function of bIL-4 concentrations ranging from 5-5000 nM.

Transformation, expansion, collection and purification of recombinant IL-4-specific affibodies

Double stranded DNA fragments encoded for the Affibody_1 and Affibody_2 sequences were purchased through IDT with a C-terminal hexahistidine tag and cysteine for protein collection and subsequent bioconjugation. the dsDNA fragments and BL21 (DE3) *E. Coli* were digested and linearized using restriction enzymes and confirmed by agarose gel electrophoresis. The DNA products were extracted from the agarose gel, ligated and transformed into competent BL21 (DE3) E. coli. The transformed products were cultured in LB media containing kanamycin, plasmid extracted, and sequence insertion was confirmed using whole plasmid sequencing.
For large-scale protein expression, affibodies were cultured overnight in 20 mL LB culture supplemented with kanamycin, transferred into 1.8 L of TB supplemented with kanamycin, and then induced with IPTG overnight. The E. coli was centrifuged, lysed to extract soluble proteins, and affibodies were collected and purified using IMAC with cobalt beads, as previously described.[300] the products at each stage of collection and purification were visualized by SDS-PAGE (Figure 4.2). A distinct band was present at the expected size of each affibody (~7.6 kDa).

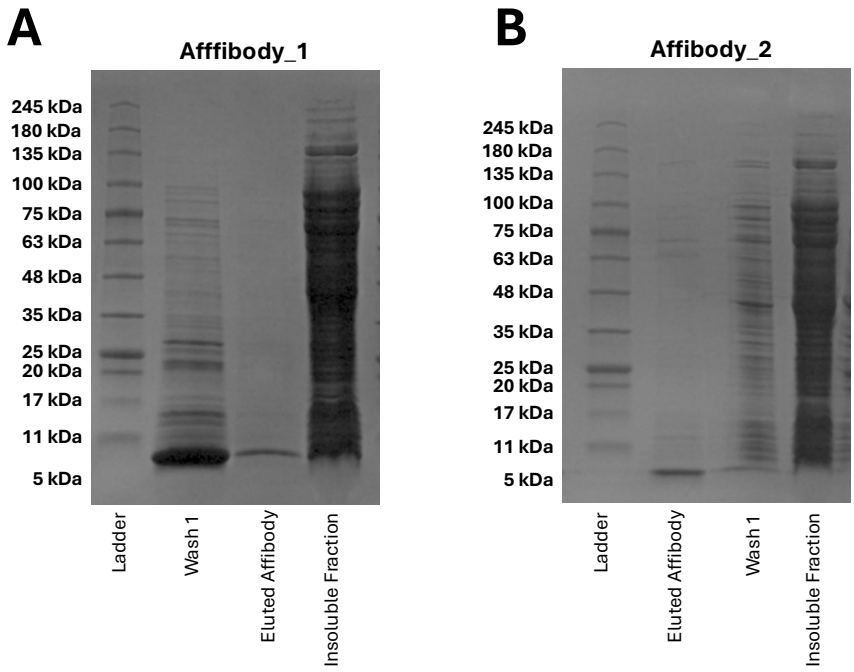


Figure 4.2: SDS-PAGE from Affibody_1 (A) and Affibody_2 (B) expression, collection, and purification. The ladder used for both is a BlueStain 2.0 protein ladder (5-245 kDa). Insoluble protein fractions were collected after cell lysis by sonication, Wash 1 was collected after the first 10 mL of cleaning of Co Bead-bound affibodies with

wash buffer, and Eluted Affibody was collected after 10 washes and a buffer exchange to PBS. A distinct band is present in the eluted affibody lanes around the expected size of the IL-4-specific affibodies (~7.5 kDa)

Synthesis, collection and purification of synthetic affibodies

Synthetic IL-4-specific affibodies were synthesized using SPPS. After synthesis, the products were cleaved from the resin and collected using precipitation centrifugation. Approximately 650 mg of crude product of each affibody was collected upon cleavage. The crude product was purified by HPLC. Affibody_1 was eluted from the column at approximately 61% V/V acetonitrile in H_2O, while Affibody-2 was eluted from the column at 63.5 %V/V acetonitrile in H_2O. Approximately 350 mg of each purified affibody was collected. The purified product was frozen at -80 °C and lyophilized until needed.

Characterization of affibodies

Synthetic and recombinant affibodies were characterized. Affibody size was confirmed using MALDI, affibody secondary structure was confirmed by circular dichroism, and affibody-IL-4-binding interactions were characterized by BLI (Figure 4.3).

Using MALDI, single prominent peaks were present at the expected masses of the recombinant and synthetic affibodies when considering potential adducts (Figure 4.3A,B). Recombinant Affibody_1 had a peak at 7538 Da, a +14 Da shift from the expected mass of 7514 Da due to methylation. Recombinant Affibody_2 had a peak at 7396 Da, a +32 Da shift from the expected mass of 7364 Da likely due to oxidation of either a proline or a tryptophan. Synthetic Affibody_1 had a peak at 6730 Da, a -18 Da shift from the expected mass of 6748 Da. Synthetic Affibody_2 had a peak at 6597 Da, a -1 Da shift from the expected mass of 6598 Da. All products had additional minor peaks attributed to charged states and homodimer/homotrimer formations. Additional minor species were present in the recombinant affibodies, attributable to collected histidine-containing proteins.[359]

Circular dichroism confirmed the secondary structure of all the collected affibodies were α-helical, with characteristic troughs at 208 and 222 nm and a peak at 193 nm (Figure 4.3C).[314] These data agree with previously collected and analyzed affibodies, demonstrating the consistency of the secondary structure of the affibody scaffold. Of note, the amplitude of signal

was greater for synthetic affibodies, which is generally attributed to a greater degree of protein folding, and has been observed when comparing recombinant and synthetic affibodies.[315,321,353] It has been previously

Biolayer interferometry was performed on the recombinant and synthetic Affibody_1 and Affibody_2 affibodies by loading 1 μg/mL of bIL-4 to streptavidin XT probes, followed by association and dissociation of a range of 15.625 to 4000 nM affibody in in PBST with 2 mg/mL BSA (Figure 4.3D-G). The equilibrium dissociation constants of the recombinant affibodies were 586 nM and 653 nM for Affibody_1 and Affibody_2, respectively, while their synthetic equivalents were 459 nM and 141 nM. There is no statistically significant difference of dissociation constants between the recombinant affibodies, though synthetic Affibody_2 is a markedly stronger affibody than synthetic Affibody_1.

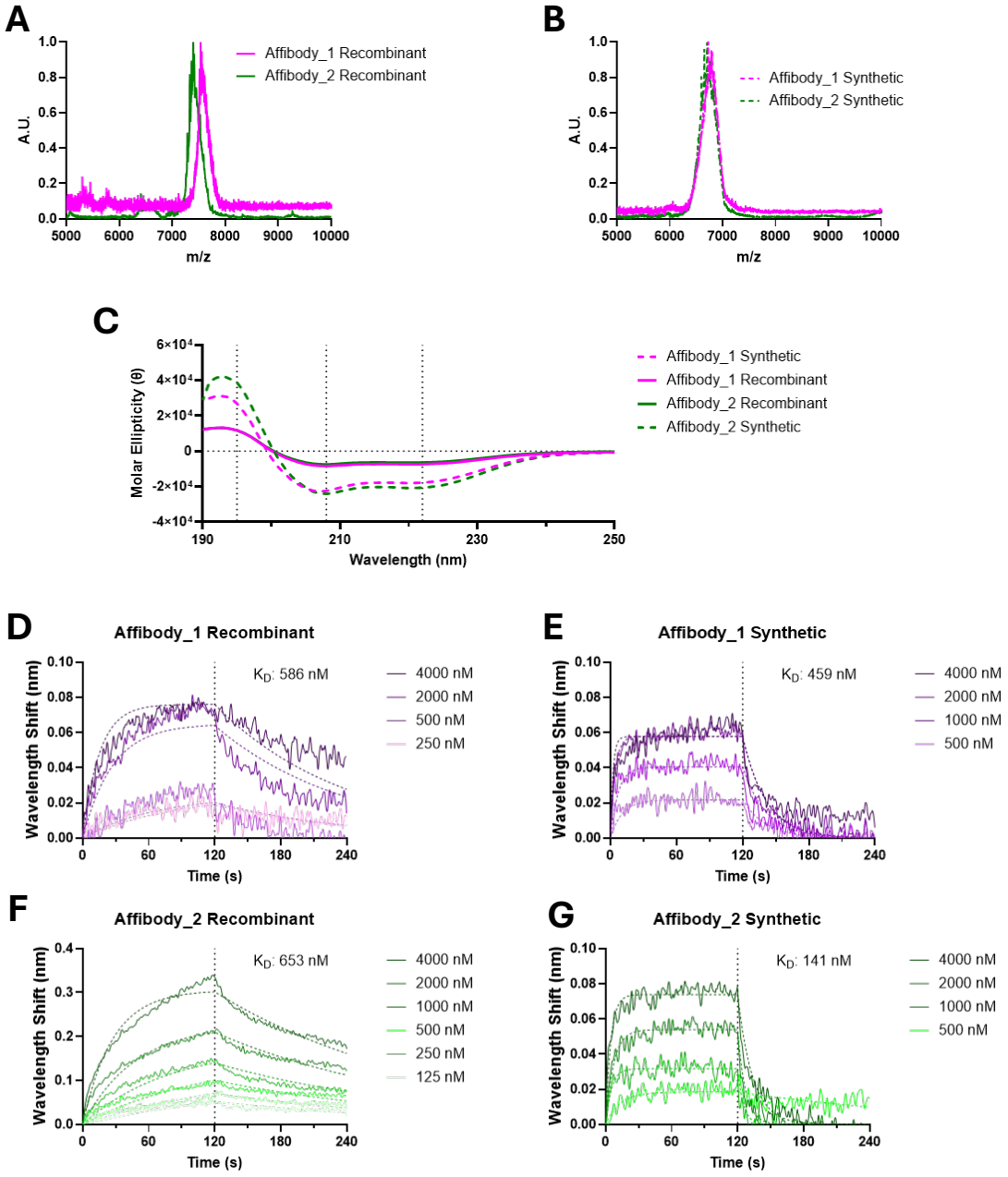


Figure 4.3: Characterization of IL-4-specific affibodies using MALDI, CD, and BLI. A,B) MALDI spectra of recombinant (A) and synthetic (B) Affibody_1 and Affibody_2. For recombinant Affibody_1, there is a peak at 7358 Da, [M+14] from the expected mass. Recombinant Affibody_2 had a peak at 7396 Da, [M+32] from the expected mass. Synthetic Affibody_1 had a peak at 6730 Da, [M-18] from the expected mass. Synthetic Affibody_2 had a peak at 6597 Da, [M-1] from the expected mass. C) CD spectra of the recombinant and synthetic Affibody_1 and Affibody_2 affibodies indicating α-helical secondary structure. D-G) Protein-protein interactions characterized by BLI. Affibody_1 had a 586 nM dissociation constant for the recombinant protein(D), and 459 nM dissociation constant for the synthetic protein (E). Affibody_2 had a dissociation constant of 653 nM for the recombinant protein (F) and 141 nM dissociation constant for the synthetic protein (G).

Computational prediction of affibody docking

Affibody docking to IL-4 was predicted computationally using AlphaFold2 Multimer tool, with 3 relaxation cycles to minimize energy states. The structural predictions were visualized using PyMol and compared to the IL-4 Receptor-α (Figure 4.4). IL-4's surface-available amino acids involved in binding with the receptor were colored cyan. Affibody_1 was predicted to have overlapping binding regions with IL4Rα, which could lead to some inhibitory behavior similar to BMP-2-specific affibodies that are predicted to interfere with BMP receptor binding.[300] Affibody_1 was also predicted to have 5 electrostatic interactions and with IL-4 and 0 hydrophobic interactions with IL-4. Conversely, Affibody_2 was not predicted to interfere with the receptor, and was predicted to have 4 electrostatic contacts and 1 hydrophobic interaction with IL-4. IL-4-affibody interactions were characterized as either electrostatic (polar contacts between IL-4 and its respective affibody) and hydrophobic (interchain hydrophobic amino acids less than 3.5 Å away). (Receptor has 12 polar contacts and 0 hydrophobic contacts)

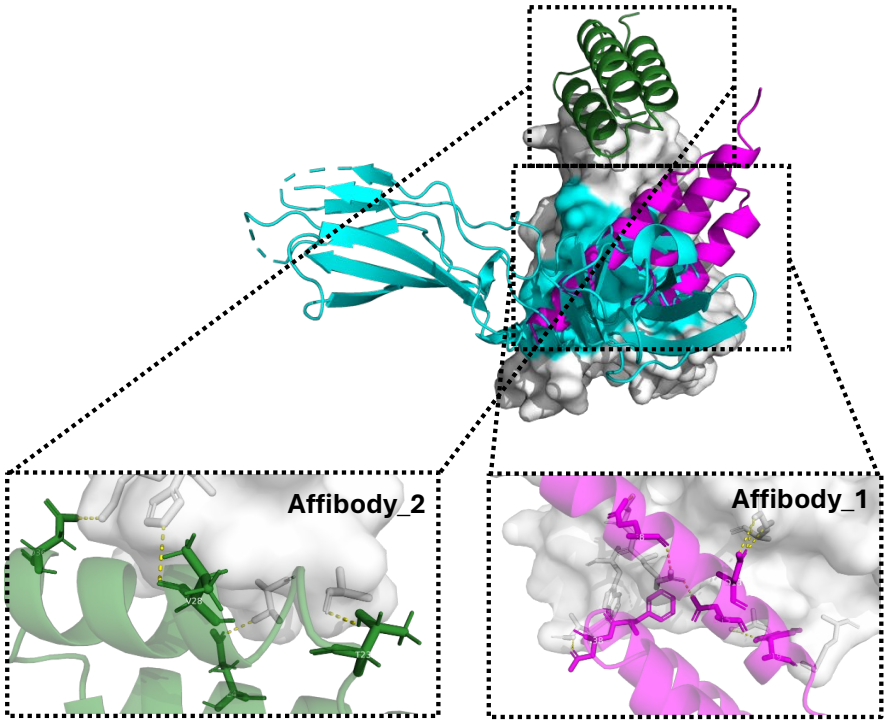


Figure 4.4: Computational docking predictions for IL4-Rα (cyan) and the Affibody_1 (magenta) and Affibody_2 (green) affibodies to IL-4 (white). The cyan surface indicates the surface residues of IL-4 that interact with the receptor. Inlays depict the electrostatic interactions of the affibodies with IL-4. Affibody_1 is predicted to dock to IL-4 in regions that overlap with the receptor.

Impacts of affibodies on THP-1 polarization

The effects of IL-4-specific affibodies on macrophage polarization were assessed with THP-1 monocyte-like cells, a model human cell line for testing various immune activation pathways. To determine the impacts of various polarizing factors, THP-1 monocyte-like cells must be differentiated to an M0 state with PMA. Due to variability in culturing protocols in literature, the optimal differentiation protocol was determined by varying PMA concentration and exposure times. THP-1s were cultures with 0-100 ng/mL PMA in base RPMI media for 48-72 hours, and then stained with a AF488 anti-CD68 conjugate and PI to quantify monocyte-to-macrophage differentiation and cell viability, respectively. The cells were analyzed by flow cytometry (Figure 4.5). Cell differentiation was observed for both timepoints at 20 ng/mL and 100 ng/mL PMA, though greater cell differentiation was observed after 72 hours. Since there was no significant difference in cell differentiation at the two concentrations, subsequent cell studies were performed with 72 hours of 20 ng/mL PMA for differentiation prior to macrophage polarization.

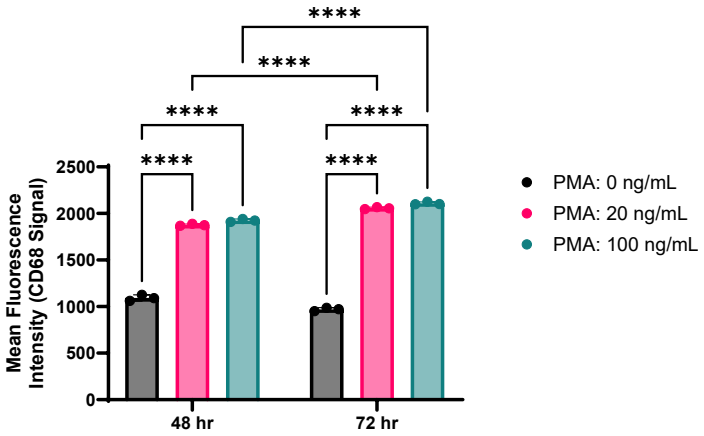


Figure 4.5: Optimization of THP-1 differentiation protocol from monocytes to macrophages. THP-1s were incubated with 0-100 ng/mL PMA for 48-72 hr. Differentiation was quantified as the mean fluorescence intensity of CD68. Statistical significance was measured by two-way ANOVA, with Tukey post-hoc test. n=3. **** $p<0.0001$

THP-1 cells were differentiated to M0s and polarized with 2-200 nM of recombinant IL-4-specific affibodies for 72 hours. After incubation, media was collected and used to quantify cytokine production as an indicator of M1 and M2 polarization through TNF-α and IL-10 ELISAs, respectively. TNF-α ELISAs revealed a concentration-dependent response to both

recombinant affibodies (Figure 4.6), suggesting an M1-polarization similar to LPS. Referring to prior efforts that compare recombinant and synthetic affibodies (Chapter 3)[353], it is hypothesized that endotoxin contamination in the recombinant product may be driving M1 polarization.[357,360,361] To overcome this issue, THP-1s were subsequently cultured with synthetic IL-4-specific affibodies that did not contain endotoxins.

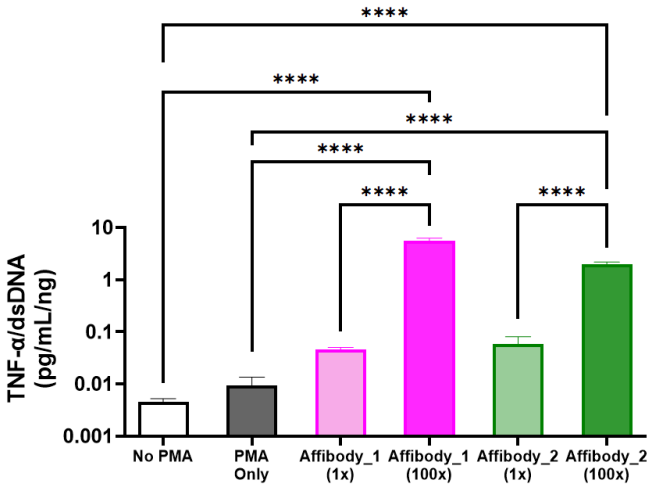


Figure 4.6: TNF-α secretion from THP-1 cells after incubation with 2-200 nM recombinant affibodies for 72 hours. TNF-α secretion was quantified by ELISA and normalized to the amount of cells by ng of dsDNA. 1x affibody quantities are 2 nM and 100x affibody is 200 nM. There is a concentration-dependent increase in TNF-α secretion, indicating an M1 polarization. This could be either an effect of the affibody alone, or in conjunction to the presence of LPS in the recombinant products. Statistical significance was measured by two-way ANOVA, with Tukey post-hoc test. n=3. **** $p<0.0001$.

An additional approach towards determining the affibody-induced macrophage activation is to inspect gene expression under stimuli through RT-qPCR.[334] THP-1s were differentiated and then polarized with LPS and IFN-γ or with GM-CSF to induce an M1 response, with IL-4 and M-CSF to induce an M2 response, and with the synthetic IL-4-specific affibodies with and without premixed IL-4 for 72 hours. The cells were lysed, and RNA was extracted and purified. cDNA was synthesized and M1-associated genes (TNF-α, iNOS, and MMP-2) and M2-associated genes (IL-10, ARG-1, and CD163) were quantified alongside GAPDH as the housekeeping gene. Relative gene expression was compared to M0 expressions (Figure 4.7). The experiment yielded unexpected results, most prominently observed by a bias for IL-10 gene expression in all samples, as well as greater gene expression for M1-associated genes upon polarization with IL-4

than with LPS and GM-CSF and a greater expression of M2-associated genes from LPS and GM-CSF stimulation.[334] While these results challenge the validity of the experiment and its analysis, the affibody experimental groups provided intriguing preliminary results. There is a concentration-dependent response to Affibody_1 leading to upregulation of all genes except TNF-α, but a concentration-independent upregulation for the same genes for Affibody_2 except CD163. However, mixing the affibodies with IL-4 prior to incubation with M0s nullified the observed upregulations in all genes from affibodies alone. The broad upregulation could be indicative of a transitional state at the collection timepoint, or a more balanced M1/M2 states.[362,363] The dose-dependent upregulation from Affibody_1 could be an indicator of the affibody interacting with or interfering with IL-4-specific cell signaling, as predicted by docking simulations. Additionally, the non-response of IL-4 with either affibody suggests that upon binding to each other, the IL-4 and/or the affibody do not effectively lead to macrophage activation. Such a result was observed with BMP-2-specific affibodies inhibiting BMP-2-induced alkaline phosphatase activity (Figure 2.6).[300]

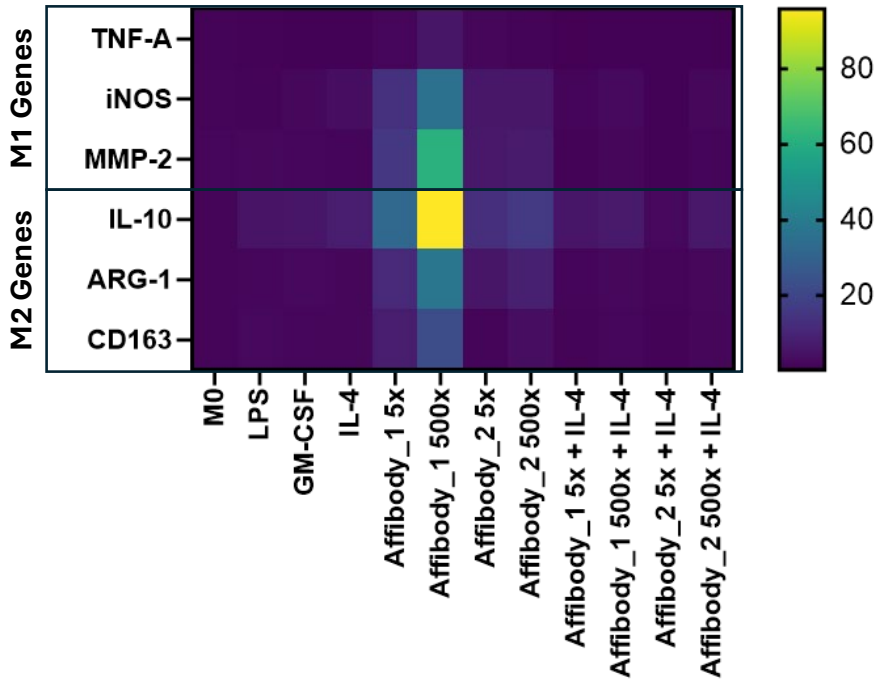


Figure 4.7: Gene expression of macrophages with various stimuli, quantified by RT-qPCR. THP-1-differentiated M0 macrophages were incubated with LPS, GM-CSF, or IL-4, with 2-1000 nM synthetic affibody, or with affibodies pre-mixed with IL-4. Statistical significance was measured by two-way ANOVA, with Tukey post-hoc test. n=4.

Extensive further troubleshooting was performed on the THP-1 cells to identify their functionality for macrophage stimulation assays. For this, THP-1 cells were first differentiated to M0s as described and confirmed above, and then polarized for 72 hour with GM-CSF-supplemented media , LPS-co-M-CSF-supplemented media, and IL-4-co-IFN-γ-supplemented media for M1 or M2 polarization. Media was collected for analysis by ELISA, and cells were assessed by both RT-qPCR and flow cytometry (Figure 4.8). By ELISA, there was a significant increase in TNF-α secretion in the LPS-stimulated group as expected, though there was no difference in IL-10 secretion amongst all groups (Figure 4.8A,B). By flow cytometry, cells stimulated with IL-4 showed an increase in the M2-associated CD163 signal compared to other cells, though the M1-associated CD86 signal was reduced amongst all stimulation groups (Figure 4.8C,D). Lastly, there was a downregulation of the M1-associated genes TNF-α, iNOS, and MMP-9 upon exposure to LPS and GM-CSF, and no notable differences amongst the M2-associated genes IL-10, ARG-1, and CD206 in any of the groups (Figure 4.8E,F). Taken together, these data indicate an issue with the cells themselves or with the cell culturing protocols used.

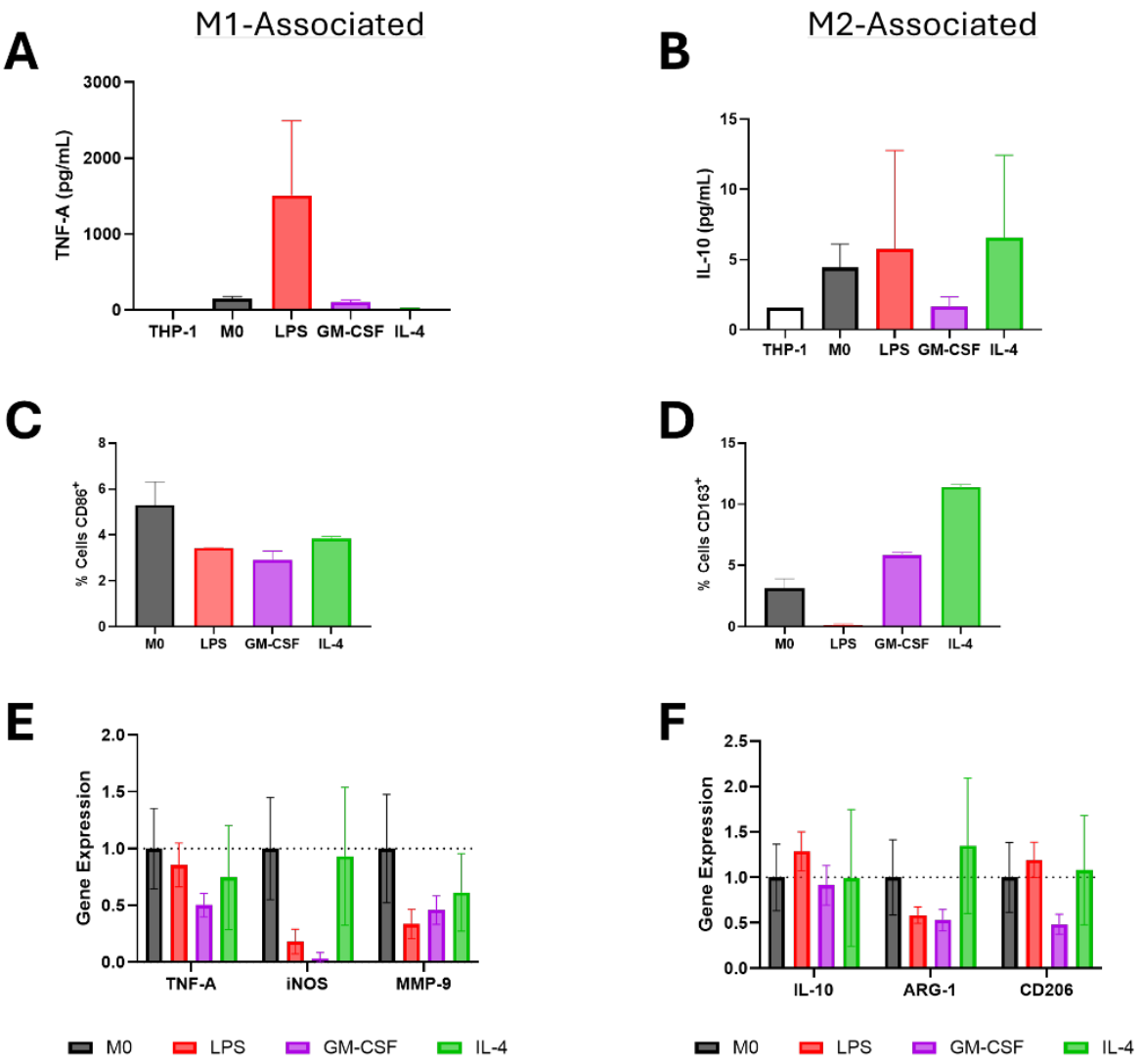


Figure 4.8: Troubleshooting of THP-1s upon differentiation with PMA and incubation with various stimuli. A,B) Cytokine secretion of cells as measured by ELISA for the M1-associated TNF-α (A) and M2-associated IL-10 (B). C,D) Flow cytometry analysis of surface-expressed markers for M1-associated CD86 (C) and M2-associated CD164 (D). E,F) RT-qPCR-based gene expression analysis of M1-associated genes TNF-α, iNOS, and MMP-9 (E) and M2-associated genes IL-10, ARG-1, and CD206 (F). Significance calculated by one-way ANOVA for ELISA and flow cytometry results and two-way ANOVA for gene expression results, with Tukey post-hoc for all experiments. n=3-4.

Controlled Release from affibody-conjugated PEG-Mal hydrogels

Hydrogels conjugated with 0 or 3.3 nmol IL-4-specific affibodies were synthesized as described, and loaded with 100 ng of IL-4 (6.625×10^{-12} mol). Encapsulation efficiency and controlled release into both PBSA (Figure 4.9A,B) and FBS (Figure 4.9C,D) were analyzed by ELISA. For the saline experiment, there was no significant difference in IL-4 encapsulation between the PEG

control and the two affibody-conjugated formulations following two wash steps (Figure 4.9A), though there was less IL-4 encapsulated in the Affibody_2 formulation in the serum experiment following a single wash step (Figure 4.9B). Further, there was no notable difference in cumulative protein release between the three formulations in saline (Figure 4.9B), but there was less cumulative release in the Affibody_1 formulation for the serum release experiment after 5 days.

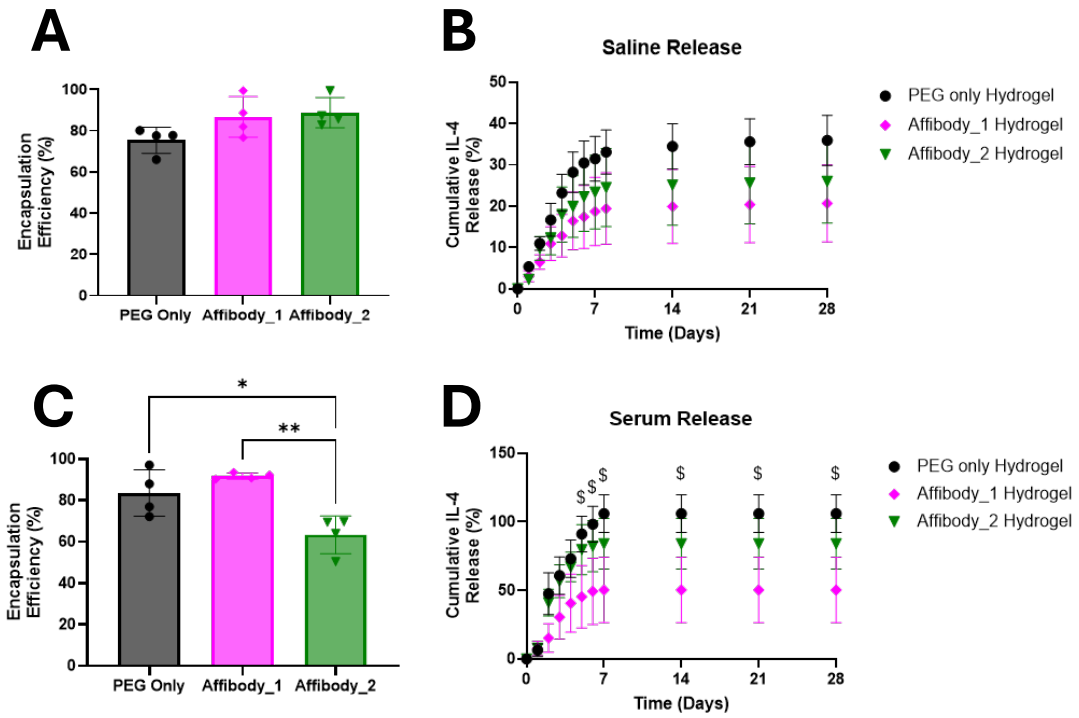


Figure 4.9: Encapsulation efficiency and protein release experiments from affibody-conjugated hydrogels. A) Encapsulation of protein for the saline release, following two wash steps. B) Release of IL-4 into saline solution for 28 days. C) Encapsulation efficiency for the serum release experiment following one wash step. D) Release of IL-4 into serum solution for 28 days. Significance calculated by one-way ANOVA for encapsulation efficiency and by two-way ANOVA for cumulative protein release, with Tukey post-hoc for all experiments. n=4. For encapsulation efficiency, * $p < 0.05$, ** $p < 0.01$. For release experiments, \$ $p < 0.05$ between the PEG gel and Affibody_1.

Discussion

A yeast surface display library was subjected to magnetic- and fluorescence-activated cell sorting to identify IL-4-specific affibodies. After 5 MACS and 3 FACS sorts, two IL-4-specific affibodies were discovered and characterized. An additional suspected affibody was identified

but not characterized further. In comparison to other protein targets, it was notably more challenging to discover and characterize IL-4-specific affibodies. To overcome these challenges, more IL-4 was required for the MACS and FACS protocols (100 pmol IL-4 for MACS and 5 μM IL-4 for FACS, compared to 33 pmol BMP-2 and 1 μM BMP-2 , respectively). An additional challenge was the mischaracterization and identification of a truncated affibody consisting of 52 amino acids instead of 58. Interestingly, this exact affibody sequence was previously found as a partner for GM-CSF – a highly unlikely occurrence. Such an event could indicate that the sequence similarities between IL-4 and GM-CSF (found to share structural overlap for 84 of 127 amino acids, per RCSB protein alignment tool[364]). Compared to BMP-2 which had been identified in Chapter 2, IL-4 is considered unstable,[292,365] which may explain why greater quantities of IL-4 were required in the identification process. There may also be a structural relationship between the target folding structure and the affibody library, as previously identified affibodies in our lab and in literature (BMP-2, VEGF, PDGF-BB, FGF-2, HER-2, TNF-α, etc.) commonly have some β-barrel structures, compared to IL-4's strictly α-helical folding.

The two IL-4-specific affibodies were made both recombinantly in BL21 (DE3) E. coli and synthetically through SPPS. Product purity was assessed using MALDI, which indicated singular peaks for the affibodies. Prior to purification, the impurities in the recombinant products were attributable to additional open reading frame products, and the synthetic impurities were attributable to inefficiencies in the stepwise growth of the affibodies. After purification, the majority of the peaks were from charged and multimeric states of the affibodies. All of the affibodies were determined to have α-helical secondary folding structures, which is as expected. Additionally, the amplitude of the CD plot was greater for the synthetic products, as seen previously, hypothesized to indicate the absence of negatively charged LPS that affects protein folding. To interrogate this hypothesis, two approaches may be taken – first, CD spectra of the synthetic affibodies may be obtained in the presence and absence of substantial LPS in solution; second, the surface charge of the recombinant and synthetic affibodies could be compared using zeta-potential tests.

Characterization of the two confirmed IL-4-specific affibodies posed additional challenges, initiated with the determination of the equilibrium dissociation constant using flow cytometry and an IL-4 concentration ramp. Beyond 1 μM, the signal for fraction protein binding reduced, counterintuitively. Due to this phenomenon, a nonlinear regression was not possible. The two

affibodies' dissociation constants could only be effectively obtained using biolayer interferometry. In its recombinant form, Affibody_1 (586 nM) had a lower equilibrium dissociation constant than Affibody_2 (653 nM), while the synthetic Affibody_1 affibody had a higher equilibrium dissociation constant (459 nM) compared to the synthetic Affibody_2 (141 nM). Due to these incongruities, it is difficult to accurately declare whether one or the other is high affinity. In Chapter 3, the relative affibody strength was retained between the synthetic and recombinant BMP-2-specific affibodies, and the BMP-2 release kinetics from hydrogels were comparable as additional confirmation. Only the recombinant affibodies were utilized for controlled protein release in this chapter, a shortcoming that could be addressed with relative ease in a short timeframe. It should be noted that we were unable to identify literature that has successfully characterized the protein-protein interaction between IL-4 and a target ligand using BLI and similar techniques such as surface plasmon resonance. This work marks significant progress towards characterizing protein-protein interactions for IL-4, and the experimental setup may be adapted to analyze other elusive and unstable proteins.

Computational protein docking predictions indicated that Affibody_1 would dock to IL-4 in a region overlapping the IL4Rα, and could potentially inhibit or modulate IL-4's interactions with macrophages. This hypothesis was built from an observed inhibition of BMP-2-induced ALP activity of C2C12s in the presence of the BMP-2-specific affibodies that interfere with their respective cell receptors.[300] Affibody_2 was not predicted to interfere with this binder, and was not expected to have such an effect. To test this hypothesis and elucidate whether the IL-4-specific affibodies could modulate macrophage polarization, synthetic affibodies were cultured with THP-1s monocyte-like cells. Synthetic affibodies were deemed necessary due to potentially impactful concentrations of LPS present in the recombinant affibody formulations. Preliminary results indicate that Affibody_1 (predicted to interfere with receptor binding) led to significant upregulation of both the M1-associated genes TNF-α, iNOS, and MMP-9 and the M2-associated genes IL-10, ARG-1, and CD163 in a concentration-dependent manner. Affibody_2 also led to an upregulation of these genes, but to a lesser extent. Combining IL-4 with the affibodies before incubating with the macrophages significantly inhibited the gene upregulation observed with the affibody-only treatments. Although these results are preliminary (as dictated by a bias of IL-10 signal throughout the assay as well as unexpected gene expressions), they indicate an extreme response to Affibody_1. It is possible that due to the structural similarities of the affibodies with

IL-4 and with other Class I cytokines (4 tightly packed α-helices)[366], that such a broad response is observed. To investigate this hypothesis, RosettaDock algorithms could be applied to specifically score the affibodies' interactions with IL-4 and with the plethora of receptors involved in macrophage polarization. In lieu of computational predictions, one can compare the IL-4-specific affibodies to the class of synthetic peptides called Innate Defense Regulators (IDRs), which have been shown to lead to intermediate M1-co-M2 macrophage polarization.[367] The transition of M1 to M2 states could also lead to this superimposed state, although it is a temporally dependent and highly dynamic state.[363,368] A single timepoint at 72 hours does not capture the rates and dynamics of macrophage polarization, which could be overcome by performing longitudinal macrophage polarization studies in the presence of these affibodies.[363,369] A 70-antibody panel has recently been developed for the identification of macrophage sub-types[370] and could be used to compare to our affibody-activated macrophages. It is possible that affibody polarization leads to a unique subset of macrophage activation that has not been previously observed.

The IL-4-specific affibodies were conjugated into PEG-Mal hydrogels to tune the release of IL-4, as mentioned above. It was found that the recombinant Affibody_1 reduced cumulative IL-4 release compared to the affibody-free control. This pattern was observed with statistical significance in FBS, but not significantly in PBSA. This aligns with results from comparable BMP-2-specific affibody release experiments,[300] predicted to be the result of the complexity of the FBS buffer that contains various proteases and molecules that affect the hydrophilic-lipophilic balance and electrostatics of the solution. Unlike the BMP-2 experiments where the high-affinity BMP-2-specific affibody had 4 more interactions than the low-affinity affibodies, both IL-4-specific affibodies have the same number of cumulative interactions (5), possibly justifying the observed results.

Conclusions

In this chapter, IL-4-specific affibodies were identified from a yeast surface display library containing 8×10^8 unique affibody sequences through magnetic and fluorescence activated cell sorting techniques. After 5 rounds of MACS and 3 rounds of FACS, 2 confirmed, 1 suspected, and 1 truncated affibodies were discovered and sequenced. The affibodies were subsequently collected and purified recombinantly in E. coli, and synthetically by SPPS. Affibody purity,

secondary structure, and protein-protein interactions were characterized by MALDI, CD, and BLI, respectively. All affibodies were α-helical in nature, as expected. The affibody named Affibody_1 was determined to have equilibrium dissociation constants of 486 nM and 459 nM in the recombinant and synthetic formats, respectively. The affibody named Affibody_2 was determined to have equilibrium dissociation constants of 653 nM and 141 nM for the recombinant and synthetic products, respectively. Due to this discrepancy, we were not confident in describing one affibody as relatively stronger than the other. Affibody-conjugated PEG-mal hydrogels were synthesized, showing that the recombinant Affibody_1 reduced the release of IL-4 compared to the affibody-free formulation. The synthetic affibodies have not yet been tested for their effects on IL-4 release.

Using computation binding prediction algorithms, the affibodies were predicted to dock to IL-4 in different regions, with the Affibody_1 affibody predicted to overlap with the IL4-Rα binding epitope. Macrophage polarization assays were performed with the common THP-1 cells by differentiating the THP-1 monocyte cells to M0 macrophages followed by polarization with various stimuli. RT-qPCR data indicated that incubating M0s with the affibodies alone led to an upregulation of both M1- and M2-associated genes, with Affibody_1 leading to greater gene upregulation than Affibody_2. Co-mixing IL-4 with the affibodies prior to incubation with the M0s reduced the upregulation, suggesting that the affibodies do not interact with the cells when bound to IL-4.

Taken together, we were able to make significant progress towards the identification and characterization of IL-4-specific affibodies. Determining the protein-protein binding strength of IL-4 binders by BLI has been challenging in literature, and the development of this protocol may be valuable going forward for other unstable proteins and Class I interleukins. The affibodies show promise for dynamic macrophage polarization stimuli or as IDRs to tune macrophage polarization, and could be interesting tools for future immune engineering studies. Affibody-conjugated PEG-mal hydrogels show promising results towards the tunable delivery of IL-4 to modulate the inflammatory response following traumatic bone fractures.

Chapter 5 - Factors Affecting Protein Release from Multipeptide and Multiaffibody-Conjugated Hydrogels

Morrhyssey Benz contributed substantially to the synthesis, collection, and purification of all affibodies described in this chapter. Payton Jefferis performed some of the controlled release studies, notability the studies characterized the presence of RGD. Morrhyssey. I was the primary contributor to all other controlled release experiments described in the chapter, I developed and analyzed the mathematical model described and did all of the writing.

Introduction

Wound healing is a highly orchestrated biological process involving the sequential and overlapping phases of inflammation, proliferation, and remodeling.[371,372] Each stage is mediated by a diverse array of proteins, including chemokines, cytokines, growth factors, and extracellular matrix components working in concert to restore structural and biological tissue function. Traumatic injuries, however, can disrupt this finely tuned cascade, leading to impaired healing or chronic wounds.[371] These disruptions are often due to the diminishment or absence of key signaling molecules at critical time points, underscoring the complexity of the biological responses required for successful tissue repair.

Conventional therapeutic approaches for promoting wound healing typically focus on the delivery of a single bioactive molecule, such as bone morphogenetic protein-2 (BMP-2)[290,373], vascular endothelial growth factor (VEGF)[374], or platelet-derived growth factor (PDGF).[214] While these interventions may address specific deficiencies in the healing process, they often fail to recapitulate the multifaceted nature of the wound-healing cascade. To better address the intricate requirements of tissue repair, there is a growing need for strategies capable of delivering multiple therapeutics in a spatially and temporally controlled manner. Such approaches have the potential to more effectively mimic and recapitulate the native wound healing environment, improving outcomes for patients with traumatic injuries.

In the context of bone healing, substantial efforts have been made to co-deliver BMP-2 for its ability to induce osteogenesis alongside other therapeutic proteins, such as VEGF[375–377], PDGF[378,379], and fibroblast growth factor-2 (FGF-2)[380,381] to promote osteogenesis. Similarly, BMP-2 delivery has been paired with the delivery of interleukin-8 (IL-8)[382], interleukin-10 (IL-

10)[383] and the overexpression of interleukin-4 (IL-4)[342,384] in mesenchymal stromal cells (MSCs) to manage inflammation. Despite the promise of these strategies, their success has been inconsistent, often due to challenges in achieving precise spatiotemporal control over the release of each protein. Additionally, high doses of BMP-2, often required to achieve therapeutic effects, can lead to adverse outcomes such as ectopic bone formation and inflammation, underscoring the need for optimized delivery systems that better mimic the native bone healing microenvironment.[385,386]

Affinity-based release has shown promise in tuning the release of payloads without drastic manipulations to the properties of the delivery vehicle.[211] Recent advances by our group and others has demonstrated that affibodies, small alpha-helical engineering affinity binders[387], may be used to modulate the delivery of BMP-2[350], FGF-2[92], VEGF[352], and more. Further, it has been demonstrated that dual-affibody integration into a single delivery could independently tune the release of separate proteins based on the ratios of protein-specific affibodies.[299] We hypothesize that this trend would be observed with other combinations of affibodies of different strengths, demonstrating that affibody affinity towards a target protein is the primary contributor to controlling protein release.

To investigate the relationships between affinity-mediated hydrogel formulations and protein release, various statistical models can be employed.[388] Simple linear models assume a linear correlation between the independent input variables and the dependent output variables, depicted in Equation 5.1, where Y is the dependent output, X is the independent variable, M is the coefficient of the independent variable, and B is the y-axis intercept.[388] The most common fit for linear correlation models is Least Squares Regression, which minimizes the residual sum of squares, described in Equation 5.2. Least squares models output coefficients to provide insight into the magnitude and direction of these effects. For instance, least squares fits have been used to identify the simple relationship between hydrogel mesh size and protein release,[205] and to evaluate the mechanisms controlling anti-inflammatory drug delivery from drug delivery tablets to treat rheumatoid arthritis.[389]

Equation 5.1: Linear regression formula

$$Y = \left(\sum_{j=1}^{n} X_j M_j \right) + B$$

Equation 5.2: Least Squares Fit model for linear regressions

$$RSS(\beta) = \sum_{i=1}^{N} (y_i - x_i \beta)^2$$

For more complex and nonlinear relationships, machine learning models like decision trees, random forests (RFs), gradient boosting (GB), and neural networks (NNs) are valuable tools for predicting interactions between input and output variables.[390,391] Decision trees aim to deduce an interaction by answering a set of consecutive true/false questions.[388] These models are simple to interpret, but are prone to overfitting data and cannot handle outliers well. The degree of overfitting may be exacerbated by the depth of the decision tree.

RFs improve upon the predictive capabilities of decision trees by using a resampling method called bootstrapping (randomly selecting a sample from a set with replacements), and an ensemble learning technique called bagging (performing bootstrapping multiple times) (Figure 5.1A).[391,392] Limiting the depth of the decision trees in a RF reduces the likelihood of overfitting. More trees provide greater stability to the model. Due to the ensemble learning approach, RFs can withstand outlier data more effectively than traditional decision trees and least squares regressions but are computationally intensive. RFs have been used to determine dose-response curves of monoclonal antibody treatments for patients based on genetic characteristics[393], and for optimizing formulations of amorphous solid dispersions to increase the solubility of active pharmaceutical ingredients.[394]

GB is an alternative forest model that may improve the predictive capabilities of RFs and overcomes their computational intensity. GB sequentially build a forest by analyzing a tree and then building subsequent weighted trees from the previous tree's error (Figure 5.1B).[392] GB generally yields better results than RFs, but require more optimization of the feature parameters (independent variables) and are more prone to overfitting errors that RFs. Recently, GB has been used to combine datasets of similar drugs, datasets of similar proteins, and datasets of drug-

protein associations to predict the function and behavior of new combination drug therapeutics.[395] GB has also been used to predict the release of drug from a fibrin biofilm more accurately than other machine learning methods.[396]

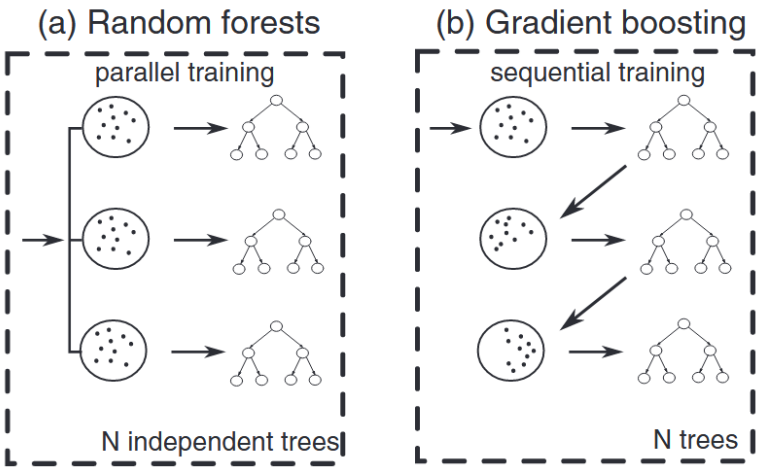


Figure 5.1: Simple tree-based predictive models. A) Random forests, which utilize parallel training of data to make for predictions. B) Gradient boosting, which sequentially trains treed based on the success of previous trees. Adapted from Kowalek et al.

Recently, random forest regression has been used to interpret and predict the interactions between whey protein isolate and hyaluronic acid for drug delivery by analyzing complicated Raman spectroscopy data. For smaller models, hybrid approaches RF models can be used to check the robustness of a least squares fit model.[397,398]

The overall objective of this thesis is to integrate BMP-2-specific affibodies with IL-4-specific affibodies, described in Chapters 2 and 4 to independently tune the release of BMP-2 and IL-4 to manage the inflammatory response as well as the formation of bone. By synthesize complex hydrogels with multiple engineered affinity binders of different binding strengths, herein we look to expand our understanding of affinity-mediated release. For this, we explore how protein-specific affinities, affibody concentrations, and the addition of multiple affibodies affect the release of BMP-2 alone, and BMP-2 in conjunction with IL-4. By categorizing variables from 8 release experiments of BMP-2 and/or IL-4 into 11 independent variables, we aim to gain a broader understanding of key variables and interactions that contribute to protein release rate or diffusivity. The dataset is populated by release of BMP-2 or IL-4 from single affibody-

conjugated hydrogels presented in Chapters 2, 3 and 4, as well as release of BMP-2 from hydrogels conjugated with affibodies and the adhesive peptide RGD (a common additive in implantable materials)[399,400], and simultaneous release of BMP-2 and IL-4 from dual affibody-conjugated hydrogels. Altogether, these datasets are fit to least squares fit models to identify key contributions to release[401,402], and to a RF predictive model to analyze more complex non-linear relationships without overfitting the datasets.[390,394]

Materials and Methods

Preparation of affibodies and peptides.

Affibodies were prepared recombinantly or synthetically as described previously in Chapter 3.[353] For the recombinant affibodies, two BMP-2-specific affibody sequences modified with a penultimate hexahistidine tag and a c-terminal cysteine were transformed into BL21 (DE3) E. coli (New England Biosciences; NEB) containing a pET28b(+) vector. Affibody-containing E. coli were cultured overnight in 20 mL Luria-Bertani (LB) (Affymetrix) supplemented with kanamycin sulfate (Millipore Sigma), and then transferred into 1.8 L of Terrific Broth (TB) (Affymetrix) containing kanamycin sulfate and expanded at 37 °C until an optical density at 600 nm (OD600) between 1.2 and 1.4. The E. coli was collected by centrifugation, followed by cell lysis by sonication, collection of soluble proteins by centrifugation, and purification by immobilized metal affinity chromatography with cobalt nitrilotriacetic acid (cobalt beads) (GoldBio). Products were further purified by size exclusion chromatography.

Synthetic affibodies and RGD and VPM peptides were prepared by solid phase peptide synthesis with a Liberty Blue 2.0 Microwave Peptide Synthesizer (CEM Corporation). The affibody sequences for the two BMP-2-specific affibodies and two IL-4-specific affibodies were modified with a penultimate cysteine and a C-terminal glycine. 0.2 M amino acid (CEM Corporation), 10% v/v pyrrolidine (Sigma Aldrich) deprotection, 1 M N,N'-diisopropylcarbodiimide (DIC) (Oakwood Chemical), and 1 M Oxyma (CEM Corporation) solutions were prepared in DMF. Affibodies were cleaved with a cleavage cocktail (1:1:1:1:36 ratios of ddH2O, triisopropyl silane (Oakwood Chemical), 2,2’-(Ethylenedioxy)diethanethiol (Tokyo Chemical Industry), thioanisole (Oakwood Chemical), trifluoroacetic acid (TFA) (Oakwood Chemical)) for 40 minutes at 42 °C. The solution was vacuum-filtered and the filtrate was purified via precipitation and

centrifugation with ice-cold diethyl ether. The product was dried overnight and purified by high-performance liquid chromatography (HPLC; CEM Prodigy using 19 x 150 mm C18 Waters column) by running a 15-75% acetonitrile gradient in ddH2O with 0.1% v/v TFA.

Preparation of hydrogels

PEG-mal hydrogels were synthesized as described previously with various combinations of affibodies and RGD. Briefly, 100 µL 5 % w/v were prepared synthesized by dissolving 5 mg of 20 kDa 4-arm PEG-mal (Laysan Bio) in PBS pH 6.9 and mixing with 0-1.98 nmol of the recombinant or synthetic BMP-2-specific affibodies, 0-3.31 nmol of the recombinant or synthetic IL-4-specific affibodies, and/or 0-200 nmol of the RGD peptide dissolved in PBS pH 6.9 to prepare an intermediate solution. The intermediate solution was dispensed into a 2 mL microcentrifuge tube and crosslinked with dithiothreitol (GoldBio) or VPM dissolved in PBS pH 6.9. The hydrogels were purified by washing in fresh PBS pH 7.4 three times over 36 hours. All reagents used were sterile filtered through a 0.22 µm filter, and reagents were handled in a biosafety cabinet to ensure sterile preparation.

Controlled Release from Hydrogels

After purification, hydrogels were loaded with 100 ng of recombinant human BMP-2 (R&D Biotechne) or with 50 ng each of BMP-2 and recombinant human IL-4 (Peprotech) by incubating with a 20 µL solution of the proteins overnight at 4 °C. Hydrogels were washed with 200 µL of sterile PBS supplemented with 1 mg/mL bovine serum albumin (BSA; altogether PBSA) to remove unbound protein. PBSA or 10 %v/v fetal bovine serum (FBS) (Gibco) in PBS were added to the tubes containing the hydrogels to a total volume of 1 mL. 200 µL aliquots were collected for 2 weeks and replenished with fresh PBSA or FBS solution. Encapsulation efficiency and cumulative release were obtained by protein-specific enzyme-linked immunosorbent assays (ELISAs) (R&D Biotechne).

For this work, seven independent studies were performed and subsequently combined. The first experiment assessed the effect of RGD concentration on BMP-2 release from a high-affinity BMP-2 affibody-conjugated hydrogel, with RGD concentrations ranging from 0-2000 µM in a hydrogel containing 500× affibody-to-BMP-2 ratio. The second assessment compared release

from hydrogels conjugated with 500× high- or low-affinity BMP-2 and with/without 1 mM RGD. The third experiment compared release was to determine the effect of affibody ratios on BMP-2 by varying the affibody excess from 0× to 500× affibody-to-BMP-2 ratio. Both high- and low-affinity BMP-2-specific affibodies were used in this experiment. The fourth experiment introduced a secondary affibody and protein – a full factorial study releasing BMP-2 and IL-4 from PEG-mal hydrogels containing no affibody or high- or low-affinity BMP-2-specific affibody and/or high- or low-affinity IL-4-specific affibody. Molar ratios of 500× affibody to loaded protein were kept consistent throughout this experiment. The last four studies had been previously described in Chapters 2, 3, and 4. The first study compared the effect of the release solution (FBS vs PBSA) on BMP-2 release from hydrogels conjugated with 500× high- or low-affinity recombinant BMP-2-specific affibodies. The second study assessed IL-4 release only from IL-4-specific affibody-conjugated hydrogels in PBSA, while the third study quantified IL-4 release into FBS from IL-4-specific affibody-conjugated hydrogels. The fourth study compared BMP-2 release from hydrogels containing either synthetic or recombinant high- or low-affinity BMP-2-specific affibodies at 500× molar ratios, released into PBSA.

Two calculations were performed to ensure the comparability of the hydrogels between experiments and total protein amounts. First, cumulative protein release was normalized to the maximum amount of protein released in each experiment (i.e. max protein at final timepoint of a singular experiment) to ensure that all release data is relative to each experiment. Second, the Korsmeyer-Peppas model was used to quantify the diffusion from slab geometry using the relationship of $M_t/M_\infty=kt^{0.5}$ where M_t/M_∞ is the fractional release of the protein over time, and k is the diffusivity constant for each sample.[403]

JMP software inputs

To identify trends in the results, data from the release experiments was input JMP 17 Pro (SAS) statistical software. Independent variables were categorized as described in Table 5.1, and the dependent variables are shown as described in Table 5.2.

Several assumptions were made when populating the tables, which are outlined herein. The relative affibody strength or affinity (high vs low) was presumed consistent between the PBSA and FBS groups. The charge of the affibodies, RGD, and proteins at various pHs were theoretically derived by inputting their respective amino acid sequences into the ProtPi

Bioinformatics toolkit developed at Zurich University of Applied Sciences. The pH of the PBSA and FBS solutions used were obtained in-house using a pHBasic pH pH probe (Sartorius).

Table 5.1: Independent variables for JMP model

Variable	**Discrete/Continuous**	**Identifier**	**Value**
BMP-2 Affibody	Ordinal	PEG baseline	0
		Low affinity affibody	1
		High affinity affibody	2
IL-4 Affibody	Ordinal	PEG baseline	0
		Low affinity affibody	1
		High affinity affibody	2
BMP-2 Affibody Ratio	Continuous	Molar excess of affibody to protein	0 to +inf
IL-4 Affibody Ratio	Continuous	Molar excess of affibody to protein	0 to +inf
RGD Concentration	Continuous	µM RGD in gel	0 to inf
Release Media	Continuous	% FBS in PBS	0 to 100
BMP-2 Affibody Charge	Ordinal	Theoretical charge at experiment pH	-inf to +inf
IL-4 Affibody Charge	Ordinal	Theoretical charge at experiment pH	-inf to +inf
RGD Charge	Ordinal	Theoretical charge at experiment pH	-inf to +inf
BMP-2 Charge	Ordinal	Theoretical charge at experiment pH	-inf to +inf
IL-4 charge	Ordinal	Theoretical charge at experiment pH	-inf to +inf

Table 5.2: Dependent variables for JMP model

Variable	**Discrete/Continuous**	**Identifier**	**Value**
BMP-2 Release	Continuous	% cumulative release in relation to final timepoint	0 - 100
IL-4 Release	Continuous	% cumulative release in relation to final timepoint	0 - 100
BMP-2 Fickian diffusion	Continuous	k from $M_t/M_\infty=kt^{0.5}$ For BMP-2 release	0 to +inf
IL-4 Fickian diffusion	Continuous	k from $M_t/M_\infty=kt^{0.5}$ For IL-4 release	0 to +inf

In all, the dataset had 172 samples, of which 11 samples were excluded due to either an incomplete data set, due to human error in synthesis of the hydrogel, or machine error during collection of the data. The data was further classified as BMP-2-relevant data or IL-4 relevant data, based on if the dependent variables had BMP-2 or IL-4 released from the hydrogel. In all, The BMP-2-specific dataset contained 148 samples and the IL-4-specific dataset had 60 samples. Data was randomly designated as training and validation sets, split 0.75 for training and 0.25 for validation. Each of the BMP-2 and IL-4 data sets were fitted to a least squares fit model and a RF ("Bootstrap Forest" in JMP) for cumulative protein release and protein diffusivity.

Results

Affibody characteristics

Affibodies used throughout in this work were previously collected, purified, and characterized (Chapters 2, 3, and 4). The equilibrium dissociation constants of the affibodies were obtained by BLI. Table 5.3 outlines the affibody dissociation constants. The affibody input variable was ordinal (categorical data with order) and organized in ascending affinity interactions. As such, PEG only, which was the baseline affinity, was given the value of 0, while low affinity affibodies were given a value of 1 and high affinity affibodies were given a value of 2.

Table 5.3: Affibody dissociation constants obtained by BLI

Protein Target	*Affibody Source*	*K_D (nM)*	*Identifier Value*
BMP-2	Recombinant	8.96	High Affinity (2)
	Recombinant	25.0	Low Affinity (1)
	Synthetic	4.78	High Affinity (2)
	Synthetic	37.4	Low Affinity (1)
IL-4	Recombinant	586	High Affinity (2)
	Recombinant	653	Low Affinity (1)
	Synthetic	141	High Affinity (2)
	Synthetic	446	Low Affinity (1)

Effects of RGD Concentration on BMP-2 Release

100 µL 5 w/v% PEG-mal hydrogels were synthesized with no affibody or with 500× molar excess high-affinity BMP-2 affibody, and 0-2 mM RGD, with DTT crosslinking. After purification, hydrogels were loaded with 100 ng of BMP-2 and allowed to load into the hydrogels overnight at 4 °C. BMP-2 release into FBS solution was quantified by ELISA over a 14-day period (Figure 5.1A). The cumulative BMP-2 release was plotted for the last day of the release experiment (Figure 5.1B). Upon inclusion of the high-affinity affibody, there was a significant reduction in cumulative BMP-2 release, as seen previously.[353] With increasing concentrations of RGD in the affibody-conjugated hydrogels, there was an increase in the *p*-value (becoming less significant) in relation to the PEG-mal hydrogel without affibodies. However, there was no significant difference between the affibody-only formulations and those conjugated with RGD.

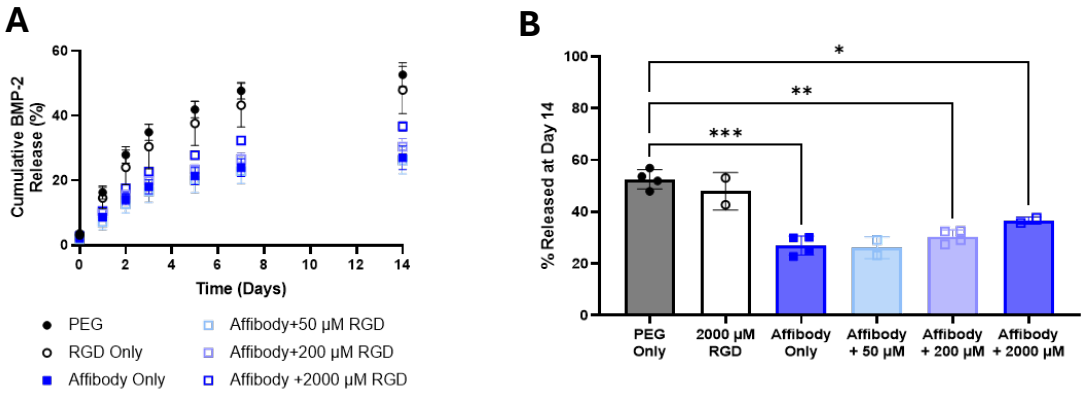


Figure 5.2: Effects of RGD concentrations in affibody-conjugated hydrogels on BMP-2 protein release. A) Cumulative protein release over 14 days, measured by BMP-2-specific ELISA. B) Cumulative protein released by the last day of the experiment (day 14). Final day statistical significance was calculated by Brown-Forsythe and Welch ANOVA with Dunnett's post-hoc test. n=2-4. * $p<0.05$, ** $p<0.01$. *** $p<0.001$, **** $p<0.0001$

Effects of RGD and Affibody Affinity on BMP-2 Release

100 µL 5 w/v% PEG-mal hydrogels were synthesized with no affibody or with 500× molar excess of synthetic high-affinity or low-affinity BMP-2 affibody, and 0 or 1 mM RGD. Hydrogels were loaded with 100 ng of BMP-2 and allowed to load into the hydrogels. BMP-2 was released into FBS and quantified by ELISA over a 14-day period (Figure 5.2A) and the cumulative BMP-2 released on the last day of the experiment was collected (Figure 5.2B). The inclusion of 1 mM RGD into each formulation did not change the total amount of protein

released by the end of the experiment. As previously observed, there was only a difference in total protein released between the high-affinity affibody formulation and the affibody-free controls.[350] However, there was no significant difference between the high-affinity affibody + 1 mM RGD formulation and the affibody-free hydrogels.

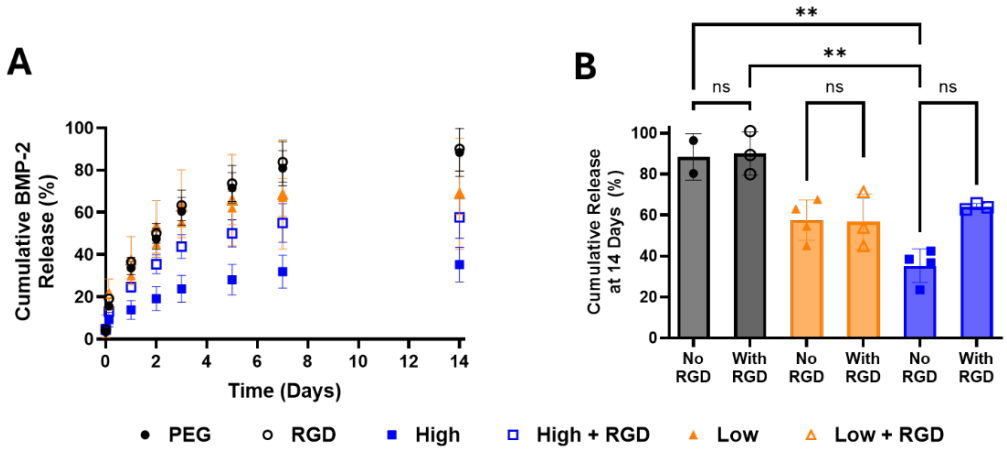


Figure 5.3: Effects of 1 mM RGD in high- and low-affinity affibody-conjugated hydrogels on BMP-2 protein release. A) Cumulative protein release over 14 days, measured by BMP-2-specific ELISA. B) Cumulative protein released on the last day of the experiment (day 14). The inclusion of 1 mM RGD into the affibody-conjugated hydrogels did not change the release from comparable no-RGD formulations. Final day statistical significance was calculated by Brown-Forsythe and Welch ANOVA with Dunnett's post-hoc test. n=2-4. * $p<0.05$, ** $p<0.01$. *** $p<0.001$, **** $p<0.0001$

Effects of Affibody concentration on BMP-2 Release

100 µL PEG-mal hydrogels were synthesized with 0 pmol, 9.62 pmol, 96.2 pmol, or 962 pmol of recombinant high- or low-affinity recombinant affibody, representing 0, 5, 50, and 500 times molar excess to the amount of BMP-2 being loaded. After washing, 1.92 pmol (50 ng) of BMP-2 was loaded into the hydrogel overnight. Controlled release was carried out in PBSA for 7 days, and cumulative release (Figure 5.3A) and total protein released at the culmination of the experiment (Figure 5.3B) were plotted. Increasing the amount of affibody led to the reduction of total protein released by the end of the experiment. Only the 5× molar excess did not result in significant reductions in protein release.

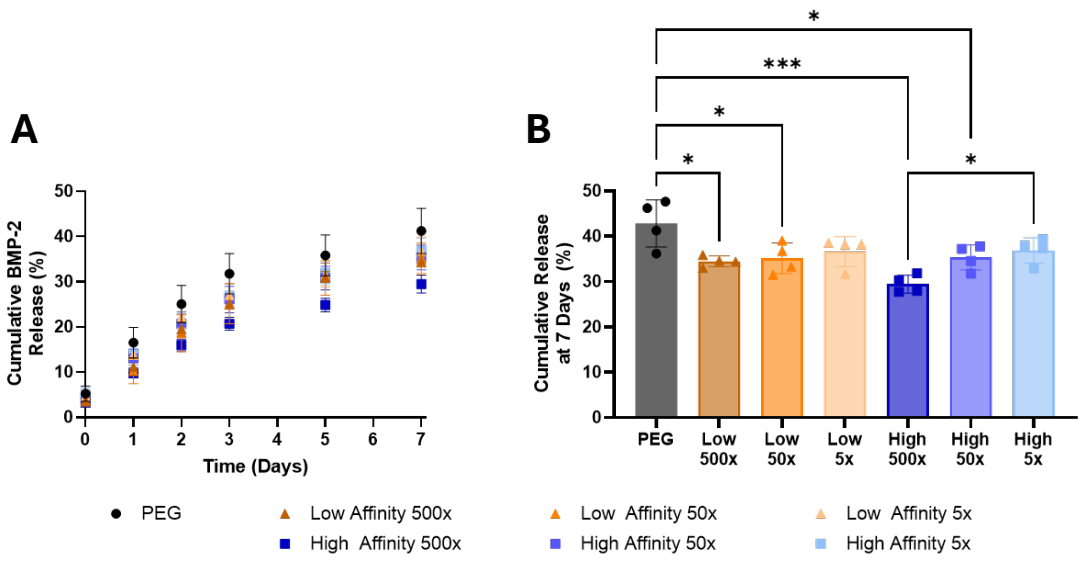


Figure 5.4: Effects of affibody concentration on BMP-2 protein release. A) Cumulative protein release over a 7-day period, measured by ELISA. B) Cumulative protein released on the last day of the experiment. Final day statistical significance was calculated by one-way ANOVA with Tukey's post-hoc test. n=4. * $p<0.05$, ** $p<0.01$. *** $p<0.001$, **** $p<0.0001$

Effects of Multiple Affibodies and Multiple Payloads on Protein Release

100 µL PEG-mal hydrogels containing no hydrogels or conjugated with 500× synthetic high- or low-affinity BMP-2-specific affibodies and/or 500× synthetic high- or low-affinity IL-4 specific affibodies were loaded with 50 ng each of BMP-2 and IL-4. Aliquots were collected for 28 days in FBS (Figure 5.4). To visually observe release trends between 9 different hydrogel formulations, release curves were organized by hydrogel formulation to show both BMP-2 and IL-4 release (Figure 5.4A-I). Final-day cumulative release of BMP-2 (Figure 5.4J) and IL-4 (Figure 5.4K) were separately plotted. Generally, formulations containing the high-affinity BMP-2 affibody released less BMP-2 than the low-affinity affibody and the no-affibody control. Hydrogels with only the IL-4-specific affibodies demonstrated similar cumulative BMP-2 release to the hydrogels without affibodies. Similarly, the use of high-affinity IL-4-specific affibodies reduced the cumulative release of IL-4 compared to hydrogels without affibodies or with only BMP-2-specific affibodies. The only high-affinity IL-4 affibody formulation that did not have a significantly different cumulative IL-4 release is the high-affinity BMP-2-co-high-affinity IL-4 hydrogel.

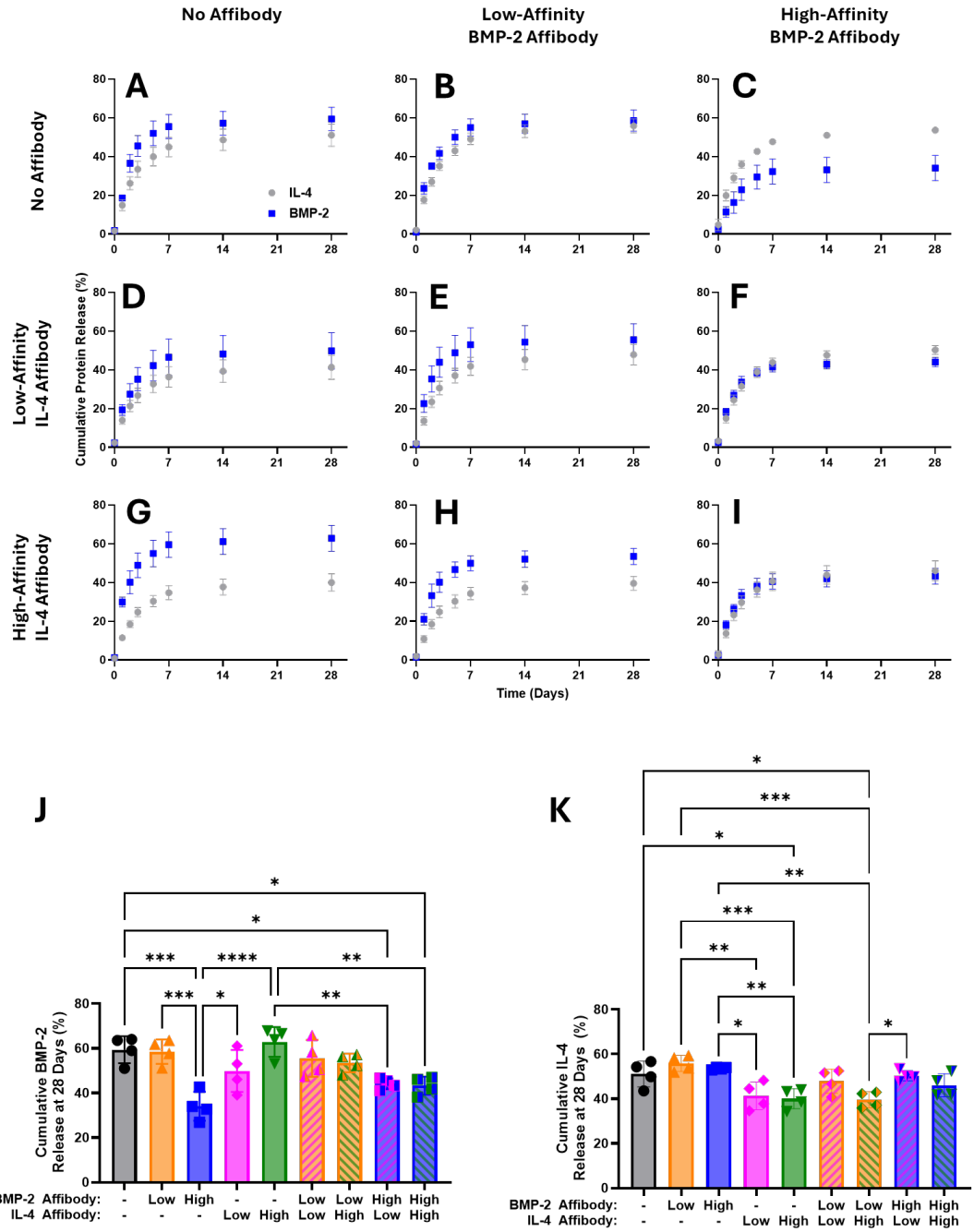


Figure 5.5: Cumulative BMP-2 and IL-4 release from dual-affibody-conjugated PEG-mal hydrogels. A-G) cumulative release of BMP-2 and IL-4 from full factorial dual-affibody-conjugated hydrogel formulations. A,B,C contain no IL-4-specific affibody; D,E,F contain the low-affinity IL-4-specific affibody; G,H,I contain the high-affinity IL-4-specific affibody; A,D,G have no BMP-2-specific affibody; B,E,H contain the low-affinity BMP-2-specific affibody; C,F,I contain the high-affinity IL-4-specific affibody. J) Cumulative BMP-2 released at the culmination of the release experiment. K) Cumulative IL-4 released at the culmination of the release experiment. Statistical significance calculated by one-way ANOVA with Tukey's post-hoc test. n=4. * $p<0.05$, ** $p<0.01$. *** $p<0.001$, **** $p<0.0001$

Normalization of data

By comparing the y-axes in Figure 5.1-5.4, it is apparent that cumulative protein release from each experiment is different. This could be attributed to using different total amounts of BMP-2 loaded into the hydrogels, the type of release medium used, the different length scales of the experiments. To overcome this issue, the data were normalized to the highest protein released within experiment (i.e. 81.6% cumulative release becomes 100%. All data is normalized by the factor of 100/81.6).

Statistical analysis of combined datasets

The 172-sample dataset was populated, including all the independent variables in Table 5.1 and the dependent variables in Table 5.2. The pH of PBSA was 7.6 and the pH of the FBS solution was 7.7. The affibody, RGD, and protein sequences were input into the ProtPI tool and the charges were recorded and integrated into the model (Table 5.4).

Table 5.4: Independent variable values as a function of release media at different pHs

Protein and Peptide	*PBSA (pH 7.6)*	*FBS (pH 7.7)*
Recombinant high-affinity BMP-2	-0.43068	-0.54890
Recombinant low-affinity BMP-2	-0.42443	-0.54104
Synthetic high-affinity BMP-2	N/A	-0.84991
Synthetic low-affinity BMP-2	N/A	-0.84205
Recombinant high-affinity IL-4	-6.40564	-6.51816
Recombinant low-affinity IL-4	-5.40594	-5.51840
Synthetic high-affinity IL-4	N/A	-5.81941
Synthetic low-affinity IL-4	N/A	-6.81917
RGD	N/A	0.18251
Recombinant human BMP-2	0.00516	-0.32325
Recombinant human IL-4	5.22467	4.92522

Least Squares Fit Models for BMP-2 Dataset

For cumulative protein release, the model had a coefficient of determination, R^2, of 0.70 (Figure 5.5A), indicating 70% of the variance of cumulative release is explained by the independent variable inputs.[404] Generally, higher values ($R^2 > 0.5$) are indicative of better model fits, and could be visualized by data points clustering close to the diagonal blue line.[394] The effect summary identified that the most likely factor to influence BMP-2 release was the "BMP-2 Affibody × BMP-2 Affibody Ratio" with a p-value of 1.92×10^{-8} **(Figure 5.5B)**. This analysis indicates that a major factor influencing the amount of BMP-2 released from the hydrogels is the interaction between the amount and strength of affibody conjugated into the formulation. Other covariates with of significance were "BMP-2 Affibody × BMP-2 Affibody Ratio × BMP-2 Affibody Charge × BMP-2 Charge" ($p = 6.95\times10^{-6}$), "BMP-2 Affibody × BMP-2 Affibody Ratio × RGD Concentration" ($p = 2.29\times10^{-5}$), "BMP-2 Affibody × BMP-2 Affibody Ratio × IL-4 Affibody × IL-4 Affibody Ratio" ($p = 3.2\times10^{-4}$), and "BMP-2 Affibody" ($p = 5.1\times10^{-4}$). The results suggest that the charge interaction between the affibody and the protein payload plays a role in determining the release amount, as seen by the Affibody charge × BMP-2 charge input. There is also indication that the integration of additional elements into the hydrogel such as RGD and other affibodies affect the amount of protein released. The least squares fit for the diffusivity of BMP-2 had an R^2 of 0.74 (Figure 5.5C). The Effect summary suggested diffusivity was most likely affected by the "Affibody Charge" variable (Figure 5.5D). The "BMP-2 Affibody × BMP-2 Affibody Ratio × RGD Concentration" and "IL-4 Affibody Charge" also predicted diffusivity. Taken together, these data support the hypothesis that greater amounts of higher affinity protein-specific affibodies reduce the amount of protein released. While protein-specific affibodies are needed to tune protein release, there may be a non-linear interaction between the BMP-2-specific affibodies and either RGD or IL-4-specific affibodies in the context of cumulative protein released. Furthermore, the charges of the affibodies and peptides integrated into the hydrogels appear to play a role in the release kinetics of the payload.

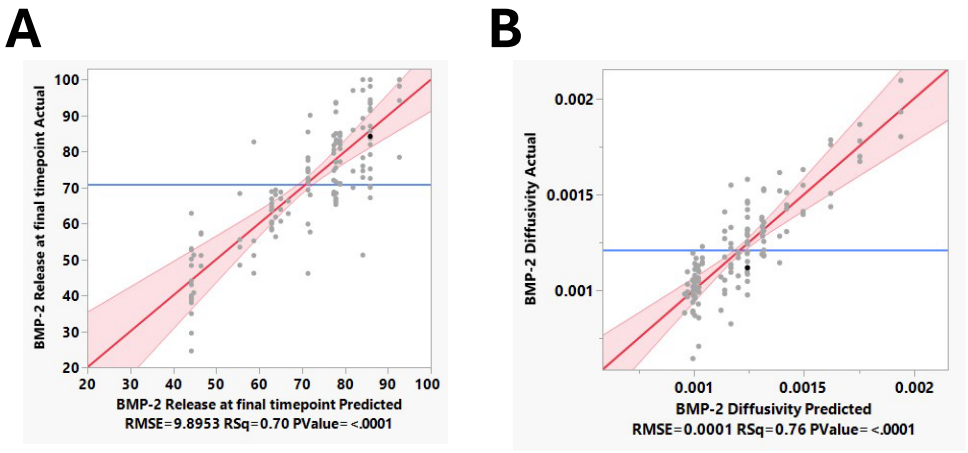


Figure 5.6: Least squares fit models for BMP-2 dataset. A) Actual vs prediction plot of model for BMP-2 cumulative release, R^2=0.70. Effect summary suggested that BMP-2 Affibody x BMP-2 Affibody Ratio interaction can predict cumulative release. B) Actual vs prediction plot of model for BMP-2 diffusivity, R^2 = 0.76. Effector summary suggesting BMP-2 Affibody Charge has the greatest effect on diffusivity. The shaded areas of the predicted vs. actual plots indicate the confidence bounds. n=140

Least Squares Fit Models for IL-4 Dataset

The least squares fit model for cumulative release of IL-4 had an R^2 of 0.59 (Figure 5.6A). The data was a better of predicter of greater quantities of total release, indicated by a narrower confidence band around 75% IL-4 cumulative release and a very wide confidence band at release < 40%. In comparison to the BMP-2 release data, the range of cumulative IL-4 release is narrower. This implies that the IL-4 affibody-conjugated hydrogel formulations were not effective for meaningful reduction of cumulative protein release compared to no affibody hydrogels. The effect summary suggested that the interaction of "IL-4 Affibody × IL-4 Affibody Ratio × BMP-2 Affibody × BMP-2 Affibody Ratio" was the greatest predictor of release with a (Figure 5.6B). However, with a *p*-value of 0.0329, this interaction is not a strong predictor IL-4 release. There were no other notable covariates below a p-value of 0.05. In fact, there was no quantifiable interaction for the IL-4 affibody and "IL-4 Affibody × IL-4 Affibody Ratio" input measures. The least squares fit model for the diffusivity of IL-4 had an R^2 of 0.53 (Figure 5.6C). The input data was clustered around a narrow range of IL-4 diffusivity, which contributed to wide confidence bands on either side of the data. The effect summary indicated that the "IL-4 Affibody Charge" was the most likely factor to affect diffusivity, and had a *p*-value of 0.00350 **(Figure 5.6D).**

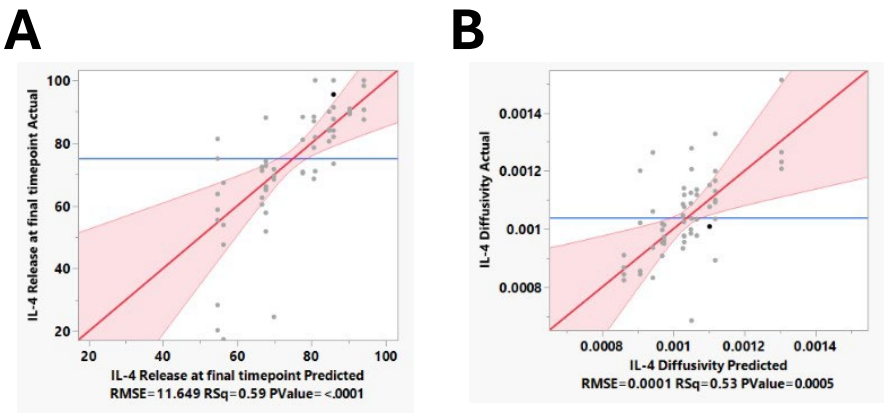


Figure 5.7: Least squares fit models for IL-4 dataset. A) Actual vs prediction plot of model for IL-4 cumulative release, R^2=0.59. Effect summary suggesting the interaction of IL-4 Affibody x IL-4 Affibody Ratio x BMP-2 Affibody x BMP-2 Affibody Ratio may contribute to cumulative release. B) Actual vs. plot prediction of model for IL-4 diffusivity, R^2 = 0.53. Effector summary indicating IL-4 Affibody Charge is a likely contributor to IL-4 diffusivity. The shaded areas of the predicted vs. actual plots indicate the confidence bounds. n=56

Random Forest Predictive Models for BMP-2 Dataset

The RF predictive model was used on BMP-2 dataset to predict and validate a model that is not overfitted and can be used to describe the complexity of the multi-variable protein delivery system. For cumulative BMP-2 release, the training data had an R^2 of 0.732 (n=102), and the validation data had an R^2 of 0.62 (n=37) (Figure 5.7A,B). Similar to the least square models, greater R^2 values indicate a more robust fit. The key predictor of cumulative BMP-2 release was the BMP-2 Affibody with a column contribution of 0.4915 (Figure 5.7C). Cumulatively, the column contributions add to a value of 1, and higher contributions indicate greater impact on the model prediction.[405] Thus, the BMP-2 affibody impacts about half of the predictive model. The second and third column contributors of importance were the BMP-2 affibody ratio and BMP-2 affibody charge with fairly similar contributions of 0.162 and 0.1537. The BMP-2 diffusivity RF model had an R^2 values of 0.753 and 0.525 for training and validation, respectively (Figure 5.7 D,E). Although the validation fit had an $R^2 > 0.5$, the deviation of the strength of fit between the training and validation sets may be indicative of an underfitted model that does not effectively capture the complexity of variables contributing to protein diffusivity.[405] The key contribution to diffusivity was predicted to be BMP-2 affibody charge (0.3524). Other contributions came from BMP-2 charge (0.1957), FBS% in media (0.1701), and BMP-2 affibody ratio (0.0972) (Figure 5.7F).

These RFs predict, and accurately validate the contributions affecting BMP-2 release and diffusivity. The model agrees with the least squares fit, suggesting that the BMP-2 affibody (specifically affibody affinity, based on the model setup) and its concentration contributes to the total amount of protein being released. The predictive model also reinforces that the rate of protein release is likely dependent on charge and more granular aspects of the affibody itself.

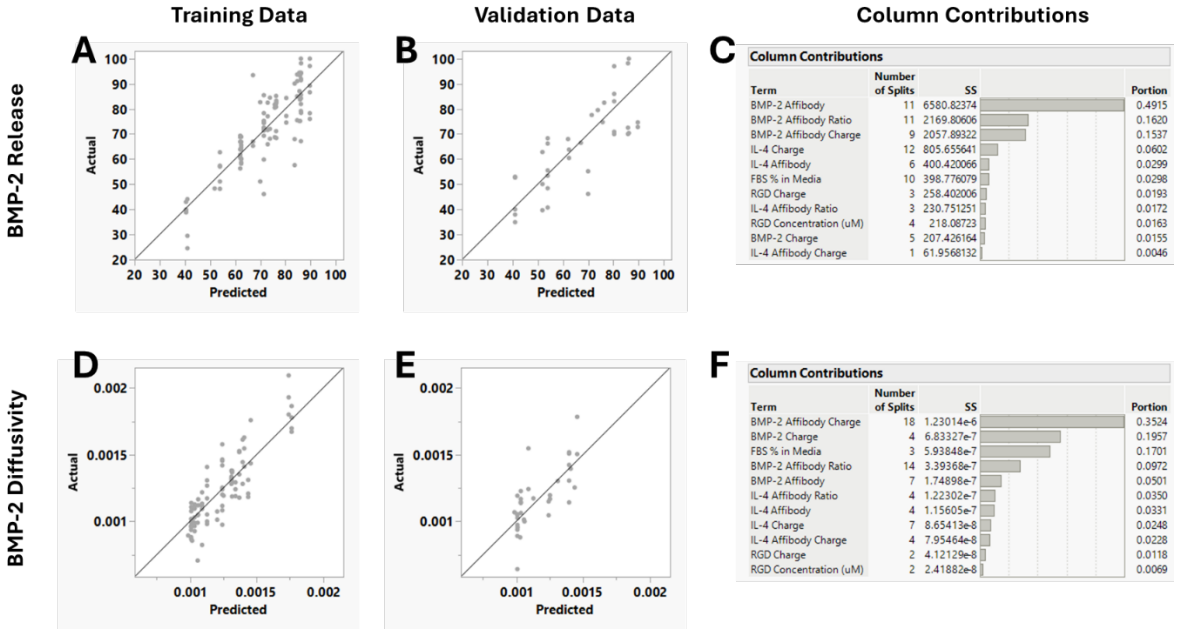


Figure 5.8: Random Forest Predictive Model for BMP-2 dataset. A-C) BMP-2 Release model. Number of trees = 7. A) Training dataset fitting $R^2 = 0.732$, B) Validation dataset fitting $R^2 = 0.620$. C) The highest column contributions from the ordinal independent variable BMP-2 Affibody. D-F) BMP-2 Diffusivity model. Number of trees = 7. D) Training dataset fitting $R^2 = 0.753$, E) Validation dataset fitting $R^2 = 0.525$. F) Highest column contribution was determined to be BMP-2 Affibody Charge. $n_{training} = 102$, $n_{validation} = 37$

Random Forest Predictive Models for IL-4 Dataset

The IL-4 data was input into a RF model as described above. For cumulative IL-4 release, the training data had a R^2 of 0.629 (n=42) and the validation data had an R^2 of 0.561 (n=15) (Figure 5.8A,B). The key contributors to IL-4 cumulative release were predicted to be the IL-4 affibody ratio (0.3589), followed by IL-4 affibody charge (0.2704), the IL-4 affibody (0.1148), and the BMP-2 affibody ratio (0.1015) (Figure 5.8C). For the IL-4 diffusivity model, the training set had a R^2 of 0.438 and the validation had a R^2 of 0.070 (Figure 5.8D,E). This data indicated a poor fit training and validation set, which could be representative of insufficient training data in relation to the model's complexity. Indeed, the IL-4-specific dataset is less than half of the BMP-2-

specific dataset. The IL-4 charge had the highest column contribution to the model (0.3985) (Figure 5.8F). BMP-2 charge (0.2922) and FBS % in media (0.1870) were also considered contributors.

With R^2 values > 0.5 for the cumulative release data, the model was able to predict which variables contribute to IL-4 release. The amount of IL-4-specific affibody may be used to predict protein release. This RF prediction does not align with the least squares fit, but the bagging (resampling with replacement process) has greater predictive capacity demonstrated through higher R^2 values. The RF is not able to definitively predict which factors affect IL-4 diffusivity, though it suggests that IL-4 charge may be used to predict IL-4 diffusivity. The results are somewhat in agreement with the least squares fit, which suggested the IL-4 affibody charge could describe the diffusivity. Both regression fits indicate that the interaction between the protein and the affibody may tune the diffusivity.

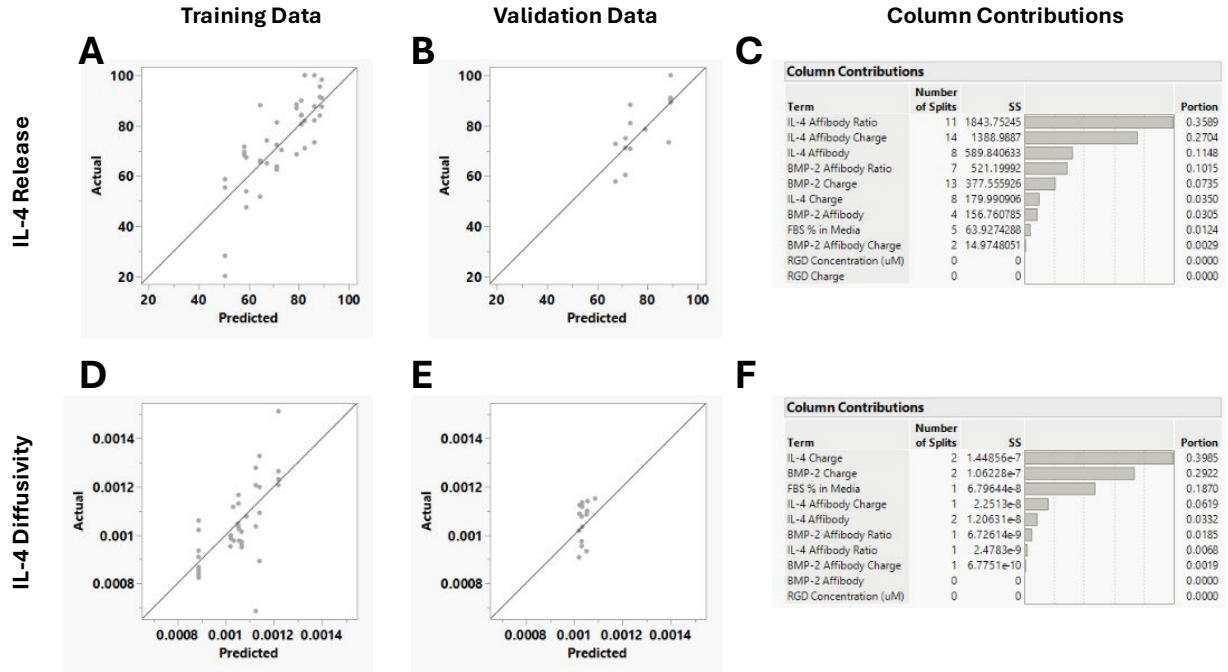


Figure 5.9: Random Forest Predictive Model for IL-4 dataset. A-C) IL-4 Release model. Number of trees = 15. A) Training dataset fitting $R^2 = 0.629$, B) Validation dataset fitting $R^2 = 0.561$. C) The highest column contribution was from the continuous independent variable IL-4 Affibody Ratio. D-F) IL-4 Diffusivity model. Number of trees = 7. D) Training dataset fitting $R^2 = 0.438$, E) Validation dataset fitting $R^2 = 0.070$. F) Highest column contribution was determined to be IL-4 Affibody Charge. $n_{training} = 42$, $n_{validation} = 15$

Discussion

In this work, we looked to evaluate which variables within our affibody-conjugated hydrogels contribute to protein release by varying the target of the affibody, the source of the affibody, the concentrations of affibody integrated, and the other additives to the hydrogel formulations.

We first analyzed each release experiment individually. It was determined that adding different concentrations of the adhesive peptide RGD to high-affinity BMP-2-specific affibody hydrogels did not significantly affect the cumulative release of protein compared to the affibody-conjugated hydrogel without RGD. Greater amounts of RGD integration into affibody-conjugated hydrogels reduced the significance of the release compared to no-affibody hydrogels, suggesting that there is a threshold amount of RGD that would make the difference not significant. As such, RGD could contribute to protein release. The experiment was then expanded to include low-affinity BMP-2-specific affibodies, and the integration of 1 mM RGD into those hydrogels also did not affect release. As had been observed previously, the higher affinity affibody reduced the amount of protein released compared to the affibody-free controls, but not the low-affinity affibody. Using greater amounts of affibody was shown to reduce protein release, as expected.

A more complex experiment in which affibodies specific to BMP-2 and IL-4 were conjugated into a hydrogel was performed. The target proteins for both sets of affibodies were loaded into the hydrogel as well. At the conclusion of the experiment, the BMP-2-specific affibody formulations retained their characteristics – formulations with high-affinity BMP-2 affibody released less BMP-2 than formulations without the high affinity affibody. This was maintained in dual-affibody hydrogels as well. The IL-4-specific release showed some similar traits, demonstrating a reduction in protein release in high-affinity IL-4-specific affibody formulations, though the effect was lost when considering the high-affinity IL-4-co-high-affinity BMP-2 formulation. As described in the introduction, the ideal release scenario would release IL-4 first to reduce excessive inflammation[406] and manage osteolysis[341] and osteoclastogenesis[345], followed by BMP-2 for bone formation.[407] Careful inspection of the formulations indicates that either the High-BMP-2 or the High-BMP-2-co-Low-IL-4 hydrogel formulations would satisfy this criteria.

To identify the underlying contributions to release, the experiments were pooled into one normalized dataset, consisting of 11 independent variables, and 4 dependent variables (BMP-2 release, BMP-2 diffusivity, IL-4 release, and IL-4 diffusivity). The dataset also included BMP-2

and IL-4 release experiments analyzed previously to ensure sufficient model training (Figures 2.7, 3.3, and 4.9). In all, there were 172 samples in the set. The linear regression least squares fit models for BMP-2 release and diffusivity had R^2 values of 0.70 and 0.74, respectively, indicating a fairly robust model, especially when considering that all of the experiments were performed at separate times with different batches of affibody and protein. The effect summary indicated that the affinity and quantity of the BMP-2 affibody were the most effective for predicting protein release, confirming our hypothesis. The diffusivity was predicted to be most affected by affibody charge, which is an indirect representation of the affibody affinity. The protein-protein interactions themselves may play a role in the release rates.

The IL-4 affibody least squares fits were comparatively worse than their BMP-2 counterparts with R^2 values of 0.59 and 0.53 for release and diffusivity, respectively. IL-4 affibody and affibody ratios were not considered integral to effecting release, though no variable exceeded a 2-Log threshold which the model used to identify for key contributions. This further indicates the weakness of fit of this model. For diffusivity, the only significant variable was IL-4 charge, indicating that this is driven more by the payload characteristic than any aspect of the hydrogel formulation. From this, it could be interpreted that the formulations used were not effective for controlling IL-4 release. Additional controlled release experiments are necessary to identify some formulations to tune IL-4 release.

The data was further scrutinized using predictive modeling. RF modeling was chosen over GB to overcome the likelihood of error incurred from pooling many different experiments together.[390] For BMP-2 release, the model had good alignment between the training and validation datasets, with R^2 values of 0.742 and 0.62, most likely affected by the BMP-2 affibody. The diffusivity modeling had a greater deviation between the training and validation fits (R^2 values 0.753 vs 0.525). The diffusivity may be most impacted by affibody charge. Both of these results agree with the least squares fit model, supporting the motivation of this work.

Although the RF model for IL-4 release was fairly consistent between its training and validation data, and likely driven by IL-4 affibody ratios, the diffusivity model was insufficiently predictive. The weakness in diffusivity mirrored the least squares fit, and the R^2 of the validation set was a dismal 0.07. The model did agree with the conclusion of the BMP-2 diffusivity model, and indicated that the charge of the target protein (IL-4) had the greatest contribution to predicting release. Although RF should be able to deduce more complex relationships than least

squares fits due to its bagging sampling technique, there was not enough separation in the dataset for the model to effectively capture and determine the variables affecting IL-4. To combat this issue, more comprehensive release experiments to improve the dataset. Since the RF suggested that IL-4 affibody concentration may guide release, it would be valuable to perform release experiments with varying amounts of IL-4 affibody, exceeding the 500× molar ratios. The results from this work may identify a threshold concentration of IL-4-specific affibody that is necessary for controlling protein release.

There are several limitations to the dataset and models as described in this work. First, there is no variable directly quantifying protein-specific affibody affinity. The ordinal variables "BMP-2 Affibody" and "IL-4 Affibody" provide a categorical determination of the affibody strength. Although this was sufficient for the BMP-2-specific dataset where there was usually a notable difference in BMP2 release and diffusivity, the categorical determination of "strong" or "weak" affibody did not accurately reflect the effect of the affibody on release and diffusivity. The continuous variables "[Protein-specific] Affibody Charge" reference the affibodies, aiming to provide a quantitative parameter for the affibodies. Charge is affected by pH, and was chosen in effort to capture the observed differences between protein release in saline and serum, which have different pHs. The variable does not accurately reflect the charge of the system in the absence of affibodies, estimating a neutral charge of 0. In practice, the absence of an affibody in a hydrogel does not reflect the overall absence of charge in a hydrogel. To accurately characterize the behavior of affibodies in a hydrogel, I attempted to develop BLI assays that quantify the equilibrium dissociation constants of PEG-mal and affibody-conjugated PEG-mal, to no avail. Briefly, PEG groups were prepared by neutralizing the maleimides of 4-arm PEG-mal (with or without affibody) with β-mercaptoethanol. Streptavidin BLI probes were loaded with 125 nM BMP-2, and the PEG samples were associated and dissociated in PBST. However, bulk polymers have significant impacts to viscosity and optical transparency that affect probe sensitivity[408,409] and would require custom-built algorithms for analysis.

Additional shortcomings of this model include the assumption that there was no affinity interaction between RGD and either BMP-2 or IL-4, and the absence of variable weighting. For RGD, these interactions could be quantified by BLI. The absence of variable weights could mischaracterize the effect of continuous variables such as theoretical charge, skewing the models

interpretation of the hydrogel. Indeed, these additives amount to less than 5% of the hydrogel network, but they are treated as equal.

To address both of the challenges associated with charge vs affinity and overall vehicle charge, it is possible to synthesize equivalent nanoparticle formulations of the bulk hydrogels.[410] Solution viscosity significantly affect the measurement sensitivity and accuracy of BLI. Since nanoparticles are suspended and not dissolved in solution (as bulk PEG), nanoparticles are more reliable for BLI, and thus can provide an estimate of protein-specific affinities that can be applied as a continuous independent variable, compared to an ordinal value.[409,411] By measuring the charge of the affibody-conjugated PEG nanoparticles using zeta potential, the model could be fit empirical data that more accurately reflects the affibody-conjugated hydrogel system as a whole. This would be particularly valuable when considering multi-affibody and multi-peptide systems and payloads of different charges.

Conclusion

The wound healing cascade is a spatiotemporally complex process that necessitates the presentation of chemokines, cytokines, growth factors, and more. In the event of traumatic injuries, the healing cascade may be disrupted, resulting in permanent non-healing. Current treatments aim to re-establish the healing cascade by delivering single key therapeutic proteins, which does not mimic the complexity of the healing process. Recent works have shown some promise through the codelivery or multiple proteins, though challenges remain in independently tuning the release of products to address the temporal aspects of the healing cascade. Affinity interactions could be leveraged to independently tune the delivery of multiple payloads, with affibodies having demonstrated the capacity to alter the release of two growth factors simultaneously by modulating protein-specific affibody concentrations.

To this end, we aimed to codeliver BMP-2 and IL-4 to modulate the inflammatory response and generation of bone upon traumatic bone fractures by using BMP-2-specific and IL-4-specific affibodies. While we performed a full-factorial study combining high- and low-affinity BMP-2- and IL-4-specific affibodies into PEG-mal hydrogels and making 9 formulations for controlled release, we also looked to establish a greater understanding of factors affecting protein release. By combining release experiments that individually assess the use of affibodies of different strengths, the concentrations of affibody-conjugation in hydrogels, the use of adhesive peptides,

and changing the properties of the release media. Least squares fit and RF models were used to uncover the underlying factors controlling release.

We found that for BMP-2, both the least squares model and the predictive RF had decent fits with $R^2 > 0.7$ for both cumulative protein release and diffusivity. The validation set for cumulative release was fairly aligned with the training data, but there was more deviation when comparing the diffusivity. The key variable for tuning the amount of protein released was the amount and strength of affibody, as predicted and demonstrated in Chapters 2 and 3. Diffusivity was affected most by affibody charge, which is an indirect parameter associated with the affinity strength of the affibody in this model.

The IL-4 samples had weaker fits to both the least squares model and the RF model, with the diffusivity being very poorly fit. With $R^2 \sim 0.6$ for both cumulative release fits, this data was most impacted by the concentration of the affibody in the hydrogels, indicating that the affibodies do indeed affect release, but there is no difference between the two. IL-4 charge was a key factor in modulating IL-4 release from the hydrogels. These data thus suggest that the IL-4 affibodies identified either require greater characterization, or need to be further engineered to have greater impacts on release. It could be that the affibody scaffold is not optimal to tuning IL-4 as a class I cytokine (strictly alpha-helical), which is further discussed in Chapter 4.

Altogether, we found that fast release of IL-4 and slower release of BMP-2 could be achieved using a hydrogel formulation consisting of the high-affinity BMP-2 affibody, and either no IL-4-specific binder or the low-affinity IL-4-specific affibody, conceptually agreeing with the principals of affinity-modulated release. The release of each protein was primarily affected by some element of the affibody interaction, but there were other notable contributions. The affinity interaction controls the amount of protein released, and the overall charge of multipeptide-enhanced hydrogels may affect the release rate of individual payloads. Care should be taken to ensure that peptides integrated into the hydrogels do not interact non-specifically with other proteins. Lastly, robust dataset sand well-characterized peptides and affinity binders could lead to greater predictive power of multipeptide-enhanced hydrogels for individually controlled protein delivery. This work shows promise as a rudimentary model to guide future developments of affinity-enhanced delivery vehicles for protein codelivery.

Chapter 6 - Shelf-Stable Melt Electrowritten Scaffold-Reinforced Affibody-Conjugated Hydrogels for Controlled Protein Delivery

Patrick Hall made substantial contributions to this work by fabricating and characterizing all MEW scaffolds. He also wrote a small portion of the methods and results sections for the MEW scaffolds. Payton Jefferis helped with the rheological characterization and mesh size assessments of the hydrogels. Guilherme Rocha synthesized the RGD affibodies used in this chapter. Yan Carlos, Kait Link, and Payton Jefferis assisted with in vivo rat surgeries. Payton Jefferis helped with postoperative care, and the X-ray, IVIS, and micro-CT collection. I was the primary contributor to hydrogel synthesis, formulation development, controlled release studies, lyophilizaton studies, subcutaneous in vivo surgeries, and did all of the remaining writing.

Introduction

Long bone fractures are common and devastating injuries, with about 500,000 annual cases in the United States alone.[412] More than 60% of these injuries require some mechanically-reinforcing surgical intervention and amount to $12.3B in annual healthcare costs.[413,414] However, 8% of long bone treatments result in non-unions[414], defined as a fracture that does not heal after a long time, requiring further surgical interventions and affecting patients' lives.
In the event of traumatic injuries such as bone fractures, the natural and localized wound healing cascade consisting of stages of inflammation, proliferation, and remodeling, may be disrupted[206], leading to permanent disabilities like non-unions. A promising treatment method to overcome such disruptions is the exogenous supplementation of one or multiple proteins involved in the healing cascade.[206] For bone fractures, these proteins often have osteoinductive properties such as bone morphogenetic protein-2 (BMP-2) and delivered in supraphysiological concentrations from hydrogels such as collagen, alginate, or polyethylene glycol (PEG).[194,415,416] However, the spatiotemporal complexity of bone injuries necessitates proteins to be delivered at precise times in precise locations.[215,417] Uncontrolled BMP-2 release can result in off-target effects such as ectopic and heterotopic ossification, as well as other conditions that reduce quality of life. It is also important for the hydrogels to withstand the mechanical loading experienced in the tissue.[418] This combination of factors poses an engineering challenge, as hydrogels need to be

cytocompatible,[419] sufficiently soft to allow cell penetration and integration, with promising results seen at or below 1 kPa, [420,420–423] and simultaneously mechanically strong to resist the stress experienced in bone.[424] Further, protein delivery rates are often linked to the mechanical properties of a hydrogel.[422,425] For clinical translation, the engineered solution should also be easy to use[426], and shelf stability.[427] Developing a product that effectively overcomes these challenges would be a significant innovation for treatment bone fractures, and could be applied to a plethora of conditions.

Affinity-mediated release, a relatively new approach to controlled release which relies on the electrostatic and hydrophobic interactions between a delivery vehicle and its payload instead of the delivery vehicle's mechanical properties,[211] could be leveraged to adjust the release rate of the therapeutic protein without drastically changing its mechanical properties. Affinity-enhanced biomaterials have also been shown to improve the localization and retention of therapeutic proteins, including BMP-2 through heparin-based microparticles.[215] Recent advanced in affinity-mediated release have demonstrated the capacity to tune protein release based on the presence or absence of engineered affinity binders[223], and varying the ratios of the binders.[299] We have previously identified engineered affinity binders called affibodies, a class of versatile and thermally stable protein binders derived from the z-domain of staphylococcal protein A,[225,387,428–430] specifically for BMP-2 binding and controlled release.[300] We demonstrated the capability of tuning the osteogenic protein's release in vitro from an affibody-conjugated PEG-based hydrogel by integrating stronger and weaker affibodies. From these results, we hypothesize that BMP-2-specific affibody-conjugated PEG hydrogels could be translated in vivo to tune protein release rates based on their binding affinity and ensure protein localization.

Hydrogel mechanical properties could be addressed from two angles – changing the bulk hydrogel stiffness by using higher concentrations of polymer or crosslinker, or reinforcing the hydrogel.[431] However, increasing the stiffness of the material overall would affect protein integration and cytocompatibility[420,422], limiting its use in this application. Thus, mechanical reinforcement, which can be applied without altering the hydrogel formulations would be more preferable.[432] Indeed, the clinically-approved BMP-2 delivery medical device is a soft absorbable collagen sponge that is caged in a hard plastic for additional mechanical stability.[194] Recent advances in 3D printing could be leveraged to integrate reinforcements into the hydrogel instead of casing it entirely.[432] High precision melt electrowriting (MEW) is an emerging additive

manufacturing technique which can generate highly porous scaffolds composed of ordered microfibers out of clinically relevant synthetic thermoplastics such a poly ε-caprolactone (PCL) and nylon.[433,434] MEW relies on electrohydrodynamic forces to draw thin fibers of molten polymer which are written into scaffolds through techniques similar to traditional extrusion-based 3D printing techniques. Due to the applied electrohydrodynamic forces, MEW fibers are typically on the scale of 1-50 μm, scaffolds retain porosity of 80-95%, and varying scaffold designs lead to broad ranges of mechanical properties.[435–437] For instance, the combination of MEW scaffolds with methacrylated gelatin hydrogels induced a 54-fold increase in ultimate strength in the composite material compared to the MEW scaffold alone.[432] Taken together, it is hypothesized that MEW-reinforced affibody-conjugated hydrogels would be able to effectively tune protein release and withstand mechanical forces without making significant changes to the hydrogel's intrinsic mechanical properties. This mechanical stability would also allow soft hydrogels to be easily handled without damage for simple surgical implantation.

Improving the shelf stability of a protein delivery system provides multiple benefits, including reduction to economics costs associated with maintaining a cold chain and reducing variability of product performance.[438,439] A common approach toward increasing shelf-stability is drying the materials through lyophilization.[438,440] While it may improve the shelf stability of the hydrogel, lyophilization may damage the polymer network of the hydrogels, resulting in less predictable protein release.[440,441] Lyophilization may also affect proteins within the hydrogel by inducing aggregation, degradation, or misfolding upon rehydration, reducing the efficacy of the therapeutic protein.[427] Determining the effect of lyophilization on protein delivery from affinity-mediated hydrogel delivery vehicles may provide valuable insight for clinical translation and improving shelf stability. The aforementioned clinically-relevant absorbable collagen sponge for BMP-2 delivery is rehydrated with a highly concentrated solution of BMP-2 prior to surgical implantation. This technique that could be applied to a scaffold-reinforced affibody-conjugated hydrogel to interrogate the effects of lyophilization on the hydrogels' mechanical properties as well as the affibodies' functions without affecting the therapeutic protein. It is hypothesized that while the polymer network of the hydrogel will be affected leading to a lower stiffness[440], the MEW scaffold would maintain the overall structural integrity of the hydrogel upon compression. Further, it is predicted that the use of the thermally-stable affibodies will mitigate the effects of

polymer network breakdown, and protein release will be slower in hydrogels conjugated with higher affinity BMP-2-specific affibodies.

In this work, we looked to engineer a shelf-stable and mechanically robust controlled BMP-2 delivery system that is simple to handle for surgical implantation. For this, we reinforced affibody-conjugated PEG hydrogels with MEW scaffolds in effort to increase the range of compressive forced the hydrogel could withstand without affecting the hydrogel polymer network, which also improved the ease of use of these hydrogels in surgery. The scaffold-reinforced hydrogels were subjected to mechanical and rheological assessments to identify the impact of the MEW scaffold on the hydrogel. The integration of affibodies into the hydrogels was used to tune the release of BMP-2, and the potential impacts of the MEW scaffold on release were which was assessed by enzyme-linked immunosorbent assays (ELISAs). The reinforced hydrogels underwent a cycle of lyophilization to evaluate and extend their shelf stability. Upon rehydration, the hydrogels underwent additional rigorous mechanical testing and protein release studies as described above.

Materials and Methods

Affibody synthesis

Recombinant affibodies were expressed in *E. coli* and purified using immobilized metal affinity chromatography followed by size exclusion chromatography, as previously described.[300] Briefly, high- and low-affinity BMP-2-specific affibody sequences modified with a C-terminal hexahistidine tag and cysteine were ligated into the pET28b+ expression vector for isopropyl β-D-1-thiogalactopyranoside (IPTG)-inducible protein expression. The plasmids were transformed into chemically competent BL21(DE3) *E. coli.* Transformed *E. coli* were grown in Luria-Bertani broth (Fisher BioReagents) supplemented with kanamycin sulfate (Millipore Sigma) (50 mg/L) overnight followed by growth in Terrific Broth (Research Products International), supplemented with kanamycin sulfate (50 mg/L) and 400 μ of Antifoam 204 (Millipore Sigma) at 37 °C in a water bath bioreactor with air sparging until an optical density at 600 nm of ~1.2 was reached. The *E. coli* were then induced to produce affibodies by adding IPTG (Gold Biotechnology) to a final concentration of 0.5 mM, and incubating at 18 °C for 20 hours. The cells were lysed by

sonication in 50 mM tris buffer supplemented with 500 mM NaCl (Fisher Scientific), 5 mM imidazole (Fisher Scientific), and 75 mg of tris(2-carboxyethyl)phosphine (TCEP) (Gold Biotechnology). The lysate was centrifuged, and the supernatant was collected and mixed with cobalt-nitrilotriacetic acid (Co-NTA) (Gold Biotechnology) beads for 60 minutes to form a chelation bond between the cobalt and the hexahistidine tag of the affibodies. The solution was transferred to an empty glass chromatography column (BioRad) and washed with 50 mM tris (Gold Biotechnology) buffer containing 500 mM NaCl and 30 mM imidazole to remove weakly bound proteins. The purified affibodies were then eluted by washing the column with 50 mM tris buffer containing 500 mM NaCl and 250 mM imidazole. Affibodies were buffer-exchanged into phosphate-buffered saline (PBS) (Fisher Scientific) and further purified by size exclusion chromatography (BioRad NGC with Enrich SEC 70, 10/300 mm column). Affibodies were stored at -20 °C until use.

Affibodies were alternatively synthesized using solid phase peptide synthesis using a CEM Liberty Blue 2.0 microwave peptide synthesizer, as previously described.[353] The high- and low-affinity BMP-2-specific affibody sequences were modified with a penultimate cysteine and a C-terminal glycine for peptide synthesis. Solutions of 0.2 M of each amino acid (CEM Corporation), Fmoc-Gly-Wang resin (CEM Corporation) (0.602 mmol/g loading), 10% v/v pyrrolidine (Millipore Sigma), 1 M N,N'-diisopropylcarbodiimide (DIC) (Oakwood Chemical), and 1 M Oxyma (CEM Corporation) were prepared in N,N-dimethylformamide (DMF) (Fisher Scientific) and loaded onto the peptide synthesizer. Synthesized crude affibodies were cleaved from the resin by mixing with a cleavage cocktail (0.5 mL H_2O, 0.5 mL triisopropyl silane (Oakwood Chemical), 0.5 mL 2,2'-(Ethylenedioxy)diethanethiol (Tokyo Chemical Industry), 0.5 mL thioanisole (Oakwood Chemical), 18 mL trifluoroacetic acid (TFA) (Oakwood Chemical)) for 40 minutes at 42 °C. The cleaved solution was vacuum filtered, and the filtrate was purified via precipitation and three rounds of centrifugation (1200 RCF, 5 minutes) using cold diethyl ether (Fisher Scientific). The precipitate was dried overnight in a dessicator and purified using a Prodigy high performance liquid chromatography (HPLC) (CEM Corporation) by running a 30-75% gradient of acetonitrile in H_2O with 0.1 %v/v TFA. Affibodies were lyophilized and stored at -20 °C until use.

The size and purity the recombinant and synthetic affibodies were measured using matrix-assisted laser desorption/ionization time of flight (MALDI-TOF) mass spectrometry (Bruker

Smart LS), and the secondary structures of the affibodies were measured using circular dichroism (JASCO J-815).[353]

Poly ε-caprolactone scaffold fabrication

Tubular MEW PCL scaffolds were printed with a diamond pore design using a custom-built, high-precision MEW system based on the Aerotech A3200 platform with a cylindrical collector.[436,437] The designed scaffold had a programmed diameter of 5 mm, a pore area of 0.5 mm^2, and a layer count of 10. The scaffolds were designed with lengths of either 6.5 or 9 mm; when accounting for fiber lag, these designs resulted in scaffolds with internal volumes of 100, 150, or 200 µL respectively. MATLAB was used to write a scaffold toolpath code to translate these input parameters into the AeroBasic programming language. PCL (Corbion PURASORB PC12, Lot #2007001491) was loaded into 3 mL glass syringes (Fortuna Optima), which were capped with 22 gauge needle tips (VitaNeedle) and heated to 80°C overnight to allow for the PCL to melt to the bottom of the needle tip and release trapped air bubbles. Then, the loaded syringe was placed into a heating jacket and fitted with a pressure connector. An input pressure of 0.75 Bar, hot-end temperature of 80°C, collector translation speed of 4.5 mm/s, needle-to-collector distance of 3 mm, applied voltage of 4.5 kV, and mandril diameter of 5 mm were used to print the scaffolds.

Physical Characterization of Tubular MEW Scaffolds

Optical and scanning electron microscopy (SEM) were used to visualize the physical structure of the MEW scaffolds. A Keyence VHX-7000 microscope was used for optical imaging of the scaffolds to analyze the structure and fiber diameter of the scaffolds. For SEM, the MEW scaffolds were first sputter-coated using an Au-Pd alloy (Cressington, Watford, UK) prior to imaging on a ThermoFisher Apreo 2 SEM using 3.2 nA, 5.00 kV, and 39-1000x magnification.

Synthesis of affibody-conjugated PEG hydrogels

100 µL 5 w/v% affibody-conjugated polyethylene glycol (PEG) hydrogels were synthesized as described.[237,300] Briefly, 20 kDa, 4-arm PEG-maleimide (Laysan Bio), high- or low-affinity BMP-2- specific affibodies, and/or cell-adhesive RGD peptides (CGRGDSG, prepared and

purified in-house using the CEM Liberty Blue 2.0 and CEM Prodigy as described for affibody synthesis) were each dissolved in PBS pH 6.9 and mixed for 30 minutes at room temperature to form PEG, PEG-affibody, PEG-RGD, or PEG-affibody-RGD intermediates. The intermediate solutions were crosslinked in 2 mL centrifuge tubes by combining with dithiothreitol (DTT) (Gold Biotechnology) dissolved in PBS pH 6.9 and reacting the solutions for 30 minutes at room temperature. Each hydrogel contained 500 times molar excess of affibody compared to the amount of BMP-2 loaded for each application and 1 mM RGD peptide for in vivo implantation. Unreacted DTT was removed from the hydrogels prior to loading with BMP-2 by submerging the hydrogels in 1 mL of PBS and exchanging 3 times with fresh PBS every 12 hours.

Effects of affibody and RGD peptide conjugation on hydrogel mesh size

Hydrogel mesh sizes were calculated using the Equilibrium Swelling Theory.[425,444–446] 100 µL 5 w/v% hydrogels were synthesized without affibodies, with 2 nmol of high-affinity BMP-2-specific affibodies, and/or with 15 µmol of RGD peptides (amino acid sequence: CGRGDSG). The masses of the hydrogels were recorded initially immediately after crosslinking (i.e., the relaxed state). The hydrogels were then swollen overnight in 1 mL of PBS at 4 °C. The PBS solution was removed, and the hydrogels were weighed again in the swollen state. The hydrogels were then frozen and lyophilized at -104 °C and 50 mTorr for 12 hours using a SP Scientific ZG benchtop lyophilizer, and their dry masses were measured. The hydrogels were also rehydrated with 100 µL of PBS, and the process of swelling and lyophilizing was repeated to determine if hydrogel mesh sizes were affected by lyophilization. Equation 6.1 and Equation 6.2 were used to determine the approximate mesh size of the hydrogels, where M_n is the number-average degree of polymerization of the 4-arm PEG-Mal (20,000), $\bar{v}$ is the specific volume of bulk PEG-mal (0.888 cm^3/g, calculated as the reciprocal of the density of 4-arm PEG-Mal (1.125 g/cm^3)), V_1 is the molar volume of water (18 mL/mol), $v_{2,s}$ is the equilibrium swollen polymer volume fraction, $v_{2,r}$ is the relaxed polymer volume fraction, χ is the Flory-Huggins interaction for PEG in water (0.426),[444] C_n is the characteristic ratio of PEG (3.96),[447] M_r is the molecular weight of PEG repeats (44 g/mol), and l is the bond length of the PEG backbone (0.146 nm).[444]

Equation 6.1: Quantification of average molecular weight between crosslinks

$$\frac{1}{\bar{M}_c} = \frac{2}{\bar{M}_n} - \frac{\left(\frac{\bar{v}}{V_1}\right)\left[\ln\left(1 - v_{2,s}\right) + v_{2,s} + \chi_1 v_{2,s}^2\right]}{v_{2,r}\left[\left(\frac{v_{2,s}}{v_{2,r}}\right)^{\frac{1}{3}} - \left(\frac{v_{2,s}}{2v_{2,r}}\right)\right]}$$

Equation 6.2: Mesh size quantified by Equilibrium Swelling Theory

$$\xi = v_{2,s}^{-\frac{1}{3}}\left(\frac{2C_n\bar{M}_c}{M_r}\right)^{\frac{1}{2}} l$$

Fabrication of scaffold-reinforced hydrogels

To form PEG-mal hydrogels within the MEW scaffolds, the scaffold was held horizontally, and the PEG intermediate solution was pipetted into the interior of the tubular scaffold. The DTT solution was then added dropwise to the interior scaffold to crosslink the hydrogel, after which the MEW scaffold was rotated such that the hydrogel would uniformly fill the interior of the tube. The scaffold was suspended for at least 10 minutes to allow the DTT to fully crosslink with the available maleimides. The scaffold-reinforced hydrogels were then transferred to 2 mL centrifuge tubes and submerged in 1 mL of PBS. The PBS was exchanged with fresh PBS 3 times every 12 hours to remove unreacted DTT.

Lyophilization of affibody-conjugated hydrogels

Scaffold-reinforced hydrogels with and without affibodies were lyophilized to investigate the effect of lyophilization on their mechanical and release properties, and potential for long-term storage. Hydrogels were transferred to a dry petri dish and flash-frozen with liquid nitrogen. The frozen hydrogels were lyophilized at -104 °C and 50 mTorr for 12 hours using a SP Scientific ZG benchtop lyophilizer. After lyophilization, the hydrogels were stored at 4 °C until use.
To rehydrate the hydrogels, 130 µL was added to the lyophilized product.

Mechanical and rheological characterization of reinforced hydrogels

Compressive testing was performed on hydrogels, MEW scaffolds, and scaffold-reinforced hydrogels using a DHR-2 hybrid rheometer (TA Instruments). 100 µL PEG-mal hydrogels were

cast in 8 mm diameter silicone molds to form discs, which were used to investigate the baseline mechanical properties of the hydrogels. Radial compressive testing of tubular MEW scaffolds, non-reinforced hydrogels, and scaffold-reinforced hydrogels was used to evaluate the interactions between the two materials. Hydrogels were compressed to 98% of their original height at loading on the DHR-2 at a rate of 10 μm/s. Hydrogel stiffness was calculated as the slope of the stress vs. strain curve to 10% compression.

Hydrogels were subjected to cyclic compressive loading experiments to determine if scaffold reinforcement would reduce hydrogel failure incidence and affect recovery from compression. Hydrogels with/without scaffold-reinforcement were compressed 8 times successively at increasing increments of 500 μm (final compression = 4000 μm) at a rate of 250 μm/s, held for 60 s, and decompressed to their initial height.

Controlled protein release from MEW scaffold-reinforced hydrogels

To assess the effects of the MEW scaffold on protein release, affibody-conjugated hydrogels were fabricated with and without MEW scaffold reinforcement, washed to remove excess DTT, and loaded with 100 ng of BMP-2 (R&D Biotechne) (~4×10^{-12} mol). Hydrogels were synthesized without affibodies, with 2 nmol of low-affinity BMP-2-specific affibody, or with 2 nmol of high-affinity BMP-2-specific affibody to achieve 500 molar excess of affibody to BMP-2, which we have demonstrated reduces the rate and total amount of protein released from PEG-mal hydrogels.[300] 20 μL of 5 μg/mL BMP-2 in PBS was added to the hydrogels for 30 minutes to mimic clinically relevant protein loading protocols.[448] 200 μL of 0.1% bovine serum albumin (BSA) in PBS were added each hydrogel and immediately removed to quantify the amount of BMP-2 loaded (i.e., encapsulation efficiency). 1 mL of 10% fetal bovine serum (FBS) (Gibco) in PBS was added to each hydrogel, and 200 μL of FBS solution were immediately removed to quantify initial protein release. 200 μL of fresh FBS solution was replaced, and 200 μL aliquots were similarly taken for 7 days. Encapsulation efficiency and protein release were quantified by BMP-2-specific enzyme linked immunosorbent assays (ELISA) (R&D Biotechne). In additional to cumulative protein release over time, the mechanism of protein release was determined by fitting the release data to the Korsemeyer-Peppas model (Equation 6.3), where M_t/M_∞ is the fraction of BMP-2 released at time t (in seconds), K is the effective diffusivity rate, and n is the diffusion exponent that indicates the mechanism of transport.[403,449] Data was fitted to $M_t/M_\infty \leq$

0.6, and the effective diffusion rate of protein from each hydrogel formulation was identified as the slope of the curve.[403,449]

Equation 6.3: Korsmeyer-Peppas diffusion model

$$\frac{M_t}{M_\infty} = Kt^n$$

Mechanical and rheological characterization of lyophilized hydrogels

Compressive testing was performed on fresh and lyophilized and rehydrated scaffold-reinforced hydrogels using a DHR-2 hybrid rheometer as described above. 100 µL scaffold-reinforced PEG-mal without affibodies or with 2 nmol high-affinity BMP-2-specific affibodies were synthesized and purified. Fresh hydrogels were stored in PBS at 4 °C until experimentation, while lyophilized hydrogels were rehydrated in PBS 30 minutes prior to assessment. Hydrogels were compressed to 98% of their original height at loading on the DHR-2 at a rate of 10 µm/s. Hydrogel stiffness was calculated as the slope of the stress vs. strain curve to 10% compression.

Controlled protein release from lyophilized hydrogels

To assess the effects of lyophilization on protein release, MEW-reinforced hydrogels were fabricated as described without affibodies, with 2 nmol of low-affinity BMP-2 affibody, or with high-affinity BMP-2 affibody, and washed to remove excess DTT. A control group was stored in PBS at 4 °C for 48 hours, and a treatment group was flash frozen, lyophilized, and stored dry as described for 48 hours. Hydrogels were transferred into dry 2 mL microcentrifuge tubes and loaded with 100 ng of BMP-2 for 30 minutes. For control hydrogels, a 20 µL of 5 µg/mL BMP-2 in PBS was added, and for the lyophilized groups, the hydrogels were fully rehydrated in a 130 µL solution of 0.633 µg/mL BMP-2 in PBS. Encapsulation efficiency and protein release were performed as described above.

In vivo implantation of scaffold-reinforced hydrogels

MEW scaffold-reinforced hydrogels were implanted subcutaneously in the back of female Sprague Dawley rats (Charles River Laboratories) to investigate local protein retention in vivo.

BMP-2 was fluorescently labeled with IRDye 800CW NHS Ester (Licor) according to the manufacturer's protocols. 150 µL of affibody-conjugated hydrogels were prepared in 8 mm long scaffolds. The hydrogels were functionalized with 1 mM RGD to promote cell infiltration and 38 nmol of high- or low-affinity BMP-2-specific affibodies to control the release of 2 µg of BMP-2. 20 µL of 0.1 mg/mL fluorescent BMP-2 were added on top of the hydrogels and allowed to soak into the hydrogel network in the dark for 3 hours. All reagents were sterile-filtered through a 0.22 µm filter and handled in a biosafety cabinet using aseptic techniques.

All animal procedures were approved by and conducted in accordance with the University of Oregon's Institutional Animal Care and Use Committee (IACUC). 5-6 week old female Sprague Dawley rats were prepared for surgery using sterile technique and anesthetized using isoflurane. Their backs and sides were shaved and cleaned using isopropyl rubbing alcohol and chlorohexidine. Two 1.5 cm incisions were made along the back of each rat, and four subcutaneous pockets were created near their hips and shoulders as previously described.[64] Fluorescent BMP-2-loaded scaffold-reinforced hydrogels were implanted in the subcutaneous pockets, and the incisions were closed with wound clips. Placement of the hydrogels from each treatment group were randomized according to location.

After 21 days, the rats were euthanized, and the hydrogels were explanted from the subcutaneous space and transferred to a 24 well plate. Fluorescent images were taken of the hydrogels using a Spectrum In Vivo Imaging System (IVIS) (Perkin Elmer) with 745 nm excitation and 800 nm emission wavelengths. To quantify fluorescent signal, regions of interest (ROIs) were drawn around each hydrogel, total radiant efficiency was measured, and background signal was subtracted.

In vivo mineralization of scaffold-reinforced hydrogels

MEW-reinforced hydrogels were implanted in femoral defects of rats to investigate whether localized protein retention would affect protein bioactivity. 150 µL MEW-reinforced hydrogels were synthesized with 1 mM RGD adhesive peptide and 0 or 96 nmol high-affinity BMP-2 affibody, and crosslinked with VPM. The hydrogels were washed 3 times, as described above, and loaded with 5 µg of BMP-2. All preparations were performed using sterile technique.

12-13 week-old female Sprague Dawley rats (Charles River Laboratories) underwent a unilateral femoral defect surgery, as previously described.[215] Briefly, rats were anesthetized, administered

analgesic, and prepared for surgery. An incision was made in the upper half of the hind left leg, and the femur was exposed and cleaned of fascia. A C-clamp was used to secure stainless steel risers and a polysulfone fixation plate (to the femur, followed by drilling of four holes. The risers and fixation plates were screwed into the femur, and 6-mm-wide defects were created using a surgical saw. Hydrogels were fitted into the defect with the excess mesh behaving as a sleeve. The defects were closed using resorbable sutures internally, non-resorbable sutures externally, and additional wound clips and metronidazole paste. Rats were observed postoperatively for any complications.

Longitudinal radiographs were collected at 4, 8, and 12 weeks after surgery (Faxitron MX-20; 37 kV, 7 s). Micro-Computed Tomography (micro-CT) was performed at the same intervals (VivaCT 80, Scanco Medical; 48 µm voxel, 55 kVp, 145 µA, 750 ms integration time for in vivo scans, and 24 µm voxel, 55 kVp, 145 µA, 750 ms integration time for ex vivo scans). Mineral was quantified within the central 5 mm of the defects.

Statistical Analysis

Compressive testing data were analyzed using MATLAB scripts to isolate the modulus and yield point. SEM images were analyzed using ImageJ to determine fiber diameters and pore sizes. Statistical significance of each experiment was determined by performing a one-way ANOVA or two-way ANOVA as applicable, n = 3 or 4, as indicated, and Tukey post-hoc test. Non-parametric t-tests were performed on the femoral defect micro-CT data, n=3 or 4. Power analysis was performed using G-Power version 3.1.9.7.

Results

Chapter 7 PEG-mal hydrogels can be uniformly synthesized within MEW scaffolds

Diamond-pore cylindrical scaffolds with a diameter of 5 mm and height of 5 mm or 7.5 mm were successfully printed using melt-electrowriting on a custom AeroTech 3200 platform (Figure 6.1A). The heights of the scaffolds differed from the designed heights due to printing above the critical translation speed of the jet, resulting in a shortening of the scaffolds.[437,450] SEM images confirmed that the scaffolds had a diamond pore design (Figure 6.1B), with fiber thickness of

29.45 ± 2.147 μm and a pore area of 0.45 ± 0.03 mm^2, as determined by image analysis (Figure 6.1C,D).

To introduce MEW scaffold reinforcement to the hydrogels, 4-arm PEG-mal was mixed with affibodies and/or RGD peptides, and the precursor PEG-mal solution was pipetted into the cylindrical scaffold. In order to ensure the precursor solution remained within the scaffold, the scaffolds were held horizontally with tweezers. Upon the addition of the DTT, the solutions were rotated horizontally to fill the space of the cylindrical scaffold (Figure 6.1E-H). Crosslinking began to occur quickly (within 10 seconds), and the scaffolds were suspended for an additional 10 minutes to ensure the DTT could fully crosslink the available maleimides. **Supplemental video S1** demonstrates the complete reinforced hydrogel fabrication process. The 5 mm height scaffolds were used to synthesize 100 μL hydrogels, and the 7.5 mm height scaffolds were used to synthesize 150 μL hydrogels.

MEW scaffolds improve hydrogel integrity without affecting stiffness

MEW scaffolds and the hydrogels within/without scaffolds were subjected to compression tests to determine the effect of scaffold reinforcement on the bulk mechanical properties of the hydrogels (Figure 6.2A). MEW scaffold alone exhibited a mean stiffness of 96.4±23.9 Pa, while the non-reinforced hydrogels displayed an elastic modulus of 159.1±29.02 Pa without affibodies and 153.4±34.8 Pa with affibodies, and the reinforced hydrogels displayed an elastic modulus of 210.1±109.0 Pa without affibodies and 209.2±55.73 Pa with affibodies (Figure 6.2B). All of these stiffnesses were comparable, demonstrating that the addition of the MEW scaffold reinforcement does not impact the stiffness of the PEG-mal hydrogels. At low compressions, the effects of the MEW scaffold are minimal, and since the reagents used to synthesize the hydrogels are unchanged the mechanical properties are expected to be unaffected. At 75% compressive strain, the reinforced hydrogels exhibited a higher stress than the non-reinforced hydrogels and MEW scaffolds (Figure 6.2C).

The non-reinforced hydrogels yielded at approximately 1 kPa, whereas the reinforced hydrogels yielded at approximately 30 kPa. Such trends have been demonstrated in literature,[432] where hydrogels were formed around 3-dimensional MEW scaffolds. However, this is the first time that hydrogels have been integrated within hollow cylindrical MEW scaffolds.

Taken together, these results suggest that MEW scaffold reinforcement only affects the amount of stress required to deform the hydrogels beyond 75% of their original structure. Furthermore, reinforced hydrogels are easier to manipulate with surgical forceps without damaging the hydrogel (**Supplemental Video S2)**, which may make them easier to implant than non-reinforced hydrogels.

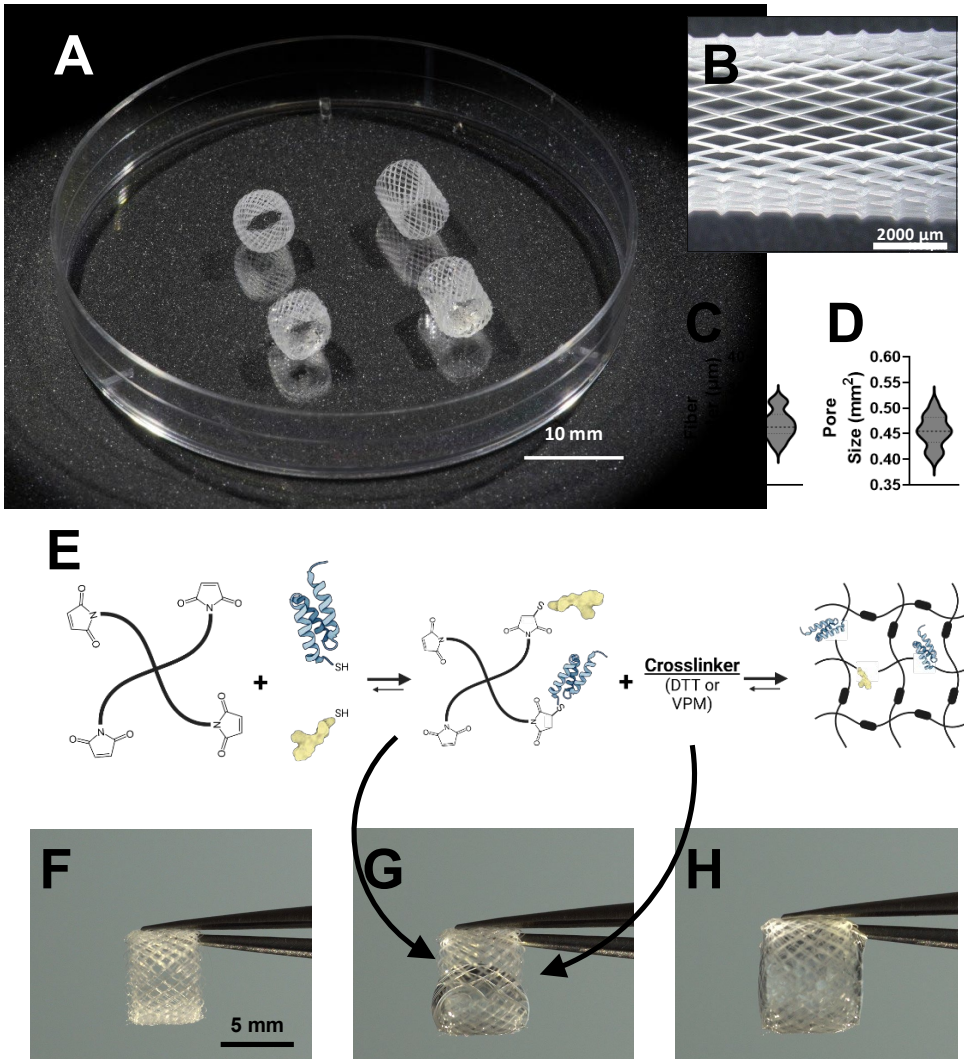


Figure 6.1: Fabrication of MEW scaffolds and scaffold-reinforced hydrogels. A) photograph of tubular MEW scaffolds. B) SEM image of diamond pore MEW scaffold. C) PCL mesh fiber diameter, obtained by ImageJ image analysis. D) Pore sizes of MEW scaffold, analyzed by ImageJ. E) Synthesis schematic for affibody- and RGD-conjugated PEG-mal hydrogels. F-H) photos of MEW scaffold-reinforced PEG-mal hydrogels.

.

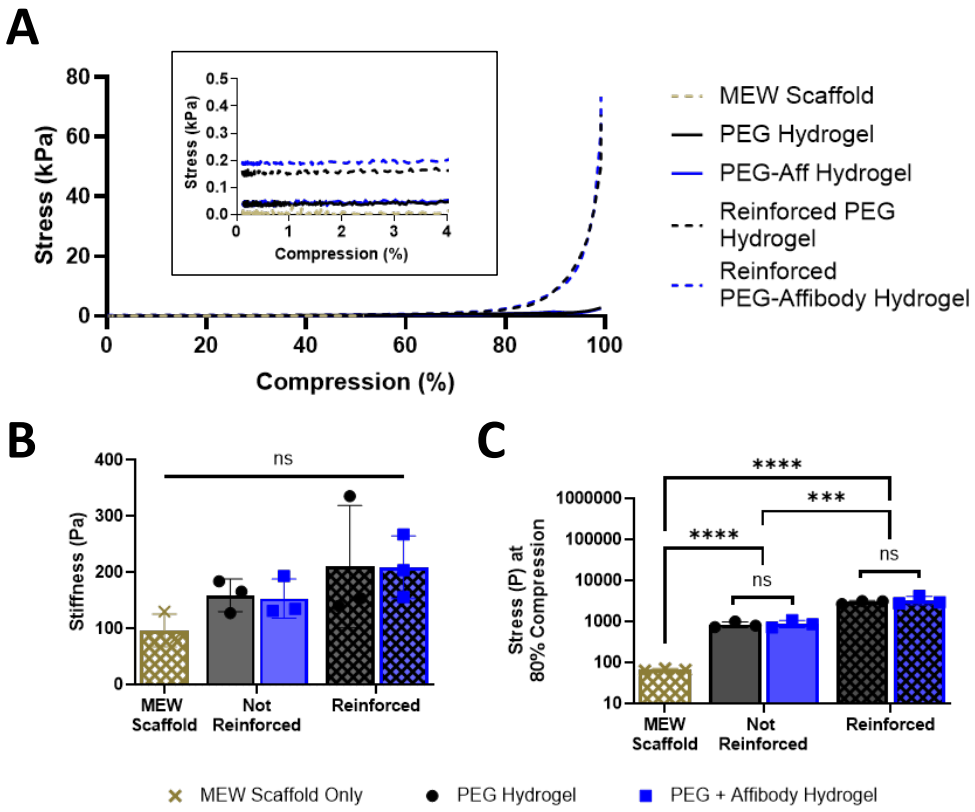


Figure 6.2: Rheological properties of hydrogels with and without MEW scaffold reinforcement and conjugated affibodies. A)Stress vs. compression of hydrogels to 98% of their original height. Inlay plot demonstrating the stress vs. compression at low compression, used for calculating stiffness. B) Stiffness of the MEW scaffold alone, PEG-mal hydrogel alone (with and without affibodies), and scaffold-reinforced hydrogels (with and without affibodies). C) Stress of individual and combined components at high compression (80%). Significance calculated by one way ANOVA with Tukey's post-hoc test. n=3. *** $p<0.001$, **** $p<0.0001$

Effect of affibodies and RGD peptides on hydrogel mesh size

The Equilibrium Swelling Theory was applied to determine the effect of affibody and RGD peptide conjugation on hydrogel mesh size. The mesh size of the PEG-mal hydrogels were not significantly affected by the conjugation of affibodies or RGD peptides and ranged from 144.3-149.6 Å (Figure 6.3), which is similar to other reported mesh sizes for 4-arm PEG-mal hydrogels.[444,451,452] In conjunction with the compression testing result (Figure 2) and the Rubber Elastic Theory, it was determined that the bulk mechanical properties were not affected by the integration of affibodies and RGD together.[444]

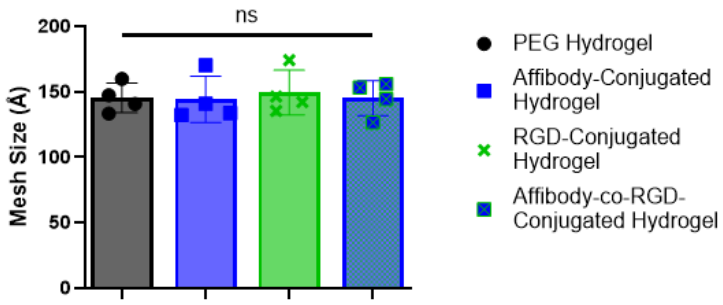


Figure 6.3: Effects of affibody and RGD conjugation on hydrogel mesh size. Significance quantified by one-way ANOVA with Tukey's post-hoc test. n=4. ns= not significant, p>0.05

Scaffold-reinforcement reduce cumulative protein release, but affibodies mitigate these effects

To investigate whether MEW scaffold reinforcement affected protein release from affibody-conjugated hydrogels, non-reinforced and reinforced affibody-conjugated hydrogels were loaded with BMP-2, and the initial encapsulation and subsequent release of BMP-2 from the constructs over 7 days was measured and quantified by ELISA. MEW scaffold reinforcement significantly increased initial BMP-2 encapsulation compared to non-reinforced hydrogels (Figure 6.4A), attributed to an increase in surface area of the cylindrical reinforced hydrogel compared to the planar slab for the non-reinforced hydrogel.[453] Over 7 days, only the affibody-free formulation was affected by scaffold reinforcement (Figure 6.4B). Comparing the affibody-conjugated hydrogels, there was only a significant reduction of protein release from the reinforced low-affinity hydrogel on Day 7, while there was no significant change in protein release in the high-affinity hydrogel over 7 days (Figure 6.4 C,D). This data confirms that mass transport of the hydrogels was affected by hydrogel geometry, and suggests that introducing engineered affinity interactions into the hydrogel reduced the effects of hydrogel geometry.

Cumulative release data were fitted to the Korsmeyer-Peppas release model to determine the mechanism of BMP-2 release from the hydrogels. The values of the diffusion exponent, n, were 0.240 ± 0.026 and 0.277 ± 0.050, for the non-reinforced and reinforced hydrogels, respectively. These values are below the calculated upper bounds of Fickian diffusion (0.50 for slab geometries for the non-reinforced hydrogels, and 0.45 for cylindrical geometries for the

reinforced hydrogels), indicating quasi-Fickian diffusion from the vehicles, suggesting that BMP-2 dissociation from the affibodies significantly contribute to the release rates.[454]

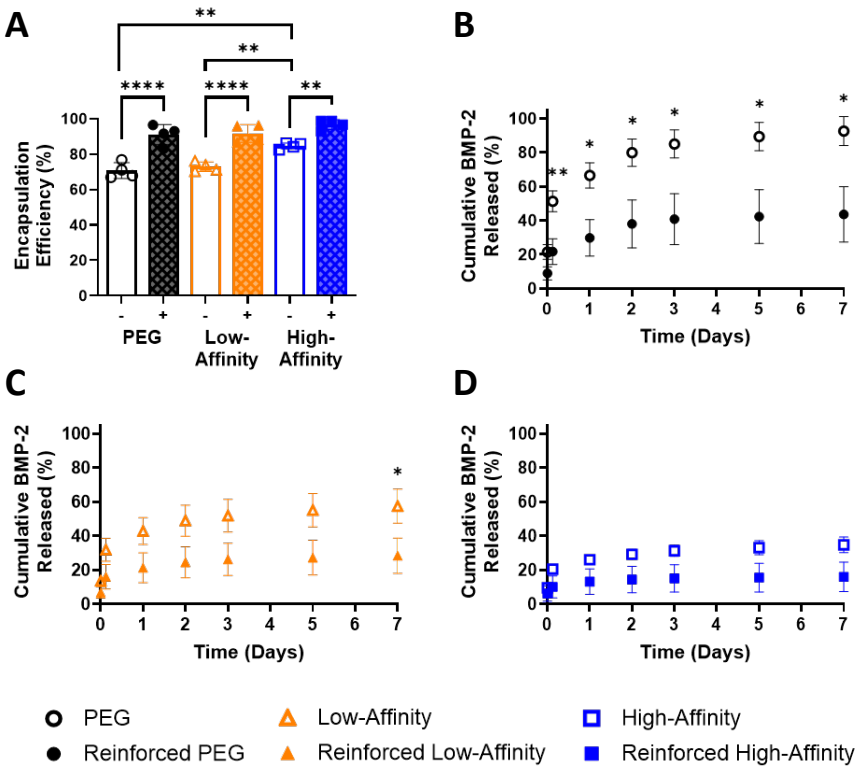


Figure 6.4: Effects of scaffold reinforcement on protein encapsulation and release A) Encapsulation efficiency as a function of hydrogel formulation and scaffold reinforcement. B-D) Release of BMP-2 from scaffold-reinforced and non-reinforced hydrogels loaded with 100 ng of BMP-2 over 1 week, without affibodies (B), with low-affinity BMP-2-specific affibodies (C), and with high-affinity BMP-2-specific affibodies (D). Statistical significance of encapsulation efficiency and controlled release calculated using two-way ANOVA with Tukey's post-hoc test. n=3-4, * $p<0.05$, ** $p<0.01$, *** $p<0.001$, **** $p<0.0001$

Lyophilized hydrogels can be rehydrated while maintaining bulk mechanical properties

Following fabrication, reinforced hydrogels were frozen and lyophilized. Hydrogels without MEW scaffolds did not retain their shape during the lyophilization process, while the reinforced hydrogels largely retained their shape within the confines of the scaffold (Figure 6.5A). Lyophilized hydrogels were rehydrated with PBS and found to uptake approximately 130 µL of liquid within one minute and remain confined within the MEW scaffold (Figure 6.5A-C).

Hydrogels were compressed to 98% after rehydration (Figure 6.5D). The stiffness of the PEG hydrogels was not affected by lyophilization, but the affibody-conjugated hydrogels' elastic modulus was reduced from 186 Pa before lyophilization to 163 Pa after lyophilization (Figure 6.5E). Conversely, neither formulation was affected by lyophilization when considering the stress applied at 80% compression (Figure 6.5F). Upon rehydration, the mesh size of the lyophilized hydrogels was reduced to ~60 Å compared to ~140 Å in the fresh affibody-conjugated hydrogels, as quantified by the Equilibrium Swelling Theory (Figure 6.5G). These results indicate that the while the hydrogels' crosslinking network is partly disrupted by the lyophilization process, the MEW scaffold reinforcement is integral to the hydrogel retention and the bulk mechanical properties pertinent for handleability.

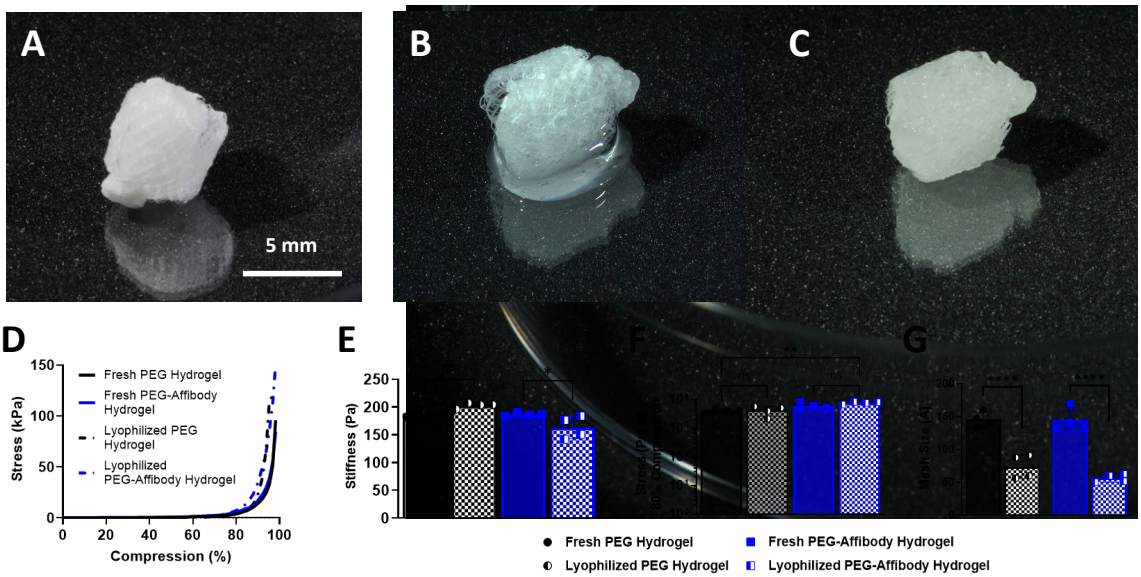


Figure 6.5: Effects of lyophilization and rehydration on mechanical properties of affibody-conjugated hydrogels. A-C) Rehydration of lyophilized hydrogel at 0 seconds (A), 20 seconds (B), and 60 seconds (C). D) Stress vs. compression of hydrogels to 98% of their original height before and after lyophilization and rehydration. E) Stiffness scaffold-reinforced hydrogels with or without hydrogels before and after lyophilization and rehydration. F) Stress of scaffold-reinforced hydrogels with or without affibodies at high compressions (80%) before and after lyophilization and rehydration. G) Mesh size of hydrogels with or without affibodies before and after lyophilization measured by Equilibrium Swelling Theory. Statistical significance quantified by two-way ANOVA with Tukey's post-hoc test. n=4, * $p<0.05$, ** $p<0.01$, **** $p<0.0001$.

Lyophilized hydrogels release more BMP-2 than fresh hydrogels, but at similar rates of release

Controlled protein release was compared between lyophilized hydrogels and fresh affibody-conjugated hydrogels (Figure 6.6A-C). Affibody-conjugated hydrogels were loaded with 100 ng of BMP-2 for a clinically relevant 30 minutes[448]; fresh hydrogels used 20 µL of 5 µg/mL BMP-2 in PBS, and lyophilized hydrogels were rehydrated with 130 µL of 0.769 µg/mL BMP-2 in PBS. Significant differences in release were only observed at the 3 hour timepoints for the PEG-only and high-affinity affibody formulations. The fresh and lyophilized high-affinity affibody formulations released significantly less BMP-2 than the fresh PEG-only formulation, consistent with previous experiments.[300,353] This data suggests that the high-affinity affibody-conjugated hydrogel retains its affinity interactions after lyophilization and behaves comparably to its fresh counterpart. By comparison, release from the lyophilized PEG-only formulation was not significantly different from the lyophilized high-affinity formulation. Taken together, this data could indicate that affibody-free hydrogels will have greater variability in release when lyophilized due to the absence of affinity interactions. There was no notable difference in effective protein diffusivity rates of BMP-2 between fresh and lyophilized equivalent hydrogel formulations, and the lyophilized high-affinity affibody hydrogel had a significantly lower diffusivity than the affibody-free controls (Figure 6.6D). This suggests that the affibodies remain functional and conjugated to the hydrogel even after lyophilization, and this is more likely a bulk material deterioration.

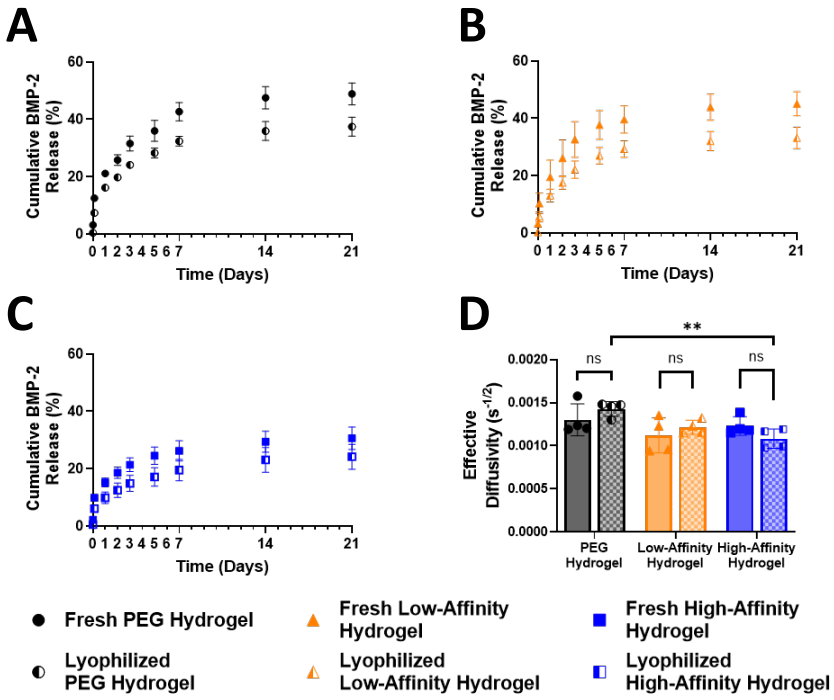


Figure 6.6: BMP-2 release from fresh and lyophilized hydrogels. A) Release from affibody-free hydrogels. B) Low-affinity affibody-conjugated hydrogel. C) High-affinity affibody-conjugated hydrogels. D) Effective diffusivity of BMP-2 from all fresh and lyophilized affibody-conjugated hydrogels calculated by the Korsmeyer-Peppas model. Stastistical significance for all data was quantified by two-way ANOVA with Tukey's post-hoc test. n=4, * $p<0.05$, ** $p<0.01$.

Affibody-conjugation leads to prolonged localized protein retention in vivo

To investigate localized protein retention in vivo, fluorescently labeled BMP-2 was loaded into 150 µL scaffold-reinforced affibody-conjugated hydrogels, and implanted in the subcutaneous space of 5-6 week old female Sprague Dawley rats. The fluorescent degree of labeling of BMP-2 was 3.86 per calculations from the manufacturer's protocols. No adverse effects were observed post operatively. After 3 weeks, the rats were euthanized, and the hydrogels were explanted. Hydrogels were photographed and fluorescently imaged (745/800 nm excitation/emission) (Figure 6.7A). The high-affinity BMP-2 affibody was shown to retain significantly more BMP-2 than both the low-affinity and the affibody-free control (Figure 6.7B).

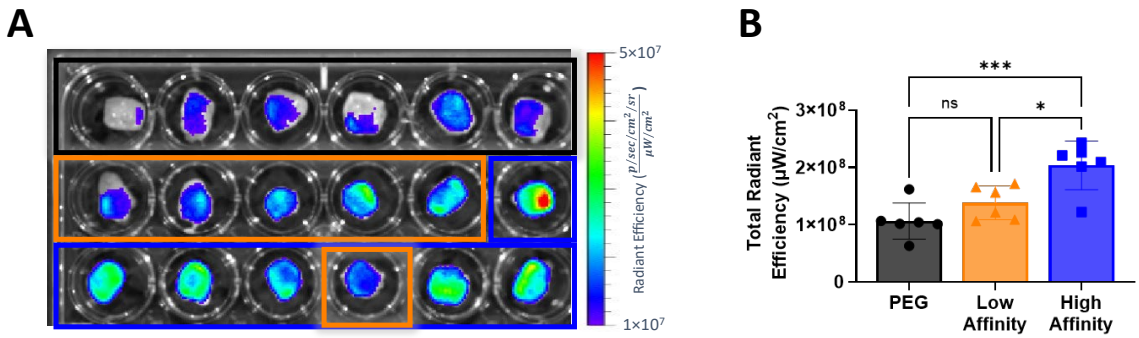


Figure 6.7: Retention of fluorescently labeled BMP-2 in scaffold-reinforced affibody-conjugated hydrogels 3 weeks after in vivo implantation in subcutaneous pockets on the backs of rats. A) Photograph of excised hydrogels with fluorescent signal overlay (745 nm/800 nm excitation and emission for 2 seconds) measured by radiant efficiency. Top row is affibody-free hydrogels. Low-affinity and high-affinity affibody-conjugated hydrogels are in orange and yellow, respectively. B) Total radiant efficiency of the excised hydrogels. Statistical significance quantified by one-way ANOVA with Tukey's post-hoc test. n=6, * $p<0.05$, *** $p<0.001$

Affibody-conjugated hydrogels do not inhibit BMP-2 activity in the regeneration of bone

Affibody-free hydrogels and high-affinity affibody-conjugated hydrogels were loaded with 5 µg of BMP-2 and implanted in 6-mm full-thickness femoral defects in 9 rats (Figure 6.8A). After 2 weeks, two rats were euthanized due to fixation plate failures. It was noted that these rats were the smallest in the study (<210 g). Longitudinal radiographs and micro-CT scans were taken at 4, 8, and 12 weeks. 3 of the 4 rats treated with the affibody-conjugated hydrogels exhibited bone bridging, and 1 of the 3 rats treated with affibody-free hydrogels exhibited bone bridging (Figure 6.8B-O). The central 5 mm of the defect were analyzed by µCT for bone formation, demonstrating progressive bone growth, measured by bone volume in mm^3 (Figure 6.8P) and mineral density in mg of hydroxyapatite per cm^3 (Figure 6.8Q). There was no difference between the affibody-conjugated and affibody-free treatments at any timepoints; however, the affibody-conjugated formulations had greater bone growth between the 4- and 8-week timepoints, suggesting greater early growth. Previous work had demonstrated that affibody-bound BMP-2 inhibited alkaline phosphatase activity in vitro, suggesting BMP-2 remained inactive while bound to the hydrogel.[300] This pilot study demonstrated sustained activity of BMP-2 in the presence of BMP-2-specific affibodies. With small group sizes, it is difficult to determine the impact of the affibodies on bone regeneration.

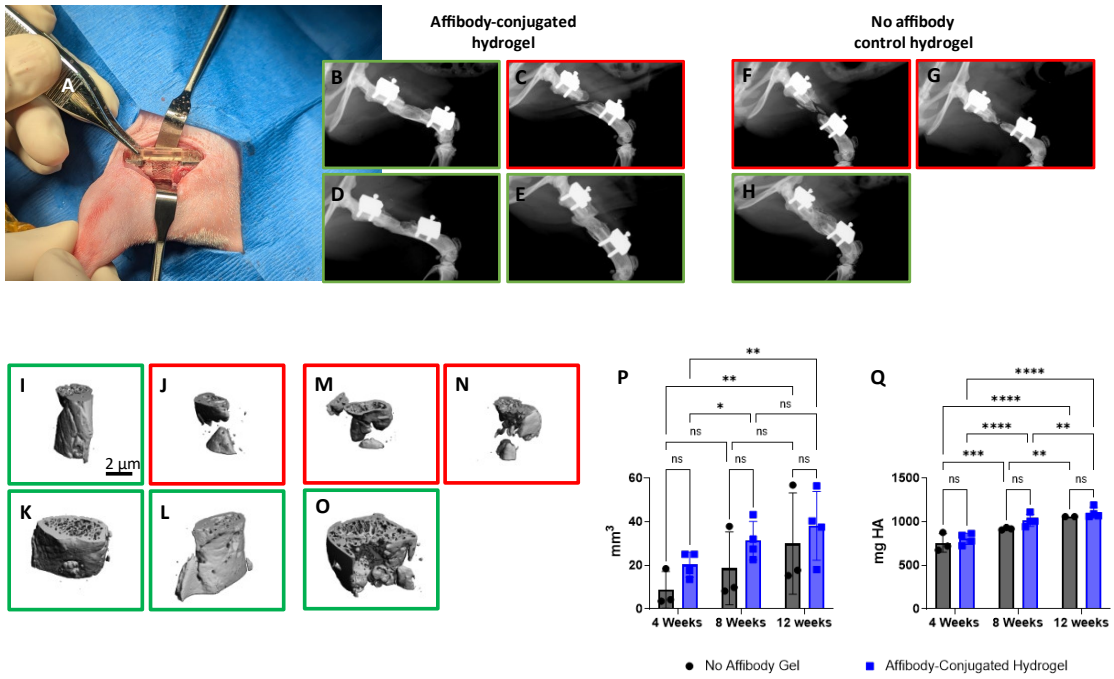


Figure 6.8: Treatment of a 6-mm femoral defect with scaffold-reinforced affibody-conjugated hydrogels loaded with 5 µg of BMP-2. A) Photo of surgical implantation of scaffold-reinforced hydrogels into a femur defect. B-H) X-ray images of rats treated with high-affinity affibody-conjugated hydrogels (B-E) and rats treated with affibody-free hydrogels (F-H) 12 weeks after surgery, imaged at 37 kV for 7 seconds. Green outlines indicate bridging and red outlines indicate non-union. I-O) 3D reconstructions of micro-CT scans of central 5-mm of the defect site 12 weeks after treatment with affibody-conjugated hydrogels (I-L) and affibody-free hydrogels (M-O). P,Q)) Longitudinal assessments of the bone volume (mm^3) (P) and bone mineral density (mg Hydroxyapatite /cm^3) of the central 5-mm of the femoral for 12 weeks of recovery. Statistical significance was measured by a mixed effects Restricted Maximum Likelihood model with Tukey post-hoc test. n=3 or 4, * $p<0.05$, ** $p<0.01$, *** $p<0.001$, **** $p<0.0001$

Discussion

Long bone fractures are a prominent injury that often require surgical intervention to ensure mechanical stabilization.[414] Despite the prevalence of surgical interventions, about 8% of patients experience non-unions and require further surgical interventions and treatment.[413,414] The exogenous supplementation of BMP-2 could be used to promote bone generation at the site of trauma, but carries several fundamental risks, including off-ectopic bone growth due to protein non-localization and lack of control over the protein presentation rates.[194] In this work, we aimed to develop a controlled BMP-2 delivery vehicle that was biocompatible, mechanically robust, and could withstand lyophilization to address challenges associated with cell infiltration for tissue growth, ease of use for surgical implantation and structural integrity in load-bearing

tissue, and broader accessibility and clinical adoption, respectively. To this end, we developed an MEW scaffold-reinforced affibody-conjugated PEG-mal hydrogel for tunable BMP-2 delivery and surgical implantation.

In previous works, we demonstrated that high- and low-affinity BMP-2-specific affibodies could be conjugated to PEG-mal hydrogels in microcentrifuge tubes to adjust BMP-2 delivery and delivery rates.[300] In this work, we adapted the same Michael thiol addition chemistry and leveraged the surface tension between the PEG hydrogel precursors and precision 3D printed PCL tubular scaffolds. This interaction yielded highly reproducible affibody-conjugated PEG-mal hydrogels confined within the scaffold. This innovation overcame challenges associated with inconsistent hydrogel structures that were affected by synthesis in molds. Further, the affibodies retained their function in the scaffold-reinforced hydrogels, slowing the release of BMP-2 based on affinity strength. This demonstrates the versatility of affinity-mediated release, and suggests that affibody-conjugated hydrogels could allow for spatiotemporal precision for protein delivery. The affibody-conjugated hydrogels were soft (~200 Pa), and scaffold-reinforcement did not affect the hydrogels' stiffness at low compressions, but did increase the stress at higher compressions. At these stiffnesses, hydrogels could support cells,[420,421] while the stress shielding from the MEW scaffold allowed for easy handling and manipulation using surgical forceps. The hydrogels' mesh sizes were not affected by the conjugation of affibodies for tuning protein release or RGD for enhanced cell adhesion. Taken together, reinforcing the PEG-mal hydrogel in a MEW scaffold allows for the enhancement of the hydrogel formulation with various cues without affecting the overall structural integrity of the hydrogel. Although other scaffold geometries were not tested in this study, prior research has demonstrated that MEW scaffold mechanical properties could be adapted based on the printing patterns[432,437] and could be used to change the overall strength of the scaffold. It should be noted that the strategy applied in this work was only shown to enhance mechanical properties in compressive regimes, and may require additional engineering if adapting to a material that is expected to deform in other ways. The scaffold-reinforced hydrogels were able to be flash frozen in liquid nitrogen and subsequently lyophilized. In comparison to non-reinforced hydrogels, the scaffold-reinforced hydrogels largely retained their original structure and remained within the confines of the tubular MEW scaffold. The scaffolds could be rehydrated with highly concentrated protein solutions, in a manner similar to the clinically used absorbable collagen sponge for BMP-2 delivery.[455]

Although the rehydrated hydrogels had consistent physical properties with their fresh-made equivalent formulations, the Equilibrium Swelling Theory suggested that lyophilization shrunk the hydrogel pores to approximately half of their original size. However, the Equilibrium Swelling Theory relies on several assumptions such as presumed perfect crosslinking and consistent swelling throughout the hydrogel, and does not account for dangling and unsatisfied chains (including by affibodies and RGD)[456], and may not accurately quantify hydrogel mesh, especially after rehydration from lyophilization. A potential alternative that could characterize the mesh size is the Rubber Elastic Theory, which looks at the storage modulus of the hydrogels. Upon rehydration, the scaffold-reinforced hydrogels also behaved similarly for controlled BMP-2 compared to the fresh products. The rehydrated high-affinity BMP-2 affibody released less protein than the no-affibody control, suggesting that the hydrogels retain their affinity-mediating properties even upon lyophilization.

Scaffold-reinforced affibody-conjugated hydrogels were implanted subcutaneously in the backs of rats. High-affinity affibody-conjugated formulations had significantly higher localized protein retention after 3 weeks compared to low-affinity and affibody-free controls. Further, scaffold-reinforced hydrogels were implanted in a 6-mm femoral defect in rats. After 12 weeks, 3 out of the 4 subjects treated with the affibody-conjugated hydrogel had bony bridging, compared to 1/3 of the affibody-free controls. Together, these results demonstrate the affibody-conjugated hydrogels' potential for localized protein delivery at tunable rates without notable impacts on the therapeutic agent's bioactivity. However, this was a small and underpowered pilot study. An *a priori* power analysis utilizing the μCT results determined that a fully powered study (α=0.1, (1-β)=0.8) would require 20 rats per group. Since the dose used in this study is a healing dose,[457] it may be beneficial to use a lower dose (i.e. 2.5 μg) to more explicitly determine the effects of affibody-conjugation on bone regeneration.

Conclusions

The development of clinically-relevant protein delivery vehicles for bone regeneration remains a challenge, as the hydrogels must deliver proteins at therapeutically-relevant times and rates to mimic the well-coordinated wound healing cascade, be cytocompatible to support cellular infiltration and viability, be mechanically robust to withstand surgical implantation and biologically-relevant stresses, and also be shelf-stable to broaden accessibility. In this work, we

engineer a MEW scaffold-reinforced affibody-conjugated hydrogel to tune BMP-2 delivery and allow for surgical implantation. The engineered hydrogels can also withstand lyophilization, and retaining their mechanical properties and their affinity-mediated release characteristics for tunable protein release. The MEW scaffold is responsible for retaining the mechanical integrity of the hydrogels and the affibodies are responsible for the protein release.

Altogether, scaffold-reinforced affibody-conjugated hydrogels show promise for locally delivering proteins (and potentially other therapeutics) in dynamic biological environments and enabling cells to proliferate, while providing surgeons with a mechanically robust product that can be easily handled and stored for extended periods when not in use. Although additional work is necessary to determine therapeutic protein doses for bone regeneration without causing off-target effects, this work is an invaluable step towards the development of treatment methods that can deliver complex treatments to complex tissue injuries.

Chapter 7 - Conclusions

Wound healing is a well-coordinated process involving many different cell types, which can be subdivided into the stages of inflammation, proliferation, and remodeling. Traumatic injuries, such as long bone fractures, may disrupt the natural healing cascade, resulting in deficient healing and non-unions. To facilitate the regeneration of bone, clinicians may treat patients with supraphysiological concentrations of BMP-2. However, uncontrolled BMP-2 release from the delivery vehicle may lead to ectopic bone formation, reducing the patient's quality of life. Additionally, supplementing a single protein does not accurately represent the various stages of the healing process. To improve the current treatment, we developed an affinity-mediated controlled delivery vehicle to deliver the anti-inflammatory cytokine IL-4 and the osteogenic BMP-2. Using affibodies, we looked to create a surgically implantable hydrogel that can locally deliver IL-4 and BMP-2 at independent rates, support cell infiltration, and withstand surgical handling.

We identified affibodies specific to the anti-inflammatory cytokine IL-4, as well as the osteogenic protein BMP-2 from a yeast surface display library encoded for 4×108 unique affibodies. We characterized these affibodies using various methods, including SDS-PAGE and mass spectrometry to find their size, CD to determine their secondary structures, and flow cytometry and BLI to characterize their binding strengths. We identified 11 BMP-2-specific affibodies and continued to use the strongest and the weakest binder, determined by flow cytometry as high-affinity and low-affinity. Only two unique IL-4-specific affibodies were identified, though flow cytometry could not determine their binding strength due to potential protein aggregation and instability.

Soluble affibodies were recombinantly expressed in BL21 (DE3) E. coli, followed by collection and purification via IMAC. Alternatively, synthetic affibodies were prepared by SPPS and purified by HPLC. All soluble proteins had single prominent peaks around their expected masses, determined by MALDI. The soluble affibodies exhibited characteristically α-helical spectra by CD, which matched the expected folding structure of affibodies. Interestingly, synthetically prepared affibodies had greater signal amplitude on CD than the recombinant affibodies, which we attributed to the absence of highly charged LPS and histidine tags. Indeed, we performed endotoxin assessments on the recombinant and synthetic products and showed that the recombinant affibody contained a significant concentration of LPS. Attempts to purify the

affibodies were unsuccessful, potentially caused by the anionic exchange mechanism of the purification process that would also bind to the hexahistidine tags on the recombinant affibodies. For BMP-2, the equilibrium dissociation constants of the affibodies were similar between the recombinant and synthetic products. For IL-4, the affibodies' equilibrium dissociation constants were more challenging to interpret, as the recombinant low-affinity IL-4 affibody had a stronger affinity for IL-4 in its synthetic form than the recombinant high-affinity affibody's synthetic form.

To predict the affibodies' interactions with their target proteins and rationalize their binding strengths to their target, we utilized the various computational docking algorithms including ZDock, AlphaFold2, and RosettaDock. For BMP-2, the computational predictions suggested that the high-affinity affibody docked to BMP-2 at the wrist epitope by 3 polar contacts and 5 hydrophobic interactions, while the low-affinity affibody docked to BMP-2 at the knuckle epitope via 3 polar contacts and 1 hydrophobic interaction. The wrist and knuckle epitopes are also the docking sites for BMPR-1A and BMPR-II, respectively, which are responsible for the osteogenic differentiation of cells. For IL-4, Affibody_1 (G3-C3) was predicted to dock to IL-4 by 5 electrostatic interactions in a region overlapping the IL4-Rα, while Affibody_2 (G3-C7) was predicted to share 4 electrostatic and 1 hydrophobic interactions with IL-4 with no overlap to any IL-4 receptors. The IL4-Rα is crucial for macrophage polarization to the M2a phenotype. To assess the functions of the affibodies on cellular activities, we cultured C2C12s murine myoblasts with BMP-2 and their respective affibodies, and THP-1 human monocytes with IL-4 and their respective affibodies. When BMP-2 was cultured with C2C12s, the cells differentiated into osteogenic phenotypes and express alkaline phosphatase. The BMP-2-specific affibodies did not induce this differentiation, and C2C12 alkaline phosphatase activity was diminished when the affibodies were mixed with BMP-2 before incubation. This inhibition reinforced the docking predictions for BMP-2-specific affibodies. Regarding IL-4, both M1- and M2-associated genes were upregulated in THP-1s in the presence of soluble Affibody_1, and to a lesser extent in the presence of Affibody_2, though these upregulations were muted when combined with IL-4 prior to incubation. Although further work is required to definitively elucidate the effects of the IL-4-specific affibodies on THP-1s, the in vitro results suggested that affibodies can mediate cell activity guided on their binding interactions with their target protein.

PEG-mal hydrogels conjugated with high- or low-affinity BMP-2 or IL-4 affibodies were synthesized to determine the effect of affibodies on protein release. BMP-2 and IL-4 were released into saline and serum solutions. High-affinity affibodies released less protein than low-affinity and affibody-free hydrogels, as expected. The stronger affibodies with lower equilibrium dissociation constants would have fewer unbound affibody-protein complexes than weaker affibodies and release less protein. BMP-2 release rates, quantified by the Korsmeyer-Peppas model, were slower for the high-affinity BMP-2-specific affibody-conjugated hydrogels than the low-affinity and affibody-free formulations. These results were consistent for IL-4 release from IL-4-specific affibody hydrogels. Recent advances have primarily tuned protein release rates by varying the affinity binders' concentrations in the hydrogels instead of changing the affinity of the binder. Our results demonstrated that tuning protein release without making substantial changes to the hydrogel delivery vehicle network is possible.

To determine which factors impact protein release, we pooled the results of 8 different protein release experiments from affibody-conjugated hydrogels, and fitted the data to least squares and RF models. These experiments varied the type of affibody, concentration of affibody, concentration of additional additives such as the cellular adhesive peptide RGD and affibodies for different proteins, and the release solution. Using least squares fits, we identified that BMP-2 release was primarily modulated by the amount and strength of BMP-2 binding affinities. Release rates were controlled by affibody charge. These models were fitted with relatively high correlations, and the RF predictive model further predicted and validated these results. For IL-4, the release was determined to be affected by the affibody, but the release rates were affected by the IL-4 charge. The IL-4 data was less robust, as there were significant deviations in RF models between the training and validation sets. These results indicated the need for more comprehensive IL-4 controlled release experiments with additional variables and controls. The most significant shortcoming of the developed model was the indirect quantification of dissociation constants of the various hydrogel formulations as well as the use of theoretical charges for affibodies and proteins instead of empirically obtained data. Even with the mentioned limitations of the model, this data indicated that well-characterized affibodies (such as the BMP-2-specific affibodies) may be used to independently tune protein release. These results provided motivations towards using affinity-enhanced biomaterials to independently tune the release of

multiple proteins from a single vehicle to more effectively mimic the wound healing cascade in long bone fractures and other complex injuries.

Lastly, we engineered a mechanically robust affibody-conjugated hydrogel for surgical implantation by synthesizing PEG-mal hydrogels inside precision 3D melt electrowritten PCL tubular scaffolds. The MEW scaffolds reinforced the hydrogels without changing their stiffness. The reinforcement allowed surgeons to handle the hydrogels with less risk of damaging the materials. Additionally, the scaffold-reinforced hydrogels could be lyophilized while retaining the hydrogel polymer network within the scaffold and rehydrated while maintaining most of the bulk mechanical properties. Before and after lyophilization, affibody conjugation in the hydrogels tuned the protein release, as seen previously with high-affinity affibody-conjugated hydrogels slowing the release of BMP-2. By lyophilizing the hydrogels, we can expand global access to affinity-based materials, as we can extend the shelf-life of the hydrogel solutions. Compared to the clinically used absorbable collagen sponges, scaffold-reinforced affibody-conjugated hydrogels may be manipulated without releasing the absorbed therapeutic protein solution. This overcomes potential issues associated with protein leaching from the delivery vehicle, which could result in ectopic bone formation. Indeed, we demonstrated that high-affinity BMP-2-specific affibody-conjugated hydrogels loaded with fluorescent BMP-2 retained more protein locally in vivo in rats over a 3-week period. In a 6-mm femoral defect pilot study, 3 of 4 rats treated with BMP-2 loaded affibody-conjugated hydrogels had bone bridging, but only 1 of 3 rats treated with BMP_2 loaded affibody-free controls had bone bridging. A follow-up study with more rats is required to ensure that the localization and controlled release of BMP-2 from affibody-conjugated hydrogels aids bone regeneration. Reinforcing affibody-conjugated hydrogels within MEW scaffolds broadens the applicability of affinity-mediated protein delivery, demonstrating the potential of using affinity-based materials to localize proteins at the site of trauma and tuning their release in a predictable manner. By lyophilizing the hydrogels, we are able to overcome a key limitation of affinity-based materials involving affibody stability and proteins, more generally.

In the immediate future, there are several studies and experiments that could be performed to further validate and expand upon this work. For BMP-2, a more comprehensive in vivo study involving more rats could be used to confirm that affibodies aid in the localization of BMP-2 and improve bone bridging outcomes. The 5-µg dose of rhBMP-2 used for treating the rats in Chapter

6 was considered a healing dose,[457] so a lower dose of 2.5 μg may help to localize the BMP-2 and separate the groups. Improving healing outcomes at lower doses of BMP-2 would also be valuable to reduce the potential for protein leaching and off-target effects.[194] Including a treatment group of hydrogels without MEW scaffold reinforcement would enable us to assess whether the MEW scaffold-reinforcement is necessary for the retention of the bulk hydrogel at the site of trauma. Studies have demonstrated that the stiffness of the stabilizing plate in a femoral defect affects the healing outcomes.[418] These results suggest that the difference in bulk hydrogel mechanical properties from the MEW scaffold could impact healing, such that the stress shielding may improve healing outcomes. More far-reaching studies could be performed with different hydrogels. As described in Chapter 1, the hydrogel material choice may determine the efficacy of the therapeutic.[458] To screen the function of different materials, a design of experiments approach would be valuable[459], utilizing a synthetic hydrogels such as PEG or more complex functional hydrogels such as polyacrboxybetaine (zwitterionic hydrogel that can be used to influence MSC differentiation by the addition of different biochemical cues[460]), as well as biologically derived hydrogels such as hyaluronic acid and gelatin.

For IL-4, the immediate next step is to perform controlled release experiments with varying amounts of Affibody_1 and Affibody_2 to determine a threshold concentration of affibodies to effectively tune IL-4 release. This data could be subsequently input into the statistical model to improve the confidence of the fits, and guide future formulation planning. Additional THP-1 studies should also be performed to understand macrophage response to the affibodies. However, macrophage polarization is a temporally complex process, and analyzing the cells at 72 hours does not effectively investigate cell behavior in response to affibodies and protein release at different time scales.[363,461] Performing longitudinal polarization studies on THP-1s or other macrophage cells (such as peripheral blood mononuclear cells[462]) would provide context to the affibody polarization rate, and the potential hybrid M1/M2 states that were observed. To modulate the immune response, it is integral to control the rate of macrophage polarization.[340] It is possible to study macrophage plasticity in the presence of different affibodies and other stimuli. Previous studies have aimed to co-deliver IL-4 and GM-CSF at different rates to polarize M0s into M1s and then M2s.[348] New literature indicates that macrophages may transition from the M2a and M2b to other macrophage phenotypes under appropriate stimulus.[330] Using GM-CSF- and IL-4-specific affibodies to deliver the opposing factors in a controlled and independent manner would establish

a new tool to modulate the inflammatory response for patients suffering from dysregulated immune systems.[339]

Lastly, a single cell line does not capture the complexity of the bone healing environment. Macrophage-BMSC in vitro co-cultures have been used to uncover the interplay of the inflammatory response and generation of bone.[463–465] Researchers have demonstrated controlled secretion of IL-4 affected macrophage polarization and increased Alizarin Red staining in MSCs in vitro, indicating a potential treatment protocol for bone growth at early or late stages of regeneration.[464] Once a well-defined codelivery formulation is established, dual-affibody-conjugated hydrogels could be used to deliver IL-4 and BMP-2 in sequence to modulate macrophage polarization and stem cell osteogenic differentiation.

The results presented in this work contribute to the field of affinity-mediate protein release by demonstrating that affibody affinity could be used to tune independent protein release, and that affibody-conjugated hydrogel formulations could retain their controlled release properties. This work also illustrates that protein docking may be used to predict how affibodies will behave in vitro and in vivo. Altogether, this work provides a valuable initial step towards the implementation of affibody-conjugated hydrogels to treat complex long bone fractures more effectively than current clinical methods.

BIBLIOGRAPHY

(1) Gaharwar, A. K.; Singh, I.; Khademhosseini, A. Engineered Biomaterials for in Situ Tissue Regeneration. *Nature Reviews Materials* **2020**, *5* (9), 686–705. https://doi.org/10.1038/s41578-020-0209-x.

(2) Guo, S.; DiPietro, L. A. Factors Affecting Wound Healing. *J Dent Res* **2010**, *89* (3), 219–229. https://doi.org/10.1177/0022034509359125.

(3) Ho, M. T.; Teal, C. J.; Shoichet, M. S. A Hyaluronan/Methylcellulose-Based Hydrogel for Local Cell and Biomolecule Delivery to the Central Nervous System. *Brain Research Bulletin* **2019**, *148*, 46–54. https://doi.org/10.1016/j.brainresbull.2019.03.005.

(4) Sinno, H.; Prakash, S. Complements and the Wound Healing Cascade: An Updated Review. *Plast Surg Int* **2013**, *2013*. https://doi.org/10.1155/2013/146764.

(5) Rand, E.; Gellhorn, A. C. The Healing Cascade: Facilitating and Optimizing the System. *Physical Medicine and Rehabilitation Clinics* **2016**, *27* (4), 765–781. https://doi.org/10.1016/j.pmr.2016.07.001.

(6) Mehta, M.; Schmidt-Bleek, K.; Duda, G. N.; Mooney, D. J. Biomaterial Delivery of Morphogens to Mimic the Natural Healing Cascade in Bone. *Advanced Drug Delivery Reviews* **2012**, *64* (12), 1257–1276. https://doi.org/10.1016/j.addr.2012.05.006.

(7) Ellis, S.; Lin, E. J.; Tartar, D. Immunology of Wound Healing. *Curr Derm Rep* **2018**, *7* (4), 350–358. https://doi.org/10.1007/s13671-018-0234-9.

(8) Bianconi, V.; Sahebkar, A.; Atkin, S. L.; Pirro, M. The Regulation and Importance of Monocyte Chemoattractant Protein-1. *Current Opinion in Hematology* **2018**, *25* (1), 44–51. https://doi.org/10.1097/MOH.0000000000000389.

(9) Ganapathy, N.; Venkataraman, S. S.; Daniel, R.; Aravind, R. J.; Kumarakrishnan, V. B. Molecular Biology of Wound Healing. *J Pharm Bioallied Sci* **2012**, *4* (Suppl 2), S334–S337. https://doi.org/10.4103/0975-7406.100294.

(10) Hettiaratchi, M. H.; Krishnan, L.; Rouse, T.; Chou, C.; McDevitt, T. C.; Guldberg, R. E. Heparin-Mediated Delivery of Bone Morphogenetic Protein-2 Improves Spatial Localization of Bone Regeneration. *Science Advances* **2020**, *6* (1), eaay1240. https://doi.org/10.1126/sciadv.aay1240.

(11) Townsend, J. M.; Sali, G.; Homburg, H. B.; Cassidy, N. T.; Sanders, M. E.; Fung, K.-M.; Andrews, B. T.; Nudo, R. J.; Bohnstedt, B. N.; Detamore, M. S. Thiolated Bone and Tendon Tissue Particles Covalently Bound in Hydrogels for in Vivo Calvarial Bone Regeneration. *Acta Biomaterialia* **2020**, *104*, 66–75. https://doi.org/10.1016/j.actbio.2019.12.035.

(12) Townsend, J. M.; Andrews, B. T.; Feng, Y.; Wang, J.; Nudo, R. J.; Van Kampen, E.; Gehrke, S. H.; Berkland, C. J.; Detamore, M. S. Superior Calvarial Bone Regeneration Using Pentenoate-Functionalized Hyaluronic Acid Hydrogels with Devitalized Tendon Particles. *Acta Biomaterialia* **2018**, *71*, 148–155. https://doi.org/10.1016/j.actbio.2018.02.013.

(13) Chen, R.; Wang, J.; Liu, C. Biomaterials Act as Enhancers of Growth Factors in Bone Regeneration. *Advanced Functional Materials* **2016**, *26* (48), 8810–8823. https://doi.org/10.1002/adfm.201603197.

(14) Cheng, A.; Krishnan, L.; Pradhan, P.; Weinstock, L. D.; Wood, L. B.; Roy, K.; Guldberg, R. E. Impaired Bone Healing Following Treatment of Established Nonunion Correlates with Serum Cytokine Expression. *J Orthop Res* **2019**, *37* (2), 299–307. https://doi.org/10.1002/jor.24186.

(15) Cho, H.; Blatchley, M. R.; Duh, E. J.; Gerecht, S. Acellular and Cellular Approaches to Improve Diabetic Wound Healing. *Advanced Drug Delivery Reviews* **2019**, *146*, 267–288. https://doi.org/10.1016/j.addr.2018.07.019.

(16) Zhai, Z.; Xu, K.; Mei, L.; Wu, C.; Liu, J.; Liu, Z.; Wan, L.; Zhong, W. Co-Assembled Supramolecular Hydrogels of Cell Adhesive Peptide and Alginate for Rapid Hemostasis and Efficacious Wound Healing. *Soft Matter* **2019**, *15* (42), 8603–8610. https://doi.org/10.1039/C9SM01296F.
(17) Bagher, Z.; Atoufi, Z.; Alizadeh, R.; Farhadi, M.; Zarrintaj, P.; Moroni, L.; Setayeshmehr, M.; Komeili, A.; Kamrava, S. K. Conductive Hydrogel Based on Chitosan-Aniline Pentamer/Gelatin/Agarose Significantly Promoted Motor Neuron-like Cells Differentiation of Human Olfactory Ecto-Mesenchymal Stem Cells. *Materials Science and Engineering: C* **2019**, *101*, 243–253. https://doi.org/10.1016/j.msec.2019.03.068.
(18) Shafei, S.; Khanmohammadi, M.; Heidari, R.; Ghanbari, H.; Nooshabadi, V. T.; Farzamfar, S.; Akbariqomi, M.; Sanikhani, N. S.; Absalan, M.; Tavoosidana, G. Exosome Loaded Alginate Hydrogel Promotes Tissue Regeneration in Full-Thickness Skin Wounds: An in Vivo Study. *Journal of Biomedical Materials Research Part A* **2020**, *108* (3), 545–556. https://doi.org/10.1002/jbm.a.36835.
(19) Wen, H.; Li, J.; Payne, G. F.; Feng, Q.; Liang, M.; Chen, J.; Dong, H.; Cao, X. Hierarchical Patterning via Dynamic Sacrificial Printing of Stimuli-Responsive Hydrogels. *Biofabrication* **2020**, *12* (3), 035007. https://doi.org/10.1088/1758-5090/ab7e74.
(20) Kiyotake, E. A.; Douglas, A. W.; Thomas, E. E.; Nimmo, S. L.; Detamore, M. S. Development and Quantitative Characterization of the Precursor Rheology of Hyaluronic Acid Hydrogels for Bioprinting. *Acta Biomaterialia* **2019**, *95*, 176–187. https://doi.org/10.1016/j.actbio.2019.01.041.
(21) Vallmajo-Martin, Q.; Broguiere, N.; Millan, C.; Zenobi-Wong, M.; Ehrbar, M. PEG/HA Hybrid Hydrogels for Biologically and Mechanically Tailorable Bone Marrow Organoids. *Advanced Functional Materials n/a* (n/a), 1910282. https://doi.org/10.1002/adfm.201910282.
(22) Kim, B. S.; Das, S.; Jang, J.; Cho, D.-W. Decellularized Extracellular Matrix-Based Bioinks for Engineering Tissue- and Organ-Specific Microenvironments. *Chem. Rev.* **2020**. https://doi.org/10.1021/acs.chemrev.9b00808.
(23) Aswathy, S. H.; Narendrakumar, U.; Manjubala, I. Commercial Hydrogels for Biomedical Applications. *Heliyon* **2020**, *6* (4). https://doi.org/10.1016/j.heliyon.2020.e03719.
(24) Catoira, M. C.; Fusaro, L.; Di Francesco, D.; Ramella, M.; Boccafoschi, F. Overview of Natural Hydrogels for Regenerative Medicine Applications. *J Mater Sci: Mater Med* **2019**, *30* (10), 115. https://doi.org/10.1007/s10856-019-6318-7.
(25) Žigon-Branc, S.; Markovic, M.; Van Hoorick, J.; Van Vlierberghe, S.; Dubruel, P.; Zerobin, E.; Baudis, S.; Ovsianikov, A. Impact of Hydrogel Stiffness on Differentiation of Human Adipose-Derived Stem Cell Microspheroids. *Tissue Engineering Part A* **2019**, *25* (19–20), 1369–1380. https://doi.org/10.1089/ten.tea.2018.0237.
(26) Caballero Aguilar, L. M.; Silva, S. M.; Moulton, S. E. Growth Factor Delivery: Defining the next Generation Platforms for Tissue Engineering. *Journal of Controlled Release* **2019**, *306*, 40–58. https://doi.org/10.1016/j.jconrel.2019.05.028.
(27) Li, J.; Mooney, D. J. Designing Hydrogels for Controlled Drug Delivery. *Nat Rev Mater* **2016**, *1* (12). https://doi.org/10.1038/natrevmats.2016.71.
(28) Townsend, J. M.; Dennis, S. C.; Whitlow, J.; Feng, Y.; Wang, J.; Andrews, B.; Nudo, R. J.; Detamore, M. S.; Berkland, C. J. Colloidal Gels with Extracellular Matrix Particles and Growth Factors for Bone Regeneration in Critical Size Rat Calvarial Defects. *AAPS J* **2017**, *19* (3), 703–711. https://doi.org/10.1208/s12248-017-0045-0.
(29) Grim, J. C.; Brown, T. E.; Aguado, B. A.; Chapnick, D. A.; Viert, A. L.; Liu, X.; Anseth, K. S. A Reversible and Repeatable Thiol–Ene Bioconjugation for Dynamic Patterning of Signaling Proteins in Hydrogels. *ACS Cent. Sci.* **2018**, *4* (7), 909–916. https://doi.org/10.1021/acscentsci.8b00325.

(30) Ma, F.; Pang, X.; Tang, B. Alginate/Chondroitin Sulfate Based Hybrid Hydrogel with Different Molecular Weight and Its Capacity to Regulate Chondrocytes Activity. *Carbohydrate Polymers* **2019**, *206*, 229–237. https://doi.org/10.1016/j.carbpol.2018.10.109.
(31) Melica, M. E.; La Regina, G.; Parri, M.; Peired, A. J.; Romagnani, P.; Lasagni, L. Substrate Stiffness Modulates Renal Progenitor Cell Properties via a ROCK-Mediated Mechanotransduction Mechanism. *Cells* **2019**, *8* (12), 1561. https://doi.org/10.3390/cells8121561.
(32) Mochizuki, M.; Güç, E.; Park, A. J.; Julier, Z.; Briquez, P. S.; Kuhn, G. A.; Müller, R.; Swartz, M. A.; Hubbell, J. A.; Martino, M. M. Growth Factors with Enhanced Syndecan Binding Generate Tonic Signalling and Promote Tissue Healing. *Nat Biomed Eng* **2020**, *4* (4), 463–475. https://doi.org/10.1038/s41551-019-0469-1.
(33) Page, D. J.; Clarkin, C. E.; Mani, R.; Khan, N. A.; Dawson, J. I.; Evans, N. D. Injectable Nanoclay Gels for Angiogenesis. *Acta Biomaterialia* **2019**, *100*, 378–387. https://doi.org/10.1016/j.actbio.2019.09.023.
(34) Tong, X.; Lee, S.; Bararpour, L.; Yang, F. Long-Term Controlled Protein Release from Poly(Ethylene Glycol) Hydrogels by Modulating Mesh Size and Degradation: Long-Term Controlled Protein Release from Poly(Ethylene Glycol) Hydrogels…. *Macromol. Biosci.* **2015**, *15* (12), 1679–1686. https://doi.org/10.1002/mabi.201500245.
(35) Perera, D.; Medini, M.; Seethamraju, D.; Falkowski, R.; White, K.; Olabisi, R. M. The Effect of Polymer Molecular Weight and Cell Seeding Density on Viability of Cells Entrapped within PEGDA Hydrogel Microspheres. *Journal of Microencapsulation* **2018**, *35* (5), 475–481. https://doi.org/10.1080/02652048.2018.1526341.
(36) Rehmann, M. S.; Skeens, K. M.; Kharkar, P. M.; Ford, E. M.; Maverakis, E.; Lee, K. H.; Kloxin, A. M. Tuning and Predicting Mesh Size and Protein Release from Step Growth Hydrogels. *Biomacromolecules* **2017**, *18* (10), 3131–3142. https://doi.org/10.1021/acs.biomac.7b00781.
(37) Kim, J.; Lima e Silva, R.; Shmueli, R. B.; Mirando, A. C.; Tzeng, S. Y.; Pandey, N. B.; Ben-Akiva, E.; Popel, A. S.; Campochiaro, P. A.; Green, J. J. Anisotropic Poly(Lactic-Co-Glycolic Acid) Microparticles Enable Sustained Release of a Peptide for Long-Term Inhibition of Ocular Neovascularization. *Acta Biomaterialia* **2019**, *97*, 451–460. https://doi.org/10.1016/j.actbio.2019.07.054.
(38) Woodard, L. N.; Grunlan, M. A. Hydrolytic Degradation and Erosion of Polyester Biomaterials. *ACS Macro Lett.* **2018**, *7* (8), 976–982. https://doi.org/10.1021/acsmacrolett.8b00424.
(39) Vey, E.; Rodger, C.; Booth, J.; Claybourn, M.; Miller, A. F.; Saiani, A. Degradation Kinetics of Poly(Lactic-Co-Glycolic) Acid Block Copolymer Cast Films in Phosphate Buffer Solution as Revealed by Infrared and Raman Spectroscopies. *Polymer Degradation and Stability* **2011**, *96* (10), 1882–1889. https://doi.org/10.1016/j.polymdegradstab.2011.07.011.
(40) Amann, L. C.; Gandal, M. J.; Lin, R.; Liang, Y.; Siegel, S. J. In Vitro–In Vivo Correlations of Scalable PLGA-Risperidone Implants for the Treatment of Schizophrenia. *Pharm Res* **2010**, *27* (8), 1730–1737. https://doi.org/10.1007/s11095-010-0152-4.
(41) Choi, D. H.; Park, C. H.; Kim, I. H.; Chun, H. J.; Park, K.; Han, D. K. Fabrication of Core–Shell Microcapsules Using PLGA and Alginate for Dual Growth Factor Delivery System. *Journal of Controlled Release* **2010**, *147* (2), 193–201. https://doi.org/10.1016/j.jconrel.2010.07.103.
(42) Yu, J. R.; Janssen, M.; Liang, B. J.; Huang, H.-C.; Fisher, J. P. A Liposome/Gelatin Methacrylate Nanocomposite Hydrogel System for Delivery of Stromal Cell-Derived Factor-1α and Stimulation of Cell Migration. *Acta Biomaterialia* **2020**, *108*, 67–76. https://doi.org/10.1016/j.actbio.2020.03.015.
(43) Mancipe Castro, L. M.; Sequeira, A.; García, A. J.; Guldberg, R. E. Articular Cartilage- and Synoviocyte-Binding Poly(Ethylene Glycol) Nanocomposite Microgels as Intra-Articular Drug

Delivery Vehicles for the Treatment of Osteoarthritis. *ACS Biomater. Sci. Eng.* **2020**, *6* (9), 5084–5095. https://doi.org/10.1021/acsbiomaterials.0c00960.

(44) Pakulska, M. M.; Elliott Donaghue, I.; Obermeyer, J. M.; Tuladhar, A.; McLaughlin, C. K.; Shendruk, T. N.; Shoichet, M. S. Encapsulation-Free Controlled Release: Electrostatic Adsorption Eliminates the Need for Protein Encapsulation in PLGA Nanoparticles. *Sci. Adv.* **2016**, *2* (5), e1600519. https://doi.org/10.1126/sciadv.1600519.

(45) Rajabi, S.; Jalili-Firoozinezhad, S.; Ashtiani, M. K.; Le Carrou, G.; Tajbakhsh, S.; Baharvand, H. Effect of Chemical Immobilization of SDF-1α into Muscle-Derived Scaffolds on Angiogenesis and Muscle Progenitor Recruitment. *Journal of Tissue Engineering and Regenerative Medicine* **2018**, *12* (1), e438–e450. https://doi.org/10.1002/term.2479.

(46) Singh, A.; Corvelli, M.; Unterman, S. A.; Wepasnick, K. A.; McDonnell, P.; Elisseeff, J. H. Enhanced Lubrication on Tissue and Biomaterial Surfaces through Peptide-Mediated Binding of Hyaluronic Acid. *Nature Mater* **2014**, *13* (10), 988–995. https://doi.org/10.1038/nmat4048.

(47) Tanase, C. E.; Qutachi, O.; White, L. J.; Shakesheff, K. M.; McCaskie, A. W.; Best, S. M.; Cameron, R. E. Targeted Protein Delivery: Carbodiimide Crosslinking Influences Protein Release from Microparticles Incorporated within Collagen Scaffolds. *Regenerative Biomaterials* **2019**, *6* (5), 279–287. https://doi.org/10.1093/rb/rbz015.

(48) Wang, Y.; Lan, H.; Yin, T.; Zhang, X.; Huang, J.; Fu, H.; Huang, J.; McGinty, S.; Gao, H.; Wang, G.; Wang, Z. Covalent Immobilization of Biomolecules on Stent Materials through Mussel Adhesive Protein Coating to Form Biofunctional Films. *Materials Science and Engineering: C* **2020**, *106*, 110187. https://doi.org/10.1016/j.msec.2019.110187.

(49) Petrone, L.; Kumar, A.; Sutanto, C. N.; Patil, N. J.; Kannan, S.; Palaniappan, A.; Amini, S.; Zappone, B.; Verma, C.; Miserez, A. Mussel Adhesion Is Dictated by Time-Regulated Secretion and Molecular Conformation of Mussel Adhesive Proteins. *Nat Commun* **2015**, *6* (1), 8737. https://doi.org/10.1038/ncomms9737.

(50) Bax, D. V.; Davidenko, N.; Hamaia, S. W.; Farndale, R. W.; Best, S. M.; Cameron, R. E. Impact of UV- and Carbodiimide-Based Crosslinking on the Integrin-Binding Properties of Collagen-Based Materials. *Acta Biomaterialia* **2019**, *100*, 280–291. https://doi.org/10.1016/j.actbio.2019.09.046.

(51) Magnan, L.; Labrunie, G.; Fénelon, M.; Dusserre, N.; Foulc, M.-P.; Lafourcade, M.; Svahn, I.; Gontier, E.; Vélez V., J. H.; McAllister, T. N.; L'Heureux, N. Human Textiles: A Cell-Synthesized Yarn as a Truly "Bio" Material for Tissue Engineering Applications. *Acta Biomaterialia* **2020**, *105*, 111–120. https://doi.org/10.1016/j.actbio.2020.01.037.

(52) Lai, J.-Y.; Luo, L.-J.; Ma, D. Effect of Cross-Linking Density on the Structures and Properties of Carbodiimide-Treated Gelatin Matrices as Limbal Stem Cell Niches. *IJMS* **2018**, *19* (11), 3294. https://doi.org/10.3390/ijms19113294.

(53) Murphy, M. C.; Howell, N. K. Effects of the Attachment of Small Molecules by Carbodiimide-Mediated Condensation on the Physicochemical and Functional Properties of Bovine Serum Albumin: Carbodiimide-Mediated Condensation and BSA Properties. *J. Sci. Food Agric.* **1991**, *55* (1), 117–140. https://doi.org/10.1002/jsfa.2740550112.

(54) Yamamoto, S.; Iwamaru, Y.; Shimizu, Y.; Ueda, Y.; Sato, M.; Yamaguchi, K.; Nakanishi, J. Epidermal Growth Factor-Nanoparticle Conjugates Change the Activity from Anti-Apoptotic to pro-Apoptotic at Membrane Rafts. *Acta Biomaterialia* **2019**, *88*, 383–391. https://doi.org/10.1016/j.actbio.2019.02.026.

(55) Vu, C. Q.; Rotkrua, P.; Soontornworajit, B.; Tantirungrotechai, Y. Effect of PDGF-B Aptamer on PDGFRβ/PDGF-B Interaction: Molecular Dynamics Study. *Journal of Molecular Graphics and Modelling* **2018**, *82*, 145–156. https://doi.org/10.1016/j.jmgm.2018.04.012.

(56) Shadish, J. A.; Benuska, G. M.; DeForest, C. A. Bioactive Site-Specifically Modified Proteins for 4D Patterning of Gel Biomaterials. *Nat. Mater.* **2019**, *18* (9), 1005–1014. https://doi.org/10.1038/s41563-019-0367-7.
(57) Hettiaratchi, M. H.; O'Meara, M. J.; Teal, C. J.; Payne, S. L.; Pickering, A. J.; Shoichet, M. S. Local Delivery of Stabilized Chondroitinase ABC Degrades Chondroitin Sulfate Proteoglycans in Stroke-Injured Rat Brains. *Journal of Controlled Release* **2019**, *297*, 14–25. https://doi.org/10.1016/j.jconrel.2019.01.033.
(58) Shadish, J. A.; DeForest, C. A. Site-Selective Protein Modification: From Functionalized Proteins to Functional Biomaterials. *Matter* **2020**, *2* (1), 50–77. https://doi.org/10.1016/j.matt.2019.11.011.
(59) Selleck, S. B. Proteoglycans and Pattern Formation: Sugar Biochemistry Meets Developmental Genetics. *Trends in Genetics* **2000**, *16* (5), 206–212. https://doi.org/10.1016/S0168-9525(00)01997-1.
(60) Shimogori, T. Embryonic Signaling Centers Expressing BMP, WNT and FGF Proteins Interact to Pattern the Cerebral Cortex. *Development* **2004**, *131* (22), 5639–5647. https://doi.org/10.1242/dev.01428.
(61) Kishigami, S.; Mishina, Y. BMP Signaling and Early Embryonic Patterning. *Cytokine & Growth Factor Reviews* **2005**, *16* (3), 265–278. https://doi.org/10.1016/j.cytogfr.2005.04.002.
(62) Miller, T.; Goude, M. C.; McDevitt, T. C.; Temenoff, J. S. Molecular Engineering of Glycosaminoglycan Chemistry for Biomolecule Delivery. *Acta Biomaterialia* **2014**, *10* (4), 1705–1719. https://doi.org/10.1016/j.actbio.2013.09.039.
(63) Tan, G.; Li, J.; Song, Y.; Yu, Y.; Liu, D.; Pan, W. Phenylboronic Acid-Tethered Chondroitin Sulfate-Based Mucoadhesive Nanostructured Lipid Carriers for the Treatment of Dry Eye Syndrome. *Acta Biomaterialia* **2019**, *99*, 350–362. https://doi.org/10.1016/j.actbio.2019.08.035.
(64) Hettiaratchi, M. H.; Rouse, T.; Chou, C.; Krishnan, L.; Stevens, H. Y.; Li, M.-T. A.; McDevitt, T. C.; Guldberg, R. E. Enhanced in Vivo Retention of Low Dose BMP-2 via Heparin Microparticle Delivery Does Not Accelerate Bone Healing in a Critically Sized Femoral Defect. *Acta Biomaterialia* **2017**, *59*, 21–32. https://doi.org/10.1016/j.actbio.2017.06.028.
(65) Meneghetti, M. C. Z.; Hughes, A. J.; Rudd, T. R.; Nader, H. B.; Powell, A. K.; Yates, E. A.; Lima, M. A. Heparan Sulfate and Heparin Interactions with Proteins. *J. R. Soc. Interface* **2015**, *12* (110), 20150589. https://doi.org/10.1098/rsif.2015.0589.
(66) Andrews, S.; Cheng, A.; Stevens, H.; Logun, M. T.; Webb, R.; Jordan, E.; Xia, B.; Karumbaiah, L.; Guldberg, R. E.; Stice, S. Chondroitin Sulfate Glycosaminoglycan Scaffolds for Cell and Recombinant Protein-Based Bone Regeneration. *STEM CELLS Translational Medicine* **2019**, *8* (6), 575–585. https://doi.org/10.1002/sctm.18-0141.
(67) Talaga, M. L.; Fan, N.; Fueri, A. L.; Brown, R. K.; Bandyopadhyay, P.; Dam, T. K. Multitasking Human Lectin Galectin-3 Interacts with Sulfated Glycosaminoglycans and Chondroitin Sulfate Proteoglycans. *Biochemistry* **2016**, *55* (32), 4541–4551. https://doi.org/10.1021/acs.biochem.6b00504.
(68) Abednejad, A.; Ghaee, A.; Morais, E. S.; Sharma, M.; Neves, B. M.; Freire, M. G.; Nourmohammadi, J.; Mehrizi, A. A. Polyvinylidene Fluoride–Hyaluronic Acid Wound Dressing Comprised of Ionic Liquids for Controlled Drug Delivery and Dual Therapeutic Behavior. *Acta Biomaterialia* **2019**, *100*, 142–157. https://doi.org/10.1016/j.actbio.2019.10.007.
(69) Bermejo-Velasco, D.; Kadekar, S.; Tavares da Costa, M. V.; Oommen, O. P.; Gamstedt, K.; Hilborn, J.; Varghese, O. P. First Aldol Cross-Linked Hyaluronic Acid Hydrogel: Fast and Hydrolytically Stable Hydrogel with Tissue Adhesive Properties. *ACS Appl. Mater. Interfaces* **2019**, *11* (41), 38232–38239. https://doi.org/10.1021/acsami.9b10239.

(70) Feng, Q.; Lin, S.; Zhang, K.; Dong, C.; Wu, T.; Huang, H.; Yan, X.; Zhang, L.; Li, G.; Bian, L. Sulfated Hyaluronic Acid Hydrogels with Retarded Degradation and Enhanced Growth Factor Retention Promote hMSC Chondrogenesis and Articular Cartilage Integrity with Reduced Hypertrophy. *Acta Biomaterialia* **2017**, *53*, 329–342. https://doi.org/10.1016/j.actbio.2017.02.015.
(71) Bhattacharyya, A.; Mukherjee, D.; Mishra, R.; Kundu, P. P. Development of pH Sensitive Polyurethane–Alginate Nanoparticles for Safe and Efficient Oral Insulin Delivery in Animal Models. *RSC Adv.* **2016**, *6* (48), 41835–41846. https://doi.org/10.1039/C6RA06749B.
(72) He, Z.; Santos, J. L.; Tian, H.; Huang, H.; Hu, Y.; Liu, L.; Leong, K. W.; Chen, Y.; Mao, H.-Q. Scalable Fabrication of Size-Controlled Chitosan Nanoparticles for Oral Delivery of Insulin. *Biomaterials* **2017**, *130*, 28–41. https://doi.org/10.1016/j.biomaterials.2017.03.028.
(73) Dong, L.; Wang, S.-J.; Zhao, X.-R.; Zhu, Y.-F.; Yu, J.-K. 3D- Printed Poly(ε-Caprolactone) Scaffold Integrated with Cell-Laden Chitosan Hydrogels for Bone Tissue Engineering. *Sci Rep* **2017**, *7* (1), 13412. https://doi.org/10.1038/s41598-017-13838-7.
(74) Pan, Y.; Xiao, C.; Tan, H.; Yuan, G.; Li, J.; Li, S.; Jia, Y.; Xiong, D.; Hu, X.; Niu, X. Covalently Injectable Chitosan/Chondroitin Sulfate Hydrogel Integrated Gelatin/Heparin Microspheres for Soft Tissue Engineering. *International Journal of Polymeric Materials and Polymeric Biomaterials* **2019**, 1–9. https://doi.org/10.1080/00914037.2019.1695210.
(75) Antich, C.; de Vicente, J.; Jiménez, G.; Chocarro, C.; Carrillo, E.; Montañez, E.; Gálvez-Martín, P.; Marchal, J. A. Bio-Inspired Hydrogel Composed of Hyaluronic Acid and Alginate as a Potential Bioink for 3D Bioprinting of Articular Cartilage Engineering Constructs. *Acta Biomaterialia* **2020**, *106*, 114–123. https://doi.org/10.1016/j.actbio.2020.01.046.
(76) Gao, Y.; Sarode, A.; Kokoroskos, N.; Ukidve, A.; Zhao, Z.; Guo, S.; Flaumenhaft, R.; Gupta, A. S.; Saillant, N.; Mitragotri, S. A Polymer-Based Systemic Hemostatic Agent. *Sci. Adv.* **2020**, *6* (31), eaba0588. https://doi.org/10.1126/sciadv.aba0588.
(77) Limasale, Y. D. P.; Atallah, P.; Werner, C.; Freudenberg, U.; Zimmermann, R. Tuning the Local Availability of VEGF within Glycosaminoglycan-Based Hydrogels to Modulate Vascular Endothelial Cell Morphogenesis. *Adv. Funct. Mater.* **2020**, 2000068. https://doi.org/10.1002/adfm.202000068.
(78) Hettiaratchi, M. H.; Miller, T.; Temenoff, J. S.; Guldberg, R. E.; McDevitt, T. C. Heparin Microparticle Effects on Presentation and Bioactivity of Bone Morphogenetic Protein-2. *Biomaterials* **2014**, *35* (25), 7228–7238. https://doi.org/10.1016/j.biomaterials.2014.05.011.
(79) Rinker, T. E.; Philbrick, B. D.; Temenoff, J. S. Core-Shell Microparticles for Protein Sequestration and Controlled Release of a Protein-Laden Core. *Acta Biomaterialia* **2017**, *56*, 91–101. https://doi.org/10.1016/j.actbio.2016.12.042.
(80) Olczyk, P.; Mencner, Ł.; Komosinska-Vassev, K. Diverse Roles of Heparan Sulfate and Heparin in Wound Repair. *BioMed Research International* **2015**, *2015*, 1–7. https://doi.org/10.1155/2015/549417.
(81) Hogwood, J.; Naggi, A.; Torri, G.; Page, C.; Rigsby, P.; Mulloy, B.; Gray, E. The Effect of Increasing the Sulfation Level of Chondroitin Sulfate on Anticoagulant Specific Activity and Activation of the Kinin System. *PLoS ONE* **2018**, *13* (3), e0193482. https://doi.org/10.1371/journal.pone.0193482.
(82) Bhattacharya, D. S.; Svechkarev, D.; Bapat, A.; Patil, P.; Hollingsworth, M. A.; Mohs, A. M. Sulfation Modulates the Targeting Properties of Hyaluronic Acid to P-Selectin and CD44. *ACS Biomater. Sci. Eng.* **2020**, *6* (6), 3585–3598. https://doi.org/10.1021/acsbiomaterials.0c00115.
(83) Peng, Y.; Tellier, L. E.; Temenoff, J. S. Heparin-Based Hydrogels with Tunable Sulfation & Degradation for Anti-Inflammatory Small Molecule Delivery. *Biomater. Sci.* **2016**, *4* (9), 1371–1380. https://doi.org/10.1039/C6BM00455E.

(84) Subbiah, R.; Cheng, A.; Ruehle, M. A.; Hettiaratchi, M. H.; Bertassoni, L. E.; Guldberg, R. E. Effects of Controlled Dual Growth Factor Delivery on Bone Regeneration Following Composite Bone-Muscle Injury. *Acta Biomaterialia* **2020**, *114*, 63–75. https://doi.org/10.1016/j.actbio.2020.07.026.

(85) Zieris, A.; Chwalek, K.; Prokoph, S.; Levental, K. R.; Welzel, P. B.; Freudenberg, U.; Werner, C. Dual Independent Delivery of Pro-Angiogenic Growth Factors from starPEG-Heparin Hydrogels. *Journal of Controlled Release* **2011**, *156* (1), 28–36. https://doi.org/10.1016/j.jconrel.2011.06.042.

(86) Hettiaratchi, M. H.; Chou, C.; Servies, N.; Smeekens, J. M.; Cheng, A.; Esancy, C.; Wu, R.; McDevitt, T. C.; Guldberg, R. E.; Krishnan, L. Competitive Protein Binding Influences Heparin-Based Modulation of Spatial Growth Factor Delivery for Bone Regeneration. *Tissue Engineering Part A* **2017**, *23* (13–14), 683–695. https://doi.org/10.1089/ten.tea.2016.0507.

(87) Casanova, M. R.; Oliveira, C.; Fernandes, E. M.; Reis, R. L.; Silva, T. H.; Martins, A.; Neves, N. M. Spatial Immobilization of Endogenous Growth Factors to Control Vascularization in Bone Tissue Engineering. *Biomater. Sci.* **2020**, *8* (9), 2577–2589. https://doi.org/10.1039/D0BM00087F.

(88) Crispim, J. F.; Fu, S. C.; Lee, Y. W.; Fernandes, H. A. M.; Jonkheijm, P.; Yung, P. S. H.; Saris, D. B. F. Bioactive Tape With BMP-2 Binding Peptides Captures Endogenous Growth Factors and Accelerates Healing After Anterior Cruciate Ligament Reconstruction. *Am J Sports Med* **2018**, *46* (12), 2905–2914. https://doi.org/10.1177/0363546518787507.

(89) Ishihara, J.; Fukunaga, K.; Ishihara, A.; Larsson, H. M.; Potin, L.; Hosseinchi, P.; Galliverti, G.; Swartz, M. A.; Hubbell, J. A. Matrix-Binding Checkpoint Immunotherapies Enhance Antitumor Efficacy and Reduce Adverse Events. *Sci. Transl. Med.* **2017**, *9* (415), eaan0401. https://doi.org/10.1126/scitranslmed.aan0401.

(90) Crispim, J.; Fernandes, H. A. M.; Fu, S. C.; Lee, Y. W.; Jonkheijm, P.; Saris, D. B. F. TGF-B1 Activation in Human Hamstring Cells through Growth Factor Binding Peptides on Polycaprolactone Surfaces. *Acta Biomaterialia* **2017**, *53*, 165–178. https://doi.org/10.1016/j.actbio.2017.01.066.

(91) Katsumata, K.; Ishihara, J.; Mansurov, A.; Ishihara, A.; Raczy, M. M.; Yuba, E.; Hubbell, J. A. Targeting Inflammatory Sites through Collagen Affinity Enhances the Therapeutic Efficacy of Anti-Inflammatory Antibodies. *Sci. Adv.* **2019**, *5* (11), eaay1971. https://doi.org/10.1126/sciadv.aay1971.

(92) Bostock, C.; Teal, C. J.; Dang, M.; Golinski, A. W.; Hackel, B. J.; Shoichet, M. S. Affibody-Mediated Controlled Release of Fibroblast Growth Factor 2. *Journal of Controlled Release* **2022**, *350*, 815–828. https://doi.org/10.1016/j.jconrel.2022.09.004.

(93) Botelho, N. K.; Tschumi, B. O.; Hubbell, J. A.; Swartz, M. A.; Donda, A.; Romero, P. Combination of Synthetic Long Peptides and XCL1 Fusion Proteins Results in Superior Tumor Control. *Front. Immunol.* **2019**, *10*, 294. https://doi.org/10.3389/fimmu.2019.00294.

(94) Romero, P.; Donda, A.; Hubbell, J. A. An Optimized Antigen–Protein Fusion. *Nat Biomed Eng* **2020**, *4* (6), 583–584. https://doi.org/10.1038/s41551-020-0572-3.

(95) Williford, J.-M.; Ishihara, J.; Ishihara, A.; Mansurov, A.; Hosseinchi, P.; Marchell, T. M.; Potin, L.; Swartz, M. A.; Hubbell, J. A. Recruitment of CD103 $^{+}$ Dendritic Cells via Tumor-Targeted Chemokine Delivery Enhances Efficacy of Checkpoint Inhibitor Immunotherapy. *Sci. Adv.* **2019**, *5* (12), eaay1357. https://doi.org/10.1126/sciadv.aay1357.

(96) Delplace, V.; Ortin-Martinez, A.; Tsai, E. L. S.; Amin, A. N.; Wallace, V.; Shoichet, M. S. Controlled Release Strategy Designed for Intravitreal Protein Delivery to the Retina. *Journal of Controlled Release* **2019**, *293*, 10–20. https://doi.org/10.1016/j.jconrel.2018.11.012.

(97) Nori, S.; Khazaei, M.; Ahuja, C. S.; Yokota, K.; Ahlfors, J.-E.; Liu, Y.; Wang, J.; Shibata, S.; Chio, J.; Hettiaratchi, M. H.; Führmann, T.; Shoichet, M. S.; Fehlings, M. G. Human Oligodendrogenic

Neural Progenitor Cells Delivered with Chondroitinase ABC Facilitate Functional Repair of Chronic Spinal Cord Injury. *Stem Cell Reports* **2018**, *11* (6), 1433–1448. https://doi.org/10.1016/j.stemcr.2018.10.017.

(98) Stejskalová, A.; Oliva, N.; England, F. J.; Almquist, B. D. Biologically Inspired, Cell-Selective Release of Aptamer-Trapped Growth Factors by Traction Forces. *Adv. Mater.* **2019**, *31* (7), 1806380. https://doi.org/10.1002/adma.201806380.

(99) Feng, Z.; Wang, H.; Xu, B. Instructed Assembly of Peptides for Intracellular Enzyme Sequestration. *J. Am. Chem. Soc.* **2018**, *140* (48), 16433–16437. https://doi.org/10.1021/jacs.8b10542.

(100) Vulic, K.; Shoichet, M. S. Tunable Growth Factor Delivery from Injectable Hydrogels for Tissue Engineering. *J Am Chem Soc* **2012**, *134* (2), 882–885. https://doi.org/10.1021/ja210638x.

(101) Pakulska, M. M.; Vulic, K.; Shoichet, M. S. Affinity-Based Release of Chondroitinase ABC from a Modified Methylcellulose Hydrogel. *Journal of Controlled Release* **2013**, *171* (1), 11–16. https://doi.org/10.1016/j.jconrel.2013.06.029.

(102) Hettiaratchi, M. H.; O'Meara, M. J.; O'Meara, T. R.; Pickering, A. J.; Letko-Khait, N.; Shoichet, M. S. Reengineering Biocatalysts: Computational Redesign of Chondroitinase ABC Improves Efficacy and Stability. *Sci. Adv.* **2020**, *6* (34), eabc6378. https://doi.org/10.1126/sciadv.abc6378.

(103) Silverman, B. R.; Champion, J. A. Presentation of Fibronectin Fragments Using Affinity Protein Interactions for Enhanced Retention and Function. *Acta Biomaterialia* **2014**, *10* (12), 4956–4960. https://doi.org/10.1016/j.actbio.2014.08.026.

(104) Woldring, D. R.; Holec, P. V.; Stern, L. A.; Du, Y.; Hackel, B. J. A Gradient of Sitewise Diversity Promotes Evolutionary Fitness for Binder Discovery in a Three-Helix Bundle Protein Scaffold. *Biochemistry* **2017**, *56* (11), 1656–1671. https://doi.org/10.1021/acs.biochem.6b01142.

(105) Teal, C. J.; Hettiaratchi, M. H.; Ho, M. T.; Ortin-Martinez, A.; Ganesh, A. N.; Pickering, A. J.; Golinski, A. W.; Hackel, B. J.; Wallace, V. A.; Shoichet, M. S. Directed Evolution Enables Simultaneous Controlled Release of Multiple Therapeutic Proteins from Biopolymer-Based Hydrogels. *Advanced Materials n/a* (n/a), 2202612. https://doi.org/10.1002/adma.202202612.

(106) Myers, D. R.; Zikherman, J.; Roose, J. P. Tonic Signals: Why Do Lymphocytes Bother? *Trends in Immunology* **2017**, *38* (11), 844–857. https://doi.org/10.1016/j.it.2017.06.010.

(107) Rinker, T. E.; Philbrick, B. D.; Hettiaratchi, M. H.; Smalley, D. M.; McDevitt, T. C.; Temenoff, J. S. Microparticle-Mediated Sequestration of Cell-Secreted Proteins to Modulate Chondrocytic Differentiation. *Acta Biomaterialia* **2018**, *68*, 125–136. https://doi.org/10.1016/j.actbio.2017.12.038.

(108) Hudalla, G. A.; Koepsel, J. T.; Murphy, W. L. Surfaces That Sequester Serum-Borne Heparin Amplify Growth Factor Activity. *Adv. Mater.* **2011**, *23* (45), 5415–5418. https://doi.org/10.1002/adma.201103046.

(109) Zeng, Y.; Shih, Y. V.; Baht, G. S.; Varghese, S. In Vivo Sequestration of Innate Small Molecules to Promote Bone Healing. *Adv. Mater.* **2020**, *32* (8), 1906022. https://doi.org/10.1002/adma.201906022.

(110) Liu, G.; Wu, R.; Yang, B.; Shi, Y.; Deng, C.; Atala, A.; Mou, S.; Criswell, T.; Zhang, Y. A Cocktail of Growth Factors Released from a Heparin Hyaluronic-Acid Hydrogel Promotes the Myogenic Potential of Human Urine-Derived Stem Cells in Vivo. *Acta Biomaterialia* **2020**, *107*, 50–64. https://doi.org/10.1016/j.actbio.2020.02.005.

(111) Lee, S. S.; Kim, J. H.; Jeong, J.; Kim, S. H. L.; Koh, R. H.; Kim, I.; Bae, S.; Lee, H.; Hwang, N. S. Sequential Growth Factor Releasing Double Cryogel System for Enhanced Bone Regeneration. *Biomaterials* **2020**, *257*, 120223. https://doi.org/10.1016/j.biomaterials.2020.120223.

(112) Wang, Y.; Cooke, M. J.; Sachewsky, N.; Morshead, C. M.; Shoichet, M. S. Bioengineered Sequential Growth Factor Delivery Stimulates Brain Tissue Regeneration after Stroke. *Journal of Controlled Release* **2013**, *172* (1), 1–11. https://doi.org/10.1016/j.jconrel.2013.07.032.
(113) Shah, N. J.; Hyder, M. N.; Quadir, M. A.; Dorval Courchesne, N.-M.; Seeherman, H. J.; Nevins, M.; Spector, M.; Hammond, P. T. Adaptive Growth Factor Delivery from a Polyelectrolyte Coating Promotes Synergistic Bone Tissue Repair and Reconstruction. *Proceedings of the National Academy of Sciences* **2014**, *111* (35), 12847–12852. https://doi.org/10.1073/pnas.1408035111.
(114) Gawade, P. M.; Shadish, J. A.; Badeau, B. A.; DeForest, C. A. Logic-Based Delivery of Site-Specifically Modified Proteins from Environmentally Responsive Hydrogel Biomaterials. *Adv. Mater.* **2019**, *31* (33), 1902462. https://doi.org/10.1002/adma.201902462.
(115) Badeau, B. A.; Comerford, M. P.; Arakawa, C. K.; Shadish, J. A.; DeForest, C. A. Engineered Modular Biomaterial Logic Gates for Environmentally Triggered Therapeutic Delivery. *Nature Chem* **2018**, *10* (3), 251–258. https://doi.org/10.1038/nchem.2917.
(116) LeValley, P. J.; Neelarapu, R.; Sutherland, B. P.; Dasgupta, S.; Kloxin, C. J.; Kloxin, A. M. Photolabile Linkers: Exploiting Labile Bond Chemistry to Control Mode and Rate of Hydrogel Degradation and Protein Release. *J. Am. Chem. Soc.* **2020**, *142* (10), 4671–4679. https://doi.org/10.1021/jacs.9b11564.
(117) Li, Z.; Tian, G.; Jiang, H.; Pan, R.; Lian, B.; Wang, M.; Gao, Z.; Zhang, B.; Wu, J. Liver-Targeting and pH-Sensitive Sulfated Hyaluronic Acid Mixed Micelles for Hepatoma Therapy. *IJN* **2019**, *Volume 14*, 9437–9452. https://doi.org/10.2147/IJN.S214528.
(118) Zhang, P.; Han, F.; Chen, T.; Wu, Z.; Chen, S. "Swiss Roll"-like Bioactive Hybrid Scaffolds for Promoting Bone Tissue Ingrowth and Tendon-Bone Healing after Anterior Cruciate Ligament Reconstruction. *Biomater. Sci.* **2020**, *8* (3), 871–883. https://doi.org/10.1039/C9BM01703H.
(119) Ishihara, A.; Sasaki, K.; Lee, S. S.-Y.; Williford, J.-M.; Ishihara, J.; Yasui, M.; Abe, H.; Potin, L.; Hosseinchi, P.; Fukunaga, K.; Raczy, M. M.; Gray, L. T.; Mansurov, A.; Katsumata, K.; Fukayama, M.; Kron, S. J.; Swartz, M. A.; Hubbell, J. A. Targeted Antibody and Cytokine Cancer Immunotherapies through Collagen Affinity. *Science Translational Medicine* **2019**, *11* (487), eaau3259.
(120) Walls, Z. F.; Schwengels, M.; Palau, V. Intracellular Sequestration of HER2 via Targeted Subcellular Peptide Delivery. *Journal of Drug Targeting* **2018**, *26* (9), 840–844. https://doi.org/10.1080/1061186X.2018.1450411.
(121) Chen, B.; Lin, H.; Wang, J.; Zhao, Y.; Wang, B.; Zhao, W.; Sun, W.; Dai, J. Homogeneous Osteogenesis and Bone Regeneration by Demineralized Bone Matrix Loading with Collagen-Targeting Bone Morphogenetic Protein-2. *Biomaterials* **2007**, *28* (6), 1027–1035. https://doi.org/10.1016/j.biomaterials.2006.10.013.
(122) Zalba, S.; Contreras, A. M.; Haeri, A.; ten Hagen, T. L. M.; Navarro, I.; Koning, G.; Garrido, M. J. Cetuximab-Oxaliplatin-Liposomes for Epidermal Growth Factor Receptor Targeted Chemotherapy of Colorectal Cancer. *Journal of Controlled Release* **2015**, *210*, 26–38. https://doi.org/10.1016/j.jconrel.2015.05.271.
(123) Seok, H.-Y.; Sanoj Rejinold, N.; Lekshmi, K. M.; Cherukula, K.; Park, I.-K.; Kim, Y.-C. CD44 Targeting Biocompatible and Biodegradable Hyaluronic Acid Cross-Linked Zein Nanogels for Curcumin Delivery to Cancer Cells: In Vitro and in Vivo Evaluation. *Journal of Controlled Release* **2018**, *280*, 20–30. https://doi.org/10.1016/j.jconrel.2018.04.050.
(124) Zhang, X.; He, F.; Xiang, K.; Zhang, J.; Xu, M.; Long, P.; Su, H.; Gan, Z.; Yu, Q. CD44-Targeted Facile Enzymatic Activatable Chitosan Nanoparticles for Efficient Antitumor Therapy and Reversal of Multidrug Resistance. *Biomacromolecules* **2018**, *19* (3), 883–895. https://doi.org/10.1021/acs.biomac.7b01676.

(125) Ledsgaard, L.; Kilstrup, M.; Karatt-Vellatt, A.; McCafferty, J.; Laustsen, A. H. Basics of Antibody Phage Display Technology. *Toxins (Basel)* **2018**, *10* (6), 236. https://doi.org/10.3390/toxins10060236.
(126) Samoylova, T. I.; Smith, B. F. Elucidation of Muscle-binding Peptides by Phage Display Screening. **1999**, 7.
(127) Kanki, S.; Jaalouk, D. E.; Lee, S.; Yu, A. Y. C.; Gannon, J.; Lee, R. T. Identification of Targeting Peptides for Ischemic Myocardium by in Vivo Phage Display. *Journal of Molecular and Cellular Cardiology* **2011**, *50* (5), 841–848. https://doi.org/10.1016/j.yjmcc.2011.02.003.
(128) Segvich, S. J.; Smith, H. C.; Kohn, D. H. The Adsorption of Preferential Binding Peptides to Apatite-Based Materials. *Biomaterials* **2009**, *30* (7), 1287–1298. https://doi.org/10.1016/j.biomaterials.2008.11.008.
(129) Ramaraju, H.; Kohn, D. H. Cell and Material-Specific Phage Display Peptides Increase iPS-MSC Mediated Bone and Vasculature Formation In Vivo. *Adv. Healthcare Mater.* **2019**, *8* (9), 1801356. https://doi.org/10.1002/adhm.201801356.
(130) Ding, L.; Jiang, Y.; Zhang, J.; Klok, H.-A.; Zhong, Z. pH-Sensitive Coiled-Coil Peptide-Cross-Linked Hyaluronic Acid Nanogels: Synthesis and Targeted Intracellular Protein Delivery to CD44 Positive Cancer Cells. *Biomacromolecules* **2018**, *19* (2), 555–562. https://doi.org/10.1021/acs.biomac.7b01664.
(131) Helguero, C. G.; Mustahsan, V. M.; Parmar, S.; Pentyala, S.; Pfail, J. L.; Kao, I.; Komatsu, D. E.; Pentyala, S. Biomechanical Properties of 3D-Printed Bone Scaffolds Are Improved by Treatment with CRFP. *J Orthop Surg Res* **2017**, *12* (1), 195. https://doi.org/10.1186/s13018-017-0700-2.
(132) Carver, W.; Goldsmith, E. C. Regulation of Tissue Fibrosis by the Biomechanical Environment. *BioMed Research International* **2013**, *2013*, 1–10. https://doi.org/10.1155/2013/101979.
(133) Bansal, S.; Mandalapu, S.; Aeppli, C.; Qu, F.; Szczesny, S. E.; Mauck, R. L.; Zgonis, M. H. Mechanical Function near Defects in an Aligned Nanofiber Composite Is Preserved by Inclusion of Disorganized Layers: Insight into Meniscus Structure and Function. *Acta Biomaterialia* **2017**, *56*, 102–109. https://doi.org/10.1016/j.actbio.2017.01.074.
(134) Cheng, X.; Tsao, C.; Sylvia, V. L.; Cornet, D.; Nicolella, D. P.; Bredbenner, T. L.; Christy, R. J. Platelet-Derived Growth-Factor-Releasing Aligned Collagen–Nanoparticle Fibers Promote the Proliferation and Tenogenic Differentiation of Adipose-Derived Stem Cells. *Acta Biomaterialia* **2014**, *10* (3), 1360–1369. https://doi.org/10.1016/j.actbio.2013.11.017.
(135) Basurto, I. M.; Mora, M. T.; Gardner, G. M.; Christ, G. J.; Caliari, S. R. *Aligned and Conductive 3D Collagen Scaffolds for Skeletal Muscle Tissue Engineering*; preprint; Bioengineering, 2020. https://doi.org/10.1101/2020.04.18.048017.
(136) Narayanan, N.; Jiang, C.; Wang, C.; Uzunalli, G.; Whittern, N.; Chen, D.; Jones, O. G.; Kuang, S.; Deng, M. Harnessing Fiber Diameter-Dependent Effects of Myoblasts Toward Biomimetic Scaffold-Based Skeletal Muscle Regeneration. *Front. Bioeng. Biotechnol.* **2020**, *8*, 203. https://doi.org/10.3389/fbioe.2020.00203.
(137) Inamdar, S. R.; Barbieri, E.; Terrill, N. J.; Knight, M. M.; Gupta, H. S. Proteoglycan Degradation Mimics Static Compression by Altering the Natural Gradients in Fibrillar Organisation in Cartilage. *Acta Biomaterialia* **2019**, *97*, 437–450. https://doi.org/10.1016/j.actbio.2019.07.055.
(138) Sophia Fox, A. J.; Bedi, A.; Rodeo, S. A. The Basic Science of Articular Cartilage: Structure, Composition, and Function. *Sports Health* **2009**, *1* (6), 461–468. https://doi.org/10.1177/1941738109350438.
(139) Parratt, K.; Smerchansky, M.; Stiggers, Q.; Roy, K. Effect of Hydrogel Material Composition on hBMSC Differentiation into Zone-Specific Neo-Cartilage: Engineering Human Articular Cartilage-

like Tissue with Spatially Varying Properties. *J. Mater. Chem. B* **2017**, *5* (31), 6237–6248. https://doi.org/10.1039/C7TB00896A.
(140) Gegg, C.; Yang, F. Spatially Patterned Microribbon-Based Hydrogels Induce Zonally-Organized Cartilage Regeneration by Stem Cells in 3D. *Acta Biomaterialia* **2020**, *101*, 196–205. https://doi.org/10.1016/j.actbio.2019.10.025.
(141) Girão, A. F.; Semitela, Â.; Ramalho, G.; Completo, A.; Marques, P. A. A. P. Mimicking Nature: Fabrication of 3D Anisotropic Electrospun Polycaprolactone Scaffolds for Cartilage Tissue Engineering Applications. *Composites Part B: Engineering* **2018**, *154*, 99–107. https://doi.org/10.1016/j.compositesb.2018.08.001.
(142) Wang, J.; Wang, Y.; Sun, X.; Liu, D.; Huang, C.; Wu, J.; Yang, C.; Zhang, Q. Biomimetic Cartilage Scaffold with Orientated Porous Structure of Two Factors for Cartilage Repair of Knee Osteoarthritis. *Artificial Cells, Nanomedicine, and Biotechnology* **2019**, *47* (1), 1710–1721. https://doi.org/10.1080/21691401.2019.1607866.
(143) Camarero-Espinosa, S.; Calore, A.; Wilbers, A.; Harings, J.; Moroni, L. Additive Manufacturing of an Elastic Poly(Ester)Urethane for Cartilage Tissue Engineering. *Acta Biomaterialia* **2020**, *102*, 192–204. https://doi.org/10.1016/j.actbio.2019.11.041.
(144) Di Luca, A.; Klein-Gunnewiek, M.; Vancso, J. G.; van Blitterswijk, C. A.; Benetti, E. M.; Moroni, L. Covalent Binding of Bone Morphogenetic Protein-2 and Transforming Growth Factor-B3 to 3D Plotted Scaffolds for Osteochondral Tissue Regeneration. *Biotechnol J* **2017**, *12* (12). https://doi.org/10.1002/biot.201700072.
(145) Lu, S.; Lam, J.; Trachtenberg, J. E.; Lee, E. J.; Seyednejad, H.; van den Beucken, J. J. J. P.; Tabata, Y.; Wong, M. E.; Jansen, J. A.; Mikos, A. G.; Kasper, F. K. Dual Growth Factor Delivery from Bilayered, Biodegradable Hydrogel Composites for Spatially-Guided Osteochondral Tissue Repair. *Biomaterials* **2014**, *35* (31), 8829–8839. https://doi.org/10.1016/j.biomaterials.2014.07.006.
(146) Oliva, N.; Almquist, B. D. Spatiotemporal Delivery of Bioactive Molecules for Wound Healing Using Stimuli-Responsive Biomaterials. *Adv Drug Deliv Rev* **2020**. https://doi.org/10.1016/j.addr.2020.07.021.
(147) Massi, L.; Najer, A.; Chapman, R.; Spicer, C. D.; Nele, V.; Che, J.; Booth, M. A.; Doutch, J. J.; Stevens, M. M. Tuneable Peptide Cross-Linked Nanogels for Enzyme-Triggered Protein Delivery. *J. Mater. Chem. B* **2020**, 10.1039.D0TB01546F. https://doi.org/10.1039/D0TB01546F.
(148) Patel, S.; Vaishya, R.; Yang, X.; Pal, D.; Mitra, A. Novel Thermosensitive Pentablock Copolymers for Sustained Delivery of Proteins in the Treatment of Posterior Segment Diseases. *PPL* **2014**, *21* (11), 1185–1200. https://doi.org/10.2174/0929866521111641001122054.
(149) Kim, Y. S.; Gulfam, M.; Lowe, T. L. Thermoresponsive- *Co* -Biodegradable Linear–Dendritic Nanoparticles for Sustained Release of Nerve Growth Factor To Promote Neurite Outgrowth. *Mol. Pharmaceutics* **2018**, *15* (4), 1467–1475. https://doi.org/10.1021/acs.molpharmaceut.7b01044.
(150) Liu, J.; Detrembleur, C.; De Pauw-Gillet, M.-C.; Mornet, S.; Elst, L. V.; Laurent, S.; Jérôme, C.; Duguet, E. Heat-Triggered Drug Release Systems Based on Mesoporous Silica Nanoparticles Filled with a Maghemite Core and Phase-Change Molecules as Gatekeepers. *J. Mater. Chem. B* **2014**, *2* (1), 59–70. https://doi.org/10.1039/C3TB21229G.
(151) Geiger, B. C.; Wang, S.; Padera, R. F.; Grodzinsky, A. J.; Hammond, P. T. Cartilage-Penetrating Nanocarriers Improve Delivery and Efficacy of Growth Factor Treatment of Osteoarthritis. *Sci. Transl. Med.* **2018**, *10* (469), eaat8800. https://doi.org/10.1126/scitranslmed.aat8800.
(152) Mahmoodzadeh, F.; Ghorbani, M.; Jannat, B. Glutathione and pH-Responsive Chitosan-Based Nanogel as an Efficient Nanoplatform for Controlled Delivery of Doxorubicin. *Journal of Drug Delivery Science and Technology* **2019**, *54*, 101315. https://doi.org/10.1016/j.jddst.2019.101315.

(153) Wu, J.; Yang, Y.; Li, S.; Shi, A.; Song, B.; Niu, S.; Chen, W.; Yao, Z. Glucose-Sensitive Nanoparticles Based On Poly(3-Acrylamidophenylboronic Acid-Block-N-Vinylcaprolactam) For Insulin Delivery. *IJN* **2019**, *Volume 14*, 8059–8072. https://doi.org/10.2147/IJN.S220936.
(154) Belbekhouche, S.; Charaabi, S.; Picton, L.; Le Cerf, D.; Carbonnier, B. Glucose-Sensitive Polyelectrolyte Microcapsules Based on (Alginate/Chitosan) Pair. *Carbohydrate Polymers* **2018**, *184*, 144–153. https://doi.org/10.1016/j.carbpol.2017.12.054.
(155) Liang, X.; Trentle, M.; Kozlovskaya, V.; Kharlampieva, E.; Bonizzoni, M. Carbohydrate Sensing Using Water-Soluble Poly(Methacrylic Acid)- Co-3-(Acrylamido)Phenylboronic Acid Copolymer. **2019**, 9.
(156) Cong, Z.; Shi, Y.; Wang, Y.; Wang, Y.; Niu, J.; Chen, N.; Xue, H. A Novel Controlled Drug Delivery System Based on Alginate Hydrogel/Chitosan Micelle Composites. *International Journal of Biological Macromolecules* **2018**, *107*, 855–864. https://doi.org/10.1016/j.ijbiomac.2017.09.065.
(157) Treenate, P.; Monvisade, P. In Vitro Drug Release Profiles of pH-Sensitive Hydroxyethylacryl Chitosan/Sodium Alginate Hydrogels Using Paracetamol as a Soluble Model Drug. *International Journal of Biological Macromolecules* **2017**, *99*, 71–78. https://doi.org/10.1016/j.ijbiomac.2017.02.061.
(158) Ballance, W. C.; Qin, E. C.; Chung, H. J.; Gillette, M. U.; Kong, H. Reactive Oxygen Species-Responsive Drug Delivery Systems for the Treatment of Neurodegenerative Diseases. *Biomaterials* **2019**, *217*, 119292. https://doi.org/10.1016/j.biomaterials.2019.119292.
(159) Holloway, J. L.; Ma, H.; Rai, R.; Burdick, J. A. Modulating Hydrogel Crosslink Density and Degradation to Control Bone Morphogenetic Protein Delivery and in Vivo Bone Formation. *J Control Release* **2014**, *191*, 63–70. https://doi.org/10.1016/j.jconrel.2014.05.053.
(160) Park, J.; Choi, J. H.; Kim, S.; Jang, I.; Jeong, S.; Lee, J. Y. Micropatterned Conductive Hydrogels as Multifunctional Muscle-Mimicking Biomaterials: Graphene-Incorporated Hydrogels Directly Patterned with Femtosecond Laser Ablation. *Acta Biomaterialia* **2019**, *97*, 141–153. https://doi.org/10.1016/j.actbio.2019.07.044.
(161) Pedrotty, D. M.; Kuzmenko, V.; Karabulut, E.; Sugrue, A. M.; Livia, C.; Vaidya, V. R.; McLeod, C. J.; Asirvatham, S. J.; Gatenholm, P.; Kapa, S. Three-Dimensional Printed Biopatches With Conductive Ink Facilitate Cardiac Conduction When Applied to Disrupted Myocardium. *Circ: Arrhythmia and Electrophysiology* **2019**, *12* (3). https://doi.org/10.1161/CIRCEP.118.006920.
(162) Feiner, R.; Engel, L.; Fleischer, S.; Malki, M.; Gal, I.; Shapira, A.; Shacham-Diamand, Y.; Dvir, T. Engineered Hybrid Cardiac Patches with Multifunctional Electronics for Online Monitoring and Regulation of Tissue Function. *Nature Mater* **2016**, *15* (6), 679–685. https://doi.org/10.1038/nmat4590.
(163) Freeman, F. E.; Pitacco, P.; van Dommelen, L. H. A.; Nulty, J.; Browe, D. C.; Shin, J.-Y.; Alsberg, E.; Kelly, D. J. 3D Bioprinting Spatiotemporally Defined Patterns of Growth Factors to Tightly Control Tissue Regeneration. *Sci. Adv.* **2020**, *6* (33), eabb5093. https://doi.org/10.1126/sciadv.abb5093.
(164) Grigsby, W. J.; Scott, S. M.; Plowman-Holmes, M. I.; Middlewood, P. G.; Recabar, K. Combination and Processing Keratin with Lignin as Biocomposite Materials for Additive Manufacturing Technology. *Acta Biomaterialia* **2020**, *104*, 95–103. https://doi.org/10.1016/j.actbio.2019.12.026.
(165) Camacho, P.; Busari, H.; Seims, K. B.; Schwarzenberg, P.; Dailey, H. L.; Chow, L. W. 3D Printing with Peptide–Polymer Conjugates for Single-Step Fabrication of Spatially Functionalized Scaffolds. *Biomater. Sci.* **2019**, *7* (10), 4237–4247. https://doi.org/10.1039/C9BM00887J.
(166) Nagao, R. J.; Marcu, R.; Wang, Y.; Wang, L.; Arakawa, C.; DeForest, C.; Chen, J.; López, J. A.; Zheng, Y. Transforming Endothelium with Platelet-Rich Plasma in Engineered Microvessels. *Adv. Sci.* **2019**, *6* (24), 1901725. https://doi.org/10.1002/advs.201901725.

(167) Arakawa, C.; Gunnarsson, C.; Howard, C.; Bernabeu, M.; Phong, K.; Yang, E.; DeForest, C. A.; Smith, J. D.; Zheng, Y. Biophysical and Biomolecular Interactions of Malaria-Infected Erythrocytes in Engineered Human Capillaries. *Sci. Adv.* **2020**, *6* (3), eaay7243. https://doi.org/10.1126/sciadv.aay7243.
(168) Zhang, M.; Lin, R.; Wang, X.; Xue, J.; Deng, C.; Feng, C.; Zhuang, H.; Ma, J.; Qin, C.; Wan, L.; Chang, J.; Wu, C. 3D Printing of Haversian Bone–Mimicking Scaffolds for Multicellular Delivery in Bone Regeneration. *Sci. Adv.* **2020**, *6* (12), eaaz6725. https://doi.org/10.1126/sciadv.aaz6725.
(169) Peak, C. W.; Singh, K. A.; Adlouni, M.; Chen, J.; Gaharwar, A. K. Printing Therapeutic Proteins in 3D Using Nanoengineered Bioink to Control and Direct Cell Migration. *Advanced Healthcare Materials* **2019**, *8* (11), 1801553. https://doi.org/10.1002/adhm.201801553.
(170) Subbiah, R.; Guldberg, R. E. Materials Science and Design Principles of Growth Factor Delivery Systems in Tissue Engineering and Regenerative Medicine. *Adv. Healthcare Mater.* **2019**, *8* (1), 1801000. https://doi.org/10.1002/adhm.201801000.
(171) Subbiah, R.; Hipfinger, C.; Tahayeri, A.; Athirasala, A.; Horsophonphong, S.; Thrivikraman, G.; França, C. M.; Cunha, D. A.; Mansoorifar, A.; Zahariev, A.; Jones, J. M.; Coelho, P. G.; Witek, L.; Xie, H.; Guldberg, R. E.; Bertassoni, L. E. 3D Printing of Microgel-Loaded Modular Microcages as Instructive Scaffolds for Tissue Engineering. *Advanced Materials* **2020**, *32* (36), 2001736. https://doi.org/10.1002/adma.202001736.
(172) Usmani, S. S.; Bedi, G.; Samuel, J. S.; Singh, S.; Kalra, S.; Kumar, P.; Ahuja, A. A.; Sharma, M.; Gautam, A.; Raghava, G. P. S. THPdb: Database of FDA-Approved Peptide and Protein Therapeutics. *PLoS One* **2017**, *12* (7). https://doi.org/10.1371/journal.pone.0181748.
(173) Thies, R. S.; Bauduy, M.; Ashton, B. A.; Kurtzberg, L.; Wozney, J. M.; Rosen, V. Recombinant Human Bone Morphogenetic Protein-2 Induces Osteoblastic Differentiation in W-20-17 Stromal Cells. *Endocrinology* **1992**, *130* (3), 1318–1324. https://doi.org/10.1210/endo.130.3.1311236.
(174) Boyne, P. J. Animal Studies of the Applications of rhBMP-2 in Maxillofacial Reconstruction. *Bone* **1996**, *19* (1), S83–S92. https://doi.org/10.1016/S8756-3282(96)00144-5.
(175) Riedel, G. E.; Valentin-Opran, A. Clinical Evaluation of rhBMP-2/ACS in Orthopedic Trauma: A Progress Report. *Orthopedics* **1999**, *22* (7), 663–665.
(176) McKay, W. F.; Peckham, S. M.; Badura, J. M. A Comprehensive Clinical Review of Recombinant Human Bone Morphogenetic Protein-2 (INFUSE® Bone Graft). *Int Orthop* **2007**, *31* (6), 729–734. https://doi.org/10.1007/s00264-007-0418-6.
(177) Lei, J.; Priddy, L. B.; Lim, J. J.; Massee, M.; Koob, T. J. Identification of Extracellular Matrix Components and Biological Factors in Micronized Dehydrated Human Amnion/Chorion Membrane. *Advances in Wound Care* **2016**, *6* (2), 43–53. https://doi.org/10.1089/wound.2016.0699.
(178) Niknejad, H.; Peirovi, H.; Jorjani, M.; Ahmadiani, A.; Ghanavi, J.; Seifalian, A. M. Properties of the Amniotic Membrane for Potential Use in Tissue Engineering. *Eur Cell Mater* **2008**, *15*, 88–99. https://doi.org/10.22203/ecm.v015a07.
(179) Frykberg, R. G.; Gibbons, G. W.; Walters, J. L.; Wukich, D. K.; Milstein, F. C. A Prospective, Multicentre, Open-Label, Single-Arm Clinical Trial for Treatment of Chronic Complex Diabetic Foot Wounds with Exposed Tendon and/or Bone: Positive Clinical Outcomes of Viable Cryopreserved Human Placental Membrane. *International Wound Journal* **2017**, *14* (3), 569–577. https://doi.org/10.1111/iwj.12649.
(180) Brandeisky, J.; Kurtz Phelan, D. Clinical Outcome of Achilles Tendon Repair Using Viable Intact Cryopreserved Umbilical Tissue Versus Standard of Case. *Wounds* **2017**, *29* (11), E111–E114.
(181) Narayan, R. Amniotic Membranes in Ocular Surface Therapy. *Optician Select* **2016**, *2016* (3), 119–1. https://doi.org/10.12968/opti.2016.3.119.

(182) Suri, K.; Kosker, M.; Raber, I. M.; Hammersmith, K. M.; Nagra, P. K.; Ayres, B. D.; Halfpenny, C. P.; Rapuano, C. J. Sutureless Amniotic Membrane ProKera for Ocular Surface Disorders: Short-Term Results. *Eye & Contact Lens* **2013**, *39* (5), 341–347. https://doi.org/10.1097/ICL.0b013e3182a2f8fa.
(183) Ha, A.; Criman, E. T.; Kurata, W. E.; Matsumoto, K. W.; Pierce, L. M. Evaluation of a Novel Hybrid Viable Bioprosthetic Mesh in a Model of Mesh Infection. *Plast Reconstr Surg Glob Open* **2017**, *5* (8). https://doi.org/10.1097/GOX.0000000000001418.
(184) Arslan-Yildiz, A.; Assal, R. E.; Chen, P.; Guven, S.; Inci, F.; Demirci, U. Towards Artificial Tissue Models: Past, Present, and Future of 3D Bioprinting. *Biofabrication* **2016**, *8* (1), 014103. https://doi.org/10.1088/1758-5090/8/1/014103.
(185) Engler, A. J.; Cooper-White, J. Academic vs Industry Perspectives in 3D Bioprinting. *APL Bioeng* **2020**, *4* (1). https://doi.org/10.1063/5.0004340.
(186) Hettiaratchi, M. H.; Schudel, A.; Rouse, T.; García, A. J.; Thomas, S. N.; Guldberg, R. E.; McDevitt, T. C. A Rapid Method for Determining Protein Diffusion through Hydrogels for Regenerative Medicine Applications. *APL Bioengineering* **2018**, *2* (2), 026110. https://doi.org/10.1063/1.4999925.
(187) Xu, F.; Corbett, B.; Bell, S.; Zhang, C.; Budi Hartono, M.; Farsangi, Z. J.; MacGregor, J.; Hoare, T. High-Throughput Synthesis, Analysis, and Optimization of Injectable Hydrogels for Protein Delivery. *Biomacromolecules* **2020**, *21* (1), 214–229. https://doi.org/10.1021/acs.biomac.9b01132.
(188) Hao, D.; Fan, Y.; Xiao, W.; Liu, R.; Pivetti, C.; Walimbe, T.; Guo, F.; Zhang, X.; Farmer, D. L.; Wang, F.; Panitch, A.; Lam, K. S.; Wang, A. Rapid Endothelialization of Small Diameter Vascular Grafts by a Bioactive Integrin-Binding Ligand Specifically Targeting Endothelial Progenitor Cells and Endothelial Cells. *Acta Biomaterialia* **2020**, *108*, 178–193. https://doi.org/10.1016/j.actbio.2020.03.005.
(189) Zambrano-Mila, M. S.; Blacio, K. E. S.; Vispo, N. S. Peptide Phage Display: Molecular Principles and Biomedical Applications. *Therapeutic Innovation & Regulatory Science 0* (0), 2168479019837624. https://doi.org/10.1177/2168479019837624.
(190) Pakulska, M. M.; Vulic, K.; Tam, R. Y.; Shoichet, M. S. Hybrid Crosslinked Methylcellulose Hydrogel: A Predictable and Tunable Platform for Local Drug Delivery. *Adv. Mater.* **2015**, *27* (34), 5002–5008. https://doi.org/10.1002/adma.201502767.
(191) Murphy, K. C.; Whitehead, J.; Falahee, P. C.; Zhou, D.; Simon, S. I.; Leach, J. K. Multifactorial Experimental Design to Optimize the Anti-Inflammatory and Proangiogenic Potential of Mesenchymal Stem Cell Spheroids: Optimizing MSC Spheroid Potential. *Stem Cells* **2017**, *35* (6), 1493–1504. https://doi.org/10.1002/stem.2606.
(192) Le, N. N. T.; Liu, T. L.; Johnston, J.; Krutty, J. D.; Templeton, K. M.; Harms, V.; Dias, A.; Le, H.; Gopalan, P.; Murphy, W. L. Customized Hydrogel Substrates for Serum-Free Expansion of Functional hMSCs. *Biomater. Sci.* **2020**, *8* (14), 3819–3829. https://doi.org/10.1039/D0BM00540A.
(193) Miyazono, K.; Kamiya, Y.; Morikawa, M. Bone Morphogenetic Protein Receptors and Signal Transduction. *The Journal of Biochemistry* **2010**, *147* (1), 35–51. https://doi.org/10.1093/jb/mvp148.
(194) James, A. W.; LaChaud, G.; Shen, J.; Asatrian, G.; Nguyen, V.; Zhang, X.; Ting, K.; Soo, C. A Review of the Clinical Side Effects of Bone Morphogenetic Protein-2. *Tissue Eng Part B Rev* **2016**, *22* (4), 284–297. https://doi.org/10.1089/ten.teb.2015.0357.
(195) Hiepen, C.; Benn, A.; Denkis, A.; Lukonin, I.; Weise, C.; Boergermann, J. H.; Knaus, P. BMP2-Induced Chemotaxis Requires PI3K P55γ/P110α-Dependent Phosphatidylinositol (3,4,5)-

Triphosphate Production and LL5β Recruitment at the Cytocortex. *BMC Biology* **2014**, *12* (1), 43. https://doi.org/10.1186/1741-7007-12-43.
(196) Borgiani, E.; Duda, G. N.; Willie, B. M.; Checa, S. Bone Morphogenetic Protein 2-Induced Cellular Chemotaxis Drives Tissue Patterning during Critical-Sized Bone Defect Healing: An in Silico Study. *Biomech Model Mechanobiol* **2021**, *20* (4), 1627–1644. https://doi.org/10.1007/s10237-021-01466-0.
(197) Lind, M.; Eriksen, E. F.; Bünger, C. Bone Morphogenetic Protein-2 but Not Bone Morphogenetic Protein-4 and -6 Stimulates Chemotactic Migration of Human Osteoblasts, Human Marrow Osteoblasts, and U2-OS Cells. *Bone* **1996**, *18* (1), 53–57. https://doi.org/10.1016/8756-3282(95)00423-8.
(198) SUN, J.; LI, J.; LI, C.; YU, Y. Role of Bone Morphogenetic Protein-2 in Osteogenic Differentiation of Mesenchymal Stem Cells. *Mol Med Rep* **2015**, *12* (3), 4230–4237. https://doi.org/10.3892/mmr.2015.3954.
(199) Briquez, P. S.; Tsai, H.-M.; Watkins, E. A.; Hubbell, J. A. Engineered Bridge Protein with Dual Affinity for Bone Morphogenetic Protein-2 and Collagen Enhances Bone Regeneration for Spinal Fusion. *Science Advances* **2021**, *7* (24), eabh4302. https://doi.org/10.1126/sciadv.abh4302.
(200) Kim, H. D.; Valentini, R. F. Retention and Activity of BMP-2 in Hyaluronic Acid-Based Scaffolds in Vitro. *J Biomed Mater Res* **2002**, *59* (3), 573–584. https://doi.org/10.1002/jbm.10011.
(201) Noshi, T.; Yoshikawa, T.; Dohi, Y.; Ikeuchi, M.; Horiuchi, K.; Ichijima, K.; Sugimura, M.; Yonemasu, K.; Ohgushi, H. Recombinant Human Bone Morphogenetic Protein-2 Potentiates the in Vivo Osteogenic Ability of Marrow/Hydroxyapatite Composites. *Artif Organs* **2001**, *25* (3), 201–208. https://doi.org/10.1046/j.1525-1594.2001.025003201.x.
(202) Kamal, A. F.; Siahaan, O. S. H.; Fiolin, J. Various Dosages of BMP-2 for Management of Massive Bone Defect in Sprague Dawley Rat. *Arch Bone Jt Surg* **2019**, *7* (6), 498–505.
(203) Rihn, J. A.; Patel, R.; Makda, J.; Hong, J.; Anderson, D. G.; Vaccaro, A. R.; Hilibrand, A. S.; Albert, T. J. Complications Associated with Single-Level Transforaminal Lumbar Interbody Fusion. *Spine J* **2009**, *9* (8), 623–629. https://doi.org/10.1016/j.spinee.2009.04.004.
(204) Weber, L. M.; Lopez, C. G.; Anseth, K. S. The Effects of PEG Hydrogel Crosslinking Density on Protein Diffusion and Encapsulated Islet Survival and Function. *J Biomed Mater Res A* **2009**, *90* (3), 720–729. https://doi.org/10.1002/jbm.a.32134.
(205) Sheth, S.; Barnard, E.; Hyatt, B.; Rathinam, M.; Zustiak, S. P. Predicting Drug Release From Degradable Hydrogels Using Fluorescence Correlation Spectroscopy and Mathematical Modeling. *Frontiers in Bioengineering and Biotechnology* **2019**, *7*.
(206) Dorogin, J.; Townsend, J. M.; Hettiaratchi, M. H. Biomaterials for Protein Delivery for Complex Tissue Healing Responses. *Biomater. Sci.* **2021**, *9* (7), 2339–2361. https://doi.org/10.1039/D0BM01804J.
(207) Rajabi, S.; Jalili-Firoozinezhad, S.; Ashtiani, M. K.; Le Carrou, G.; Tajbakhsh, S.; Baharvand, H. Effect of Chemical Immobilization of SDF-1α into Muscle-Derived Scaffolds on Angiogenesis and Muscle Progenitor Recruitment. *Journal of Tissue Engineering and Regenerative Medicine* **2018**, *12* (1), e438–e450. https://doi.org/10.1002/term.2479.
(208) Hettiaratchi, M. H.; Miller, T.; Temenoff, J. S.; Guldberg, R. E.; McDevitt, T. C. Heparin Microparticle Effects on Presentation and Bioactivity of Bone Morphogenetic Protein-2. *Biomaterials* **2014**, *35* (25), 7228–7238. https://doi.org/10.1016/j.biomaterials.2014.05.011.
(209) Benoit, D. S. W.; Durney, A. R.; Anseth, K. S. The Effect of Heparin-Functionalized PEG Hydrogels on Three-Dimensional Human Mesenchymal Stem Cell Osteogenic Differentiation. *Biomaterials* **2007**, *28* (1), 66–77. https://doi.org/10.1016/j.biomaterials.2006.08.033.

(210) Sakiyama-Elbert, S. E.; Hubbell, J. A. Controlled Release of Nerve Growth Factor from a Heparin-Containing Fibrin-Based Cell Ingrowth Matrix. *Journal of Controlled Release* **2000**, *69* (1), 149–158. https://doi.org/10.1016/S0168-3659(00)00296-0.
(211) Abune, L.; Wang, Y. Affinity Hydrogels for Protein Delivery. *Trends in Pharmacological Sciences* **2021**, *42* (4), 300–312. https://doi.org/10.1016/j.tips.2021.01.005.
(212) Wang, Y.; Lan, H.; Yin, T.; Zhang, X.; Huang, J.; Fu, H.; Huang, J.; McGinty, S.; Gao, H.; Wang, G.; Wang, Z. Covalent Immobilization of Biomolecules on Stent Materials through Mussel Adhesive Protein Coating to Form Biofunctional Films. *Materials Science and Engineering: C* **2020**, *106*, 110187. https://doi.org/10.1016/j.msec.2019.110187.
(213) Mardilovich, A.; Craig, J. A.; McCammon, M. Q.; Garg, A.; Kokkoli, E. Design of a Novel Fibronectin-Mimetic Peptide−Amphiphile for Functionalized Biomaterials. *Langmuir* **2006**, *22* (7), 3259–3264. https://doi.org/10.1021/la052756n.
(214) Soontornworajit, B.; Zhou, J.; Shaw, M. T.; Fan, T.-H.; Wang, Y. Hydrogel Functionalization with DNA Aptamers for Sustained PDGF-BB Release. *Chem. Commun.* **2010**, *46* (11), 1857–1859. https://doi.org/10.1039/B924909E.
(215) Hettiaratchi, M. H.; Krishnan, L.; Rouse, T.; Chou, C.; McDevitt, T. C.; Guldberg, R. E. Heparin-Mediated Delivery of Bone Morphogenetic Protein-2 Improves Spatial Localization of Bone Regeneration. *Sci. Adv.* **2020**, *6* (1), eaay1240. https://doi.org/10.1126/sciadv.aay1240.
(216) Peysselon, F.; Ricard-Blum, S. Heparin–Protein Interactions: From Affinity and Kinetics to Biological Roles. Application to an Interaction Network Regulating Angiogenesis. *Matrix Biology* **2014**, *35*, 73–81. https://doi.org/10.1016/j.matbio.2013.11.001.
(217) Shaughnessy, A. F. Monoclonal Antibodies: Magic Bullets with a Hefty Price Tag. *BMJ* **2012**, *345* (dec12 1), e8346–e8346. https://doi.org/10.1136/bmj.e8346.
(218) Sexton, K.; Tichauer, K.; Samkoe, K. S.; Gunn, J.; Hoopes, P. J.; Pogue, B. W. Fluorescent Affibody Peptide Penetration in Glioma Margin Is Superior to Full Antibody. *PLoS One* **2013**, *8* (4), e60390. https://doi.org/10.1371/journal.pone.0060390.
(219) Sachdeva, S.; Joo, H.; Tsai, J.; Jasti, B.; Li, X. A Rational Approach for Creating Peptides Mimicking Antibody Binding. *Sci Rep* **2019**, *9* (1), 997. https://doi.org/10.1038/s41598-018-37201-6.
(220) Trier, N.; Hansen, P.; Houen, G. Peptides, Antibodies, Peptide Antibodies and More. *Int J Mol Sci* **2019**, *20* (24), 6289. https://doi.org/10.3390/ijms20246289.
(221) Muñoz, E. M.; Linhardt, R. J. Heparin-Binding Domains in Vascular Biology. *Arteriosclerosis, Thrombosis, and Vascular Biology* **2004**, *24* (9), 1549–1557. https://doi.org/10.1161/01.ATV.0000137189.22999.3f.
(222) Ren, C.; Wen, X.; Mencius, J.; Quan, S. Selection and Screening Strategies in Directed Evolution to Improve Protein Stability. *Bioresources and Bioprocessing* **2019**, *6* (1), 53. https://doi.org/10.1186/s40643-019-0288-y.
(223) Wang, J.; Youngblood, R.; Cassinotti, L.; Skoumal, M.; Corfas, G.; Shea, L. An Injectable PEG Hydrogel Controlling Neurotrophin-3 Release by Affinity Peptides. *Journal of Controlled Release* **2021**, *330*, 575–586. https://doi.org/10.1016/j.jconrel.2020.12.045.
(224) Löfblom, J.; Feldwisch, J.; Tolmachev, V.; Carlsson, J.; Ståhl, S.; Frejd, F. Y. Affibody Molecules: Engineered Proteins for Therapeutic, Diagnostic and Biotechnological Applications. *FEBS Letters* **2010**, *584* (12), 2670–2680. https://doi.org/10.1016/j.febslet.2010.04.014.
(225) Frejd, F. Y.; Kim, K.-T. Affibody Molecules as Engineered Protein Drugs. *Exp Mol Med* **2017**, *49* (3), e306–e306. https://doi.org/10.1038/emm.2017.35.
(226) Alexis, F.; Basto, P.; Levy-Nissenbaum, E.; Radovic-Moreno, A. F.; Zhang, L.; Pridgen, E.; Wang, A. Z.; Marein, S. L.; Westerhof, K.; Molnar, L. K.; Farokhzad, O. C. HER-2-Targeted Nanoparticle-

Affibody Bioconjugates for Cancer Therapy. *ChemMedChem* **2008**, *3* (12), 1839–1843. https://doi.org/10.1002/cmdc.200800122.
(227) Persson, J.; Puuvuori, E.; Zhang, B.; Velikyan, I.; Åberg, O.; Müller, M.; Nygren, P.-Å.; Ståhl, S.; Korsgren, O.; Eriksson, O.; Löfblom, J. Discovery, Optimization and Biodistribution of an Affibody Molecule for Imaging of CD69. *Sci Rep* **2021**, *11* (1), 19151. https://doi.org/10.1038/s41598-021-97694-6.
(228) Güler, R.; Svedmark, S. F.; Abouzayed, A.; Orlova, A.; Löfblom, J. Increasing Thermal Stability and Improving Biodistribution of VEGFR2-Binding Affibody Molecules by a Combination of in Silico and Directed Evolution Approaches. *Sci Rep* **2020**, *10* (1), 18148. https://doi.org/10.1038/s41598-020-74560-5.
(229) Case, B. A.; Kruziki, M. A.; Stern, L. A.; Hackel, B. J. Evaluation of Affibody Charge Modification Identified by Synthetic Consensus Design in Molecular PET Imaging of Epidermal Growth Factor Receptor. *Mol. Syst. Des. Eng.* **2018**, *3* (1), 171–182. https://doi.org/10.1039/C7ME00095B.
(230) Hackel, B. J.; Kapila, A.; Dane Wittrup, K. Picomolar Affinity Fibronectin Domains Engineered Utilizing Loop Length Diversity, Recursive Mutagenesis, and Loop Shuffling. *Journal of Molecular Biology* **2008**, *381* (5), 1238–1252. https://doi.org/10.1016/j.jmb.2008.06.051.
(231) Chao, G.; Lau, W. L.; Hackel, B. J.; Sazinsky, S. L.; Lippow, S. M.; Wittrup, K. D. Isolating and Engineering Human Antibodies Using Yeast Surface Display. *Nature Protocols* **2006**, *1* (2), 755–769. https://doi.org/10.1038/nprot.2006.94.
(232) Mahmood, T.; Yang, P.-C. Western Blot: Technique, Theory, and Trouble Shooting. *N Am J Med Sci* **2012**, *4* (9), 429–434. https://doi.org/10.4103/1947-2714.100998.
(233) Stern, L. A.; Csizmar, C. M.; Woldring, D. R.; Wagner, C. R.; Hackel, B. J. Titratable Avidity Reduction Enhances Affinity Discrimination in Mammalian Cellular Selections of Yeast-Displayed Ligands. *ACS Comb Sci* **2017**, *19* (5), 315–323. https://doi.org/10.1021/acscombsci.6b00191.
(234) Colabroy, K. L.; Mayer, K. Benchtop Immobilized Metal Affinity Chromatography, Reconstitution and Assay of a Polyhistidine Tagged Metalloenzyme for the Undergraduate Laboratory. *J Vis Exp* **2018**, No. 138, 58012. https://doi.org/10.3791/58012.
(235) Robichon, C.; Luo, J.; Causey, T. B.; Benner, J. S.; Samuelson, J. C. Engineering Escherichia Coli BL21(DE3) Derivative Strains To Minimize E. Coli Protein Contamination after Purification by Immobilized Metal Affinity Chromatography ▿. *Appl Environ Microbiol* **2011**, *77* (13), 4634–4646. https://doi.org/10.1128/AEM.00119-11.
(236) Asiimwe, N.; Al Mazid, M. F.; Murale, D. P.; Kim, Y. K.; Lee, J.-S. Recent Advances in Protein Modifications Techniques for the Targeting N-Terminal Cysteine. *Peptide Science* **2022**, *114* (3), e24235. https://doi.org/10.1002/pep2.24235.
(237) Phelps, E. A.; Enemchukwu, N. O.; Fiore, V. F.; Sy, J. C.; Murthy, N.; Sulchek, T. A.; Barker, T. H.; García, A. J. Maleimide Cross-Linked Bioactive PEG Hydrogel Exhibits Improved Reaction Kinetics and Cross-Linking for Cell Encapsulation and In Situ Delivery. *Advanced Materials* **2012**, *24* (1), 64–70. https://doi.org/10.1002/adma.201103574.
(238) Fisher, S. A.; Baker, A. E. G.; Shoichet, M. S. Designing Peptide and Protein Modified Hydrogels: Selecting the Optimal Conjugation Strategy. *J. Am. Chem. Soc.* **2017**, *139* (22), 7416–7427. https://doi.org/10.1021/jacs.7b00513.
(239) Arbour, C. A.; Mendoza, L. G.; Stockdill, J. L. Recent Advances in the Synthesis of C-Terminally Modified Peptides. *Org Biomol Chem* **2020**, *18* (37), 7253–7272. https://doi.org/10.1039/d0ob01417f.
(240) Benavides, I.; Raftery, E. D.; Bell, A. G.; Evans, D.; Scott, W. A.; Houk, K. N.; Deming, T. J. Poly(Dehydroalanine): Synthesis, Properties, and Functional Diversification of a Fluorescent Polypeptide. *J. Am. Chem. Soc.* **2022**, *144* (9), 4214–4223. https://doi.org/10.1021/jacs.2c00383.

(241) Nielsen, R. W.; Tachibana, C.; Hansen, N. E.; Winther, J. R. Trisulfides in Proteins. *Antioxidants & Redox Signaling* **2011**, *15* (1), 67–75. https://doi.org/10.1089/ars.2010.3677.
(242) Zeng, J.; Davies, M. J. Evidence for the Formation of Adducts and S-(Carboxymethyl)Cysteine on Reaction of α-Dicarbonyl Compounds with Thiol Groups on Amino Acids, Peptides, and Proteins. *Chem. Res. Toxicol.* **2005**, *18* (8), 1232–1241. https://doi.org/10.1021/tx050074u.
(243) Greenfield, N. J. Using Circular Dichroism Spectra to Estimate Protein Secondary Structure. *Nat Protoc* **2006**, *1* (6), 2876–2890. https://doi.org/10.1038/nprot.2006.202.
(244) Rodger, A.; Marshall, D. Beginners Guide to Circular Dichroism. *The Biochemist* **2021**, *43* (2), 58–64. https://doi.org/10.1042/bio_2020_105.
(245) Mirdita, M.; Schütze, K.; Moriwaki, Y.; Heo, L.; Ovchinnikov, S.; Steinegger, M. ColabFold: Making Protein Folding Accessible to All. *Nature Methods* **2022**. https://doi.org/10.1038/s41592-022-01488-1.
(246) Mirdita, M.; Steinegger, M.; S"oding, J. MMseqs2 Desktop and Local Web Server App for Fast, Interactive Sequence Searches. *Bioinformatics* **2019**, *35* (16), 2856–2858. https://doi.org/10.1093/bioinformatics/bty1057.
(247) Mirdita, M.; von den Driesch, L.; Galiez, C.; Martin, M. J.; S"oding, J.; Steinegger, M. Uniclust Databases of Clustered and Deeply Annotated Protein Sequences and Alignments. *Nucleic Acids Res.* **2017**, *45* (D1), D170–D176. https://doi.org/10.1093/nar/gkw1081.
(248) Evans, R.; O'Neill, M.; Pritzel, A.; Antropova, N.; Senior, A.; Green, T.; Zidek, A.; Bates, R.; Blackwell, S.; Yim, J.; Ronneberger, O.; Bodenstein, S.; Zielinski, M.; Bridgland, A.; Potapenko, A.; Cowie, A.; Tunyasuvunakool, K.; Jain, R.; Clancy, E.; Kohli, P.; Jumper, J.; Hassabis, D. Protein Complex Prediction with AlphaFold-Multimer. *bioRxiv* **2021**. https://doi.org/10.1101/2021.10.04.463034v1.
(249) Mitchell, A. L.; Almeida, A.; Beracochea, M.; Boland, M.; Burgin, J.; Cochrane, G.; Crusoe, M. R.; Kale, V.; Potter, S. C.; Richardson, L. J.; Sakharova, E.; Scheremetjew, M.; Korobeynikov, A.; Shlemov, A.; Kunyavskaya, O.; Lapidus, A.; Finn, R. D. MGnify: The Microbiome Analysis Resource in 2020. *Nucleic Acids Res.* **2019**. https://doi.org/10.1093/nar/gkz1035.
(250) Jumper, J.; Evans, R.; Pritzel, A.; Green, T.; Figurnov, M.; Ronneberger, O.; Tunyasuvunakool, K.; Bates, R.; Žídek, A.; Potapenko, A.; Bridgland, A.; Meyer, C.; Kohl, S. A. A.; Ballard, A. J.; Cowie, A.; Romera-Paredes, B.; Nikolov, S.; Jain, R.; Adler, J.; Back, T.; Petersen, S.; Reiman, D.; Clancy, E.; Zielinski, M.; Steinegger, M.; Pacholska, M.; Berghammer, T.; Bodenstein, S.; Silver, D.; Vinyals, O.; Senior, A. W.; Kavukcuoglu, K.; Kohli, P.; Hassabis, D. Highly Accurate Protein Structure Prediction with AlphaFold. *Nature* **2021**, *596* (7873), 583–589. https://doi.org/10.1038/s41586-021-03819-2.
(251) Nivón, L. G.; Moretti, R.; Baker, D. A Pareto-Optimal Refinement Method for Protein Design Scaffolds. *PLOS ONE* **2013**, *8* (4), e59004. https://doi.org/10.1371/journal.pone.0059004.
(252) Tyka, M. D.; Keedy, D. A.; André, I.; DiMaio, F.; Song, Y.; Richardson, D. C.; Richardson, J. S.; Baker, D. Alternate States of Proteins Revealed by Detailed Energy Landscape Mapping. *Journal of Molecular Biology* **2011**, *405* (2), 607–618. https://doi.org/10.1016/j.jmb.2010.11.008.
(253) Conway, P.; Tyka, M. D.; DiMaio, F.; Konerding, D. E.; Baker, D. Relaxation of Backbone Bond Geometry Improves Protein Energy Landscape Modeling. *Protein Sci* **2014**, *23* (1), 47–55. https://doi.org/10.1002/pro.2389.
(254) Pierce, B. G.; Wiehe, K.; Hwang, H.; Kim, B.-H.; Vreven, T.; Weng, Z. ZDOCK Server: Interactive Docking Prediction of Protein–Protein Complexes and Symmetric Multimers. *Bioinformatics* **2014**, *30* (12), 1771–1773. https://doi.org/10.1093/bioinformatics/btu097.
(255) Schrödinger, LLC. The PyMOL Molecular Graphics System, Version 1.8, 2015.

(256) Rahman, M. S.; Akhtar, N.; Jamil, H. M.; Banik, R. S.; Asaduzzaman, S. M. TGF-β/BMP Signaling and Other Molecular Events: Regulation of Osteoblastogenesis and Bone Formation. *Bone Res* **2015**, *3*, 15005. https://doi.org/10.1038/boneres.2015.5.
(257) Maguire, J. B.; Haddox, H. K.; Strickland, D.; Halabiya, S. F.; Coventry, B.; Griffin, J. R.; Pulavarti, S. V. S. R. K.; Cummins, M.; Thieker, D. F.; Klavins, E.; Szyperski, T.; DiMaio, F.; Baker, D.; Kuhlman, B. Perturbing the Energy Landscape for Improved Packing during Computational Protein Design. *Proteins* **2021**, *89* (4), 436–449. https://doi.org/10.1002/prot.26030.
(258) Hagemans, D.; van Belzen, I. A. E. M.; Morán Luengo, T.; Rüdiger, S. G. D. A Script to Highlight Hydrophobicity and Charge on Protein Surfaces. *Frontiers in Molecular Biosciences* **2015**, *2*.
(259) Martino, M. M.; Briquez, P. S.; Güç, E.; Tortelli, F.; Kilarski, W. W.; Metzger, S.; Rice, J. J.; Kuhn, G. A.; Müller, R.; Swartz, M. A.; Hubbell, J. A. Growth Factors Engineered for Super-Affinity to the Extracellular Matrix Enhance Tissue Healing. *Science* **2014**, *343* (6173), 885–888. https://doi.org/10.1126/science.1247663.
(260) Boraschi-Diaz, I.; Wang, J.; Mort, J. S.; Komarova, S. V. Collagen Type I as a Ligand for Receptor-Mediated Signaling. *Frontiers in Physics* **2017**, *5*.
(261) Kotzsch, A.; Nickel, J.; Seher, A.; Heinecke, K.; van Geersdaele, L.; Herrmann, T.; Sebald, W.; Mueller, T. D. Structure Analysis of Bone Morphogenetic Protein-2 Type I Receptor Complexes Reveals a Mechanism of Receptor Inactivation in Juvenile Polyposis Syndrome*. *Journal of Biological Chemistry* **2008**, *283* (9), 5876–5887. https://doi.org/10.1074/jbc.M706029200.
(262) Kirsch, T.; Nickel, J.; Sebald, W. BMP-2 Antagonists Emerge from Alterations in the Low-Affinity Binding Epitope for Receptor BMPR-II. *EMBO J* **2000**, *19* (13), 3314–3324. https://doi.org/10.1093/emboj/19.13.3314.
(263) Katagiri, T.; Tsukamoto, S. The Unique Activity of Bone Morphogenetic Proteins in Bone: A Critical Role of the Smad Signaling Pathway. *Biological Chemistry* **2013**, *394* (6), 703–714. https://doi.org/10.1515/hsz-2012-0310.
(264) Karim, Md. S.; Madamanchi, A.; Dutko, J. A.; Mullins, M. C.; Umulis, D. M. Heterodimer-Heterotetramer Formation Mediates Enhanced Sensor Activity in a Biophysical Model for BMP Signaling. *PLoS Comput Biol* **2021**, *17* (9), e1009422. https://doi.org/10.1371/journal.pcbi.1009422.
(265) Liu, R.; Ginn, S. L.; Lek, M.; North, K. N.; Alexander, I. E.; Little, D. G.; Schindeler, A. Myoblast Sensitivity and Fibroblast Insensitivity to Osteogenic Conversion by BMP-2 Correlates with the Expression of Bmpr-1a. *BMC Musculoskeletal Disorders* **2009**, *10* (1), 51. https://doi.org/10.1186/1471-2474-10-51.
(266) Song, R.; Wang, D.; Zeng, R.; Wang, J. Synergistic Effects of Fibroblast Growth Factor-2 and Bone Morphogenetic Protein-2 on Bone Induction. *Molecular Medicine Reports* **2017**, *16* (4), 4483–4492. https://doi.org/10.3892/mmr.2017.7183.
(267) Zernik, J.; Twarog, K.; Upholt, W. B. Regulation of Alkaline Phosphatase and Alpha 2(I) Procollagen Synthesis during Early Intramembranous Bone Formation in the Rat Mandible. *Differentiation* **1990**, *44* (3), 207–215. https://doi.org/10.1111/j.1432-0436.1990.tb00619.x.
(268) Sepulveda, J. L. Chapter 10 - Challenges in Routine Clinical Chemistry Analysis: Proteins and Enzymes. In *Accurate Results in the Clinical Laboratory (Second Edition)*; Dasgupta, A., Sepulveda, J. L., Eds.; Elsevier, 2019; pp 141–163. https://doi.org/10.1016/B978-0-12-813776-5.00010-8.
(269) Zhang, J.; Lu, X.; Lei, Y.; Hou, X.; Wu, P. Exploring the Tunable Excitation of QDs to Maximize the Overlap with the Absorber for Inner Filter Effect-Based Phosphorescence Sensing of Alkaline Phosphatase. *Nanoscale* **2017**, *9* (40), 15606–15611. https://doi.org/10.1039/C7NR03673F.

(270) Friess, W.; Uludag, H.; Foskett, S.; Biron, R.; Sargeant, C. Characterization of Absorbable Collagen Sponges as rhBMP-2 Carriers. *International Journal of Pharmaceutics* **1999**, *187* (1), 91–99. https://doi.org/10.1016/S0378-5173(99)00174-X.
(271) Yang, H. S.; La, W.-G.; Cho, Y.-M.; Shin, W.; Yeo, G.-D.; Kim, B.-S. Comparison between Heparin-Conjugated Fibrin and Collagen Sponge as Bone Morphogenetic Protein-2 Carriers for Bone Regeneration. *Exp Mol Med* **2012**, *44* (5), 350–355. https://doi.org/10.3858/emm.2012.44.5.039.
(272) Jansen, L. E.; Negrón-Piñeiro, L. J.; Galarza, S.; Peyton, S. R. Control of Thiol-Maleimide Reaction Kinetics in PEG Hydrogel Networks. *Acta Biomaterialia* **2018**, *70*, 120–128. https://doi.org/10.1016/j.actbio.2018.01.043.
(273) Guo, Y.; Gu, J.; Jiang, Y.; Zhou, Y.; Zhu, Z.; Ma, T.; Cheng, Y.; Ji, Z.; Jiao, Y.; Xue, B.; Cao, Y. Regulating the Homogeneity of Thiol-Maleimide Michael-Type Addition-Based Hydrogels Using Amino Biomolecules. *Gels* **2021**, *7* (4), 206. https://doi.org/10.3390/gels7040206.
(274) Abouelmagd, S. A.; Sun, B.; Chang, A. C.; Ku, Y. J.; Yeo, Y. *Release Kinetics Study of Poorly Water-Soluble Drugs from Nanoparticles: Are We Doing It Right?*. ACS Publications. https://doi.org/10.1021/mp500817h.
(275) Jensen, S. S.; Jensen, H.; Møller, E. H.; Cornett, C.; Siepmann, F.; Siepmann, J.; Østergaard, J. In Vitro Release Studies of Insulin from Lipid Implants in Solution and in a Hydrogel Matrix Mimicking the Subcutis. *European Journal of Pharmaceutical Sciences* **2016**, *81*, 103–112. https://doi.org/10.1016/j.ejps.2015.10.011.
(276) Gstraunthaler, G.; Lindl, T.; van der Valk, J. A Plea to Reduce or Replace Fetal Bovine Serum in Cell Culture Media. *Cytotechnology* **2013**, *65* (5), 791–793. https://doi.org/10.1007/s10616-013-9633-8.
(277) Metters, A.; Hubbell, J. Network Formation and Degradation Behavior of Hydrogels Formed by Michael-Type Addition Reactions. *Biomacromolecules* **2005**, *6* (1), 290–301. https://doi.org/10.1021/bm049607o.
(278) Mellott, M. B.; Searcy, K.; Pishko, M. V. Release of Protein from Highly Cross-Linked Hydrogels of Poly(Ethylene Glycol) Diacrylate Fabricated by UV Polymerization. *Biomaterials* **2001**, *22* (9), 929–941. https://doi.org/10.1016/s0142-9612(00)00258-1.
(279) Leach, J. B.; Schmidt, C. E. Characterization of Protein Release from Photocrosslinkable Hyaluronic Acid-Polyethylene Glycol Hydrogel Tissue Engineering Scaffolds. *Biomaterials* **2005**, *26* (2), 125–135. https://doi.org/10.1016/j.biomaterials.2004.02.018.
(280) Zustiak, S. P.; Leach, J. B. Characterization of Protein Release from Hydrolytically Degradable Poly(Ethylene Glycol) Hydrogels. *Biotechnol Bioeng* **2011**, *108* (1), 197–206. https://doi.org/10.1002/bit.22911.
(281) Wang, Y.; Delgado-Fukushima, E.; Fu, R. X.; Doerk, G. S.; Kim, J. Controlling Drug Absorption, Release and Erosion of Photopatterned Protein Engineered Hydrogels.
(282) Vermonden, T.; Censi, R.; Hennink, W. E. Hydrogels for Protein Delivery. *Chem. Rev.* **2012**, *112* (5), 2853–2888. https://doi.org/10.1021/cr200157d.
(283) Gregoritza, M.; Messmann, V.; M. Goepferich, A.; P. Brandl, F. Design of Hydrogels for Delayed Antibody Release Utilizing Hydrophobic Association and Diels–Alder Chemistry in Tandem. *Journal of Materials Chemistry B* **2016**, *4* (19), 3398–3408. https://doi.org/10.1039/C6TB00223D.
(284) Quaas, B.; Burmeister, L.; Li, Z.; Satalov, A.; Behrens, P.; Hoffmann, A.; Rinas, U. Stability and Biological Activity of E. Coli Derived Soluble and Precipitated Bone Morphogenetic Protein-2. *Pharm Res* **2019**, *36* (12), 184. https://doi.org/10.1007/s11095-019-2705-5.
(285) Sundermann, J.; Zagst, H.; Kuntsche, J.; Wätzig, H.; Bunjes, H. Bone Morphogenetic Protein 2 (BMP-2) Aggregates Can Be Solubilized by Albumin—Investigation of BMP-2 Aggregation by Light

Scattering and Electrophoresis. *Pharmaceutics* **2020**, *12* (12), 1143. https://doi.org/10.3390/pharmaceutics12121143.
(286) Ritger, P. L.; Peppas, N. A. A Simple Equation for Description of Solute Release II. Fickian and Anomalous Release from Swellable Devices. *Journal of Controlled Release* **1987**, *5* (1), 37–42. https://doi.org/10.1016/0168-3659(87)90035-6.
(287) Lowe, S.; O'Brien-Simpson, N. M.; Connal, L. A. Antibiofouling Polymer Interfaces: Poly(Ethylene Glycol) and Other Promising Candidates. *Polym. Chem.* **2014**, *6* (2), 198–212. https://doi.org/10.1039/C4PY01356E.
(288) Kuo, J.-H. S. Effect of Pluronic-Block Copolymers on the Reduction of Serum-Mediated Inhibition of Gene Transfer of Polyethyleneimine–DNA Complexes. *Biotechnology and Applied Biochemistry* **2003**, *37* (3), 267–271. https://doi.org/10.1042/BA20020123.
(289) Fung, S. L.; Wu, X.; Maceren, J. P.; Mao, Y.; Kohn, J. In Vitro Evaluation of Recombinant Bone Morphogenetic Protein-2 Bioactivity for Regenerative Medicine. *Tissue Engineering Part C: Methods* **2019**, *25* (9), 553–559. https://doi.org/10.1089/ten.tec.2019.0156.
(290) Hettiaratchi, M. H.; Krishnan, L.; Rouse, T.; Chou, C.; McDevitt, T. C.; Guldberg, R. E. Heparin-Mediated Delivery of Bone Morphogenetic Protein-2 Improves Spatial Localization of Bone Regeneration. *Sci. Adv.* **2020**, *6* (1), eaay1240. https://doi.org/10.1126/sciadv.aay1240.
(291) Jung, T.; Lee, J. H.; Park, S.; Kim, Y.-J.; Seo, J.; Shim, H.-E.; Kim, K.-S.; Jang, H.-S.; Chung, H.-M.; Oh, S.-G.; Moon, S.-H.; Kang, S.-W. Effect of BMP-2 Delivery Mode on Osteogenic Differentiation of Stem Cells. *Stem Cells Int* **2017**, *2017*, 7859184. https://doi.org/10.1155/2017/7859184.
(292) Zhao, B.; Katagiri, T.; Toyoda, H.; Takada, T.; Yanai, T.; Fukuda, T.; Chung, U.; Koike, T.; Takaoka, K.; Kamijo, R. Heparin Potentiates the in Vivo Ectopic Bone Formation Induced by Bone Morphogenetic Protein-2 *. *Journal of Biological Chemistry* **2006**, *281* (32), 23246–23253. https://doi.org/10.1074/jbc.M511039200.
(293) Van Hove, A. H.; Beltejar, M.-J.; Benoit, D. S. W. Development and in Vitro Assessment of Enzymatically-Responsive Poly(Ethylene Glycol) Hydrogels for the Delivery of Therapeutic Peptides. *Biomaterials* **2014**, *35* (36), 9719–9730. https://doi.org/10.1016/j.biomaterials.2014.08.019.
(294) Shih, H.; Lin, C.-C. Crosslinking and Degradation of Step-Growth Hydrogels Formed by Thiol-Ene Photo-Click Chemistry. *Biomacromolecules* **2012**, *13* (7), 2003–2012. https://doi.org/10.1021/bm300752j.
(295) Marty, M. T.; Baldwin, A. J.; Marklund, E. G.; Hochberg, G. K. A.; Benesch, J. L. P.; Robinson, C. V. Bayesian Deconvolution of Mass and Ion Mobility Spectra: From Binary Interactions to Polydisperse Ensembles. *Anal. Chem.* **2015**, *87* (8), 4370–4376. https://doi.org/10.1021/acs.analchem.5b00140.
(296) Khatib, F.; Cooper, S.; Tyka, M. D.; Xu, K.; Makedon, I.; Popović, Z.; Baker, D.; Players, F. Algorithm Discovery by Protein Folding Game Players. *Proceedings of the National Academy of Sciences* **2011**, *108* (47), 18949–18953. https://doi.org/10.1073/pnas.1115898108.
(297) Keller, S.; Nickel, J.; Zhang, J.-L.; Sebald, W.; Mueller, T. D. Molecular Recognition of BMP-2 and BMP Receptor IA. *Nat Struct Mol Biol* **2004**, *11* (5), 481–488. https://doi.org/10.1038/nsmb756.
(298) Guo, J.; Liu, B.; Thorikay, M.; Yu, M.; Li, X.; Tong, Z.; Salmon, R. M.; Read, R. J.; ten Dijke, P.; Morrell, N. W.; Li, W. Crystal Structures of BMPRII Extracellular Domain in Binary and Ternary Receptor Complexes with BMP10. *Nat Commun* **2022**, *13* (1), 2395. https://doi.org/10.1038/s41467-022-30111-2.
(299) Teal, C. J.; Hettiaratchi, M. H.; Ho, M. T.; Ortin-Martinez, A.; Ganesh, A. N.; Pickering, A. J.; Golinski, A. W.; Hackel, B. J.; Wallace, V. A.; Shoichet, M. S. Directed Evolution Enables Simultaneous Controlled Release of Multiple Therapeutic Proteins from Biopolymer-Based

Hydrogels. *Advanced Materials* **2022**, *34* (34), 2202612. https://doi.org/10.1002/adma.202202612.
(300) Dorogin, J.; Hochstatter, H. B.; Shepherd, S. O.; Svendsen, J. E.; Benz, M. A.; Powers, A. C.; Fear, K. M.; Townsend, J. M.; Prell, J. S.; Hosseinzadeh, P.; Hettiaratchi, M. H. Moderate-Affinity Affibodies Modulate the Delivery and Bioactivity of Bone Morphogenetic Protein-2. *Advanced Healthcare Materials n/a* (n/a), 2300793. https://doi.org/10.1002/adhm.202300793.
(301) Schwarz, H.; Schmittner, M.; Duschl, A.; Horejs-Hoeck, J. Residual Endotoxin Contaminations in Recombinant Proteins Are Sufficient to Activate Human CD1c+ Dendritic Cells. *PLoS One* **2014**, *9* (12), e113840. https://doi.org/10.1371/journal.pone.0113840.
(302) Gorbet, M. B.; Sefton, M. V. Review: Biomaterial-Associated Thrombosis: Roles of Coagulation Factors, Complement, Platelets and Leukocytes. In *The Biomaterials: Silver Jubilee Compendium*; Williams, D. F., Ed.; Elsevier Science: Oxford, 2004; pp 219–241. https://doi.org/10.1016/B978-008045154-1.50025-3.
(303) Silva, F.; Sitia, L.; Allevi, R.; Bonizzi, A.; Sevieri, M.; Morasso, C.; Truffi, M.; Corsi, F.; Mazzucchelli, S. Combined Method to Remove Endotoxins from Protein Nanocages for Drug Delivery Applications: The Case of Human Ferritin. *Pharmaceutics* **2021**, *13* (2), 229. https://doi.org/10.3390/pharmaceutics13020229.
(304) Cohen, D. T.; Zhang, C.; Fadzen, C. M.; Mijalis, A. J.; Hie, L.; Johnson, K. D.; Shriver, Z.; Plante, O.; Miller, S. J.; Buchwald, S. L.; Pentelute, B. L. A Chemoselective Strategy for Late-Stage Functionalization of Complex Small Molecules with Polypeptides and Proteins. *Nature Chemistry* **2019**, *11* (1), 78–85. https://doi.org/10.1038/s41557-018-0154-0.
(305) Hirayama, C.; Sakata, M. Chromatographic Removal of Endotoxin from Protein Solutions by Polymer Particles. *Journal of Chromatography B* **2002**, *781* (1), 419–432. https://doi.org/10.1016/S1570-0232(02)00430-0.
(306) Teodorowicz, M.; Perdijk, O.; Verhoek, I.; Govers, C.; Savelkoul, H. F. J.; Tang, Y.; Wichers, H.; Broersen, K. Optimized Triton X-114 Assisted Lipopolysaccharide (LPS) Removal Method Reveals the Immunomodulatory Effect of Food Proteins. *PLoS One* **2017**, *12* (3), e0173778. https://doi.org/10.1371/journal.pone.0173778.
(307) Mamat, U.; Wilke, K.; Bramhill, D.; Schromm, A. B.; Lindner, B.; Kohl, T. A.; Corchero, J. L.; Villaverde, A.; Schaffer, L.; Head, S. R.; Souvignier, C.; Meredith, T. C.; Woodard, R. W. Detoxifying Escherichia Coli for Endotoxin-Free Production of Recombinant Proteins. *Microbial Cell Factories* **2015**, *14* (1), 57. https://doi.org/10.1186/s12934-015-0241-5.
(308) Almo, S. C.; Love, J. D. Better and Faster: Improvements and Optimization for Mammalian Recombinant Protein Production. *Curr Opin Struct Biol* **2014**, *26*, 39–43. https://doi.org/10.1016/j.sbi.2014.03.006.
(309) Khan, K. H. Gene Expression in Mammalian Cells and Its Applications. *Adv Pharm Bull* **2013**, *3* (2), 257–263. https://doi.org/10.5681/apb.2013.042.
(310) Collins, J. M.; Singh, S. K.; White, T. A.; Cesta, D. J.; Simpson, C. L.; Tubb, L. J.; Houser, C. L. Total Wash Elimination for Solid Phase Peptide Synthesis. *Nat Commun* **2023**, *14* (1), 8168. https://doi.org/10.1038/s41467-023-44074-5.
(311) Stráner, P.; Taricska, N.; Szabó, M.; Tóth, G. K.; Perczel, A. Bacterial Expression and/or Solid Phase Peptide Synthesis of 20-40 Amino Acid Long Polypeptides and Miniproteins, the Case Study of Class B GPCR Ligands. *Curr Protein Pept Sci* **2016**, *17* (2), 147–155. https://doi.org/10.2174/1389203716666151102105215.
(312) Clement, H.; Flores, V.; Diego-Garcia, E.; Corrales-Garcia, L.; Villegas, E.; Corzo, G. A Comparison between the Recombinant Expression and Chemical Synthesis of a Short Cysteine-Rich

Insecticidal Spider Peptide. *J Venom Anim Toxins Incl Trop Dis* **2015**, *21*, 19. https://doi.org/10.1186/s40409-015-0018-7.
(313) Shubin, A. D.; Felong, T. J.; Schutrum, B. E.; Joe, D. S. L.; Ovitt, C. E.; Benoit, D. S. W. Encapsulation of Primary Salivary Gland Cells in Enzymatically Degradable Poly(Ethylene Glycol) Hydrogels Promotes Acinar Cell Characteristics. *Acta Biomater* **2017**, *50*, 437–449. https://doi.org/10.1016/j.actbio.2016.12.049.
(314) Wei, Y.; Thyparambil, A. A.; Latour, R. A. Protein Helical Structure Determination Using CD Spectroscopy for Solutions with Strong Background Absorbance from 190-230 Nm. *Biochim Biophys Acta* **2014**, *1844* (12), 2331–2337. https://doi.org/10.1016/j.bbapap.2014.10.001.
(315) Martin, S. R.; Schilstra, M. J. Circular Dichroism and Its Application to the Study of Biomolecules. In *Methods in Cell Biology*; Biophysical Tools for Biologists, Volume One: In Vitro Techniques; Academic Press, 2008; Vol. 84, pp 263–293. https://doi.org/10.1016/S0091-679X(07)84010-6.
(316) HAYASHI, N.; TITANI, K. N-Myristoylated Proteins, Key Components in Intracellular Signal Transduction Systems Enabling Rapid and Flexible Cell Responses. *Proc Jpn Acad Ser B Phys Biol Sci* **2010**, *86* (5), 494–508. https://doi.org/10.2183/pjab.86.494.
(317) Kuznetsova, K. G.; Solovyeva, E. M.; Kuzikov, A. V.; Gorshkov, M. V.; Moshkovskii, S. A. [Modification of cysteine residues for mass spectrometry-based proteomic analysis: facts and artifacts]. *Biomed Khim* **2020**, *66* (1), 18–29. https://doi.org/10.18097/PBMC20206601018.
(318) Fu, D.; Maloney, P. C. Evaluation of Secondary Structure of OxlT, the Oxalate Transporter of *Oxalobacter Formigenes*, by Circular Dichroism Spectroscopy*. *Journal of Biological Chemistry* **1997**, *272* (4), 2129–2135. https://doi.org/10.1074/jbc.272.4.2129.
(319) Mack, L.; Brill, B.; Delis, N.; Groner, B. Endotoxin Depletion of Recombinant Protein Preparations through Their Preferential Binding to Histidine Tags. *Analytical Biochemistry* **2014**, *466*, 83–88. https://doi.org/10.1016/j.ab.2014.08.020.
(320) Bulieris, P. V.; Behrens, S.; Holst, O.; Kleinschmidt, J. H. Folding and Insertion of the Outer Membrane Protein OmpA Is Assisted by the Chaperone Skp and by Lipopolysaccharide*. *Journal of Biological Chemistry* **2003**, *278* (11), 9092–9099. https://doi.org/10.1074/jbc.M211177200.
(321) Schaub, L. J.; Campbell, J. C.; Whitten, S. T. Thermal Unfolding of the N-Terminal Region of P53 Monitored by Circular Dichroism Spectroscopy. *Protein Sci* **2012**, *21* (11), 1682–1688. https://doi.org/10.1002/pro.2146.
(322) Raran-Kurussi, S.; Cherry, S.; Zhang, D.; Waugh, D. S. Removal of Affinity Tags with TEV Protease. *Methods Mol Biol* **2017**, *1586*, 221–230. https://doi.org/10.1007/978-1-4939-6887-9_14.
(323) Engfeldt, T.; Renberg, B.; Brumer, H.; Nygren, P. Å.; Eriksson Karlström, A. Chemical Synthesis of Triple-Labelled Three-Helix Bundle Binding Proteins for Specific Fluorescent Detection of Unlabelled Protein. *ChemBioChem* **2005**, *6* (6), 1043–1050. https://doi.org/10.1002/cbic.200400388.
(324) Lindgren, J.; Ekblad, C.; Abrahmsén, L.; Eriksson Karlström, A. A Native Chemical Ligation Approach for Combinatorial Assembly of Affibody Molecules. *ChemBioChem* **2012**, *13* (7), 1024–1031. https://doi.org/10.1002/cbic.201200052.
(325) Chaplin, D. D. Overview of the Immune Response. *J Allergy Clin Immunol* **2010**, *125* (2 Suppl 2), S3-23. https://doi.org/10.1016/j.jaci.2009.12.980.
(326) Park, M. D.; Silvin, A.; Ginhoux, F.; Merad, M. Macrophages in Health and Disease. *Cell* **2022**, *185* (23), 4259–4279. https://doi.org/10.1016/j.cell.2022.10.007.
(327) Luo, M.; Zhao, F.; Cheng, H.; Su, M.; Wang, Y. Macrophage Polarization: An Important Role in Inflammatory Diseases. *Front Immunol* **2024**, *15*, 1352946. https://doi.org/10.3389/fimmu.2024.1352946.

(328) Lendeckel, U.; Venz, S.; Wolke, C. Macrophages: Shapes and Functions. *ChemTexts* **2022**, *8* (2), 12. https://doi.org/10.1007/s40828-022-00163-4.
(329) Kiseleva, V.; Vishnyakova, P.; Elchaninov, A.; Fatkhudinov, T.; Sukhikh, G. Biochemical and Molecular Inducers and Modulators of M2 Macrophage Polarization in Clinical Perspective. *International Immunopharmacology* **2023**, *122*, 110583. https://doi.org/10.1016/j.intimp.2023.110583.
(330) Wang, L.; Zhang, S.; Wu, H.; Rong, X.; Guo, J. M2b Macrophage Polarization and Its Roles in Diseases. *J Leukoc Biol* **2019**, *106* (2), 345–358. https://doi.org/10.1002/JLB.3RU1018-378RR.
(331) Heideveld, E.; Horcas-Lopez, M.; Lopez-Yrigoyen, M.; Forrester, L. M.; Cassetta, L.; Pollard, J. W. Methods for Macrophage Differentiation and in Vitro Generation of Human Tumor Associated-like Macrophages. In *Methods in Enzymology*; Elsevier, 2020; Vol. 632, pp 113–131. https://doi.org/10.1016/bs.mie.2019.10.005.
(332) Shay, A. E.; Diwakar, B. T.; Guan, B.-J.; Narayan, V.; Urban, J. F.; Prabhu, K. S. IL-4 up-Regulates Cyclooxygenase-1 Expression in Macrophages. *J Biol Chem* **2017**, *292* (35), 14544–14555. https://doi.org/10.1074/jbc.M117.785014.
(333) Li, P.; Hao, Z.; Wu, J.; Ma, C.; Xu, Y.; Li, J.; Lan, R.; Zhu, B.; Ren, P.; Fan, D.; Sun, S. Comparative Proteomic Analysis of Polarized Human THP-1 and Mouse RAW264.7 Macrophages. *Front Immunol* **2021**, *12*, 700009. https://doi.org/10.3389/fimmu.2021.700009.
(334) Genin, M.; Clement, F.; Fattaccioli, A.; Raes, M.; Michiels, C. M1 and M2 Macrophages Derived from THP-1 Cells Differentially Modulate the Response of Cancer Cells to Etoposide. *BMC Cancer* **2015**, *15* (1), 577. https://doi.org/10.1186/s12885-015-1546-9.
(335) Thompson, K. B.; Krispinsky, L. T.; Stark, R. J. Late Immune Consequences of Combat Trauma: A Review of Trauma-Related Immune Dysfunction and Potential Therapies. *Military Medical Research* **2019**, *6* (1), 11. https://doi.org/10.1186/s40779-019-0202-0.
(336) Kimura, F.; Shimizu, H.; Yoshidome, H.; Ohtsuka, M.; Miyazaki, M. Immunosuppression Following Surgical and Traumatic Injury. *Surg Today* **2010**, *40* (9), 793–808. https://doi.org/10.1007/s00595-010-4323-z.
(337) Cheng, A.; Vantucci, C. E.; Krishnan, L.; Ruehle, M. A.; Kotanchek, T.; Wood, L. B.; Roy, K.; Guldberg, R. E. Early Systemic Immune Biomarkers Predict Bone Regeneration after Trauma. *Proceedings of the National Academy of Sciences* **2021**, *118* (8), e2017889118. https://doi.org/10.1073/pnas.2017889118.
(338) Gentile, L. F.; Cuenca, A. G.; Efron, P. A.; Ang, D.; McKinley, B. A.; Moldawer, L. L.; Moore, F. A. Persistent Inflammation and Immunosuppression: A Common Syndrome and New Horizon for Surgical Intensive Care. *J Trauma Acute Care Surg* **2012**, *72* (6), 1491–1501. https://doi.org/10.1097/TA.0b013e318256e000.
(339) Makkoukdji, N.; Pundit, V.; Wyke, M.; Giraldo, J.; Satnarine, T.; Kleiner, G. I.; Gans, M. Targeted Treatments for Immune Dysregulation in Inborn Errors of Immunity. *Explor Immunol.* **2024**, *4* (2), 218–237. https://doi.org/10.37349/ei.2024.00138.
(340) Reeves, A. R. D.; Spiller, K. L.; Freytes, D. O.; Vunjak-Novakovic, G.; Kaplan, D. L. Controlled Release of Cytokines Using Silk-Biomaterials for Macrophage Polarization. *Biomaterials* **2015**, *73*, 272–283. https://doi.org/10.1016/j.biomaterials.2015.09.027.
(341) Sato, T.; Pajarinen, J.; Behn, A.; Jiang, X.; Lin, T.; Loi, F.; Yao, Z.; Egashira, K.; Yang, F.; Goodman, S. B. The Effect of Local IL-4 Delivery or CCL2 Blockade on Implant Fixation and Bone Structural Properties in a Mouse Model of Wear Particle Induced Osteolysis. *Journal of Biomedical Materials Research Part A* **2016**, *104* (9), 2255–2262. https://doi.org/10.1002/jbm.a.35759.
(342) Ueno, M.; Lo, C.-W.; Barati, D.; Conrad, B.; Lin, T.; Kohno, Y.; Utsunomiya, T.; Zhang, N.; Maruyama, M.; Rhee, C.; Huang, E.; Romero-Lopez, M.; Tong, X.; Yao, Z.; Zwingenberger, S.; Yang,

F.; Goodman, S. B. Interleukin-4 Overexpressing Mesenchymal Stem Cells within Gelatin-Based Microribbon Hydrogels Enhance Bone Healing in a Murine Long Bone Critical-Size Defect Model. *Journal of Biomedical Materials Research Part A* **2020**, *108* (11), 2240–2250. https://doi.org/10.1002/jbm.a.36982.

(343) Gadani, S. P.; Cronk, J. C.; Norris, G. T.; Kipnis, J. Interleukin-4: A Cytokine to Remember. *J Immunol* **2012**, *189* (9), 4213–4219. https://doi.org/10.4049/jimmunol.1202246.

(344) Skaria, T.; Burgener, J.; Bachli, E.; Schoedon, G. IL-4 Causes Hyperpermeability of Vascular Endothelial Cells through Wnt5A Signaling. *PLoS One* **2016**, *11* (5), e0156002. https://doi.org/10.1371/journal.pone.0156002.

(345) Zhou, P.; Zheng, T.; Zhao, B. Cytokine-Mediated Immunomodulation of Osteoclastogenesis. *Bone* **2022**, *164*, 116540. https://doi.org/10.1016/j.bone.2022.116540.

(346) Xu, J.; Yu, L.; Liu, F.; Wan, L.; Deng, Z. The Effect of Cytokines on Osteoblasts and Osteoclasts in Bone Remodeling in Osteoporosis: A Review. *Front Immunol* **2023**, *14*, 1222129. https://doi.org/10.3389/fimmu.2023.1222129.

(347) Yamada, A.; Takami, M.; Kawawa, T.; Yasuhara, R.; Zhao, B.; Mochizuki, A.; Miyamoto, Y.; Eto, T.; Yasuda, H.; Nakamichi, Y.; Kim, N.; Katagiri, T.; Suda, T.; Kamijo, R. Interleukin-4 Inhibition of Osteoclast Differentiation Is Stronger than That of Interleukin-13 and They Are Equivalent for Induction of Osteoprotegerin Production from Osteoblasts. *Immunology* **2007**, *120* (4), 573–579. https://doi.org/10.1111/j.1365-2567.2006.02538.x.

(348) Spiller, K. L.; Nassiri, S.; Witherel, C. E.; Anfang, R. R.; Ng, J.; Nakazawa, K. R.; Yu, T.; Vunjak-Novakovic, G. Sequential Delivery of Immunomodulatory Cytokines to Facilitate the M1-to-M2 Transition of Macrophages and Enhance Vascularization of Bone Scaffolds. *Biomaterials* **2015**, *37*, 194–207. https://doi.org/10.1016/j.biomaterials.2014.10.017.

(349) Löfblom, J.; Feldwisch, J.; Tolmachev, V.; Carlsson, J.; Ståhl, S.; Frejd, F. Y. Affibody Molecules: Engineered Proteins for Therapeutic, Diagnostic and Biotechnological Applications. *FEBS Letters* **2010**, *584* (12), 2670–2680. https://doi.org/10.1016/j.febslet.2010.04.014.

(350) Dorogin, J.; Hochstatter, H. B.; Shepherd, S. O.; Svendsen, J. E.; Benz, M. A.; Powers, A. C.; Fear, K. M.; Townsend, J. M.; Prell, J. S.; Hosseinzadeh, P.; Hettiaratchi, M. H. Moderate-Affinity Affibodies Modulate the Delivery and Bioactivity of Bone Morphogenetic Protein-2. *Advanced Healthcare Materials n/a* (n/a), 2300793. https://doi.org/10.1002/adhm.202300793.

(351) Cossarizza, A.; Chang, H.-D.; Radbruch, A.; Abrignani, S.; Addo, R.; Akdis, M.; Andrä, I.; Andreata, F.; Annunziato, F.; Arranz, E.; Bacher, P.; Bari, S.; Barnaba, V.; Barros-Martins, J.; Baumjohann, D.; Beccaria, C. G.; Bernardo, D.; Boardman, D. A.; Borger, J.; Böttcher, C.; Brockmann, L.; Burns, M.; Busch, D. H.; Cameron, G.; Cammarata, I.; Cassotta, A.; Chang, Y.; Chirdo, F. G.; Christakou, E.; Čičin-Šain, L.; Cook, L.; Corbett, A. J.; Cornelis, R.; Cosmi, L.; Davey, M. S.; De Biasi, S.; De Simone, G.; del Zotto, G.; Delacher, M.; Di Rosa, F.; Di Santo, J.; Diefenbach, A.; Dong, J.; Dörner, T.; Dress, R. J.; Dutertre, C.-A.; Eckle, S. B. G.; Eede, P.; Evrard, M.; Falk, C. S.; Feuerer, M.; Fillatreau, S.; Fiz-Lopez, A.; Follo, M.; Foulds, G. A.; Fröbel, J.; Gagliani, N.; Galletti, G.; Gangaev, A.; Garbi, N.; Garrote, J. A.; Geginat, J.; Gherardin, N. A.; Gibellini, L.; Ginhoux, F.; Godfrey, D. I.; Gruarin, P.; Haftmann, C.; Hansmann, L.; Harpur, C. M.; Hayday, A. C.; Heine, G.; Hernández, D. C.; Herrmann, M.; Hoelsken, O.; Huang, Q.; Huber, S.; Huber, J. E.; Huehn, J.; Hundemer, M.; Hwang, W. Y. K.; Iannacone, M.; Ivison, S. M.; Jäck, H.-M.; Jani, P. K.; Keller, B.; Kessler, N.; Ketelaars, S.; Knop, L.; Knopf, J.; Koay, H.-F.; Kobow, K.; Kriegsmann, K.; Kristyanto, H.; Krueger, A.; Kuehne, J. F.; Kunze-Schumacher, H.; Kvistborg, P.; Kwok, I.; Latorre, D.; Lenz, D.; Levings, M. K.; Lino, A. C.; Liotta, F.; Long, H. M.; Lugli, E.; MacDonald, K. N.; Maggi, L.; Maini, M. K.; Mair, F.; Manta, C.; Manz, R. A.; Mashreghi, M.-F.; Mazzoni, A.; McCluskey, J.; Mei, H. E.; Melchers, F.; Melzer, S.; Mielenz, D.; Monin, L.; Moretta, L.; Multhoff, G.; Muñoz, L. E.; Muñoz-Ruiz, M.; Muscate, F.; Natalini, A.;

Neumann, K.; Ng, L. G.; Niedobitek, A.; Niemz, J.; Almeida, L. N.; Notarbartolo, S.; Ostendorf, L.; Pallett, L. J.; Patel, A. A.; Percin, G. I.; Peruzzi, G.; Pinti, M.; Pockley, A. G.; Pracht, K.; Prinz, I.; Pujol-Autonell, I.; Pulvirenti, N.; Quatrini, L.; Quinn, K. M.; Radbruch, H.; Rhys, H.; Rodrigo, M. B.; Romagnani, C.; Saggau, C.; Sakaguchi, S.; Sallusto, F.; Sanderink, L.; Sandrock, I.; Schauer, C.; Scheffold, A.; Scherer, H. U.; Schiemann, M.; Schildberg, F. A.; Schober, K.; Schoen, J.; Schuh, W.; Schüler, T.; Schulz, A. R.; Schulz, S.; Schulze, J.; Simonetti, S.; Singh, J.; Sitnik, K. M.; Stark, R.; Starossom, S.; Stehle, C.; Szelinski, F.; Tan, L.; Tarnok, A.; Tornack, J.; Tree, T. I. M.; van Beek, J. J. P.; van de Veen, W.; van Gisbergen, K.; Vasco, C.; Verheyden, N. A.; von Borstel, A.; Ward-Hartstonge, K. A.; Warnatz, K.; Waskow, C.; Wiedemann, A.; Wilharm, A.; Wing, J.; Wirz, O.; Wittner, J.; Yang, J. H. M.; Yang, J. Guidelines for the Use of Flow Cytometry and Cell Sorting in Immunological Studies (Third Edition). *European Journal of Immunology* **2021**, *51* (12), 2708–3145. https://doi.org/10.1002/eji.202170126.

(352) Svendsen, J. E.; Ford, M. R.; Asnes, C. L.; Oh, S. C.; Dorogin, J.; Fear, K. M.; O'Hara-Smith, J. R.; Harms, M. J.; Hosseinzadeh, P.; Hettiaratchi, M. H. Applying Computational Protein Design to Engineer Affibodies for Affinity-Controlled Delivery of Vascular Endothelial Growth Factor and Platelet-Derived Growth Factor. bioRxiv December 21, 2024, p 2024.12.18.629300. https://doi.org/10.1101/2024.12.18.629300.

(353) Dorogin, J.; Benz, M. A.; Moore, C. J.; Benoit, D. S. W.; Hettiaratchi, M. H. Recombinant and Synthetic Affibodies Function Comparably for Modulating Protein Release. *Cel. Mol. Bioeng.* **2024**. https://doi.org/10.1007/s12195-024-00815-0.

(354) Müller, T.; Oehlenschläger, F.; Buehner, M. Human Interleukin-4 and Variant R88Q: Phasing X-Ray Diffraction Data by Molecular Replacement Using X-Ray and Nuclear Magnetic Resonance Models. *Journal of Molecular Biology* **1995**, *247* (2), 360–372. https://doi.org/10.1006/jmbi.1994.0144.

(355) Hage, T.; Sebald, W.; Reinemer, P. Crystal Structure of the Interleukin-4/Receptor α Chain Complex Reveals a Mosaic Binding Interface. *Cell* **1999**, *97* (2), 271–281. https://doi.org/10.1016/S0092-8674(00)80736-9.

(356) Chanput, W.; Mes, J. J.; Wichers, H. J. THP-1 Cell Line: An in Vitro Cell Model for Immune Modulation Approach. *International Immunopharmacology* **2014**, *23* (1), 37–45. https://doi.org/10.1016/j.intimp.2014.08.002.

(357) Huang, Y.; Tian, C.; Li, Q.; Xu, Q. TET1 Knockdown Inhibits Porphyromonas Gingivalis LPS/IFN-γ-Induced M1 Macrophage Polarization through the NF-κB Pathway in THP-1 Cells. *International Journal of Molecular Sciences* **2019**, *20* (8), 2023. https://doi.org/10.3390/ijms20082023.

(358) Daigneault, M.; Preston, J. A.; Marriott, H. M.; Whyte, M. K. B.; Dockrell, D. H. The Identification of Markers of Macrophage Differentiation in PMA-Stimulated THP-1 Cells and Monocyte-Derived Macrophages. *PLoS One* **2010**, *5* (1), e8668. https://doi.org/10.1371/journal.pone.0008668.

(359) Bolanos-Garcia, V. M.; Davies, O. R. Structural Analysis and Classification of Native Proteins from E. Coli Commonly Co-Purified by Immobilised Metal Affinity Chromatography. *Biochimica et Biophysica Acta (BBA) - General Subjects* **2006**, *1760* (9), 1304–1313. https://doi.org/10.1016/j.bbagen.2006.03.027.

(360) Chanput, W.; Mes, J. J.; Savelkoul, H. F. J.; Wichers, H. J. Characterization of Polarized THP-1 Macrophages and Polarizing Ability of LPS and Food Compounds. *Food Funct.* **2013**, *4* (2), 266–276. https://doi.org/10.1039/C2FO30156C.

(361) Orecchioni, M.; Ghosheh, Y.; Pramod, A. B.; Ley, K. Macrophage Polarization: Different Gene Signatures in M1(LPS+) vs. Classically and M2(LPS–) vs. Alternatively Activated Macrophages. *Frontiers in Immunology* **2019**, *10*.

(362) He, L.; Jhong, J.-H.; Chen, Q.; Huang, K.-Y.; Strittmatter, K.; Kreuzer, J.; DeRan, M.; Wu, X.; Lee, T.-Y.; Slavov, N.; Haas, W.; Marneros, A. G. Global Characterization of Macrophage Polarization Mechanisms and Identification of M2-Type Polarization Inhibitors. *Cell reports* **2021**, *37* (5), 109955. https://doi.org/10.1016/j.celrep.2021.109955.
(363) Yin, C.; Cai, J.; Gou, Y.; Li, D.; Tang, H.; Wang, L.; Liu, H.; Luo, B. Dynamic Changes in Human THP-1-Derived M1-to-M2 Macrophage Polarization during Thelazia Callipaeda MIF Induction. *Front Immunol* **2023**, *13*, 1078880. https://doi.org/10.3389/fimmu.2022.1078880.
(364) Bittrich, S.; Segura, J.; Duarte, J. M.; Burley, S. K.; Rose, Y. RCSB Protein Data Bank: Exploring Protein 3D Similarities via Comprehensive Structural Alignments. *Bioinformatics* **2024**, *40* (6), btae370. https://doi.org/10.1093/bioinformatics/btae370.
(365) Conlon, P. J.; Tyler, S.; Grabstein, K. H.; Morrissey, P. Interleukin-4 (B-Cell Stimulatory Factor-1) Augments the in Vivo Generation of Cytotoxic Cells in Immunosuppressed Animals. *Biotechnol Ther* **1989**, *1* (1), 31–41.
(366) Mertowska, P.; Mertowski, S.; Smarz-Widelska, I.; Grywalska, E. Biological Role, Mechanism of Action and the Importance of Interleukins in Kidney Diseases. *Int J Mol Sci* **2022**, *23* (2), 647. https://doi.org/10.3390/ijms23020647.
(367) Pena, O. M.; Afacan, N.; Pistolic, J.; Chen, C.; Madera, L.; Falsafi, R.; Fjell, C. D.; Hancock, R. E. W. Synthetic Cationic Peptide IDR-1018 Modulates Human Macrophage Differentiation. *PLoS ONE* **2013**, *8* (1), e52449. https://doi.org/10.1371/journal.pone.0052449.
(368) Muñoz-Rojas, A. R.; Kelsey, I.; Pappalardo, J. L.; Chen, M.; Miller-Jensen, K. Co-Stimulation with Opposing Macrophage Polarization Cues Leads to Orthogonal Secretion Programs in Individual Cells. *Nat Commun* **2021**, *12* (1), 301. https://doi.org/10.1038/s41467-020-20540-2.
(369) Wang, N.; Liang, H.; Zen, K. Molecular Mechanisms That Influence the Macrophage M1–M2 Polarization Balance. *Frontiers in Immunology* **2014**, *5*.
(370) Ohradanova-Repic, A.; Machacek, C.; Fischer, M. B.; Stockinger, H. Differentiation of Human Monocytes and Derived Subsets of Macrophages and Dendritic Cells by the HLDA10 Monoclonal Antibody Panel. *Clinical & Translational Immunology* **2016**, *5* (1), e55. https://doi.org/10.1038/cti.2015.39.
(371) Guo, S.; DiPietro, L. A. Factors Affecting Wound Healing. *J Dent Res* **2010**, *89* (3), 219–229. https://doi.org/10.1177/0022034509359125.
(372) Ellis, S.; Lin, E. J.; Tartar, D. Immunology of Wound Healing. *Curr Derm Rep* **2018**, *7* (4), 350–358. https://doi.org/10.1007/s13671-018-0234-9.
(373) Bouyer, M.; Guillot, R.; Lavaud, J.; Plettinx, C.; Olivier, C.; Curry, V.; Boutonnat, J.; Coll, J.-L.; Peyrin, F.; Josserand, V.; Bettega, G.; Picart, C. Surface Delivery of Tunable Doses of BMP-2 from an Adaptable Polymeric Scaffold Induces Volumetric Bone Regeneration. *Biomaterials* **2016**, *104*, 168–181. https://doi.org/10.1016/j.biomaterials.2016.06.001.
(374) Bigalke, C.; Luderer, F.; Wulf, K.; Storm, T.; Löbler, M.; Arbeiter, D.; Rau, B. M.; Nizze, H.; Vollmar, B.; Schmitz, K.-P.; Klar, E.; Sternberg, K. VEGF-Releasing Suture Material for Enhancement of Vascularization: Development, in Vitro and in Vivo Study. *Acta Biomaterialia* **2014**, *10* (12), 5081–5089. https://doi.org/10.1016/j.actbio.2014.09.002.
(375) Dashtimoghadam, E.; Fahimipour, F.; Tongas, N.; Tayebi, L. Microfluidic Fabrication of Microcarriers with Sequential Delivery of VEGF and BMP-2 for Bone Regeneration. *Sci Rep* **2020**, *10* (1), 11764. https://doi.org/10.1038/s41598-020-68221-w.
(376) Kempen, D. H. R.; Lu, L.; Heijink, A.; Hefferan, T. E.; Creemers, L. B.; Maran, A.; Yaszemski, M. J.; Dhert, W. J. A. Effect of Local Sequential VEGF and BMP-2 Delivery on Ectopic and Orthotopic Bone Regeneration. *Biomaterials* **2009**, *30* (14), 2816–2825. https://doi.org/10.1016/j.biomaterials.2009.01.031.

(377) Wang, Q.; Zhang, Y.; Li, B.; Chen, L. Controlled Dual Delivery of Low Doses of BMP-2 and VEGF in a Silk Fibroin–Nanohydroxyapatite Scaffold for Vascularized Bone Regeneration. *J. Mater. Chem. B* **2017**, *5* (33), 6963–6972. https://doi.org/10.1039/C7TB00949F.
(378) Fiedler, J.; Röderer, G.; Günther, K.-P.; Brenner, R. E. BMP-2, BMP-4, and PDGF-Bb Stimulate Chemotactic Migration of Primary Human Mesenchymal Progenitor Cells. *J Cell Biochem* **2002**, *87* (3), 305–312. https://doi.org/10.1002/jcb.10309.
(379) Moncal, K. K.; Tigli Aydın, R. S.; Godzik, K. P.; Acri, T. M.; Heo, D. N.; Rizk, E.; Wee, H.; Lewis, G. S.; Salem, A. K.; Ozbolat, I. T. Controlled Co-Delivery of pPDGF-B and pBMP-2 from Intraoperatively Bioprinted Bone Constructs Improves the Repair of Calvarial Defects in Rats. *Biomaterials* **2022**, *281*, 121333. https://doi.org/10.1016/j.biomaterials.2021.121333.
(380) Kuhn, L. T.; Ou, G.; Charles, L.; Hurley, M. M.; Rodner, C. M.; Gronowicz, G. Fibroblast Growth Factor-2 and Bone Morphogenetic Protein-2 Have a Synergistic Stimulatory Effect on Bone Formation in Cell Cultures From Elderly Mouse and Human Bone. *The Journals of Gerontology: Series A* **2013**, *68* (10), 1170–1180. https://doi.org/10.1093/gerona/glt018.
(381) Charles, L. F.; Woodman, J. L.; Ueno, D.; Gronowicz, G.; Hurley, M. M.; Kuhn, L. T. Effects of Low Dose FGF-2 and BMP-2 on Healing of Calvarial Defects in Old Mice. *Experimental Gerontology* **2015**, *64*, 62–69. https://doi.org/10.1016/j.exger.2015.02.006.
(382) Lin, D.; Chai, Y.; Ma, Y.; Duan, B.; Yuan, Y.; Liu, C. Rapid Initiation of Guided Bone Regeneration Driven by Spatiotemporal Delivery of IL-8 and BMP-2 from Hierarchical MBG-Based Scaffold. *Biomaterials* **2019**, *196*, 122–137. https://doi.org/10.1016/j.biomaterials.2017.11.011.
(383) Brooker, J. E.; Bykowski, M. R.; Camison, L.; Yerneni, S.; Campbell, P. G.; Weiss, L.; Mooney, M. P.; Cray, J. J.; Cooper, G. M.; Losee, J. E. Interleukin-10 Does Not Augment Osseous Regeneration in the Scarred Calvarial Defect Achieved with Low-Dose Biopatterned BMP2. *Plastic and Reconstructive Surgery* **2019**, *143* (6), 1215e. https://doi.org/10.1097/PRS.0000000000005640.
(384) Maruyama, M.; Rhee, C.; Utsunomiya, T.; Zhang, N.; Ueno, M.; Yao, Z.; Goodman, S. B. Modulation of the Inflammatory Response and Bone Healing. *Frontiers in Endocrinology* **2020**, *11*.
(385) Tachi, K.; Takami, M.; Sato, H.; Mochizuki, A.; Zhao, B.; Miyamoto, Y.; Tsukasaki, H.; Inoue, T.; Shintani, S.; Koike, T.; Honda, Y.; Suzuki, O.; Baba, K.; Kamijo, R. Enhancement of Bone Morphogenetic Protein-2-Induced Ectopic Bone Formation by Transforming Growth Factor-B1. *Tissue Eng Part A* **2011**, *17* (5–6), 597–606. https://doi.org/10.1089/ten.TEA.2010.0094.
(386) Krishnan, L.; Priddy, L. B.; Esancy, C.; Klosterhoff, B. S.; Stevens, H. Y.; Tran, L.; Guldberg, R. E. Delivery Vehicle Effects on Bone Regeneration and Heterotopic Ossification Induced by High Dose BMP-2. *Acta Biomaterialia* **2017**, *49*, 101–112. https://doi.org/10.1016/j.actbio.2016.12.012.
(387) Barozzi, A.; Lavoie, R. A.; Day, K. N.; Prodromou, R.; Menegatti, S. Affibody-Binding Ligands. *IJMS* **2020**, *21* (11), 3769. https://doi.org/10.3390/ijms21113769.
(388) Hastie, T.; Tibshirani, R.; Friedman, J. *The Elements of Statistical Learning*; Springer Series in Statistics; Springer New York: New York, NY, 2009. https://doi.org/10.1007/978-0-387-84858-7.
(389) Philip, A. K.; Pathak, K. Osmotic Flow through Asymmetric Membrane: A Means for Controlled Delivery of Drugs with Varying Solubility. *AAPS PharmSciTech* **2006**, *7* (3), E1–E11. https://doi.org/10.1208/pt070356.
(390) Hastie, T.; Tibshirani, R.; Friedman, J. Random Forests. In *The Elements of Statistical Learning: Data Mining, Inference, and Prediction*; Hastie, T., Tibshirani, R., Friedman, J., Eds.; Springer: New York, NY, 2009; pp 587–604. https://doi.org/10.1007/978-0-387-84858-7_15.
(391) Bannigan, P.; Aldeghi, M.; Bao, Z.; Häse, F.; Aspuru-Guzik, A.; Allen, C. Machine Learning Directed Drug Formulation Development. *Advanced Drug Delivery Reviews* **2021**, *175*, 113806. https://doi.org/10.1016/j.addr.2021.05.016.

(392) Kowalek, P.; Loch-Olszewska, H.; Szwabiński, J. Classification of Diffusion Modes in Single-Particle Tracking Data: Feature-Based versus Deep-Learning Approach. *Phys. Rev. E* **2019**, *100* (3), 032410. https://doi.org/10.1103/PhysRevE.100.032410.
(393) Rahman, R.; Dhruba, S. R.; Ghosh, S.; Pal, R. Functional Random Forest with Applications in Dose-Response Predictions. *Sci Rep* **2019**, *9* (1), 1628. https://doi.org/10.1038/s41598-018-38231-w.
(394) Di Mare, E. J.; Punia, A.; Lamm, M. S.; Rhodes, T. A.; Gormley, A. J. Data-Driven Design of Novel Polymer Excipients for Pharmaceutical Amorphous Solid Dispersions. *Bioconjugate Chem.* **2024**, *35* (9), 1363–1372. https://doi.org/10.1021/acs.bioconjchem.4c00294.
(395) Liu, H.; Zhang, W.; Nie, L.; Ding, X.; Luo, J.; Zou, L. Predicting Effective Drug Combinations Using Gradient Tree Boosting Based on Features Extracted from Drug-Protein Heterogeneous Network. *BMC Bioinformatics* **2019**, *20*, 645. https://doi.org/10.1186/s12859-019-3288-1.
(396) Alshahrani, S. M.; Alotaibi, H. F.; Begum, M. Y. Computational Analysis of Controlled Drug Release from Porous Polymeric Carrier with the Aid of Mass Transfer and Artificial Intelligence Modeling. *Sci Rep* **2024**, *14* (1), 28422. https://doi.org/10.1038/s41598-024-79749-6.
(397) Reddy, N.; Gebreslasie, M.; Ismail, R. A Hybrid Partial Least Squares and Random Forest Approach to Modelling Forest Structural Attributes Using Multispectral Remote Sensing Data. *South African Journal of Geomatics* **2017**, *6* (3), 377–394. https://doi.org/10.4314/sajg.v6i3.8.
(398) Tahraoui, H.; Amrane, A.; Belhadj, A.-E.; Zhang, J. Modeling the Organic Matter of Water Using the Decision Tree Coupled with Bootstrap Aggregated and Least-Squares Boosting. *Environmental Technology & Innovation* **2022**, *27*, 102419. https://doi.org/10.1016/j.eti.2022.102419.
(399) Guarnieri, D.; De Capua, A.; Ventre, M.; Borzacchiello, A.; Pedone, C.; Marasco, D.; Ruvo, M.; Netti, P. A. Covalently Immobilized RGD Gradient on PEG Hydrogel Scaffold Influences Cell Migration Parameters. *Acta Biomaterialia* **2010**, *6* (7), 2532–2539. https://doi.org/10.1016/j.actbio.2009.12.050.
(400) Ouyang, L.; Dan, Y.; Shao, Z.; Yang, S.; Yang, C.; Liu, G.; Duan, D. MMP-Sensitive PEG Hydrogel Modified with RGD Promotes bFGF, VEGF and EPC-Mediated Angiogenesis. *Exp Ther Med* **2019**, *18* (4), 2933–2941. https://doi.org/10.3892/etm.2019.7885.
(401) Reiser, A.; Woschée, D.; Mehrotra, N.; Krzysztoń, R.; Strey, H. H.; Rädler, J. O. Correlation of mRNA Delivery Timing and Protein Expression in Lipid-Based Transfection. *Integrative Biology* **2019**, *11* (9), 362–371. https://doi.org/10.1093/intbio/zyz030.
(402) Dai, Q.; Guo, M.; Guo, Y.; Liu, X.; Liu, Y.; Teng, Z. A Least Square Method Based Model for Identifying Protein Complexes in Protein-Protein Interaction Network. *Biomed Res Int* **2014**, *2014*, 720960. https://doi.org/10.1155/2014/720960.
(403) Paarakh, M. P.; Jose, P. A.; Setty, C.; Peterchristoper, G. V. RELEASE KINETICS – CONCEPTS AND APPLICATIONS. *International Journal of Pharmacy Research & Technology (IJPRT)* **2018**, *8* (1), 12–20. https://doi.org/10.31838/ijprt/08.01.02.
(404) Chicco, D.; Warrens, M. J.; Jurman, G. The Coefficient of Determination R-Squared Is More Informative than SMAPE, MAE, MAPE, MSE and RMSE in Regression Analysis Evaluation. *PeerJ Comput Sci* **2021**, *7*, e623. https://doi.org/10.7717/peerj-cs.623.
(405) Goodfellow, I.; Bengio, Y.; Courville, A. *Deep Learning*; Adaptive computation and machine learning; The MIT Press: Cambridge, Massachusetts, 2016.
(406) Luzina, I. G.; Keegan, A. D.; Heller, N. M.; Rook, G. A. W.; Shea-Donohue, T.; Atamas, S. P. Regulation of Inflammation by Interleukin-4: A Review of "Alternatives." *J Leukoc Biol* **2012**, *92* (4), 753–764. https://doi.org/10.1189/jlb.0412214.
(407) Betz, O. B.; Betz, V. M.; Nazarian, A.; Egermann, M.; Gerstenfeld, L. C.; Einhorn, T. A.; Vrahas, M. S.; Bouxsein, M. L.; Evans, C. H. Delayed Administration of Adenoviral BMP-2 Vector Improves the

Formation of Bone in Osseous Defects. *Gene Ther* **2007**, *14* (13), 1039–1044. https://doi.org/10.1038/sj.gt.3302956.
(408) Vignon, A.; Flaget, A.; Michelas, M.; Djeghdir, M.; Defrancq, E.; Coche-Guerente, L.; Spinelli, N.; Van der Heyden, A.; Dejeu, J. Direct Detection of Low-Molecular-Weight Compounds in 2D and 3D Aptasensors by Biolayer Interferometry. *ACS Sens.* **2020**, *5* (8), 2326–2330. https://doi.org/10.1021/acssensors.0c00925.
(409) Xu, H.; Wang, H.; Zhao, Y.; Zhan, W.; Chen, S.; Wang, P. Detection of Small Molecule Compounds Bound to Proteins. *Chinese Journal of Analytical Chemistry* **2024**, *52* (6), 100398. https://doi.org/10.1016/j.cjac.2024.100398.
(410) Gabryelczyk, B.; Szilvay, G. R.; Singh, V. K.; Mikkilä, J.; Kostiainen, M. A.; Koskinen, J.; Linder, M. B. Engineering of the Function of Diamond-like Carbon Binding Peptides through Structural Design. *Biomacromolecules* **2015**, *16* (2), 476–482. https://doi.org/10.1021/bm501522j.
(411) Luo, L.; Xu, H.; Wang, C.; Li, Z.; Guo, L.; Li, X.; Luo, L.; Wang, J.; Kang, W.; Xie, J. Double Amplification upon Immuno-Gold Nanoparticles Promoted Trace Measurement of Ricin by Biolayer Interferometry. *Sensors and Actuators B: Chemical* **2022**, *358*, 131472. https://doi.org/10.1016/j.snb.2022.131472.
(412) Antonova, E.; Le, T. K.; Burge, R.; Mershon, J. Tibia Shaft Fractures: Costly Burden of Nonunions. *BMC Musculoskelet Disord* **2013**, *14* (1), 42. https://doi.org/10.1186/1471-2474-14-42.
(413) Chitnis, A.; Ray, B.; Sparks, C.; Grebenyuk, Y.; Vanderkarr, M.; Holy, C. E. Long Bone Fractures: Treatment Patterns and Factors Contributing to Use of Intramedullary Nailing. *Expert Review of Medical Devices* **2020**, *17* (7), 731–737. https://doi.org/10.1080/17434440.2020.1779055.
(414) Vanderkarr, M. F.; Ruppenkamp, J. W.; Vanderkarr, M.; Holy, C. E.; Blauth, M. Risk Factors and Healthcare Costs Associated with Long Bone Fracture Non-Union: A Retrospective US Claims Database Analysis. *Journal of Orthopaedic Surgery and Research* **2023**, *18* (1), 745. https://doi.org/10.1186/s13018-023-04232-3.
(415) De La Riva, B.; Nowak, C.; Sánchez, E.; Hernández, A.; Schulz-Siegmund, M.; Pec, M. K.; Delgado, A.; Évora, C. VEGF-Controlled Release within a Bone Defect from Alginate/Chitosan/PLA-H Scaffolds. *European Journal of Pharmaceutics and Biopharmaceutics* **2009**, *73* (1), 50–58. https://doi.org/10.1016/j.ejpb.2009.04.014.
(416) Schoonraad, S. A.; Jaimes, A. A.; Singh, A. J. X.; Croland, K. J.; Bryant, S. J. Osteogenic Effects of Covalently Tethered rhBMP-2 and rhBMP-9 in an MMP-Sensitive PEG Hydrogel Nanocomposite. *Acta Biomaterialia* **2023**, *170*, 53–67. https://doi.org/10.1016/j.actbio.2023.08.045.
(417) E. Vantucci, C.; Krishan, L.; Cheng, A.; Prather, A.; Roy, K.; E. Guldberg, R. BMP-2 Delivery Strategy Modulates Local Bone Regeneration and Systemic Immune Responses to Complex Extremity Trauma. *Biomaterials Science* **2021**, *9* (5), 1668–1682. https://doi.org/10.1039/D0BM01728K.
(418) Klosterhoff, B. S.; Kaiser, J.; Nelson, B. D.; Karipott, S. S.; Ruehle, M. A.; Hollister, S. J.; Weiss, J. A.; Ong, K. G.; Willett, N. J.; Guldberg, R. E. Wireless Sensor Enables Longitudinal Monitoring of Regenerative Niche Mechanics during Rehabilitation That Enhance Bone Repair. *Bone* **2020**, *135*, 115311. https://doi.org/10.1016/j.bone.2020.115311.
(419) Zhang, Y.; Liu, S.; Li, T.; Zhang, L.; Azhar, U.; Ma, J.; Zhai, C.; Zong, C.; Zhang, S. Cytocompatible and Non-Fouling Zwitterionic Hyaluronic Acid-Based Hydrogels Using Thiol-Ene "Click" Chemistry for Cell Encapsulation. *Carbohydrate Polymers* **2020**, *236*, 116021. https://doi.org/10.1016/j.carbpol.2020.116021.
(420) Schweller, R. M.; Wu, Z. J.; Klitzman, B.; West, J. L. Reducing Stiffness of Protease Sensitive and Cell Adhesive PEG Hydrogels Promotes Neovascularization In Vivo. *Ann Biomed Eng* **2017**, *45* (6), 1387–1398. https://doi.org/10.1007/s10439-017-1822-8.

(421) Sun, M.; Chi, G.; Li, P.; Lv, S.; Xu, J.; Xu, Z.; Xia, Y.; Tan, Y.; Xu, J.; Li, L.; Li, Y. Effects of Matrix Stiffness on the Morphology, Adhesion, Proliferation and Osteogenic Differentiation of Mesenchymal Stem Cells. *Int. J. Med. Sci.* **2018**, *15* (3), 257–268. https://doi.org/10.7150/ijms.21620.
(422) Lee, S.; Tong, X.; Yang, F. The Effects of Varying Poly(Ethylene Glycol) Hydrogel Crosslinking Density and the Crosslinking Mechanism on Protein Accumulation in Three-Dimensional Hydrogels. *Acta Biomaterialia* **2014**, *10* (10), 4167–4174. https://doi.org/10.1016/j.actbio.2014.05.023.
(423) Žigon-Branc, S.; Markovic, M.; Van Hoorick, J.; Van Vlierberghe, S.; Dubruel, P.; Zerobin, E.; Baudis, S.; Ovsianikov, A. Impact of Hydrogel Stiffness on Differentiation of Human Adipose-Derived Stem Cell Microspheroids. *Tissue Eng Part A* **2019**, *25* (19–20), 1369–1380. https://doi.org/10.1089/ten.tea.2018.0237.
(424) Sarrigiannidis, S. O.; Rey, J. M.; Dobre, O.; González-García, C.; Dalby, M. J.; Salmeron-Sanchez, M. A Tough Act to Follow: Collagen Hydrogel Modifications to Improve Mechanical and Growth Factor Loading Capabilities. *Materials Today Bio* **2021**, *10*, 100098. https://doi.org/10.1016/j.mtbio.2021.100098.
(425) Brandl, F.; Kastner, F.; Gschwind, R. M.; Blunk, T.; Tessmar, J.; Göpferich, A. Hydrogel-Based Drug Delivery Systems: Comparison of Drug Diffusivity and Release Kinetics. *J Control Release* **2010**, *142* (2), 221–228. https://doi.org/10.1016/j.jconrel.2009.10.030.
(426) Hagedorn, T. J.; Krishnamurty, S.; Grosse, I. R. An Information Model to Support User-Centered Design of Medical Devices. *Journal of Biomedical Informatics* **2016**, *62*, 181–194. https://doi.org/10.1016/j.jbi.2016.07.010.
(427) Akbarian, M.; Chen, S.-H. Instability Challenges and Stabilization Strategies of Pharmaceutical Proteins. *Pharmaceutics* **2022**, *14* (11), 2533. https://doi.org/10.3390/pharmaceutics14112533.
(428) Škrlec, K.; Štrukelj, B.; Berlec, A. Non-Immunoglobulin Scaffolds: A Focus on Their Targets. *Trends in Biotechnology* **2015**, *33* (7), 408–418. https://doi.org/10.1016/j.tibtech.2015.03.012.
(429) Nord, K.; Gunneriusson, E.; Ringdahl, J.; Ståhl, S.; Uhlén, M.; Nygren, P.-Å. Binding Proteins Selected from Combinatorial Libraries of an α-Helical Bacterial Receptor Domain. *Nat Biotechnol* **1997**, *15* (8), 772–777. https://doi.org/10.1038/nbt0897-772.
(430) Ståhl, S.; Gräslund, T.; Eriksson Karlström, A.; Frejd, F. Y.; Nygren, P.-Å.; Löfblom, J. Affibody Molecules in Biotechnological and Medical Applications. *Trends in Biotechnology* **2017**, *35* (8), 691–712. https://doi.org/10.1016/j.tibtech.2017.04.007.
(431) Li, X.; Gong, J. P. Design Principles for Strong and Tough Hydrogels. *Nat Rev Mater* **2024**, *9* (6), 380–398. https://doi.org/10.1038/s41578-024-00672-3.
(432) Visser, J.; Melchels, F. P. W.; Jeon, J. E.; Van Bussel, E. M.; Kimpton, L. S.; Byrne, H. M.; Dhert, W. J. A.; Dalton, P. D.; Hutmacher, D. W.; Malda, J. Reinforcement of Hydrogels Using Three-Dimensionally Printed Microfibres. *Nat Commun* **2015**, *6* (1), 6933. https://doi.org/10.1038/ncomms7933.
(433) Dalton, P. D. Melt Electrowriting with Additive Manufacturing Principles. *Current Opinion in Biomedical Engineering* **2017**, *2*, 49–57. https://doi.org/10.1016/j.cobme.2017.05.007.
(434) Saiz, P. G.; Reizabal, A.; Vilas-Vilela, J. L.; Dalton, P. D.; Lanceros-Mendez, S. Materials and Strategies to Enhance Melt Electrowriting Potential. *Advanced Materials* **2024**, *36* (24), 2312084. https://doi.org/10.1002/adma.202312084.
(435) O'Neill, K. L.; Dalton, P. D. A Decade of Melt Electrowriting. *Small Methods* **2023**, *7* (7), 2201589. https://doi.org/10.1002/smtd.202201589.
(436) Devlin, B. L.; Kuba, S.; Hall, P. C.; McCosker, A. B.; Pickering, E.; Dalton, P. D.; Klein, T. J.; Woodruff, M. A.; Paxton, N. C. A Melt Electrowriting Toolbox for Automated G-Code Generation

and Toolpath Correction of Flat and Tubular Constructs. *Advanced Materials Technologies n/a* (n/a), 2400419. https://doi.org/10.1002/admt.202400419.
(437) Pickering, E.; Paxton, N. C.; Bo, A.; O'Connell, B.; King, M.; Woodruff, M. A. 3D Printed Tubular Scaffolds with Massively Tailorable Mechanical Behavior. *Advanced Engineering Materials* **2022**, *24* (11), 2200479. https://doi.org/10.1002/adem.202200479.
(438) Wang, W. Lyophilization and Development of Solid Protein Pharmaceuticals. *International Journal of Pharmaceutics* **2000**, *203* (1), 1–60. https://doi.org/10.1016/S0378-5173(00)00423-3.
(439) Marco-Dufort, B.; Janczy, J. R.; Hu, T.; Lütolf, M.; Gatti, F.; Wolf, M.; Woods, A.; Tetter, S.; Sridhar, B. V.; Tibbitt, M. W. Thermal Stabilization of Diverse Biologics Using Reversible Hydrogels. *Sci. Adv.* **2022**, *8* (31), eabo0502. https://doi.org/10.1126/sciadv.abo0502.
(440) Luong, P. T.; Browning, M. B.; Bixler, R. S.; Cosgriff-Hernandez, E. Drying and Storage Effects on Poly(Ethylene Glycol) Hydrogel Mechanical Properties and Bioactivity. *J Biomed Mater Res A* **2014**, *102* (9), 3066–3076. https://doi.org/10.1002/jbm.a.34977.
(441) Odziomek, K.; Drabczyk, A. K.; Kościelniak, P.; Konieczny, P.; Barczewski, M.; Bialik-Wąs, K. The Role of Freeze-Drying as a Multifunctional Process in Improving the Properties of Hydrogels for Medical Use. *Pharmaceuticals* **2024**, *17* (11), 1512. https://doi.org/10.3390/ph17111512.
(442) Tarabarova, A. G.; Lopukhov, A.; Fedorov, A. N.; Yurkova, M. S. Novel His-Tag Variants for Insertion Inside Polypeptide Chain. *ACS Omega* **2024**, *9* (1), 858–865. https://doi.org/10.1021/acsomega.3c06682.
(443) Greenfield, N. J. Using Circular Dichroism Collected as a Function of Temperature to Determine the Thermodynamics of Protein Unfolding and Binding Interactions. *Nat Protoc* **2006**, *1* (6), 2527–2535. https://doi.org/10.1038/nprot.2006.204.
(444) Rehmann, M. S.; Skeens, K. M.; Kharkar, P. M.; Ford, E. M.; Maverakis, E.; Lee, K. H.; Kloxin, A. M. Tuning and Predicting Mesh Size and Protein Release from Step Growth Hydrogels. *Biomacromolecules* **2017**, *18* (10), 3131–3142. https://doi.org/10.1021/acs.biomac.7b00781.
(445) Raeber, G. P.; Lutolf, M. P.; Hubbell, J. A. Molecularly Engineered PEG Hydrogels: A Novel Model System for Proteolytically Mediated Cell Migration. *Biophysical Journal* **2005**, *89* (2), 1374–1388. https://doi.org/10.1529/biophysj.104.050682.
(446) Peppas, N. Hydrogels in Pharmaceutical Formulations. *European Journal of Pharmaceutics and Biopharmaceutics* **2000**, *50* (1), 27–46. https://doi.org/10.1016/S0939-6411(00)00090-4.
(447) Kokubo, S.; Vana, P. Easy Access to the Characteristic Ratio of Polymers Using Ion-Mobility Mass Spectrometry. *Macromolecular Chemistry and Physics* **2017**, *218* (1), 1600373. https://doi.org/10.1002/macp.201600373.
(448) Liu, Y.; Puthia, M.; Sheehy, E. J.; Ambite, I.; Petrlova, J.; Prithviraj, S.; Oxborg, M. W.; Sebastian, S.; Vater, C.; Zwingenberger, S.; Struglics, A.; Bourgine, P. E.; O'Brien, F. J.; Raina, D. B. Sustained Delivery of a Heterodimer Bone Morphogenetic Protein-2/7 via a Collagen Hydroxyapatite Scaffold Accelerates and Improves Critical Femoral Defect Healing. *Acta Biomaterialia* **2023**, *162*, 164–181. https://doi.org/10.1016/j.actbio.2023.03.028.
(449) Ritger, P. L.; Peppas, N. A. A Simple Equation for Description of Solute Release I. Fickian and Non-Fickian Release from Non-Swellable Devices in the Form of Slabs, Spheres, Cylinders or Discs. *Journal of Controlled Release* **1987**, *5* (1), 23–36. https://doi.org/10.1016/0168-3659(87)90034-4.
(450) Hochleitner, G.; Chen, F.; Blum, C.; Dalton, P. D.; Amsden, B.; Groll, J. Melt Electrowriting below the Critical Translation Speed to Fabricate Crimped Elastomer Scaffolds with Non-Linear Extension Behaviour Mimicking That of Ligaments and Tendons. *Acta Biomaterialia* **2018**, *72*, 110–120. https://doi.org/10.1016/j.actbio.2018.03.023.

(451) Lee, H.; Venable, R. M.; MacKerell, A. D.; Pastor, R. W. Molecular Dynamics Studies of Polyethylene Oxide and Polyethylene Glycol: Hydrodynamic Radius and Shape Anisotropy. *Biophysical Journal* **2008**, *95* (4), 1590–1599. https://doi.org/10.1529/biophysj.108.133025.
(452) Welzel, P. B.; Prokoph, S.; Zieris, A.; Grimmer, M.; Zschoche, S.; Freudenberg, U.; Werner, C. Modulating Biofunctional starPEG Heparin Hydrogels by Varying Size and Ratio of the Constituents. *Polymers* **2011**, *3* (1), 602–620. https://doi.org/10.3390/polym3010602.
(453) Siepmann, J.; Siepmann, F. Modeling of Diffusion Controlled Drug Delivery. *Journal of Controlled Release* **2012**, *161* (2), 351–362. https://doi.org/10.1016/j.jconrel.2011.10.006.
(454) Viswanadha, L. S.; Arcot, Y.; Lin, Y.-T.; Akbulut, M. E. S. A Comparative Investigation of Release Kinetics of Paclitaxel from Natural Protein and Macromolecular Nanocarriers in Nanoscale Drug Delivery Systems. *JCIS Open* **2024**, *15*, 100120. https://doi.org/10.1016/j.jciso.2024.100120.
(455) Glassman, S. D.; Carreon, L.; Djurasovic, M.; Campbell, M. J.; Puno, R. M.; Johnson, J. R.; Dimar, J. R. Posterolateral Lumbar Spine Fusion with INFUSE Bone Graft. *The Spine Journal* **2007**, *7* (1), 44–49. https://doi.org/10.1016/j.spinee.2006.06.381.
(456) Valentín, J. L.; Carretero-González, J.; Mora-Barrantes, I.; Chassé, W.; Saalwächter, K. Uncertainties in the Determination of Cross-Link Density by Equilibrium Swelling Experiments in Natural Rubber. *Macromolecules* **2008**, *41* (13), 4717–4729. https://doi.org/10.1021/ma8005087.
(457) Boerckel, J. D.; Kolambkar, Y. M.; Stevens, H. Y.; Lin, A. S. P.; Dupont, K. M.; Guldberg, R. E. Effects of in Vivo Mechanical Loading on Large Bone Defect Regeneration. *J Orthop Res* **2012**, *30* (7), 1067–1075. https://doi.org/10.1002/jor.22042.
(458) Liu, J.; Yang, L.; Liu, K.; Gao, F. Hydrogel Scaffolds in Bone Regeneration: Their Promising Roles in Angiogenesis. *Front. Pharmacol.* **2023**, *14*. https://doi.org/10.3389/fphar.2023.1050954.
(459) Mozipo, E. A.; Galindo, A. N.; Khachatourian, J. D.; Harris, C. G.; Dorogin, J.; Spaulding, V. R.; Ford, M. R.; Singhal, M.; Fogg, K. C.; Hettiaratchi, M. H. Statistical Optimization of Hydrazone-Crosslinked Hyaluronic Acid Hydrogels for Protein Delivery. *J. Mater. Chem. B* **2024**. https://doi.org/10.1039/D3TB01588B.
(460) Bai, T.; Sun, F.; Zhang, L.; Sinclair, A.; Liu, S.; Ella-Menye, J.-R.; Zheng, Y.; Jiang, S. Restraint of the Differentiation of Mesenchymal Stem Cells by a Nonfouling Zwitterionic Hydrogel. *Angewandte Chemie International Edition* **2014**, *53* (47), 12729–12734. https://doi.org/10.1002/anie.201405930.
(461) Unuvar Purcu, D.; Korkmaz, A.; Gunalp, S.; Helvaci, D. G.; Erdal, Y.; Dogan, Y.; Suner, A.; Wingender, G.; Sag, D. Effect of Stimulation Time on the Expression of Human Macrophage Polarization Markers. *PLoS One* **2022**, *17* (3), e0265196. https://doi.org/10.1371/journal.pone.0265196.
(462) Shiratori, H.; Feinweber, C.; Luckhardt, S.; Linke, B.; Resch, E.; Geisslinger, G.; Weigert, A.; Parnham, M. J. THP-1 and Human Peripheral Blood Mononuclear Cell-Derived Macrophages Differ in Their Capacity to Polarize in Vitro. *Molecular Immunology* **2017**, *88*, 58–68. https://doi.org/10.1016/j.molimm.2017.05.027.
(463) Peshkova, M.; Korneev, A.; Suleimanov, S.; Vlasova, I. I.; Svistunov, A.; Kosheleva, N.; Timashev, P. MSCs' Conditioned Media Cytokine and Growth Factor Profiles and Their Impact on Macrophage Polarization. *Stem Cell Research & Therapy* **2023**, *14* (1), 142. https://doi.org/10.1186/s13287-023-03381-w.
(464) Lin, T.; Kohno, Y.; Huang, J.-F.; Romero-Lopez, M.; Maruyama, M.; Ueno, M.; Pajarinen, J.; Nathan, K.; Yao, Z.; Yang, F.; Wu, J. Y.; Goodman, S. B. Preconditioned or IL4-Secreting Mesenchymal Stem Cells Enhanced Osteogenesis at Different Stages. *Tissue Eng Part A* **2019**, *25* (15–16), 1096–1103. https://doi.org/10.1089/ten.tea.2018.0292.

(465) Moravej, A.; Kouhpayeh, A.; Geramizadeh, B.; Azarpira, N.; Yaghobi, R.; Mansoori, Y.; Karimi, M.-H. The Effect of Mesenchymal Stem Cells on the Expression of IDO and Qa2 Molecules in Dendritic Cells. *Adv Pharm Bull* **2019**, *9* (1), 56–63. https://doi.org/10.15171/apb.2019.007.